Improving Strain-Sensing Electronic Skins Based on Electrical Impedance Tomography

A thesis submitted to Auckland University of Technology
in fulfilment of the requirements for the degree of
Doctor of Philosophy

Supervisors:
Prof. Andrew Lowe
Dr. Anubha Kalra

By
Huiyang Zhang

2022

School of Engineering, Computer and Mathematical Sciences
Auckland University of Technology

Abstract

Background: Electrical impedance tomography (EIT) possesses the capability of converting almost any electrically conductive material into an electronic skin (E-skin) that detects and transduces spatially distributed pressures and strains. In recent years, EIT-based E-skins have gained considerable research interest due to their potential applications in wearable devices, human-machine interfaces, soft robotics, and prosthetics. However, their practicality is limited due to a severe lack of accuracy.

Aim: This research aims to discover new strategies for integrating EIT with flexible strain-transducing materials to realize an EIT-based E-skin that offers improved performance in sensing two-dimensional strain distribution. Towards this goal, the critical limitations possessed by the existing approach for realizing EIT-based E-skins are mitigated by adopting a novel structural model, constraining the solution space, and utilizing a material that provides consistent strain-signal transduction.

Method: First, the limitations of various strain-sensing materials and conventional reconstruction algorithms were analysed via a literature review and a simulation study. Second, the reconstruction algorithms of EIT were adapted by replacing the conventional structural model with a new model inspired by the nodal admittance matrix (NAM) and constraining the solution space according to material properties. The effectiveness of the proposed reconstruction method was verified by an additional simulation study. Third, comprehensive material testing was performed to examine the strain-sensing characteristics of two candidate materials and allow the selection of a more suitable material. Finally, the selected material was used to fabricate an E-skin sensor, whose performance was validated experimentally.

Results: The experimental results showed that the sensor successfully achieved detecting, localizing, and transducing spatially distributed strains. The average percentage of mismatch between the applied strains and the reconstructed strains was less than 20%.

Conclusions: The results confirm that the NAM-based structural model, the method of constraining the solution space, and the material preparation procedures proposed in this work are promising for realizing E-skin sensors that offer improved strain-sensing performance.

Table of Contents

List of Figures

List of Tables

Attestation of Authorship

I hereby declare that this submission is my own work and that, to the best of my knowledge and belief, it contains no material previously published or written by another person (except where explicitly defined in the acknowledgements), nor material which to a substantial extent has been submitted for the award of any other degree or diploma of a university.

Signature of candidate

Acknowledgement

I would like to express my gratitude to my supervisor, Prof. Andrew Lowe, for providing me with the opportunity to pursue this PhD research and supporting me with inspiring ideas, which helped me overcome various challenges throughout the journey. Also, I would like to express my appreciation to my secondary supervisor, Dr. Anubha Kalra, for her encouragement and advice, which allowed me to improve the quality of this work and achieve better results.

I would like to acknowledge several financial supports provided by the Institute of Biomedical Technologies (IBTec) and Auckland University of Technology. These funds enabled me to attend research events and purchase essential materials for conducting experiments.

I appreciate all the people who have offered me assistance during the process of completing this study.

Finally, I would like to thank my beloved mom, dad and sisters, who never lose their faith in me.

Symbols

ϵ	Strain
A	Area
l	Length
i	Index of nodes
k	Index of element
σ	Electrical conductivity
I	Current injection patterns
U	Electric potential distribution
u	Point-wise electric potential
H	Jacobian matrix
R	Regularization matrix
C	Admittance
χ	Capacitance
L	Number of electrodes
N	Number of nodes
K	Number of elements
P	A path in space
J	Current density
$\nabla \cdot$	Divergence operator
$\nabla \times$	Curl operator
∇	Gradient
$\times$	Vector cross product
$\cdot$	Vector dot product
B	Magnetic field
E	Electric field
g	Injecting current density
$\hat{n}$	Unit norm vector

S	Boundary of domain
γ	Space
V	Test function
Φ	Basis function
e_l	boundary electrodes
$\|e_l\|$	Length of electrodes
z	Contact impedance of electrodes
G	Number of current injections
e	Error
e_{LS}	Least-square error
Y	Nodal admittance matrix
Z	Electrode voltage variation
f	Frequency
$\sum$	Matrix column and row index operator
$*$	Matrix dimension (rows by columns)

Abbreviations

EIT	Electrical Impedance Tomography
CT	Computed Tomography
MRI	Magnetic Resonance Imaging
GF	Gauge Factor
1D	One-dimensional
2D	Two-dimensional
DC	Direct Current
AC	Alternating Current
PDMS	Polydimethylsiloxane
TPU	Thermoplastic polyurethane
PG	Propylene Glycol
CVD	Chemical Vapor Deposition
CNT	Carbon Nanotube
SWCNT	Singlewall Carbon Nanotube
MWCNT	Multiwall Carbon Nanotube
NiNW	Nickel Nanowire
ZnO	Zinc Oxide
GNP	Graphene Nanoplatlet
GNF	Graphene Nanofibre
CuNW	Copper Nanowire
DS	Dragon Skin
NiCr	Nichrome
Au	Gold
AuNP	Gold Nanoparticle
PS	Polystyrene
PSNF	Polystyrene Nanofiber
HDPE	High-Density Polyethene

PBT	Polybutylene Terephthalate
EGaIn	Eutectic Gallium Indium
PC	Polycarbonate
SR	Silicone Rubber
NR	Natural Rubber
UV	Ultraviolet
PAAm	Poly(acrylamide) Momomer
MBAA	N,N'-Methylenebisacrylamide
HMI	Structural Health Monitoring
SEM	Scanning Electron Microscope
ECG	Electrocardiography
EEG	Electroencephalography
EMG	Electromyography
OLS	Ordinary Least Square
NNLS	Non-negative Least Square
BVLS	Bounded-Value Least Square
OLS	Ordinary Least Square
WR	Weighted Residual
ADC	Analog-To-Digital Converter
MUX	Multiplexer
PCB	Printed Circuit Board
I^2C	Inter-Integrated Circuit
PDE	Partial Differential Equation
TLS	Total Least Squares
SVD	Singular Value Decomposition
TV	Total Variation
SNR	Signal-to-Noise Ratio

Chapter 1 Introduction

1.1 Electronic Skins

An electronic skin (E-skin) is an artificial skin that imitates the sensory function of human skin while also preserving mechanical flexibility. E-skins were invented for acquiring information regarding the spatial distribution of mechanical stimuli applied to their surface. Compared to conventional tactile sensors, which can only detect mechanical stimuli applied to a single point or along a fixed direction, E-skins based on integrated sensor arrays incorporating abundant sensing nodes allow transducing mechanical stimuli received at multiple locations and directions. Although several E-skins for sensing other parameters, such as temperature, humidity and bioelectrical signals have also been reported in previous research[1], [2], the E-skins addressed in this thesis refer to only tactile sensors for transducing mechanical stimuli, which are strains and pressures.

An E-skin is generally composed of three layers following a sandwich structure. A protective layer covers the top surface to provide mechanical encapsulation and electrical insulation. A substrate layer at the bottom provides conformity to the object. A sensor layer in the middle is formed by a plurality of sensing nodes and their connecting circuitry. Each sensing node serves as an individual sensor, which transduces mechanical stimuli into electrical signals independently via a resistive[15] or a capacitive[16] approach. The circuitry connects each sensing node to an external data acquisition device. Figure 1-1 shows an example of such an E-skin fabricated by depositing patterned Indium (III) Selenide (In_2Se_3) as strain sensing element and gold electrodes on a thin Polyethylene Terephthalate (PET) polymer film[3].

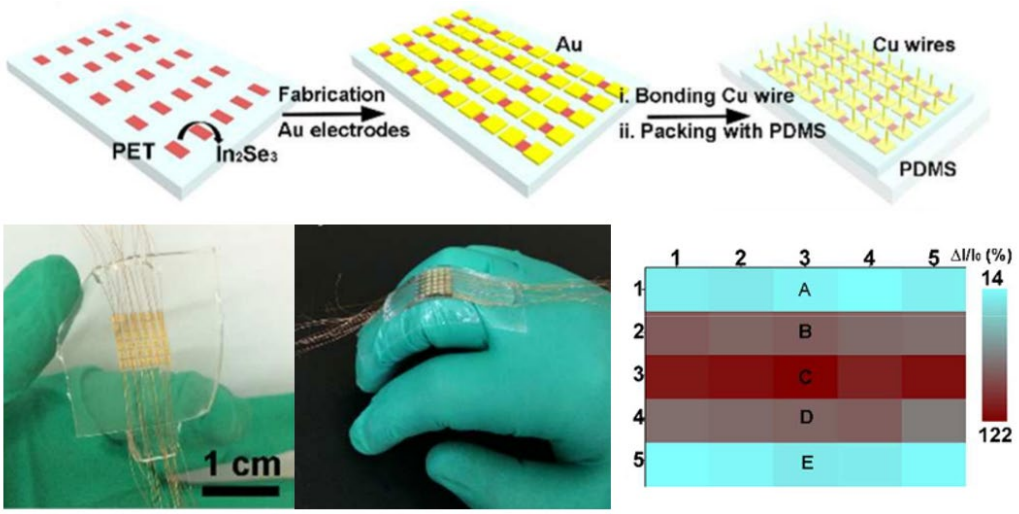

Figure 1-1 An electronic-skin strain sensor for sensing spatial distribution of strain[3] (Copyright 2016, American Chemical Society. Adapted with permission).

There are a few previous works on development of electronic skins. For example, Lipomi et al.[4] fabricated an optically transparent electronic skin based on depositing carbon nanotubes in a polymer to form the structure of a parallel plate capacitor. Takahashi et al.[5] developed an carbon nanotubes-based electronic skin that possesses a honeycomb mesh structure. Cheng et al.[6] proposed an electronic skin fabricated using pre-cracked silver nanowire based fibers for measuring pressure, strain, and bending.

Electronic skins possess the ability to detect, localize, and quantify applied mechanical stimuli with enhanced spatial resolution; hence allowing a more comprehensive range of practical applications. Tekscan™ located in Boston, US, has successfully commercialized a wide range of products targeting industrial users, using their spatial tactile sensing technology. Examples include a body pressure measurement system for measuring pressure distribution between the human body and support surfaces, an I-scan system for estimating the reaction force distribution under the soles for gait analysis, a grip system for quantifying the distribution of grasping forces applied by the human hand or a robotic hand while grasping objects, and a wiper system for evaluating wiper blade force profiles and interface pressure distribution. Apart from Tekscan, there are a variety of other companies around the globe that provide spatial

tactile sensing systems developed for various purposes, such as PPS (UK), Sensor Products Inc (US), Vista Medical (Canada).

Electronic-skin sensors exhibited versatile utilization in various applications and commercialized products. However, according to Tekscan Industrial Sensor Catalog, they have a limited service life, which is application-dependent. The intricate and delicately patterned sensor arrays embedded in their sensing layer are vulnerable to damage caused by excessive force, abrasion, and penetration caused by sharp objects. After repeated service, loss in precision is inevitable due to material fatigue and degradation. Replacing defective sensors yields extra cost and raises the burden in budgeting. For example, a Tekscan in-shoe pressure mapping sensor costs approximately US$ 350. Seeking novel methods for developing electronic skins in a more low-cost manner has become a new trend in related research.

1.2 E-skins Inspired by Electrical Impedance Tomography

A recently emerging approach for achieving electronic skins features incorporating flexible piezoresistive materials with a real-time imaging technology known as electrical impedance tomography (EIT). EIT is a non-invasive imaging method invented by John G. Webster over 40 years ago[7]. The original purpose of inventing EIT was for lung ventilation monitoring; later, it was also implemented for tumour detection[8] and heartbeat monitoring[9].

Briefly, EIT utilizes voltage data measured from the surface of an electrically conductive object to estimate its internal conductivity distribution. The typical operating procedure for performing EIT is shown in Figure 1-2. A plurality of electrodes are attached around the area of interest, which in this case is around the chest for lung ventilation imaging. An electric potential distribution over the cross-section is

produced when a current is fed and sunk via a selected pair of electrodes. Meanwhile, voltages at the remaining electrodes are measured and recorded. This procedure is repeated as the current feeding is switched to all other different electrode pairings. The recorded voltage data corresponding to each current injection pattern is then used as the input to a selected reconstruction algorithm, which calculates an output that conveys the electrical conductivity distribution in the cross section.

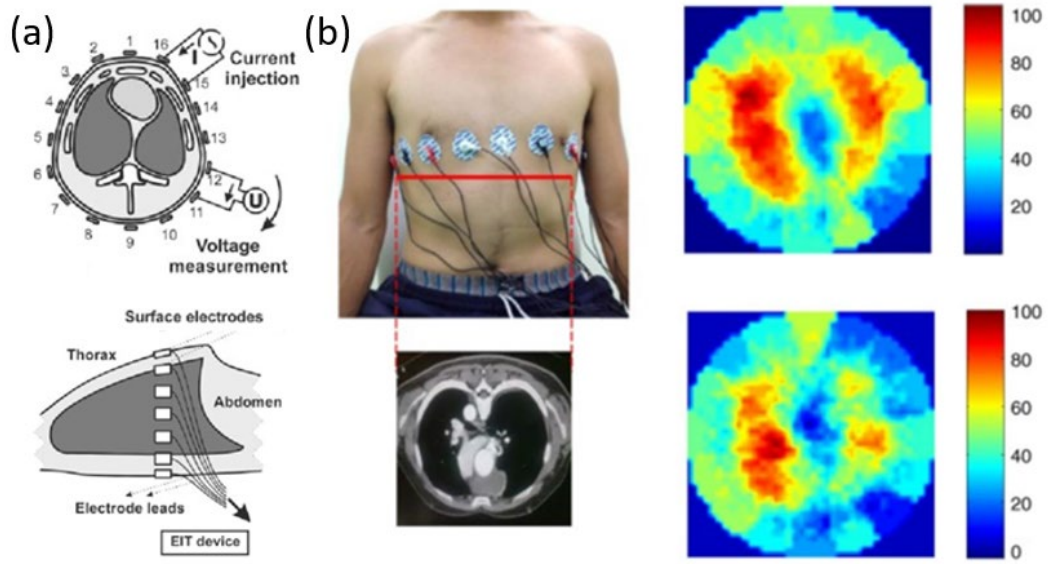

Figure 1-2 Electrical impedance tomography. (a) Electrodes are attached around the chest *[10]*. (Copyright 2002 the American Physiological Society. Reused with permission) . (b) Image reconstruction *[11]* (Copyright 2015 Elsevier Ltd. Redistributed with permission).

By adopting the working principle of EIT, the electrical conductivity distribution in a flexible piezoresistive material, typically in the form of a conductive membrane or fabric, can also be estimated in a similar style to imaging the human body. An example of applying EIT for achieving strain and pressure mapping is depicted in Figure 1-3[12], where a piece of stretchable and conductive fabric is bound to a rigid ring to constrain its boundary, along which 16 electrodes are connected to conduct current injection and voltage measurement. The electrical conductivity of the fabric is sensitive to physical deformation. When mechanical stimuli that cause elongation in the yarns are induced, the conductivity of the elongated yarns decreases. Under the electrical potential distribution produced by constant current injection patterns, this change in the interior

conductivity leads to alterations in voltages measured by the boundary electrodes. The time-variant difference in electrode voltage data is measured before and after applying the mechanical stimuli. The voltage variation then serves as the input to a selected reconstruction algorithm, which outputs estimated conductivity distributions. Finally, the applied mechanical stimuli are localized and evaluated according to the obtained estimation.

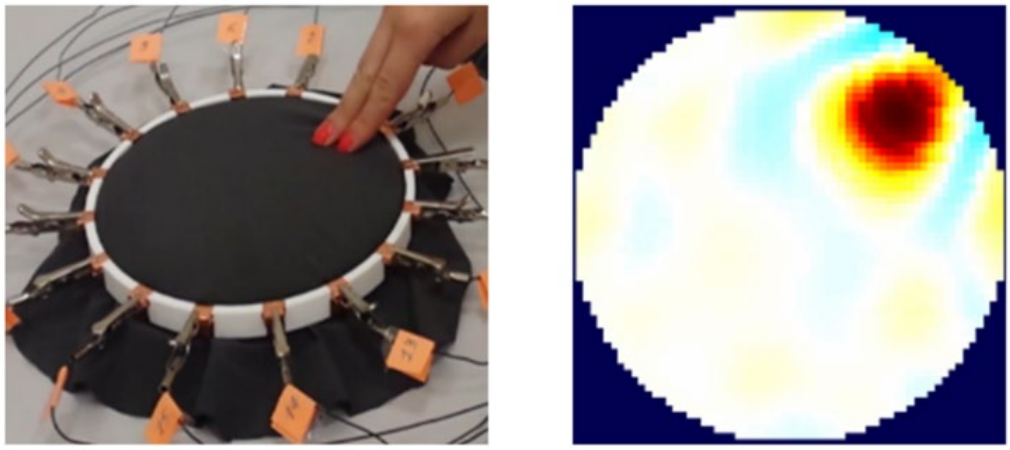

Figure 1-3 Implementing EIT on a piece of conductive fabric for spatial tactile sensing*[12]*. (Copyright 2017 Russo et al. Reused with permission)

Electronic skins based on the incorporation of EIT with flexible sensing materials have several advantages. First of all, EIT possesses well-matched compatibility with piezoresistive sensors in terms of electrical properties. It is convenient to employ EIT on piezoresistive sensors because both technologies produce their signal outputs equivalent to electrical conductivity. The mutually shared outputs allow the ready incorporation of EIT and soft sensors without a need to modify the hardware or software.

Secondly, EIT provides good temporal resolution for transducing mechanical stimuli received by sensing material. For example, 107 frames per second (fps) was achieved by a wearable EIT system developed by Yu et al.[13], and 650 fps was reported for V5R, a commercialized product developed by Industrial Tomography Systems Limited, UK. Contrary to low frame rates, which may cause missing information in dynamic imaging, the high frame rate makes EIT a particularly suitable method for actualizing

real-time sensing applications. For instance, a motion-detection glove used as a human-machine interface may involve rapid finger movements, which can only be captured at a high frame rate.

Furthermore, another advantage of EIT-based electronic skins is simplicity in both data acquisition hardware and sensor fabrication methods. The hardware for implementing EIT typically only requires three basic functional blocks: a constant current source, a current switching circuit, and an analog-to-digital converter for voltage measurements. The entire set of hardware for implementing EIT can be realized on a small, printed circuit board (PCB) connected to an external CPU for data processing and reconstruction. The tiny footprint allows portable applications of electronic skins under various scenarios. In terms of sensor fabrication, the sensing material can be easily fabricated without the additional effort required for array patterning. Any piezoresistive sensing material in the form of a thin film can be readily upgraded into an electronic skin simply by attaching a number of electrodes around its perimeter. The simplicity in sensor architecture and the versatility in material selection suggest EIT-based electronic skins can be produced in a low-cost manner.

The EIT-based approach for realizing electronic skins is attractive due to its simplicity in structure and versatility in available materials. However, EIT suffers from a significant lack of accuracy in practice. A considerable mismatch between the reconstructed results and the reality is typically present during EIT imaging. Furthermore, additional errors may be introduced due to the measurement instrument's noise and the sensing material's inconsistency. Therefore, EIT-based electronic skins lack the capability of providing reliable estimations for interpreting the applied mechanical stimuli. The accuracy of EIT-based electronic skins must be significantly improved to allow their practical utilization and grant them commercial value.

1.3 Motivations and Scope

In a nutshell, conventional E-skins based on integrated sensor arrays have a limited lifespan and are costly. On the other hand, E-skins based on the new EIT-based approach offer low cost, but they exhibit poor accuracy. Electronic-skin sensors that possess both cost-effectiveness and reliability are demanded for practical utilization. Therefore, the primary motivation of this thesis is to achieve a low-cost and reliable E-skin sensor by improving the accuracy of the EIT-based sensing approach.

Moreover, it is worth noting that most of the existing E-skin sensors, including the commercialized ones, can only measure the distribution of normal pressures; they cannot directly convey material deformation, which is described by the strain distribution. The downside to this limitation is that the sensors' applications are restricted within a narrow scope, and the sensors are only useful for specialised purposes. On the other hand, a major benefit of allowing sensors to acquire strain distribution information is enabling motion detection and deformation monitoring, which significantly expand such sensors' potential applications in wider fields, including soft robotics, wearable devices, structural health monitoring, and human-machine interface. For example, an electronic skin granted with the strain sensing capability can be mounted onto a glove to recognize hand gestures; it can be mounted onto a robotic arm to provide feedback regarding rotation, bending, torsion and elongation; it can be attached to the surface of fragile objects or solid structures to detect crack, deformation, and damage; it can also be integrated with prosthetics[14] to provide the sensation of stretching. In the past, although some works[15]–[17] have attempted to employ EIT-based E-skins in sensing strain distribution, the persistent issue with poor accuracy of EIT remains unresolved, and there is a lack of methods of mitigation. Therefore, another motivation of this thesis is to improve the versatility in

the usage of E-skin sensors by finding an effective method to achieve strain distribution sensing.

1.4 Thesis Overview

Briefly, this research aims to investigate the limitations of EIT-based electronic skins and improve their accuracy in performing spatial strain sensing, such that they can gain better practicality in a wider range of applications. This thesis is structured as follows:

- Chapter 1 introduces the background of flexible strain sensors and electronic skins for spatial tactile sensing. The emerging approach of realizing electronic skins using electrical impedance tomography is introduced.
- Chapter 2 provides a literature review to demonstrate the basic working principle of EIT and the current state-of-art progress on flexible strain sensing materials. Various transduction mechanisms and previous works on EIT-based electronic skins are reviewed and discussed. Based on the literature review, research gaps and objectives are identified.
- Chapter 3 presents a simulation study to evaluate the performance of EIT to determine the reasons that lead to the lack of accuracy in EIT-based sensors. The reconstruction algorithms of EIT are explained in detail. A stimulation study is performed to reveal several critical limitations associated with using EIT for enabling spatial strain sensing. The limitations have not been adequately identified or mitigated by previous studies. Some preliminary attempts for mitigating the limitations are performed.
- Chapter 4 proposes an adapted reconstruction algorithm as a novel approach to overcome the identified limitations. The concepts of nodal admittance matrix and non-negative least squares are introduced. A simulation for demonstrating its effectiveness is presented.

- Chapter 5 describes the selection and preparation of piezoresistive materials suitable for constituting a strain-sensing electronic skin. A comprehensive set of material testing for evaluating the reliability of the performance of the prepared sensors is demonstrated to reveal various sensor parameters, including stretchability, hysteresis, overshoot, dynamic stability, and durability.
- Chapter 6 validates the proposed reconstruction method experimentally by implementing the algorithm on a physical grid-network sensor. The sensor is fabricated using a novel and cost-effective method. A simple hardware system for implementing EIT is introduced. The experimental results that convey pressure and strain distribution are demonstrated.
- Chapter 7 provides a summary of this thesis and clarifies its contributions. Recommendations for future work are discussed.

Chapter 2 Literature Review

2.1 Introduction

This literature review consists of three subsections associated with EIT-based E-skins. These sections cover the fundamentals of EIT, the basics of strain-sensing materials, and previous works that combine the former two technologies for realizing electronic skins, respectively.

Section 2.2 introduces the literature related to EIT technology. The basic operating principles of EIT are described. Different structural models and reconstruction algorithms for performing EIT are reviewed. The typical hardware systems used for data acquisition involved in EIT are illustrated. Commonly used measurement methodologies are explained.

In section 2.3, existing literature regarding flexible strain sensing materials is reviewed. This section includes various transduction mechanisms, sensing materials, and fabrication methods. Ideally, a sensing material is expected to transduce mechanical stimuli into electrical signals in an accurate and reproducible manner. However, most sensing materials possess some defects. In order to evaluate the reliability of different types of sensing materials, the critical parameters that characterise their strain-sensing performance are addressed. Based on these parameters, their advantages and limitations are compared and discussed.

Section 2.4 reviews previously reported electronic skins based on integrating flexible piezoresistive materials and EIT technology. The materials utilized for transducing mechanical stimuli into electrical signals are introduced. Their performance in spatial tactile sensing is discussed.

In section 2.5, research gaps are identified based on the information gathered from the literature review. Research objectives for filling the gaps are clarified accordingly. A

suitable research methodology is designed in section 2.6 to achieve the ultimate objective of developing an EIT-based electronic skin with improved strain-sensing performance.

2.2 Electrical Impedance Tomography

2.2.1 Operating Principles of Tomography Imaging

EIT takes the electrical voltages measured at each electrode under a selected current injection pattern as the input to a selected reconstruction algorithm. The algorithm produces estimations of the electrical conductivity distribution within the area of interest. In order to create an electric field distribution inside the area of interest, an electric current must be injected into the domain. The injected current can be alternating current (AC) or direct current (DC). For imaging the human body, DC injection simplifies the system design substantially but introduces problems due to the effect of electrode polarization, which results in the charge accumulation on the electrode-skin interface causing a drift in the interfacial potential difference at lower frequencies[18]. The effect of electrode polarization can be alleviated using AC injection. When AC is injected, the output voltage data is measured as fluctuating voltages, and the result of reconstruction is the electrical impedance distribution; When DC is injected, time-invariant voltages are measured, and the reconstructed result is the electrical resistance distribution. A schematic[19] that illustrates the current injection applied to a domain is shown in Figure 2-1(a). A number of electrodes are attached around the targeted cross-sectional area. A current is fed into the domain through one of the electrodes and flows out through another selected electrode. The presence of the current flow creates a field of electrical potential distributed over the domain. Voltage measurements are taken between every electrode and a selected ground reference point. Then the current source and the current sink are switched to the next pair of electrodes according to a

selected current injection pattern, and voltage measurements are repeated for all remaining electrodes. This procedure is repeated until the selected current injection pattern is completed. All measured voltages under each current injection are recorded as the input data to reconstruct the electrical impedance or resistance distribution within the domain. Note that the electrodes carrying current are typically excluded from voltage measurement to reduce the effects of noise caused by the electrode contact impedance[20], which is the impedance possessed by the interfacial layer between electrodes and the skin.

The reconstruction algorithm of EIT consists of two parts: constructing the forward problem and solving the inverse problem[21], as illustrated in Figure 2-1 (b). The forward problem is associated with creating a mathematical model for predicting the electrical potential distribution (U) yielded from a known electrical conductivity distribution, such that the voltage data at each boundary electrode (U_L) can be obtained by extracting them from U. Due to the mathematical complexity possessed by analytical methods for solving such a problem, the finite element method (FEM) is typically employed to obtain approximate results numerically[22]. FEM first discretizes the entire domain into a finite number of triangular elements. Then, it takes the current injection (I), conductivity (σ), and the mesh geometry for all elements including nodal coordinates, sizes of the elements, and lengths of edges as the input data, to find a numerical solution of electrical potentials (U) at each node. The electric potential at the electrodes (U_L) is then extracted from U.

The inverse problem reverses the structural model derived from the forward problem to estimate an unknown conductivity distribution from known electrode voltage data. Ideally, reconstruction of absolute values of conductivity distribution is obtained; in this case, the inverse problem takes the electrical potential (U_L) at each electrode as the input to calculate the conductivity distribution (σ). In practice, however, reconstruction of time-difference variation in conductivity distribution is typically employed, because the time-difference approach offers better accuracy than the absolute approach by allowing self-cancellation due to mismatch in domain shapes, skin-electrode contact

and initially assumed impedance distribution[23], [24]. For time-difference EIT, a Jacobian matrix is derived from the structural model to map the electrical potential variation at each electrode, denoted as ΔU_L, towards the variation in conductivity distribution, denoted as $\Delta\sigma$. Because ΔU_L is only a tiny fraction of the information in ΔU, the inverse problem is heavily ill-posed. Based on the definition provided by Jacques Hadamard, a French mathematician in the early 20th century, the ill-posedness essentially means that the system of equations for solving the inverse problem is underdetermined, and consequently, there are non-unique solutions. Therefore, regularization-based methods[25] are employed to produce a final solution of $\Delta\sigma$ with either a least L_1 error or a least L_2 error.

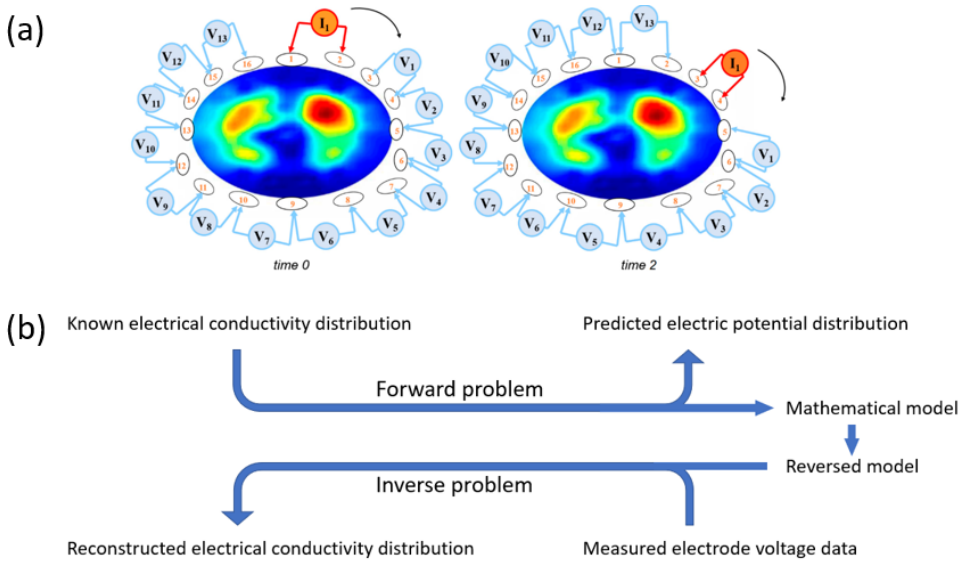

Figure 2-1 Working principles of EIT. (a)Current injection and voltage measurement*[19]*. (Copyright 2019 Putensen et al. Reused with permission). Injected current gives rise to an electric field that distributes uneven electrical potentials over the domain. Voltages at boundary electrodes are measured and used as input data for image reconstruction. (b) The structure of EIT reconstruction algorithms.

2.2.2 The Forward Problem

The objective of the forward problem of EIT is to construct a mathematical model which can be used to predict the electric potential distribution over a domain of interest,

such that predicted electrode voltage data can be further extracted to serve as the input to the inverse problem. The model derived from the forward problem serves as the foundation of EIT imaging, as the inverse solvers are constructed based on this model. Thus, finding a suitable method for solving the forward problem is vital for ensuring the accuracy of EIT imaging.

Currently, several methods based on different structure models for solving the forward problem of EIT are utilized, including the boundary element method[26], the finite element difference method[27], and the currently most commonly employed finite element method[28]–[30].

The boundary element method (BEM) is based on the discretization of an integral equation that gives an implicit relationship between a conductor's boundary potentials with a piecewise constant conductivity[26]. This method discretizes only the boundary region of a target domain into dense meshes, where the electrical field is typically the strongest because they are near the electrodes. The advantage of BEM is that it allows a significantly reduced size of the derived model matrix, and hence considerable computation cost can be saved. However, BEM alone is only valid for domains with homogeneous inner regions[21]. For inhomogeneous regions, this method must be combined with the finite element method. However, the dense coupling between the boundary meshes of BEM and the inner meshes of FEM can easily result in notable numerical error[21]. Therefore, BEM has limited use in practice.

The finite difference method (FDM) uses a bi-directional grid system to discretize a domain of interest into numerous squares with a uniform area and homogeneous conductivity. The derivatives in the governing equations of EIT are replaced with difference quotients, i.e., the admittance variation between adjacent squares, such that the governing equations are converted into an algebraic system of linear equations[31]. The difference in voltage values at each mesh point can be determined from the obtained system. The FDM is a convenient way of solving the forward problem, but the limitation possessed by this method is that it only applies to media with simple and

regular geometries[32], and its efficiency is poor in dealing with the curved boundary problem[33]. Therefore, its rarely used for EIT imaging in practice.

The finite element method (FEM) discretises the domain of interest into numerous finite elements and converts the governing equations of EIT into element-wise local functions in their discrete form, which are reformulated into a system of linear equations. The forward solution that conveys node-wise electrical potential is approximated using a known current injection pattern and a known element-wise conductivity distribution. This method is normally based on an incomplete set of Maxwell equations which neglect the effect of the coupling between electric fields and magnetic fields[34]; thus, more errors may be present when a high-frequency current is used for excitation. Nonetheless, the error introduced due to this limitation is usually small and acceptable for producing a tomography image. Because FEM can effectively simplify the forward model and can be applied to domains of complex geometries, for example, the human body, without specific restrictions[35], it has become the most commonly employed method for solving the forward problem of EIT in various applications.

2.2.3 The Inverse Problem

The objective of the inverse problem is to use the measured electrode voltage data as the input to the inverse (i.e. reversed) mathematical model, which reconstructs the distribution of element-wise conductivity. Due to the electrode voltage data being only a small portion extracted from the complete output of the forward problem, the algebraic system of equations for solving the inverse problem is underdetermined, and non-unique solutions exist. Therefore, solving the inverse problem is reformulated as finding a solution that fits the model with minimum error.

Regularization is the most common approach for determining a unique solution from an underdetermined system. According to the norms that the error minimization is based on, the regularization algorithms currently used for solving the inverse problem of EIT are comprised of two styles: algorithms that minimize errors in terms of the L_2 norm, i.e., the sum of squared errors, including Tikhonov regularization and Noser regularization, and algorithms that minimize errors in terms of the L_1 norm, i.e., the sum of absolute errors, including sparse regularization and total variation regularization. The equations associated with several commonly used regularization methods are provided later in Chapter 3.

Tikhonov regularization[25] is a commonly used algorithm in EIT imaging. Its working principle is to impose a penalty term to a cost function, such that the ill-posed problem gains balanced ranks and becomes a well-posed problem; therefore, a unique solution can be obtained. The major limitation this method possesses is that it penalizes the L_2 norm in the obtained solutions. In other words, a bias towards a minimum L_2 norm is imposed on the inverse solver. Minimizing L_2 tends to remove outliers from the solution space; therefore, Tikhonov regularization is more suitable for imaging a conductive medium with smooth conductivity variations. However, most objects to be imaged, like the human body, have a considerable discontinuity in the conductivity distribution. Thus, the accuracy of this regularization is limited.

Similar to Tikhonov regularization, Noser regularization[36] also approaches a unique solution by minimizing the error measured by the L_2 norm. Compared to Tikhonov regularization, which utilizes an identity matrix for penalization and provides uniform regularization to all finite elements, the Noser regularization method utilizes the diagonal elements of the Jacobian matrix derived from the inverse problem as the penalty term. This approach allows the penalization imposed on the L_2 norm of the solution to be less intense on the interior elements of the domain than the elements closer to the surface[37]; hence, more discontinuities in the interior region can be maintained in the solutions. This effect can be seen in Figure 2-2. Due to the

penalization on the L_2 norm, Noser regularization also suffers from limited accuracy in reconstructing images of objects with sharp discontinuities in their conductivity.

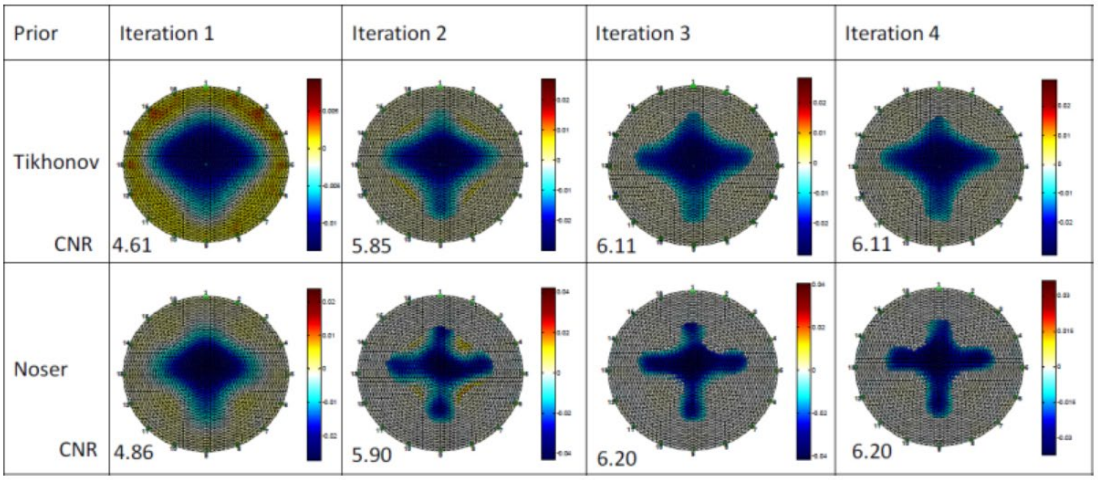

Figure 2-2 Reconstructions of a cross-shaped contrast using Tikhonov regularization and Noser regularization*[37]* using a DeTER optimization method proposed by Ranade and Gharpure. (Copyright 2019 Ranade, Gharpure. Reused with permission). The results in "Iteration 1" are the originally reconstructed results prior to optimization. The rest of the iterations show the results obtained by extracting some of the original solutions from "iteration 1" according to a specific threshold and then optimizing them. It can be seen from the original results that Noser regularization offers better feature details in the interior region than Tikhonov regularization. CNR denotes the contrast-to-noise ratio.

Instead of minimizing the error in L_2 norms, sparse regularization[38] approaches a unique solution by minimizing the error in the sense of L_1 norms. In this case, an L_1 penalty that corresponds to the conductivity change on the whole FEM mesh[39] is enforced in the cost function and balances the ranks in the system such that a unique solution can be produced. The L_1-based regularization mitigates the limitations in imaging objects with sharp discontinuities in their conductivity and can produce non-smooth images. The defect is that the L_1 norm of the estimated solution is also minimized along with the error, resulting in a mismatch between the estimation and the reality.

Total variation regularization[40] also relies on the minimization of L_1 norms to produce a unique solution. The total variation method imposes the sum of differences in the conductivity of adjacent elements as the penalty term, such that discontinuity (i.e., outliers) in the solutions can be preserved[41]. This method can produce images

with non-smooth conductivity distribution; however, the staircasing effect[35] may be observed for imaging objects with smooth conductivity distribution.

In addition to the above regularization algorithms, various types of hybrid methods for enhancing the accuracy of the reconstructed solutions were reported in previous studies. For example, Liu et al.[42] proposed a hybrid regularization method by combining Tikhonov regularization with total variation regularization. The hybrid approach provides sharper solutions and is more robust against gaussian white noise. Tehrani et al.[43] proposed a L_1 norm-based regularization method by integrating the cost function with the concept of the Pareto frontier curve, such that the sparsity of the problem can be controlled. Farha et al.[44] also combined total variation regularization with Tikhonov regularization. The hybrid method improved the accuracy in distinguishing the positions and the sizes of an object placed in a water tank. Borsic et al.[45] proposed a regularization method based on the Primal Dual-Interior Point method as a framework for TV regularization, which enhanced the solution accuracy in reconstructing non-smooth conductivity distribution under moderate measurement noise.

Several previous works showed that enhancing the accuracy of EIT reconstruction can also be approached by combining the time-difference information with multi-frequency information. Using a simulation study, Cao et al.[46] showed that the solutions reconstructed from this approach were of better quality and were more immune to noise. Bai et al.[47] employed a similar hybrid approach that combined both frequency and time information for imaging lung ventilation using a phantom. The experimental result showed that the method provided relative shapes, sizes, and positions of the inclusions in the phantom, with reduced distortions. Moreover, Kuen et al.[48] proposed a hybrid reconstruction algorithm based on the concept of the equivalent homogeneous complex. This method exhibited improved results in imaging human lungs, from which the air distribution in the lung could be identified.

Furthermore, machine learning has been adopted in a few studies for optimizing the solutions to the inverse problem or directly solving the inverse problem. For example,

Martin et al.[49] employed neural networks as a post-processing scheme for refining the solutions obtained from reconstructions. Using the data trained from a deep neural network, Li et al.[50] performed reconstruction for a water tank containing a non-conductive object. Fernández-Fuentes et al.[51] proposed an inverse problem solver based on a convolutional neural network. Although machine learning-based reconstruction can provide high-quality images, the obtained solutions are subject to the training data. It has limited use in imaging the human body due to its instability[52].

2.2.4 Hardware System

The hardware required for implementing EIT is considerably more straightforward than other imaging tools, such as computed tomography (CT), magnetic resonance imaging (MRI), and ultrasound. This simplicity is attributed to the fact that the data acquisition associated with an EIT system does not involve generating and capturing X-ray, magnetic waves, or sound waves, which requires more sophisticated technology than electrical voltages required for performing EIT. Essentially, EIT requires producing an excitation current of a changing polarity and measuring voltages, which can be accomplished using simple electrical components.

A schematic of the function blocks of the hardware used in EIT imaging[53] is illustrated in Figure 2-3. An EIT system typically consists of a current injector, multiplexers, a data acquisition unit, and a computer. The current injector is usually a constant current source or a digital-to-analog converter (DAC). It produces an excitation current for the human body or a sensing material to generate an electric potential distribution over its conductive region. The multiplexers are responsible for switching the injected current between different pairs of electrodes such that the polarity of the current injected into the sensing material shifts according to a predefined pattern. Typically, two multiplexers are employed; one controls the selection of the injection electrode, and the other controls the selection of the sink electrode. The data

acquisition unit captures the electric potential generated by the current injection for each polarity. The data acquisition unit is a multi-channel analog-to-digital converter (ADC), which measures the differential voltage between electrodes and a ground reference point. A high-precision ADC is preferred to ensure accuracy in voltage measurement. Finally, the computer receives the measured voltage information transferred from the data acquisition unit. Via a software program, the voltage data is reconstructed into the conductivity distribution within the cross-sectional area of the object being imaged.

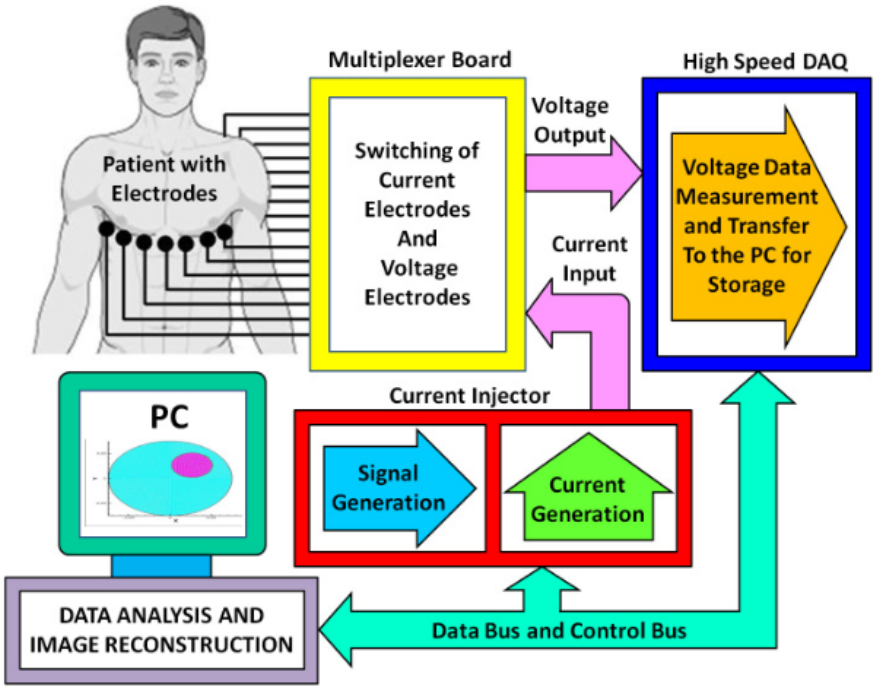

Figure 2-3 The functional blocks of a typical data acquisition hardware for EIT*[53]*. (Copyright 2010 IEEE. Reused with permission)

2.2.5 Current Injection Strategies

Although there is no strict rule determining the drive patterns based on which the excitation current must be injected into a conductive medium, the current injection

patterns utilized in practical EIT imaging are generally of two types: the adjacent pattern and the opposite pattern[54].

The adjacent pattern, also known as the neighbouring pattern, is most commonly employed. As shown in Figure 2-4(a), a current is supplied through a pair of adjacent electrodes. Meanwhile, voltages at the remaining electrodes are measured. The current injection is then switched to the next pair of electrodes, and the voltage measurements are repeated. The order of the current switching does not necessarily follow a clockwise or anticlockwise direction. This procedure is repeated until each pair of adjacent electrodes has received a current injection. For example, in a system with eight electrodes, the complete set of the recorded voltage for performing a single imaging frame comprises 48 individually measured voltages. Under the adjacent injection pattern, the injected current mostly flows through the outer region of the domain. Therefore, the current density is highest between the injecting electrodes and near the boundary. The advantage of this pattern is enhanced sensitivity near the domain's boundary. Conversely, the defect is the perturbations caused by the shape of the domain and the electrode positioning[55].

The opposite pattern is shown in Figure 2-4 (b). Current is injected and sunk through two electrodes located at opposite ends of the domain; meanwhile, voltages at the remaining electrodes are measured. This process is repeated for all opposite pairs of electrodes. The opposite pattern allows the current to flow across the domain and passes the central region more uniformly. Compared to the adjacent pattern, which is more sensitive near the boundary[163], the opposite pattern has a relatively higher sensitivity in the centre [194] and is more immune to boundary shape and electrode perturbations.

In addition to the adjacent and opposite patterns, several other drive patterns were reported but are rarely used in practice, such as the cross pattern and the adaptive pattern. The cross pattern has relatively more uniform sensitivity over the domain, but its performance is limited due to reduced sensitivity near the boundary region[20], [54], [56], [57]. The adaptive pattern, also known as the trigonometric pattern, requires many independent current injectors to enable simultaneous current injections; thus, the

hardware for implementing this pattern is more sophisticated. Moreover, due to a large number of current injections, the adaptive pattern suffers from significant errors caused by the contact impedance of electrodes[57].

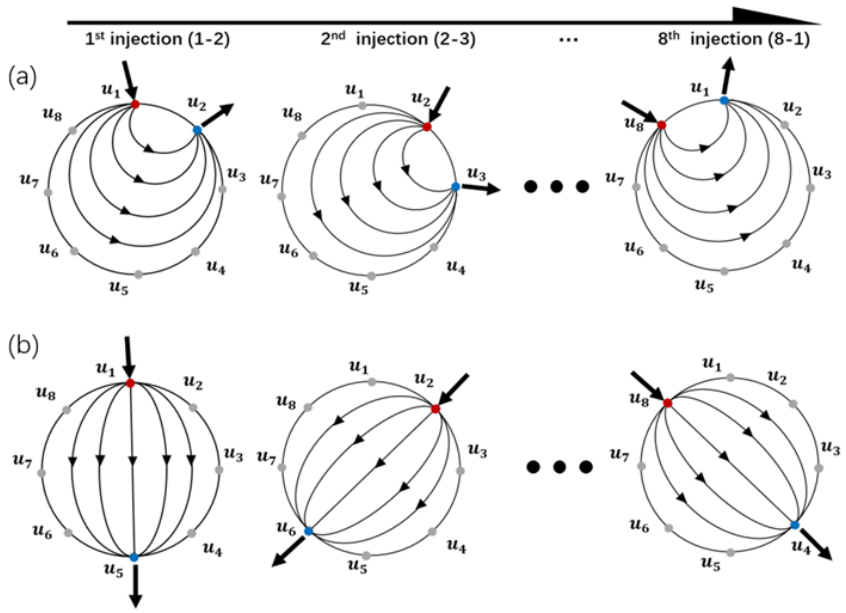

Figure 2-4 Typical drive patterns utilized in EIT imaging. (a) the adjacent current injection pattern. (b) the opposite pattern.

2.3 Strain-Sensing Materials: Mechanisms, Fabrication Techniques, and Performance

2.3.1 Piezoresistive Strain Sensors Based on Cracks In Conductive Layers

The signal transduction of coating-based piezoresistive materials relies on the propagation of cracks in the conductive coating layer caused by mechanical deformation when the sensor is stretched. This transduction mechanism is demonstrated in Figure 2-5(a). An applied strain causes the expansion of the polymer substrate and induces numerous cracks in the conductive layer. These cracks limit the

electric current that flows through the conductive layer due to increased length and reduced width of the available conductive paths. Therefore, the sensor gains increased electrical resistance. After the sensor is released, the deformed sensor recovers its original shape and dimension. The recovery allows the conductive paths to be restored; thus, the electrical resistance of the sensor regains its initial value.

A considerable number of flexible strain sensors reported in previous studies are based on coating a thin layer of conductive particles, which are often nano-sized, on the surface of a polymer substrate. Figure 2-5(b) shows an example of a sensor fabricated by coating carbon nanotubes onto a polydimethylsiloxane (PDMS) substrate[58]. The coated conductive particles with random orientations overlap and create a surface through which electrons can be transferred from one side to another. The inter-layer adhesion between nanoparticles and polymer relies on the wettability of polymer and surface energy of nanoparticles[59]. The output signal is typically electrical resistance measured across a pair of electrodes attached at both ends of the conductive coating. The coating is often encapsulated by an additional layer of polymer, which provides mechanical protection and electrical insulation from the surrounding.

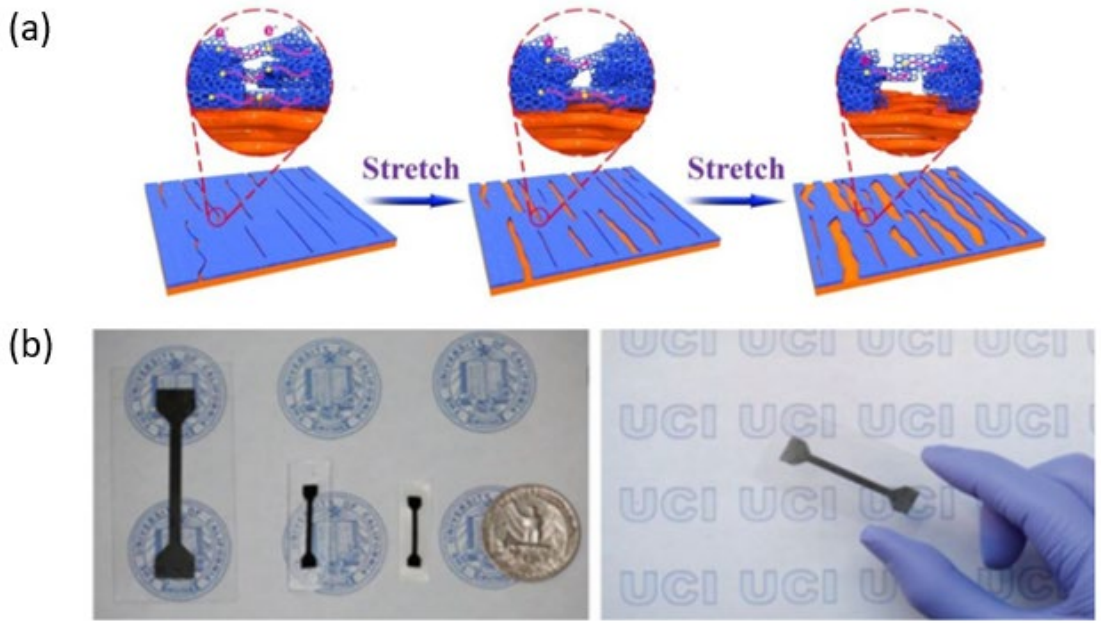

Figure 2-5 Crack-based flexible strain sensors. (a) Strain sensing mechanism based on strain-induced cracks*[60]* (Copyright 2019 American Chemical Society. Reused with permission). (b) A flexible strain sensor made by coating PDMS with MWCNTs *[58]* (Copyright 2016 WILEY‐VCH Verlag GmbH & Co. KgaA, Weinheim. Reused with permission).

As a popular type of flexible strain sensor, a crack-based sensor can be fabricated using a diverse range of methods, which are demonstrated in Figure 2-6. Drop casting is a fast and straightforward way of producing a thin coating of conductive particles and a thin film of polymer. This method does not require sophisticated tools. A thin polymeric film is made by directly casting liquid polymer into a mould or onto a flat surface. After an adequate period of curing, the solidified polymer is peeled off and ready to be used as the substrate that carries a conductive coating. As illustrated in Figure 2-6(a), to prepare a thin layer of particle coating on the surface of the substrate, conductive particles, such as graphene, copper powders, and carbon nanotubes, are first dissolved in an organic solvent. An ultrasonication process is typically applied to the solvent to break the linkage between particles to achieve uniformity in the suspension. The particle suspension is cast onto the surface of the substrate, followed by the evaporation of solvents. Once the solvents fully evaporate, a thin layer of particles is left as residuals. A thermal annealing process can accelerate this procedure.

A broad range of materials can be utilized in strain sensors through the drop-casting method. For example, Zhang et al.[61] fabricated a strain sensor by coating silver nanoparticles and carbon nanotubes onto a PDMS substrate. Liu et al.[62] fabricated a strain sensor using a combination of copper nanowires and poly(3,4-ethylenedioxythiophene) polystyrene sulfonate (PEDOT: PSS) encapsulated in PDMS. Yang et al.[63] developed a strain sensor based on silver nanoparticles-bridged graphene, coated onto a PDMS layer, for detecting both subtle and large deformation. Kim et al.[64] proposed a strain sensor by coating silver nanowires onto a Dragon Skin™ silicone rubber substrate for improved measurement range. Ha et al.[65] designed a strain sensor based on poly(3-hexylthiophene-2,5-diyl) (P3HT) nanofibers and PDMS for measuring the strain in perpendicular directions.

Although possessing simplicity, drop-casting has a notable defect: the difficulty in controlling the thickness and the uniformity of the obtained coating. The thickness of the obtained coating is affected by various parameters, including the volume of solvents used, the concentration of nanoparticles, and the wetness of substrates. Variation in the evaporation rate of solvents is also related to the temperature and the surrounding pressure. Moreover, liquid surface tension often leads to uneven thickness due to the coffee ring effect and Marangoni flow[66].

The spin-coating technique can produce thin layers with uniform and ultra-thin thickness, as illustrated in Figure 2-6(b). First, the particles coated on a substrate are dissolved in a suitable solvent and ultrasonicated to form a homogenous suspension. Then, the suspension is deposited on top of a flat polymer substrate placed on a rotating platform of a spin coater. The platform rotates at high speed. After some time, the solvents in the suspension fully evaporate, and only solid particles are left on the substrate. The spin-coating method can also fabricate thin polymer films to serve as the substrates of flexible strain sensors. A multi-layered structure can be produced by depositing the particles and polymers successively. In previous works, Lee et al.[67] fabricated an optically transparent strain sensor by spin coating silver nanowires onto

a PDMS substrate. Ryu et al.[68] spin-coated carbon nanotubes onto an Ecoflex film which can be stretched to up to a strain of 900%.

The advantage of spin coating is that the produced polymeric thin films and particle layers possess an even thickness. Excellent uniformity is achieved thanks to the surface tension and the centripetal force provided by the rapid rotational speed of the coater. The thickness of the product can be controlled by tailoring the viscosity of solvents, the concentration of particle suspensions, and the rotational speed of the coater[69]–[71]. Moreover, spin coating is often employed for coating photoresists in photolithography, which allows the formation of microstructure sensing patterns in conductive layers[72], [73]. The primary defect of spin coating is the limited efficiency in utilizing the material, as a large portion of the material is often flung off and wasted during the coating process.

Alternatively, the ultrafiltration technique can prepare a uniform and thin layer of particles without considerable material waste. This method is illustrated in Figure 2-6I. First, a particle suspension is cast onto a suction vessel through a piece of filter paper. As the suspension passes through the filter paper due to vacuum suction, the particle component is blocked by the filter paper and accumulated on its surface. Only the solvent component passes through the paper and is collected in the vessel. After filtration, a thin layer of the deposited particles is formed on the filter paper. The layer is then peeled off the paper and transferred onto a polymer substrate using contact transfer with a PDMS stamp[74], [75]. The surface of the polymer substrate is typically applied with plasma treatment for improving its hydrophilicity which allows for better surface adhesion. The layer of particles is encapsulated by covering it with an additional polymer layer. Previously, Lu et al.[76] utilized the ultrafiltration method to fabricate a strain sensor based on silver nanowires coated on thermoplastic polyurethane (TPU). In another work, Wang et al.[77] proposed a strain sensor made by encapsulating filtered nickle nanowires using Ecoflex™ silicone rubber.

Chemical vapour deposition (CVD) is another reliable method for producing an ultra-thin and uniform layer of particles on the surface of a substrate. CVD is commonly

used in chemical engineering to produce carbide nanoparticles, such as graphene nanoplatelets and carbon nanotubes[78], [79]. The schematic of CVD is illustrated in Figure 2-6(d). Flowing reactant gas is delivered into a reaction chamber. As the flowing gas skims over a heated substrate placed inside the chamber, chemical reactions occur on the surface to synthesize a layer of nanoparticles with a micrometre-sized thickness. CVD has the advantages of directly synthesizing an ultra-thin and uniform layer on a substrate; however, the disadvantages are that CVD requires highly expensive instrumentation and often produces toxic gaseous by-products during reaction[80]. Using the CVD method, Chen et al.[81] proposed a low-cost strain sensor by directly synthesizing a graphene layer on a PDMS substrate. Similarly, Daewoong et al.[82] fabricated a sensor based on carbon nanotubes.

Screen printing is a helpful method for producing a layer of conductive particles patterned into desired shapes. As shown in Figure 2-6(e), a meshed screen has a stencil of open apertures which allow a particle suspension to freely pass through, while the apertures in the remaining meshed area are sealed to prevent the suspension from permeation. As the screen is tightly pressed against a substrate, a particle suspension is cast on top of the screen. The suspension is pressed towards the substrate through the open apertures using a plastic or wooden blade. After several repetitions, the screen is detached from the substrate and leaves a layer of patterned particles in place. Although the uniformity in the printed layers can not be ensured, the screen printing technique has been a popular choice in fabricating soft sensors due to its ease of patterning and low cost[83]–[85]. Castro[86] proposed a strain sensor by screen printing multiwall carbon nanotubes (MWCNT) into a Wheatstone bridge circuit, with each resistor connected by serpentine-shaped “wires”, which were also made by screen printing. In soft circuits, a serpentine shape can effectively prevent printed “wires” from breaking and also assists in maximum elongation[87], [88]. In other work, Yeo et al.[89] screen printed silver nanowires onto a PDMS substrate and integrated the sensor into a motion detection glove.

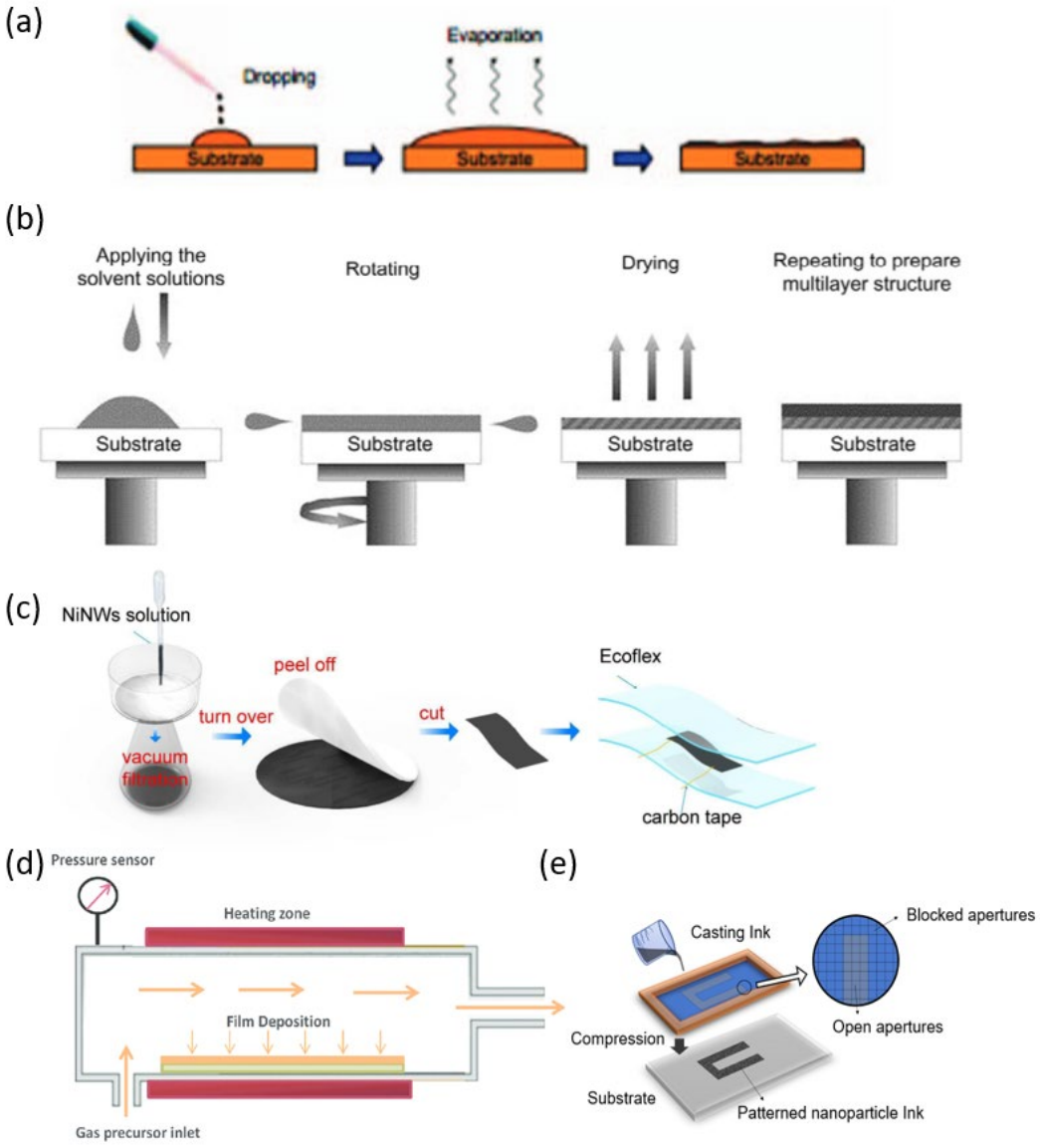

Figure 2-6 Fabrication techniques for producing crack-based flexible strain sensors. (a) Drop casting*[90]*. (Copyright 2015 IEEE. Reused with permission). (b) Spin coating*[91]*. (Copyright 2019 Elsevier Inc. Reused with permission). (c) Ultrafiltration*[77]*.(Copyright 2018 Royal Society of Chemistry. Reused with permission). (d) Chemical vapor deposition*[92]*. (Copyright 2016 Royal Society of Chemistry. Reused with permission). (e) Screen printing.

There are several additional methods for fabricating crack-based strain sensors. The exfoliation and infusion technique incorporates nanoparticles into the shallow surface of a polymer[93]–[95]. A piece of polymer is soaked in an organic solvent for sufficient time to allow swelling in its volume. The swelling creates numerous pores. The swelled polymer is then settled in a particle suspension to allow the infusion of nanoparticles

into its pores. Afterwards, the polymer with infused particles is dried to allow shrinkage in size. Finally, the shrunk polymer is washed with deionized water to remove excess particles on its surface. Spray coating is another convenient method for coating and patterning conductive particles onto soft substrates[58], [96]. It utilizes a nebulizer or a spray gun to generate an aerosolized stream that applies to the target substrate; however, the uniformity in the coated nanoparticle layer is limited[97].

The crack-based piezoresistive strain sensors reported in previous studies are summarized in Table 1, including their adopted materials, maximum measurable strain, sensitivity, and fabrications methods. The maximum measurable strain of a sensor indicates the strain that can be applied to the sensor without causing material failure and disrupting the repeatability of the signal. The sensitivity of a strain sensor is described by the gauge factor (GF), which is the slope of the relative change in the electrical resistance(R) or capacitance (C) of sensors with respect to their initial values (R_0 or C_0) against the applied strain (ε). Gauge factors are expressed as $GF = \frac{\triangle \frac{R}{R_0}}{\varepsilon}$ for resistive sensors and $GF = \frac{\triangle \frac{C}{C_0}}{\varepsilon}$ for capacitive sensors. Sensors with larger gauge factors offer higher resolutions when a signal is converted from mechanical strain into electric signals. Sensitivity and several additional factors that indicate sensor performance will be discussed in detail in section 2.3.6.

Conductive particles	**Polymer substrates**	**Maximum measurable strain**	**Gauge factors**	**Fabrication methods**	**Reference**
AgNP/Graphene	PDMS	14.5%	183~475	Drop casting	[63]
AgNW	Dragon skin	60%	9-24	Drop casting	[98]
GNF	SR	350%	2~160	Infusion	[93]
Graphene	NR	800%	10~35	Infusion	[95]
ZnO/PSNF	PDMS	50%	116	Electrospinning	[99]
Graphene	PDMS	30%	5~30	CVD and Transfer	[81]
Graphene	PDMS	30%	0.55	Etching and Transfer	[100]
CNT	Ecoflex	750%	0.65~48	Spray coating	[58]
AgNP	PDMS	20%	0.06~2.05	Stamp coating	[75]
AgNW	TPU	20%	3~12.9	Filtration	[76]

Graphene/AgNP	TPU	1000%	7~476	Infusion	[94]
CNT	Ecoflex	510%	1.13~2.42	Spray coating	[101]
AgNW	PDMS	100%	Up to 30	Spin coating	[67]
AgNW	PDMS	35%	20	Filtration	[102]
CNT	PDMS	45%	8.74~35.75	Spray coating	[103]
CuNW/PEDOT:PSS	PDMS	120%	2.5~3	Drop casting	[62]
CNT	Ecoflex	900%	0.54~64	Spin coating	[104]
CNT	PDMS	10%	30.1	CVD	[82]
P3HT nanofiber	PDMS	100%	25~32	Drop casting	[65]
NiNW	Ecoflex	100%	75~200	Filtration and Transfer	[77]
Ag/CNT	PDMS	54.8%	14.9	Drop casting	[105]
AgNP/CNT	PDMS	95.8%	21~39.8	Drop casting	[61]
AgNW	TPU	10%	24-28	Screen Printing	[83]

Table 1 Crack-based piezoresistive strain sensors reported in previous literature. (The definition of each abbreviation can be found in the "Abbreviations" section)

2.3.2 Piezoresistive Strain Sensors Based on Disconnection Of Conductive Networks

An alternative resistive approach for constructing a flexible strain sensor is to create a conductive network formed by interconnected nanoparticles dispersed uniformly into a polymer matrix. According to the percolation theory, the percentage of nanoparticle fillers in a polymer substrate significantly impacts the electrical conductivity of the nanocomposite. When the percentage increases, the nanocomposite experiences a transition from an electrical insulator to a conductor. When the percentage passes a critical threshold, the electrical conductivity of the composite is increased by several orders of magnitude due to the formation of conductive networks. This critical threshold is known as the percolation threshold[106]. A few examples of percolation thresholds for several commonly used nanomaterials are listed in Table 2.

Nanoparticle	**Polymer Matrix**	**Weight or Volume Fraction**	**Reference**
MWCNT	HDPE	0.15 vol%	[107]
SWCNT	PS	0.3 vol%	[108]
GNP	HDPE	1.0 vol%	[107]
GNP	Epoxy	0.22 vol%	[109]
AgNW	PS	0.49 vol%	[110]
MWCNT	PDMS	0.03 vol%	[111]

MWCNT	Ecoflex	0.74 vol%	[112]
SWCNT	PBT	0.2 wt%	[113]
AgNW	PC	0.04 wt%	[114]
MWCNT	PDMS	5 wt%	[115]

Table 2 Percolation thresholds for several nanomaterials. (The definition of each abbreviation can be found in the "Abbreviations" section)

The working mechanism of such strain sensors is known as the disconnection mechanism. The schematic of this mechanism is illustrated in Figure 2-7(a). When nanoparticles are uniformly dispersed into a substrate, they are interconnected to create numerous intercepting junctions that result in numerous conductive paths. Along these paths, electrons are free to flow from one side of the sensor to the other. As the sensor is stretched, these junctions partially lose connections and lead to fewer available conductive paths; therefore, the overall electrical resistance of the networks in the sensor is increased. When the sensor is released, conducting junctions are reconnected, and thus overall electrical resistance of the networks is restored.

The total electrical resistance through a nanoparticle network is attributed to three states of connectivity. As shown in Figure 2-7(b), the factors that contribute to network resistance include the resistance of nanoparticles themselves, the contact resistance when nanoparticles are connected, and the tunnelling resistance between two nanoparticles when they are extremely close to each other but are not in direct contact[116]–[118]. The tunnelling effect is a phenomenon that cannot be predicted using classical physics. It describes that electrons can pass through a potential barrier between two neighbouring nanoparticles, even when they are not in direct contact [119]. The phenomenon is only present where the distance between two particles is below a tunnelling threshold[120], [121]. In this case, the applied strain causes losses in the physically connected junctions and the tunnelling junctions, thus raising the electrical resistance of the networks[120], [122]. The tunnelling threshold is extremely tiny. For example, in a network formed by carbon nanotubes (CNT), the tunnelling threshold is only about 1.8 nm[123]. Tunnelling resistance is a dominant component contributing to the nanoparticle network's electrical conductivity [123].

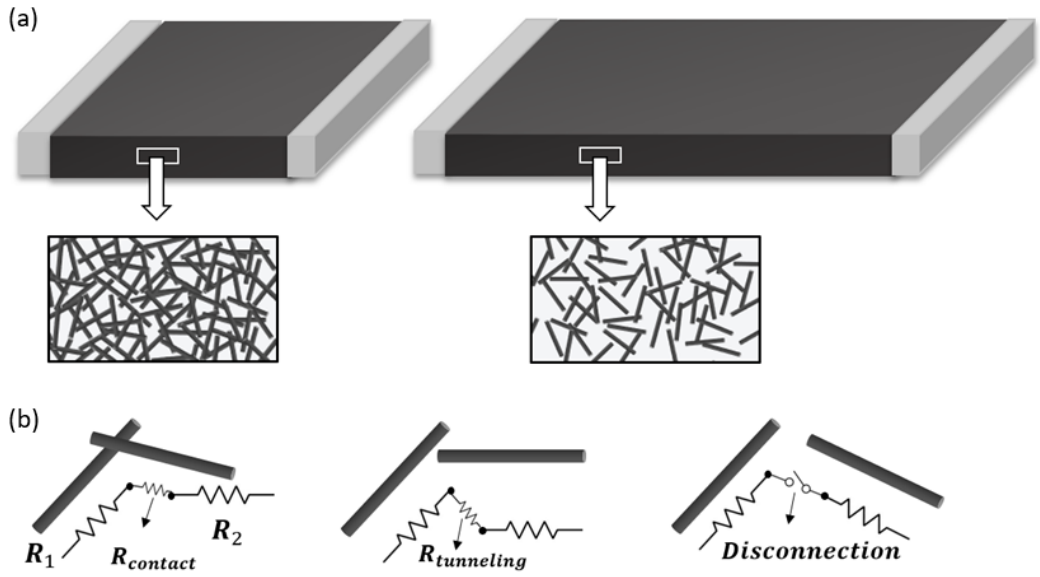

Figure 2-7 Structure of a strain sensor based on disconnection of conductive networks: (a) Connectivity of networks before (left) and after (right) strain is applied; (b) Three states of connectivity of adjacent nanoparticles: direct contact, tunnelling contact and disconnection.

The formation of conductive networks in disconnection-based strain sensors requires the doped nanoparticles to be uniformly dispersed into the liquid prepolymer before curing the polymer. The homogeneous dispersion of nanoparticles in prepolymers is typically achieved by applying ultrasonication to the nanoparticle suspension, followed by magnetic stirring. This method is illustrated in Figure 2-8. Nanoparticles are first dissolved in a suitable solvent, and then an ultrasonicator is used to produce ultrasonication energy into the suspension to break the inter-particle adhesion between neighbouring nanoparticles. The processed suspension is mixed with the liquid prepolymer and magnetically stirred for over an hour to enhance the uniformity of nanoparticles in the mixture. The mixture is thermally annealed to remove all the solvent through evaporation. Afterwards, only the prepolymer incorporated with the dispersed nanoparticles is left in the residual product. A curing agent for the polymer is added to the product, followed by vigorously blending. The final mixture is cast into a mould and degassed inside a vacuum chamber to remove the air bubbles induced during the preparation process. After settling the material for sufficient time under the

required curing temperature, the material becomes a solid nanocomposite and is released from the mould.

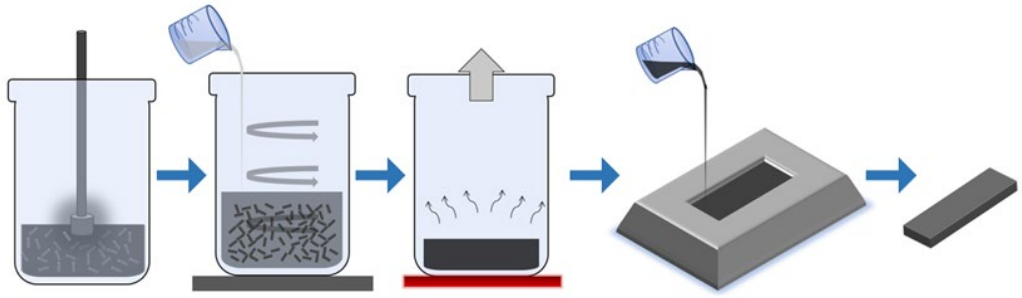

Figure 2-8 Fabrication procedure of a strain sensor by dispersing nanoparticles into a polymer.

The resistance of the conductive network is dependent on the type of material used. For example, silver nanowires have better electrical conductivity than copper nanowires[124]; nanowires with longer length have increased electrical resistance; an increase in diameter of nanowires reduces their electrical resistance[125]; networks with a higher nanowire density have increased conductivity because of an increased number of overlapped conductive junctions[126]. Notably, electrical properties and network morphology may also be controlled by various methods, such as applying high pressure, electrical annealing, optical sintering, and thermal annealing [127] during the sensor production. The orientations of nanowires in the network can be controlled by a nanowire alignment technique which results in anisotropic behaviour [128].

In polymer materials, silicone rubber is the most popular material constituting the substrate of wearable strain sensors, mainly due to its high elasticity and excellent biocompatibility[129]. There are different types of systems for curing silicone rubbers: addition curing and condensation curing. Addition-cured silicones like Ecoflex and dragon skin are cured through an addition reaction between a vinyl group and a hydride group, with the presence of a platinum catalyst. Condensation cured polymer like PDMS relies on cross-linkers as the curing agent to vulcanize the polymer base to solidify. It is worth noting that the addition-cured silicones may fail to cure when exposed to contaminants like sulphur, latex, amines, and some alcohols. For this reason, PDMS instead of Ecoflex is generally adopted for fabricating disconnection-based

sensors. However, inhibition is also observed when PDMS is filled with too many nanoparticles. For example, PDMS doped by gold nanoparticles (AuNP) does not cure when the fraction of AuNP is over 0.005 wt%[130]. Thus, the amount of conductive nanofiller must be carefully controlled for fabricating dispersion-based sensors, i.e., the added nanofiller must reach the required percolation threshold to enable the electrical conductivity of the nanocomposite, but they must not be over-doped to avoid cure inhibition. Therefore, the number of available materials suitable for this approach is limited. Most strain sensors based on the disconnection mechanism utilized CNT for constructing their conductive networks and PDMS as their substrates[131]–[134]. The reason is that CNT's immense aspect ratio allows the formation of the conductive networks with only a tiny amount of dopant, and the wettability of PDMS on CNT allows proper adhesion between the two materials.

The infiltration method is another efficient but less commonly used way of producing interlinked nanoparticle networks within a polymer. Unlike the dispersion method addressed above, which aims to disperse nanofiller in liquid prepolymers uniformly, the infiltration approach involves casting liquid prepolymer on top of a dried layer of nanoparticles and allows the liquid prepolymer to impregnate into the gaps between nanofiller. Sensors produced by this method are similar to crack-based sensors. Still, the difference is that the conductive networks formed using this method are not a thin layer of nanoparticles deposited on a polymer surface but a layer of nanoparticles whose inner gaps are filled with polymer. Using the infiltration method, Song et al.[135] fabricated a strain sensor using carbon nanotubes and PDMS. And Wang et al.[103] produced a patterned CNT network on a PDMS substrate via spray-coating and then infiltrated the network using an additional layer of PDMS. The images produced by scanning electron microscopy (SEM) of the two sensors are demonstrated in Figure 2-9. It can be seen that PDMS successfully fills gaps in the CNT layer. Notably, the sensors fabricated in both works demonstrated a linear relationship between the relative change in resistance and the applied strain.

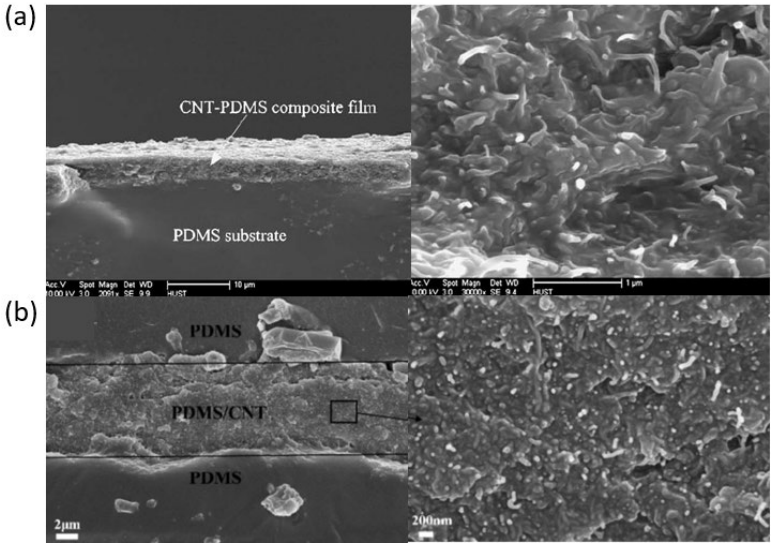

Figure 2-9 Scanning electron microscope (SEM) image of the cross-section of a CNT/PDMS composites made by infiltration. (a) PDMS infiltrates a CNT layer. *[135]* (Copyright 2009 Elsevier B.V. Reused with permission). (b) PDMS infiltrates a CNT layer made by spray deposition. (Copyright 2018, American Chemical Society. Reused with permission).

In addition to the methods addressed above, more tangible methods involving a shear milling machine and a planetary mixture machine have also been utilized to produce conductive polymers[136]–[139]. The characteristics of the disconnection-based piezoresistive strain sensors reported in previous works are summarized in Table 3.

Conductive particles	**Polymer substrates**	**Maximum measurable strain**	**Gauge factors**	**Fabrication methods**	**Reference**
CNT/CB	SR	120%	1.25	Magnetic stirring	[140]
CNT	PDMS	40%	2.7	Magnetic stirring	[133]
CNT	PDMS	40%	5~9	Magnetic stirring	[134]
CNT	PDMS	45%	1.5-2	Magnetic stirring	[131]
ZnO/GNP	PDMS	44%	8.8~12.8	Magnetic stirring	[141]
CNT	PDMS	25%	11	Magnetic stirring	[132]
CNT	PDMS	45%	1.25	Infiltration	[135]
CNT	PDMS	45%	35.75	Infiltration	[103]

Table 3 Disconnection-based piezoresistive strain sensors reported from previous literature. (The definition of each abbreviation can be found in the "Abbreviations" section)

2.3.3 Piezocapacitive Strain Sensors

A capacitive approach for realizing flexible strain sensors is to adopt the principle of a parallel plate capacitor. The schematic of this sensing mechanism is illustrated in Figure 2-10(a). Two conductive sheets enclose the dielectric layer made of polymer to form a sandwich structure. Two additional polymer layers encapsulate the sandwich structure for electrical insulation. Electric charges are stored between the parallel particle sheets when the sensor is supplied with an electric current. The theoretical value of the capacitance resulting from this structure can be calculated using the standard capacitance formula for a parallel plate capacitor, which is expressed as:

$$\chi = \frac{E_0 E_r A}{D} \qquad 2\text{-}1$$

where E_0 is the permittivity of air, E_r is the relative permittivity of the dielectric (i.e., the enclosed polymer), A is the area of overlapped electrode plates, and D is the thickness of the dielectric layer. When the sensor is stretched along its longitudinal direction, the overlapped area (A) increases due to the applied strain. In the meantime, the thickness (D) is reduced due to the Poisson effect and causes an increase in capacitance (χ). After the sensor is released, the overlapped area and the dielectric thickness are recovered. Hence the capacitance of the sensor is restored.

Alternatively, capacitive strain sensing can also be achieved using the structure of an in-plane capacitor, as illustrated in Figure 2-10(b). Similar to the parallel plate capacitor, this in-plane structure also works as a capacitor that stores electric charge; the difference is that the charge is stored between each pair of adjacent electrode teeth. The theoretical capacitance of an in-plane capacitor can be calculated using the formula[142] expressed as:

$$\chi = \frac{\kappa \, l \, D}{d}(n - 1) \qquad 2\text{-}2$$

where κ is the permittivity of the dielectric substrate, D is the thickness of the patterned conductive layer, d is the distance between each pair of adjacent electrodes, l is the intersected length between electrodes, and n is the number of electrode teeth. Using this mechanism, Kim et al.[142] fabricated such strain sensor using AgNW (silver nanowires)/PDMS nanocomposites. The sensor shows stable cyclic sensing performance for strains up to 30%. However, equation 2-2 may be no longer satisfied when a large strain that causes morphological deformation of the sensor is applied; therefore, in-plane capacitive sensors are more suitable for sensing microstrain (με). For example, sensors based on gold (Au)[143], nichrome (NiCr)[144], and silver nanoparticles (AgNP)[145] for measuring microstrain under 0.1% have been reported in previous works.

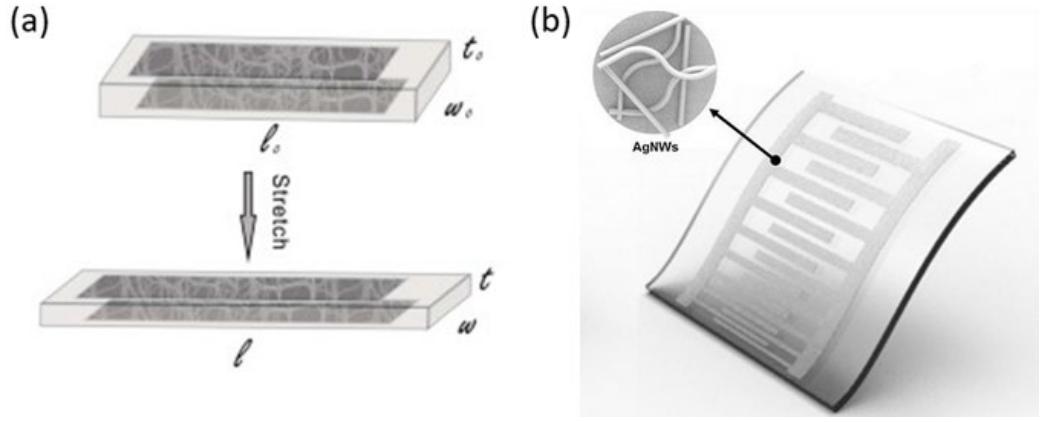

Figure 2-10 Capacitive sensing mechanisms based on: (a) A parallel plate capacitor*[146]*. (Copyright 2013 Le Cai et al. Reused with permission). (b) An In-plane capacitor*[142]* (Copyright 2017, American Chemical Society. Reused with permission).

Capacitive strain sensors are commonly fabricated using the contact transfer method. The schematic of the contact transfer method is illustrated in Figure 2-11. First, oxygen plasma treatment is typically applied to the dielectric polymer substrate to modify its surface hydrophilicity. A thin layer of conductive particles is formed using various methods such as the aforementioned chemical vapour deposition method or ultrafiltration technique[146]–[148]. The obtained particle sheet is then transferred onto the treated polymer surface by direct contact. The same procedure is repeated for the other surface of the polymer layer, such that the polymer layer is sandwiched

between two layers of conductive sheets. Finally, the sensor is encapsulated by coating additional polymer layers. In addition, for fabricating sensors with the structure of an in-plane capacitor, which requires patterning in its conductive particle layer, a phase mask produced using photolithography or soft lithography can be used to partially cover the polymer layer such that only the exposed portion of the polymer receives plasma treatment and become hydrophilic. The selectively processed polymer layer is then placed in contact with the particle sheet to transfer the particles to the plasma processed area. Afterwards, the layer coated with patterned particles is further encapsulated.

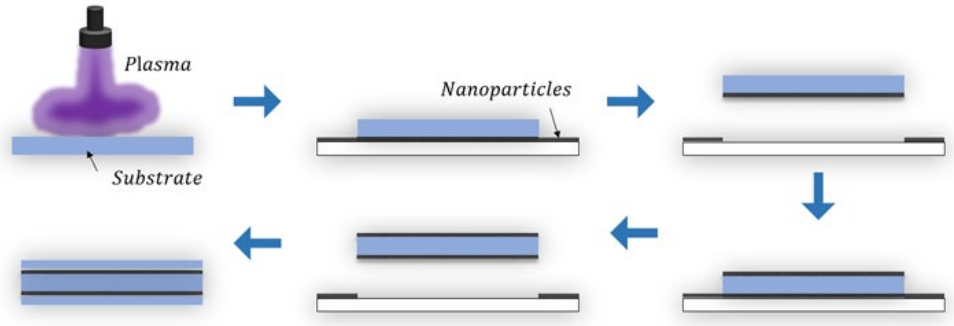

Figure 2-11 The fabrication procedure for a capacitive strain sensor using the contact transfer method

Apart from the contact transfer method, several methods mentioned in section 2.3.1, such as spray coating and screen printing[149], [150], have also been employed for fabricating capacitive strain sensors. The characteristics of the capacitive strain sensors reported in previous literature are summarized in Table 4.

Conductive particles	Polymer dielectric	Structure	Maximum measurable strain	Gauge factors	Fabrication methods	Reference
CNT	SR	Parallel	100%	0.99	Contact transfer	[148]
CNT	TPU	Parallel	13.6%	1.95	Spray coating	[150]
CNT	Ecoflex	Parallel	150%	1.00	Contact transfer	[147]
CNT	Dragon skin	Parallel	300%	0.99	Contact transfer	[146]
AgNW	Ecoflex	Parallel	50%	0.7	Screen printing	[149]
AgNW	PDMS	In-plane	30%	1.57	Contact transfer	[142]
CNT	SR	Parallel	100%	0.99	Contact transfer	[148]

Table 4 Capacitive strain sensors reported in previous studies. (The definition of each abbreviation can be found in the "Abbreviations" section)

2.3.4 Liquid-Based Strain Sensors

Instead of using solid composite materials, strain sensors can also adopt electrically conductive liquids as their strain-sensing elements, such as a room temperature liquid metal alloy or ionic liquid.

Liquid metals refer to metals with melting points lower than room temperature. They remain in the liquid state and have freely deformable natures at room temperature. Mercury is the most well-known liquid metal as it has been commonly used in medical devices such as thermometers for measuring body temperature and sphygmomanometers for measuring blood pressure. However, mercury is phasing out gradually due to its toxicity. As a safer replacement, gallium-based alloys have gained increased attention in research. Like mercury, gallium-based alloys are also freely deformable liquids. They possess low toxicity, making them more suitable than mercury in various applications. In soft sensors, gallium-based alloys are usually referred to as the eutectic gallium indium (EGaIn), composed of approximately 75% Gallium and 25% Indium by weight. Another alloy known as Galinstan comprises 68.5%

gallium, 21.5% indium, and 10.0% tin by weight. The melting temperature is 15.5 ℃ for EGaIn and 10.5 °C for Galinstan.

Compared to conductive polymers made of nanocomposites, liquid metals possess incredibly high electrical conductivity, making it difficult to directly relate their electrical resistance to the applied strain. For example, the electrical conductivity for EGaIn is 3.4×10^6 S m^{-1} [151] whereas a MWCNT-PDMS composite material with a filler ratio of 20 wt% has only 0.38 S m^{-1}[152].

Therefore, the fluid channels for embedding liquid metals are usually patterned with a small cross-sectional area and long channel length to increase their electrical resistance and improve signal resolution. Typically, a zigzag pattern is used, as illustrated in Figure 2-12(a). In addition, a specialized circuit for measuring small resistance values, such as a Wheatstone bridge circuit, is generally required for precise measurement of the relative change in the resistance of liquid metals when a strain is applied to the sensor.

Ionic liquids are excellent alternatives to liquid metals. Ionic liquids are formed by compounds composed of ions with a melting temperature below 100 °C[153]. Compared with sensors based on liquid metals, sensors based on ionic liquids are relatively simple as their fluid channels do not necessarily require complex patterns to accommodate the high conductivity possessed by liquid metals. A sensor that utilizes ionic liquids can be fabricated by simply embedding a small amount of ionic liquids into a linear channel. For example, Figure 2-12(b) shows that a medical-grade silicone tube[154] is utilized as a fluid channel to embed the ionic liquid and realize a strain sensor.

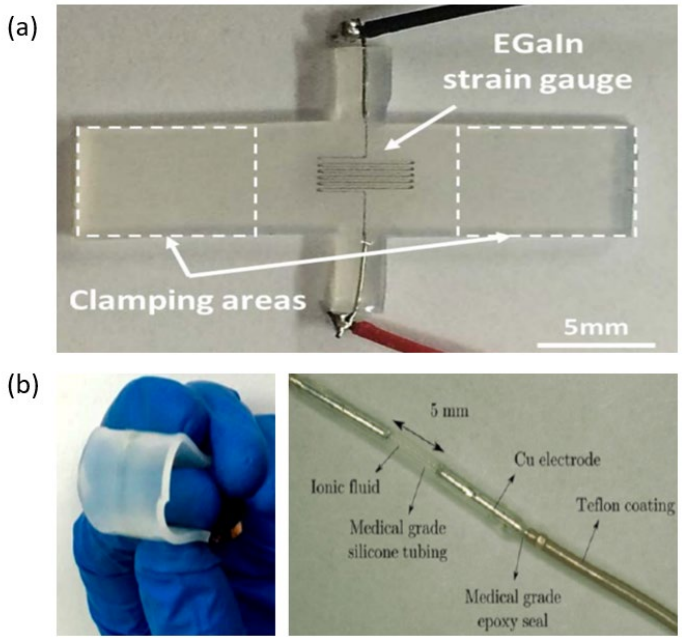

Figure 2-12 Strain sensors based on liquid sensing elements. (a) Strain sensor fabricated by embedding EGaIn into a PDMS substrate*[155]*. (Copyright 2015, IEEE. Reused with permission). (b) A simple ionic liquid strain sensor using a medical-grade silicone tube*[154]*. (Copyright 2014 Elsevier Ltd. Reused with permission).

In previous studies, a wide range of ionic liquids have been utilized for constituting strain sensors. Examples include 1-Butyl-1-methylpyrrolidinium bisimide[154], 1-ethyl-3-methylimidazoliumbis ([EMIM][TFSI])[156], [Bmim][BF4][157], and 1-methyl-3-octylimidazolium chloride[158]. Essentially, there is no limitation on the type of the ionic liquid. Any ionic liquids can serve as the sensing elements as long as they possess suitable electrical conductivity and, ideally, low toxicity. However, unlike liquid metals, whose electrical conduction is the transfer of electrons, ionic liquids conduct electricity through ionic conduction, which is the transport of charge-carrying cations and anions. While measuring the electrical resistance of an ionic liquid-based strain sensor, AC excitation is generally preferred instead of using DC excitation[159], [160]. The preference for using AC is due to the electrode polarization problem, which occurs when the ionic liquid is continuously charged using DC and results in charge separation near electrodes, known as the electrode double layer[160]. With the presence of the electrode double layer, the sensor would behave like a capacitor to some extent. Therefore, AC is generally preferred in sensors based on ionic liquids.

Although both liquid metals and ionic liquids need to be embedded into fluid channels for functioning as a strain sensor, the fabrication techniques for the two types of liquid are different. Fluid channels for embedding ionic liquids are usually made by casting prepolymers into a mould of desired shapes. The mould is fabricated by various methods such as machining, 3D printing[161], and laser cutting[159]. Figure 2-13(a)[116] depicts a typical moulding process for producing a fluid channel. A rigid template is placed into a polytetrafluoroethylene mould made by conventional machining. Next, Ecoflex prepolymer is cast into the mould, covering the lower mould with the upper mould, and curing under a suitable temperature. After the polymer is cured, the template is extracted, and an open channel is left in the Ecoflex. The channel is then injected with ionic liquids and closed with electrodes at both ends. Another simple method for producing a liquid channel is to fabricate an open and single-sided fluid channel by moulding. Then another layer of the polymer is placed on top of the open channel[162]. The two parts are sealed together using the same prepolymer, and the ionic liquid is injected after the sealing is cured.

Fluid channels for embedding liquid metals can be fabricated with more diverse methods. Due to the high surface tension, liquid metals tend to adhere together. This self-adherence allows them to be patterned prior to further encapsulation. The lift-off method[163] is illustrated in Figure 2-13(b). A layer of photoresist is patterned on a polymer substrate using photolithography; a liquid metal is then deposited onto the photoresist-covered polymer. Afterwards, the photoresist layer is removed along with the liquid metal, leaving only a pattern of the liquid metal that adheres to the exposed area of the polymer. The selective wetting method[164] is depicted in Figure 2-13(c). This method relies on a soft stamp to transfer the liquid metal into the desired pattern. The wettability of the liquid metal on the stamp is modified by applying an ultraviolet (UV) laser or other chemical-based methods on the stamp surface. The wettability modification allows the synthesis of a liquid alloy-phobic area on the surface and therefore allows the pattern to be transferred onto a more liquid-alloy-philic substrate. Another method for patterning liquid metals is contact moulding [165]. As indicated in

Figure 2-13(d), a polymer layer moulded with a microchannel is bonded to another UV-treated polymer layer, and then EGaIn is attracted into the microchannel by applying vacuum from the other exit of the channel. The unsealed channel embedded with the liquid metal is cooled on a cold plate to allow the liquid metal to temporality transit into a solid. Afterwards, the top polymer layer is removed, and the remainder is placed on a hot plate such that the liquid metal regains its liquid state.

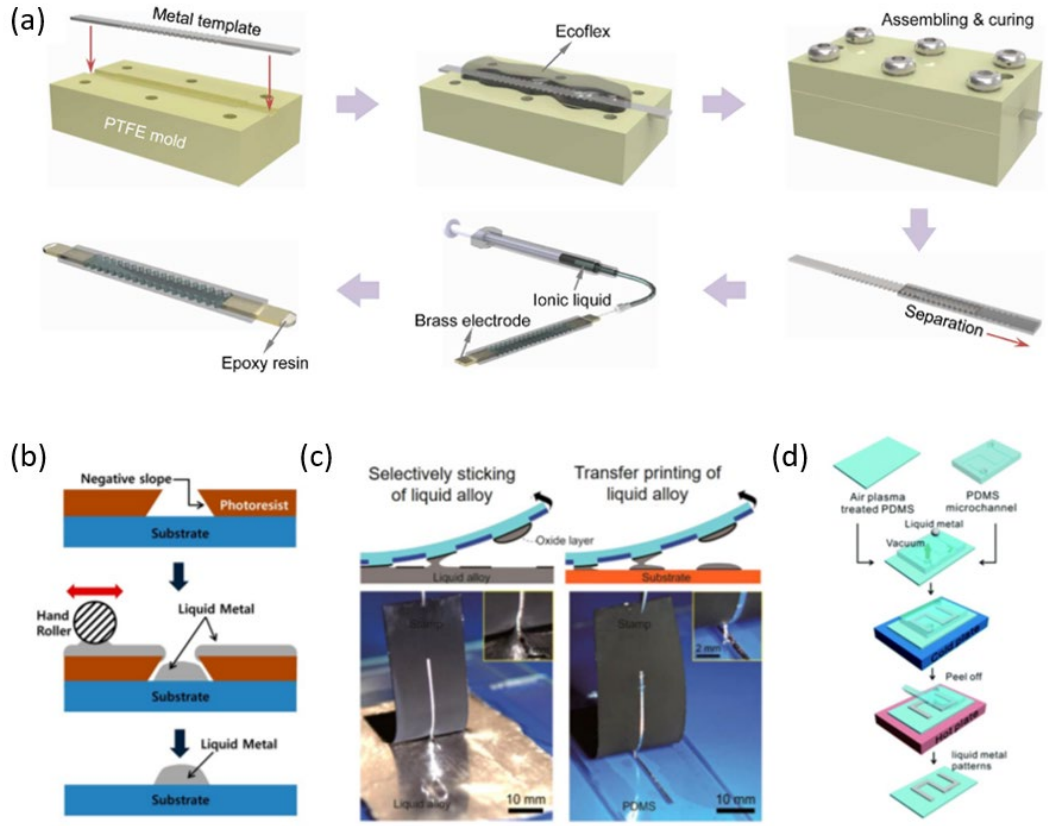

Figure 2-13 Fabrication techniques for strain sensors based on liquid sensing elements. (a)The fabrication process of an ionic liquid-based strain sensor by moulding *[166]*. (Copyright 2016 American Chemical Society. Reused with permission) (b) The lift-off method for patterning liquid metals*[163]*. (Copyright 2016 American Chemical Society. Reused with permission). (c) Modified wettability mediated patterning for patterning liquid metals*[164]*. (Copyright 2019 American Chemical Society. Reused with permission). (d) The contact patterning method for patterning liquid metals*[165]*. (Copyright 2017 Royal Society of Chemistry. Reused with permission).

Some liquid-based strain sensors reported in previous studies, including both sensors based on ionic liquids and liquid metals, are summarized in Table 5.

Conductive elements	Polymer substrates	Maximum measurable strain	Gauge factors	Reference
1-Butyl-1-methylpyrrolidiniumbisimide	Silicone tube	10%	2~2.5	[154]
1-ethyl-3-methylimidazolium-bis ([EMIM][TFSI])	Ecoflex	400%	1.7~7.9	[156]
Sodium chloride (NaCl), Ethylene glycol	Ecoflex	250%	1.8~3.9	[166]
Sodium chloride (NaCl), water, glycerol	Ecoflex	100%	Up to 3.08	[159]
1-methyl-3-octylimidazolium chloride	Ecoflex	500%	2~3	[158]
Sodium chloride (NaCl), water, glycerin	PDMS	40%	-	[160]
potassium iodide, glycerol	Ecoflex	50%	2.2	[167]
[Bmim][BF4]	PDMS	55%	-	[157]
EGaIn liquid metal alloy	PDMS	700%	-	[155]
EGaIn liquid metal alloy	Ecoflex	320%	Up to 4.91	[168]
EGaIn liquid metal alloy	Polyimide	160%	Up to 2.5	[169]

Table 5 Liquid-based strain sensors reported in previous works

2.3.5 Hydrogel-Based Strain Sensors

In addition to embedding ionic liquids inside a microchannel, ionic liquids can also be contained by hydrogels. Hydrogels are a type of soft material comprised of a crosslinked hydrophilic polymer network[124] that contains a large amount of liquid. Like the ionic liquids embedded in a fluid channel, the ionic liquids absorbed by a hydrogel network also forms an electrically conductive path that allows the flow of electric current. The electrical resistance of the conductive path is affected by the strain of the hydrogel; therefore, the hydrogel is capable of working as a strain sensor.

As shown in Figure 2-14(a), Han et al.[170] proposed a hydrogel sensor based on potassium chloride (KCl), glycerol, and gluten. The gluten was extracted from wheat flour and enabled the gel to stick to various objects like skin and rubber naturally.

In another work, Qin et al.[171] fabricated a gelatine hydrogel that contains deep eutectic solvents, as illustrated in Figure 2-14(b). A capacitive strain sensor was achieved by sandwiching a thin layer of VHB^{TM} tape between two hydrogel films.

Moreover, the integration of hydrogels is not limited to ionic liquids only; some other conductive substances can also be utilized together with hydrogels to construct a conductive path within the gel. For example, Hardman et al.[172] developed a strain sensor by doping carbon black into glycerin-containing gelatin. The product is shown in Figure 2-14(c). The purpose of including glycerin in the hydrogel is to increase the bound-water content of the hydrogel. A conductive network is formed by the dispersed carbon black particles within the hydrogel; thus, the product can work similarly to disconnection-based strain sensors. Another similar work was reported by Jing et al. [173], who doped silver nanowires into a gelatin hydrogel to realize a strain sensor.

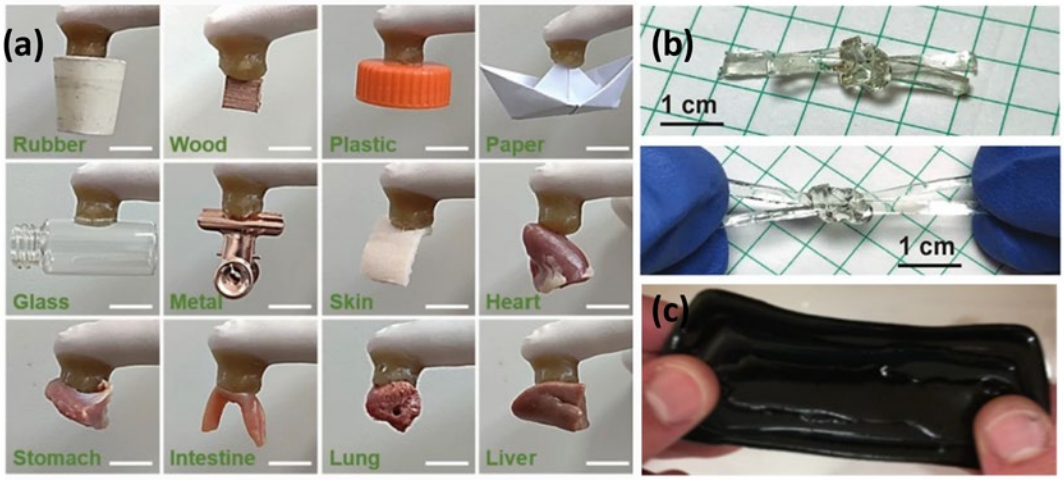

Figure 2-14 Flexible sensors fabricated using hydrogels. (a) A strain sensor made of gluten extracted from wheat*[170]*. (Copyright 2020 Springer Science Business Media, LLC. Reused with permission). (b) A gelatin hydrogel that contains eutectic solvents*[171]*. (Copyright 2018 Royal Society of Chemistry. Reused with permission). (c) A gelatin hydrogel filled with carbon black*[172]*. (Copyright Hardman et al. Reused with permission)

A major drawback of hydrogels is their fragile and brittle mechanical properties and degradation over time. Commonly used hydrogels like gelatin and agar are weak against tearing, and more importantly, they tend to dry out fast as the water contents evaporate into the surrounding environment. In recent years, there has been a new concept for fabricating more durable hydrogels by incorporating two networks of different gel materials. This type of hydrogel is known as the double network (DN) hydrogel. Double network hydrogels are characterized by a unique network structure consisting of two types of polymer components with opposite physical natures: the

minor component is abundantly cross-linked polyelectrolytes that provide a rigid skeleton, and the primary component is comprised of poorly cross-linked neutral polymers that offer ductility. The difference between a polyelectrolyte and a neutral polymer is that the polyelectrolytes can fully dissociate in a wide range of pH, whereas the neutral polymers dissociate only within a specific pH range. According to Gong et al.[174], there are several essential requirements that the materials of double network hydrogels must meet. The first constituting network should be a rigid and brittle polyelectrolyte, and the second network should be a soft and ductile neutral polymer. The molar concentration of the second network should be 20 to 30 times the first network. The first network should be tightly cross-linked, while the second network should be loosely cross-linked, which requires the second polymer to possess a very high molecular weight. The strength of DN gel increases when the molar ratio of the second network to the first one increases.

A robust method for producing double network hydrogels is the one-pot method proposed by Chen et al.[175]. The schematic of the method is illustrated in Figure 2-15. In Chen's work, a double network hydrogel is produced by interpenetrating a hydrogen-bond linked agar network and a covalently cross-linked polyacrylamide (PAAm) network. All reactants, including agar, acrylamide monomer, UV-initiator, N,N'-Methylenebis acrylamide(MBAA), and water were added into a single pot to prepare the hydrogels via a heating–cooling– photopolymerization method. MBAA is a crosslinker used during the formation of polymers such as PAAM. It creates networks rather than linear chains, which helps maintain the firmness of the gel. Upon heating all reactants to 90 ℃ under nitrogen gas protection, the agars were dissolved in solution, which resulted in a transparent and low viscous solution. The solution was then cooled down to room temperature to allow the gelation process of agar. This part of the process refers to the heating-cooling method, often used to produce gelatin and agar-based hydrogels. This process involves a coil-to-helix transition which builds up a three-dimensional agar network via helical bundles. The agar network serves as the first network, containing the precursor for the second network. The obtained agar hydrogel

and other unreacted substances are then photo-polymerized to form the second chemically cross-linked PAAm network, which interpenetrates with the first agar network. The one-pot method does not involve a swelling or diffusion process; hence it can readily produce double network hydrogels in a fast and controllable manner. The one-pot method takes less than two hours to complete the fabrication. In a similar work[176], gelatin instead of agar was used to produce DN hydrogels with the same method.

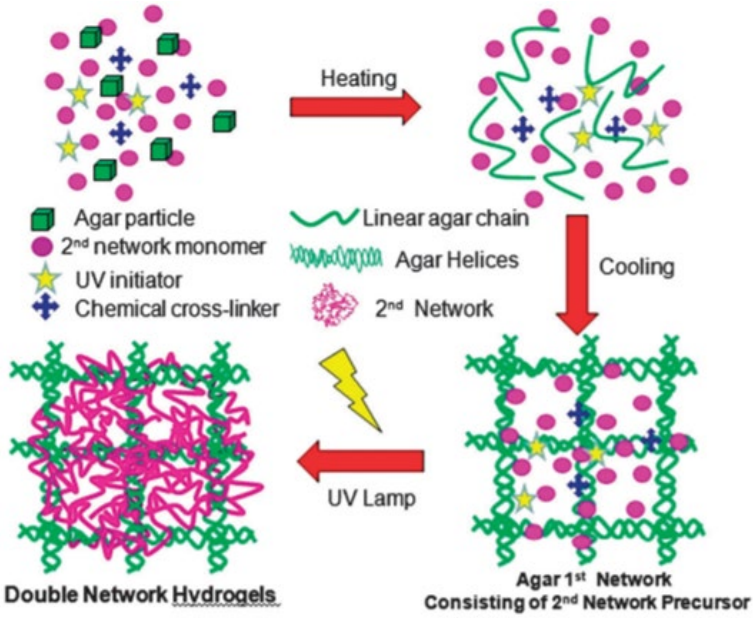

Figure 2-15 One-pot method for preparing a double network hydrogel based on agar and PAAm. The portion of the heating and cooling process can be used to prepare gelatin and agar-based hydrogels*[175]*. (Copyright 2015 Royal Society of Chemistry. Reused with permission).

Although a significant number of DN hydrogels have been proposed, fewer have been tested for their capability in strain sensing. Hou et al. [177] utilized the one-pot method to fabricate a strain sensor based on agar-PAAM DN hydrogel, which contains NaCl dissolved in water as the ionic liquid for the conductive component. The sensor exhibits an extensive sensing range and good signal repeatability. Liu et al.[178] also utilized the one-pot method to fabricate a strain sensor using κ-carrageenan and PAAm, and applied 3D printing technology to pattern the hydrogel. In another work, Sun et al.[179] fabricated a strain sensing using Gelatin-PAAM DN networks and achieved a maximum stretchability of 2850% strain. The characteristics of previously reported

strain sensors based on hydrogels and double network hydrogels are summarized in Table 6.

Conductive component	**Polymer substrates**	**Maximum measurable strain**	**Gauge factors**	**Fabrication methods**	**Reference**
carbon black	Glycerin and gelatin	300%	2.5	Heating and cooling	[172]
Silver nanowires	Gelatin	350%	0.9	Heating and cooling	[173]
VHB tape (dielectric)	Gelatin filled with deep eutectic solvents	300%	0.5	Heating and cooling	[171]
KCL and water	Gluten and glycerol	600%	2.1	Heating and cooling	[170]
NaCl dissolved in water	Agar-PAAM DN hydrogel	1500%	0.2~2.1	One-pot method	[177]
KCl dissolved in water	κ-arrageenan -PAAm DN hydrogel	1000%	0.23~0.63	One-pot method	[178]
PEDOT: PSS suspended in water	Gelatin-PAAM DN hydrogel	2850%	0.46~1.58	One-pot method	[179]
AlCl3·6H2O	Chitosan-PAAM DN hydrogel	800%	1.7~12.1	One-pot method	[180]
NaCl dissolved in water	Gelatin-PAAM DN hydrogel	1200%	Up to 4.58	One-pot method	[181]
Dissociated ions	Agar-acrylic acid-PAAM DN hydrogel	1000%	0.46~0.83	One-pot method	[182]

Table 6 Characteristics of hydrogel-based strain sensors reported by previous studies. (The definition of each abbreviation can be found in the "Abbreviations" section)

2.3.6 Performance of Strain Sensors

2.3.6.1 Sensitivity and Linearity

This section discusses the parameters that affect the performance of flexible strain sensors. Apart from the sensitivity that has already been introduced in section 2.3.1, other parameters include linearity, hysteresis, overshoot, and dynamic stability.

Signal linearity is a parameter closely related to sensitivity, which describes the direct proportionality of signals to applied strain. Ideally, to minimize the difficulty in signal interpretation, the signals of a strain sensor prefer having a constant gauge factor such that it responds to the applied strain with constant proportionality. A nonlinear signal has a gauge factor that changes with strain. High nonlinearity may bring complexities in signal conversion and raise difficulty in calibration[121], particularly when the sensor has an instable baseline signal. The linearity of a signal is usually quantified using the coefficient of determination (CoD), denoted as R^2, of a best-fitted line of regression[183]; however, this R^2 data for sensors reported in previous studies were infrequently provided. Alternatively, a less formal indicator of signal linearity is the change in gauge factors over the entire measurement range of strain sensors. Sensors with larger variations in their gauge factors suggest higher nonlinearity, as they respond to different levels of strain on more contrasting scales.

From the data previously shown in the tables from Table 1 to Table 6, it can be seen that crack-based sensors generally exhibit significantly larger sensitivity but also more severe nonlinearity than other types of sensors. For example, a sensor with an enormous gauge factor of 475, fabricated using graphene bridged silver nanoparticles, was reported by Yang et al.[63]. The sensitivity of crack-based piezoresistive sensors is dependent on many factors. Apart from their differences in terms of fabrication methods, other parameters, including piezoresistivity of conductive particles[184], [185] and their length, diameter, orientations, and density[124], [125], [127], [128], [186], [187] all have an impact on the sensitivity. Several works also indicate that

increasing the fraction of dopant particles in crack-based strain sensors leads to reduced gauge factors[95], [98], [101], [105], but results in improved signal linearity[105].

The signal nonlinearity of crack-based and disconnection-based strain sensors is caused by their morphological change from a homogeneous state to an inhomogeneous state during material deformation[121]. On the other hand, capacitive sensors, liquid-based sensors, and sensors based on hydrogels, which are relatively more homogeneous in their sensing elements, generally show much more stable GFs than resistive sensors, indicating they possess better linearity. Figure 2-16 shows several examples of these types of sensors that provide an excellent linear signal response to the applied strains, including a capacitive sensor based on a liquid metal[188], a sensor based on a potassium iodide-glycerol ionic liquid[167], and a sensor based on cellulose hydrogel[189].

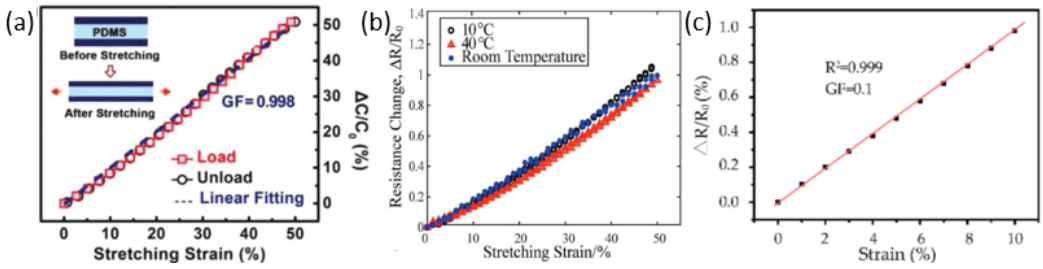

Figure 2-16 Linear response of signals provided by strain sensors. (a) A capacitive sensor based on liquid metals *[188]*.(Copyright 2018 WILEY-VCH Verlag Gmbh & Co. KGaA, Weinheim. Reused with permission). (b) A resistive sensor based on ionic liquids *[167]*.(Copyright 2018 WILEY-VCH Verlag Gmbh & Co. KGaA, Weinheim. Reused with permission). (c) A resistive sensor based on hydrogels*[189]*. (Copyright 2019 Tong et al. Reused with permission).

Notably, all of the capacitive sensors reported in previous works exhibited excellent signal linearity. Cai et al.[105] clarified the theory behind their signal linearity. According to his theory, the capacitance value of a capacitive sensor upon stretching can be predicted using the following derivation:

$$C = E_0 E_r \frac{l\,w}{t_0} = E_0 E_r \cdot \frac{\lambda\, l_0 \frac{1}{\sqrt{\lambda}} w_0}{\frac{1}{\sqrt{\lambda}} t_0} = E_0 E_r \cdot \frac{\lambda \cdot l_0 \cdot w_0}{t_0} = \lambda \cdot C_0 \qquad 2\text{-}3$$

where l_0, w_0 and t_0 denote the sensor's length, width, and thickness at its initial state, respectively; ε denotes the applied strain. When a strain is applied, the length becomes $l = \lambda l_0$ where $\lambda = 1 + \varepsilon$. If the material is assumed to be incompressible (i.e., its volume is conservative), then according to the Poisson deformation theory[190], the width changes to $w = \frac{1}{\sqrt{\lambda}} w_0$, and the thickness changes to $t = \frac{1}{\sqrt{\lambda}} t_0$. As aforementioned, the gauge factor of a capacitive strain sensor is calculated as $GF = \frac{\triangle \frac{C}{C_0}}{\varepsilon}$. Thus, a linear response of capacitance to strain with a gauge factor equal to 1 can be derived as

$$k = \frac{\frac{\triangle C}{C_0}}{\varepsilon} = \frac{\frac{(\lambda - 1)C_0}{C_0}}{\varepsilon} = \frac{\lambda - 1}{\varepsilon} = \frac{\varepsilon}{\varepsilon} = 1 \qquad 2\text{-}4$$

However, this derivation assumes that the material follows the ideal parallel plate model and the Poisson deformation, which may not hold in practice, mainly when the applied strain is large and causes morphological deformation. Although capacitive sensors fabricated by contact transfer of CNTs on different substrates show an identical gauge factor close to 1[65], [66], [67], an increased linear gauge factor of 1.57 was reported when AgNWs are used instead of CNT in a sensor fabricated using the same method[142]. Additionally, a gauge factor of 1.95 was reported by a strain sensor fabricated by spray coating CNT on a TPU substrate[150].

2.3.6.2 Hysteresis and Overshoot

The hysteresis of a strain sensor describes the lag in the electric signals in response to the applied strain that induced the signal. Two examples that show the difference between sensors with significant hysteresis and sensors with negligible hysteresis are illustrated in Figure 2-17(a). The sensor with significant hysteresis, proposed by Guo et al.[140], was fabricated by coating single-wall CNTs onto a PDMS substrate. It can be seen that the presence of hysteresis results in noticeably mismatched signals between

stretching and releasing. The signal responds to the applied strain in the form of two separate curves, which suggests inconsistency in signal interpretation, as ambiguous readings exist for an identical strain value. On the other hand, a strain sensor based on liquid metals exhibited negligible hysteresis. The sensor proposed by Wu et al.[191] utilized an encapsulated liquid metal inside a hollow fibre made by extrusion curing of PDMS. Without visible hysteresis, the sensor provides a well-matched signal between stretching and releasing.

Hysteresis of piezoresistive sensors is caused by the viscoelastic property of the sensing elements[192]. During polymer relaxation upon release, a time duration is required to recover its original shape. This time delay leads to a lag in restoring conducting paths and thus postponing the restoration of electrical resistance. This defect is particularly severe in crack-based and disconnection-based strain sensors, whose conductive paths are interlinked by conductive particles. On the other hand, the sensing elements of strain sensors based on liquid metal, ionic liquid, and hydrogels are present in the form of homogenous liquid; their conductive paths are continually connected when strain is applied. Therefore, the hysteresis of these types of sensors exhibited is insignificant[155], [166], [168], [182]. In addition, capacitive sensors reported in previous works employed dielectric materials as their sensing elements, which did not involve transition in their electrical connectivity; thus, capacitive sensors also exhibit negligible hysteresis[142], [146]–[148].

Similar to hysteresis, overshoot is also caused by the relaxation of polymer materials after their deformation[193]. Overshoot occurs when the applied strain stops, but the signal continues to rise until it extends over the correct value and gradually falls back. An illustration that demonstrates the performance of strain sensors with and without overshoot during cyclic loadings is shown in Figure 2-17(b). A sensor proposed by Chhetry et al.[194], made by coating porous graphene nanoflakes on a PI film, showed significant overshoot at the end of each stretch phase, whereas a sensor proposed by Park et al.[195], developed using a capacitive approach, which relies on the change in

the dielectric constant of a photonic crystal doped PDMS layer, exhibited slight overshoot.

Overshoot is generally present along with hysteresis. Compared to crack-based and disconnection-based strain sensors, sensors based on the capacitive approach and those based on liquid sensing elements and hydrogels whose electrical conductivity is not affected by polymer relaxation generally possess negligible overshoot behaviour [147], [148]. Both hysteresis and overshoot are related to the strain rate, which is the speed a sensor is stretched and released at. Muth et al.[196] proposed a strain sensor by embedding a carbon conductive grease inside an Ecoflex matrix. The sensor demonstrates different hysteresis and overshoot behaviours in response to strains of the same magnitude at 100%, which are applied under different strain rates. As illustrated in Figure 2-17I(c), the hysteresis and the overshoot in the signal provided by the sensor are more severe at higher strain rates and less noticeable when the strain rates are lower. In addition, the magnitude of overshoot is also found to be associated with a range of other parameters, including the magnitude of strain, the number of loading cycles, and sensor's sensitivity to strain[75], [81], [101], [103], [197].

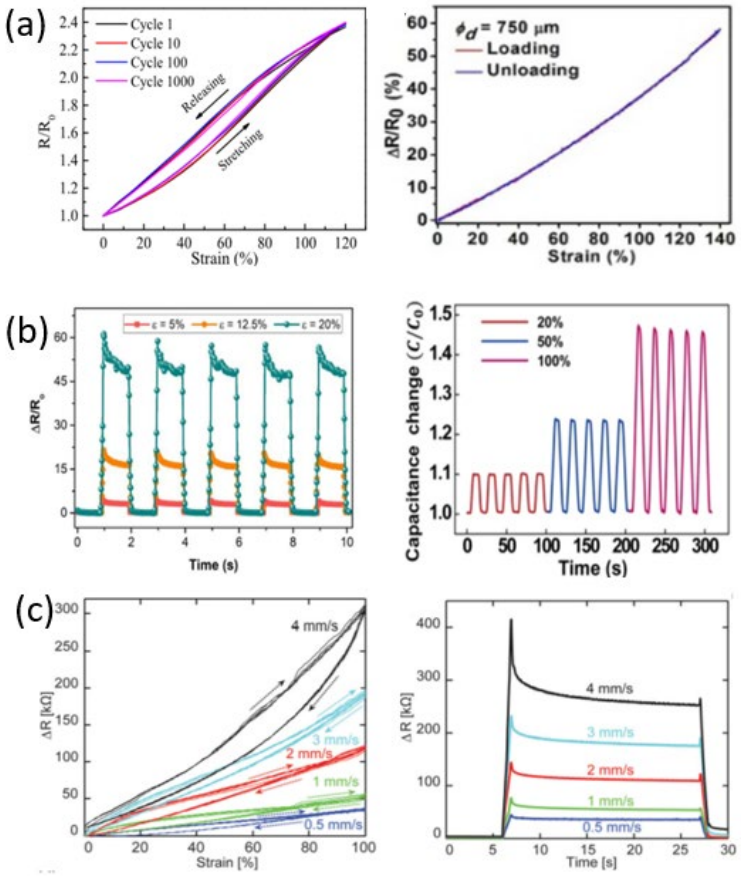

Figure 2-17 Hysteresis and overshoot behaviour of flexible strain sensors. (a) Hysteresis behaviour of strain sensors. Left: significant hysteresis of a strain sensor based on a resistive composite material*[140]* (Copyright 2017, IOP Publishing Ltd. Reused with permission). Right: negligible hysteresis of a sensor based on liquid metals*[191]* (Copyright 2017, Royal Society of Chemistry. Reused with permission). (b)Overshoot. Left: noticeable overshoot of a strain sensor based on porous graphene nanoflakes coated on a PI film*[194]*(Copyright 2019, American Chemical Society. Reused with permission). Right: negligible overshoot of a capacitive strain sensor based on a self-assembled block copolymer (BCP) photonic*[195]*(Copyright 2018 Park et al. Reused with permission). (c) Dependence on strain rates. Left: hysteresis; Right: overshoot.*[196]*(Copyright 2014 WILEY‐VCH Verlag gmbH & Co. KGaA, Weinheim. Reused with permission).

2.3.6.3 Dynamic Stability

Dynamic stability describes the consistency in the signal that a sensor produces when it undergoes dynamically changing strains contrary to cyclic strains. The majority of previous works only report the performance of flexible strain sensors in cyclic loading tests, in which the sensor is stretched and released periodically. Their performance in transducing dynamic strain with changing magnitudes was hardly addressed. However,

dynamic stability should always be considered as it is a vital parameter determining strain sensors' reliability.

When strain is applied in a dynamic manner instead of a cyclic manner, the performance of sensors may vary significantly. A few examples of strain sensors reported in previous studies that show limited performance in transducing dynamic strain are demonstrated in Figure 2-18. In (a), the left part of the figure shows the signal produced by a crack-based sensor[58], fabricated by spray coating CNTs onto a PDMS substrate, when it experiences a set of cyclic strains with a magnitude of 300%. The signal has exhibited a good consistency. However, the right part of the figure shows the difference in signals when the sensor was used to measure dynamic strains with different magnitudes of 100% and 300%. It can be seen that the signal is severely hindered by hysteresis, and ambiguously mismatched signal readings were obtained for the same values of strain. This defect cannot be observed if only cyclic loading tests were performed to evaluate the sensor performance. Similar results are demonstrated in (b), where a disconnection-based sensor[98] fabricated by dispersing P3HT nanofibers in a PDMS matrix was tested for measuring dynamic strains. The sensor showed promising results in sensing cyclic strains but exhibited a noticeable mismatch in sensing dynamic strain. The signals corresponding to each peak strain with a different magnitude show notable inconsistency in their shared portion.

It has been pointed out by previous research[4], [146], [198]–[200] that the poor dynamic response of resistive sensors is due to the viscoelasticity of the polymer matrix and ubiquitous frictions between the doped conductive particles and the polymer molecules[146], i.e., poor adhesion between conductive particle dopants and polymer substrates. The poor interfacial bindings between polymer and fillers lead to slippage, buckling, delamination, and reorientation of conductive filler, which prevent the successful restoration of the initial conduction paths and results in the dependence of the signal on strain history. This defect means the signal provided by sensors utilizing conductive particles as their sensing elements is affected by previously applied strains. For example, in the first stretch-release cycle, a sensor is stretched to a peak strain of

20% before it is released, and the signal follows a specific path for recovery. In the next cycle, when the sensor is stretched to an increased strain of 40% and released, the signal follows a new path for recovery and fails to regain its original values exhibited in the first cycle.

Although the dependency on strain history is considered a critical defect by crack-based sensors because the dependency causes enormous errors in sensing dynamic strains, the crack-based sensing mechanism possessing the dependency was found suitable for constructing electrode layers in capacitive sensors.

An example is illustrated in (c), which shows the resistance change of a conductive polymer layer proposed by Lipomi et al.[4], in response to applied strain. This conductive layer fabricated by spray coating CNT onto a PDMS substrate was intended to constitute the electrode layer in a capacitive strain sensor, even though the same method and material were previously employed for fabricating crack-based strain sensors in several works[60], [96]. It can be observed from the signal that the resistance of the electrode layer possessed strong dependence on strain history during a dynamic loading test in which the sensor is successively stretched to 50%, 100%, and 150% strain, followed by release. Afterwards, the electrode layer gained repetitive electrical resistance for cyclic loadings of 50% strain. The dependence of the resistance of strain sensors on their strain history was also reported by Cai et al.[146] who proposed a soft electrode for capacitive sensor fabricated by contract transferring CNT onto a PDMS substrate. As illustrated in (d), the signal produced by the composite sensor exhibited nearly constant values during stretching and releasing at each progressively increased strain. Moreover, Shin et al.[147] also fabricated soft electrodes for capacitive sensors by contact-transferring CNT onto an Ecoflex substrate. The resistance of the produced electrode as it underwent dynamic strains is demonstrated in (e).

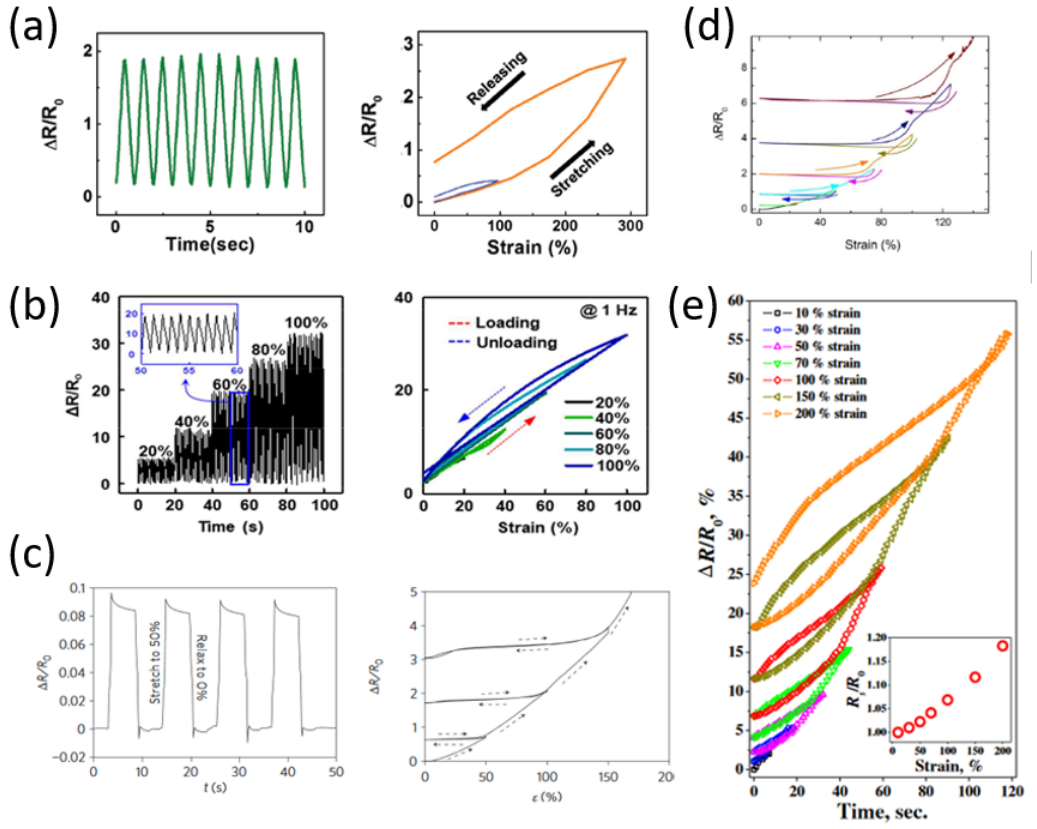

Figure 2-18 Difference in the signal provided by strain sensors when used to sense cyclic and dynamic strains. (a) a strain sensor fabricated by spray coating CNTs onto a PDMS substrate*[58]*.(Copyright 2016 WILEY‐VCH Verlag GmbH & Co. KGaA, Weinheim. Reused with permission). (b) A disconnection-based sensor*[98]* fabricated by dispersing P3HT nanofibers in a PDMS matrix*[98]*. (Copyright 2018 American Chemical Society. Reused with permission). (c). An electrode layer fabricated by spray coating CNT onto a PDMS substrate *[4]*. (Copyright 2011 Nature Publishing Group. Reused with permission). (d) An electrode layer fabricated by contact transferring CNT onto a PDMS substrate*[146]*. (Copyright 2013 Cai et al. Reused with permission). (e). An electrode layer fabricated by contact transferring CNT onto an Ecoflex substrate*[147]*. (Copyright 2014 Elsevier Ltd. Reused with permission).

Resistive sensors based on the crack-based sensing mechanism lack the reliability for sensing dynamic strain[4], [146], [198], [199]. On the other hand, Capacitive sensors do not require precise recovery of their original electrical conduction paths; instead, their capacitance is mainly affected by the size of overlapped electrode area. Thus, they are merely affected by the reorientation of conductive fillers. According to previous studies[146], [148], [201], [202], capacitive sensors possess excellent consistency in transducing dynamic strain.

An iconic work that exhibits the difference in dynamic stability between resistive and capacitive sensors was reported by Shintake et al.[202], who fabricated a strain sensor

by sandwiching a dielectric Ecoflex layer with two layers of carbon black (CB)-filled Ecoflex. The CB-filled Ecoflex layers served as electrode plates. The parallel-plate layout formed a capacitive strain sensor; meanwhile, the electrode layers themselves served as resistive sensors. Via this approach, the difference in performance between resistive sensing and capacitive sensing was compared. The results are shown in Figure 2-19. It can be observed that, in comparison with the resistive approach, the capacitive approach exhibits much more reliable performance, including negligible hysteresis, excellent linearity ($R^2 = 0.9995$), and outstanding repeatability. The capacitive approach measured strains consistently for different peak magnitudes ranging from 50% to 500%. Notably, the strain rate used for testing in this work is 50% s^{-1}, which is significantly higher than the strain rates adopted by most other works.

Furthermore, another example that shows the excellent performance of capacitive sensors for sensing dynamic strain is proposed by Cai et al.[146]. the proposed capacitive sensor showed negligible hysteresis and excellent linearity of R^2=0.9999. The dynamic stability of the sensor was examined by applying a sequence of strains whose magnitudes significantly differed from each other. As shown in Figure 2-19(b), the result showed an excellent linear response of capacitance to strain and well-matched capacitance change for different values of progressively applied strain, indicating the sensor possessed remarkable dynamic stability.

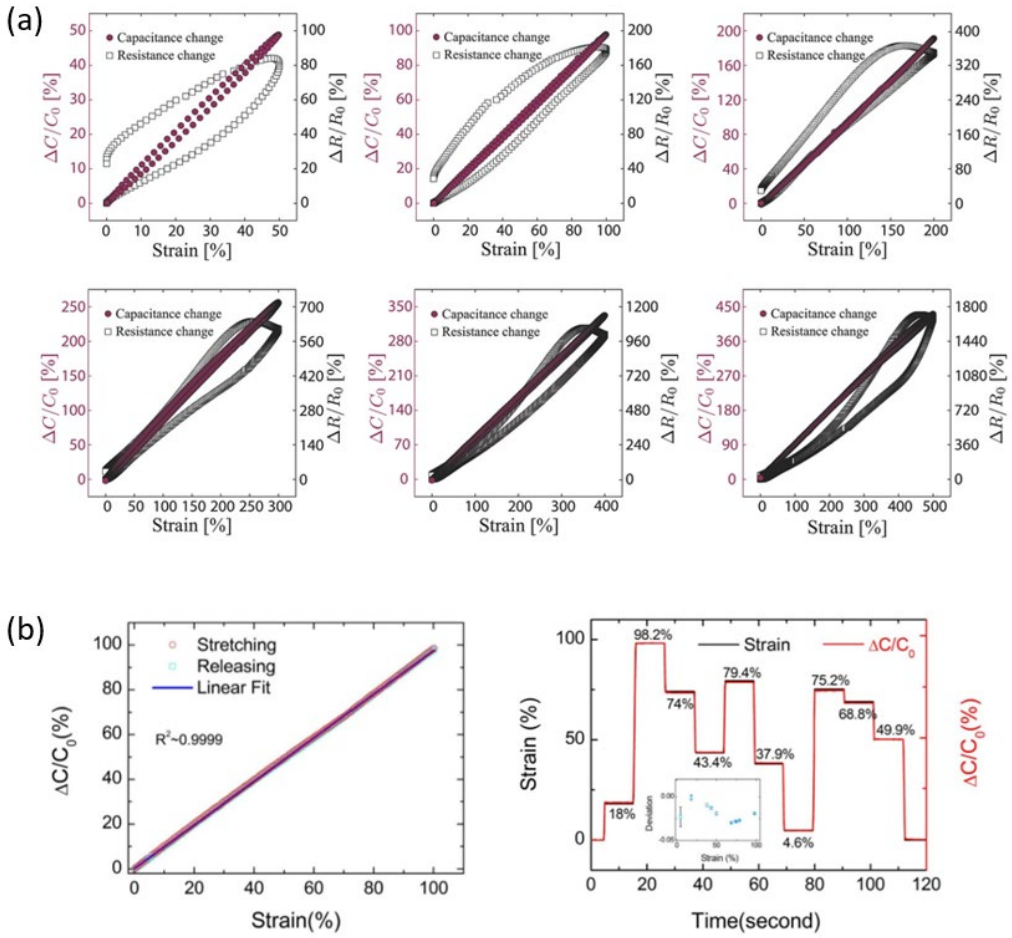

Figure 2-19 Capacitive strain sensors exhibit excellent dynamic stability. (a) A comparison of the performance of the CB-Ecoflex-based strain sensor between resistive sensing and capacitive sensing under one cycle of strain with different amplitudes*[202]*. (Copyright 2017 WILEY-VCh Verlag GmbH & Co. KGaA, Weinheim. Reused with permission) (b) The performance of a capacitive CNT/Dragon Skin strain sensor*[146]*. Left: linear response of capacitance values in response to strain. Right: capacitance in response to dynamic strain. (Copyright 2013 Cai et al. Reused with permission).

Besides capacitive sensors, sensors based on liquid sensing elements and hydrogels exhibit excellent dynamic stability. Liquid-based sensors rely on the geometrical change of their sensing element rather than the conductive paths formed by solid particles. For example, as demonstrated in Figure 2-20(a), Chen et al.[168] developed a strain sensor using wavy-patterned liquid metals. The resistance of the sensor provided a consistent response to the applied dynamic strain with insignificant overshoot and negligible hysteresis. The sensor could accurately indicate the finger bending angles of changing magnitudes. In another work demonstrated in Figure

2-20(b), Choi et al.[166] fabricated a strain sensor by encapsulating a solution of ethylene glycol and sodium chloride inside a wavy fluid channel. The sensor showed a well-matched signal to dynamic strains and provided consistent signals during the detection of several types of motions. Moreover, in Figure 2-20(c), Hou et al.[177] synthesized a DN-hydrogel-based strain sensor using agar, sodium chloride, and polyacrylamide. The sensor exhibited excellent performance for detecting finger and elbow bending angles of dynamically changing magnitudes.

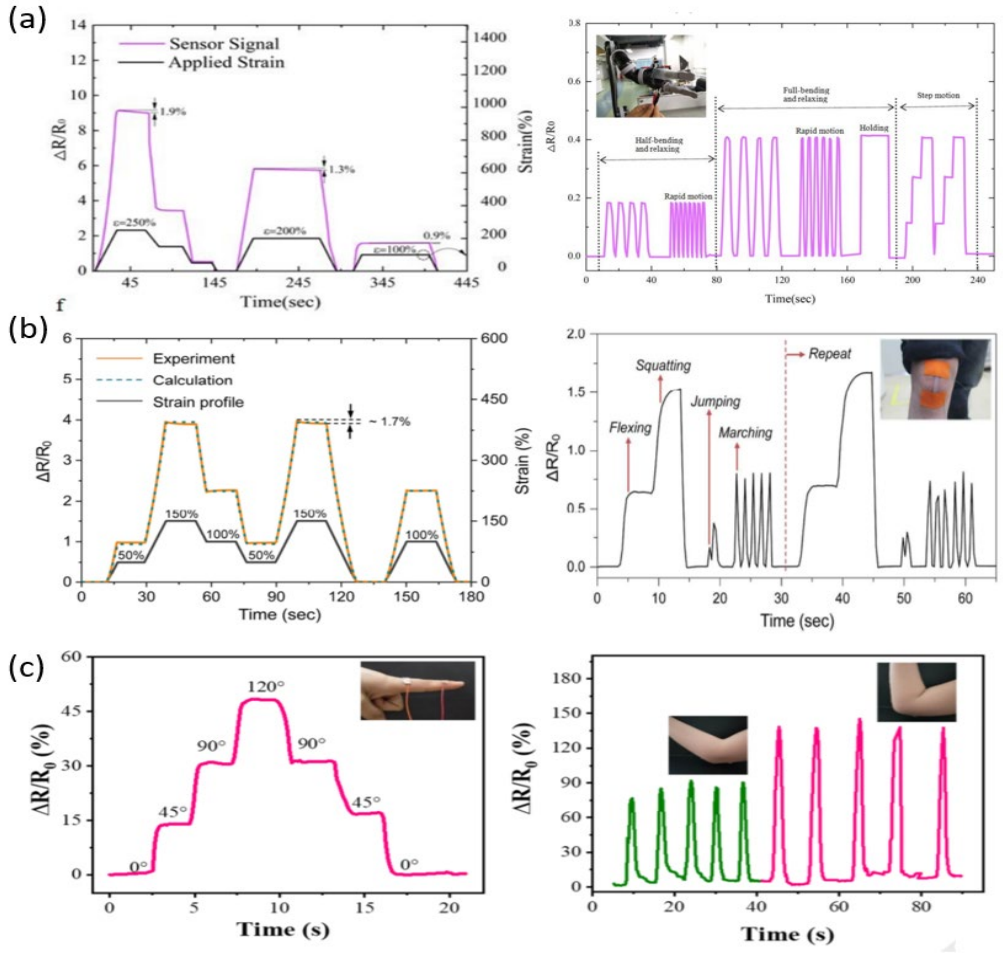

Figure 2-20 Consistent response of flexible strain sensors for transducing dynamic strains. (a) A liquid metal-based strain sensor*[168]*. (Copyright 2020 American Chemical Society. Reused with permission). (b) A sensor based on ionic liquid*[166]*. (Copyright 2016 American Chemical Society. Reused with permission). (c) A sensor based on double-network hydrogel*[177]*. (Copyright 2019 Elsevier Ltd. Reused with permission).

2.3.7 Discussion

In summary, flexible strain sensors based on various sensing mechanisms exhibit different characteristics during their performance. Piezoresistive sensors based on the crack mechanism can provide several orders higher sensitivity than other types of sensors. However, they typically possess considerable hysteresis and overshoot, and more notably, they behave poorly for sensing dynamic strains due to the dependence of their signals on strain history, implying a lack of reliability in practice. Similarly, sensors based on the disconnection mechanism also suffer from noticeable hysteresis behaviour. Sensors based on liquid metal and ionic liquids are promising in possessing negligible hysteresis and overshoot, and they can transduce dynamic strains with excellent consistency, but both types of sensors have their drawbacks. Due to the high electrical conductivity possessed by liquid metals, strain sensors of this type must be embedded in a long and thin microfluid channel to increase their resistance value such that they can be accurately interpreted into strain. Sensors based on ionic liquids do not necessarily require a sophisticated fluid channel, but their signals should be acquired by measurement instruments using AC excitation to avoid the charge separation problem. The electrolysis effect associated with certain types of liquids should also be considered to avoid the formation of gas bubbles in the liquid channel. Sensors based on hydrogels often suffer from the problem of degradation over time; although sensors that utilize double networks hydrogels exhibit outstanding stretchability, their fabrication requires toxic chemical crosslinkers, which often leave residue in their final products.

Notably, capacitive sensors reported in previous literature possess a range of outstanding attributes, including relatively simple fabrication methods, negligible hysteresis and overshoot, excellent signal linearity, and reliable performance for sensing dynamic strains. However, previous works did not address a critical limitation that prevents the effective use of capacitive sensors from a practical perspective. The main issue with capacitive sensors is the lack of a low-cost and portable measurement

method that can accurately measure extremely tiny capacitance typically valued at the picofarad level. The capacitance values of the strain sensors reported in previous works are within the range between 2.2 pF to 35 pF[148], [201], [203]–[207], and they require a high excitation frequency of 10 kHz~1 MHz[146], [148], [205] to achieve good performance. The interpretation of capacitance to strain requires the measurement instruments to possess femtofarad-scaled increments[206], [207]. Currently, reliable measurement of capacitance value at the level of femtofarad relies on the use of an LCR meter[147], [204], [205] or a capacitance meter[206], [207], which is only available within the setting of a laboratory environment. Simple methods such as the RC time constant method, digital multimeter, and capacitor divider circuit are unreliable due to their insufficient resolution and substantial interference of measurement noise. It is also worth paying attention to parasitic capacitance and the contact impedance in the electrical connection, as they can easily dominate over the valid signal of picofarad-level capacitance. Moreover, the impact of the electrical resistance variation of the electrode plates that form the capacitive structure on the measured signal must also be considered as it may further hinder the accuracy of capacitance measurement.

2.4 Previous Works on EIT-Based Electronic-Skin Sensors

By combining the two concepts from separate fields into one, i.e., integrating flexible strain sensors with the working principle of EIT, electronic skins that enable spatial tactile sensing using a flexible material have been realized in several previous studies. Essentially, the integration is achieved by connecting a number of electrodes to a flexible and electrically conductive material, such that electrical excitation and voltage measurement can be performed to allow the implementation of EIT, which estimates the electrical conductivity distribution of the material. An example is illustrated in Figure 2-21, which shows a tactile sensor proposed by Lee et al.[15] for sensing strain

and pressure distribution and localizing the contact point. The sensor was fabricated by mixing MWCNT (2.5 wt%) into Ecoflex polymer using a centrifugal mixer and shear milling machine, followed by injection moulding to enable shape formation. The film was attached with a number of electrodes whose electrical connection with the film was ensured by applying a highly conductive silver paste. Current injections and voltage measurements were performed at these electrodes to provide input data for EIT reconstruction. Notably, the current was only injected into electrodes in parallel with the stretched direction, such that the directions of the current flow inside the material were relatively more focused along the stretched direction; therefore, the reconstructed resistivity can better represent the strain along that direction. The reconstructed results show the estimated resistivity roughly matched with the applied strain. The points of contact could be roughly located.

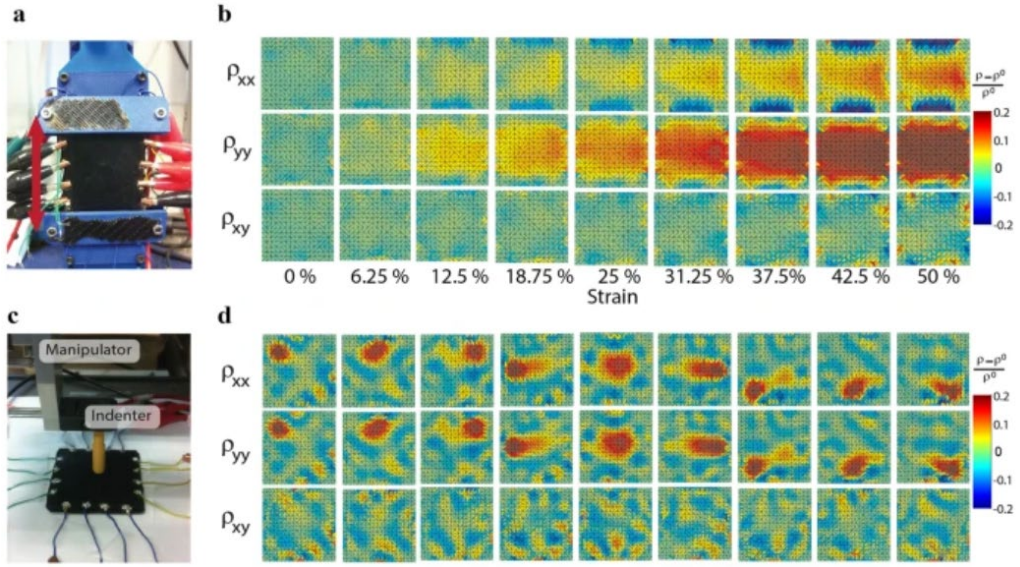

Figure 2-21 EIT-based strain mapping sensor made of MWCNT/Ecoflex composite*[15]*. (Copyright 2017 Lee et al. Reused with permission).

In another work, Oh et al.[16] developed a spatial strain sensor featuring sensitivity only to strain applied in parallel with the planar surface but not to perpendicular pressure applied in the vertical direction. The sensor was made of MWCNT/PDMS composite via a solution-based water-in-oil emulsion process which enables the formation of the porous structure of the film. The aqueous phase was made by mixing

MWCNT and its surfactant in deionized water, and the oil phase was made by dissolving PDMS in hexane. The two phases were mixed together and ultrasonicated for 30 minutes before they were cast into a mould, followed by thermal heating at 70 °C for 4 hours for curing the PDMS and heating at 120 °C for 2 hours for removing the water content, leaving the porous structure of the residual product. The film is then connected with multiple electrodes to enable the implementation of EIT.

Due to the porous structure, the applied normal pressure theoretically only closes the pores without distorting the percolation network of conductive MWCNT; therefore, there is no change in conductivity due to applied pressure. The reconstructed result is shown in Figure 2-22. It can be seen that pressing the sensor in the normal direction did not induce a noticeable change in the reconstructed conductivity, whereas stretching the sensor in the planar direction led to notable conductivity variation.

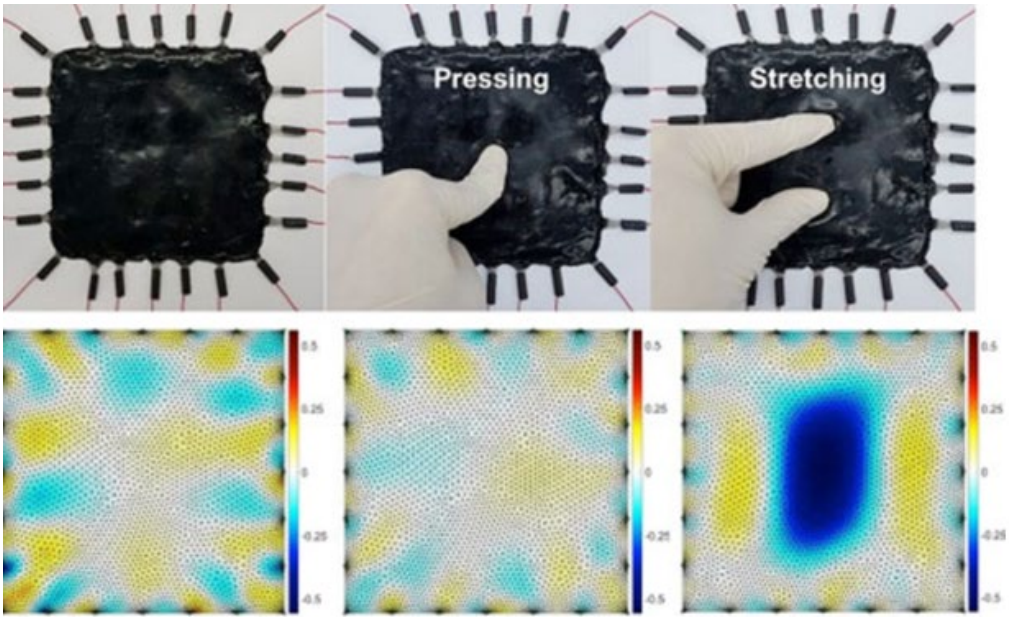

Figure 2-22 EIT-based porous MWCNT/PDMS sensor for estimating planar strain distribution*[16]*. (Copyright 2018, American Chemical Society. Reused with permission).

Dai et al.[208] applied EIT to a CNT-modified nonwoven aramid fabric for achieving damage detection. The conductive fabric was made by coating CNT onto a trimmed fabric. The fabric was first dipped into a commercially available CNT sizing agent diluted with distilled water at a weight ratio of 1:2 and sonicated for 15 minutes. The

CNT-modified fabric was dried at 130 °C and infused with epoxy resin. After finishing the resin infusion, the sensor was cured at 130 °C for 6 hours. Then the sensor was attached to 32 electrodes along its boundary. All electrodes were coated with a silver paste to enhance their electrical connection. As shown in Figure 2-23, different types of damage were induced on the sensor to examine its ability to detect cracks. The reconstructed electrical conductivity distribution under the presence of damage showed a good match in terms of the damage positions, although the shape of the damage could not be approximated.

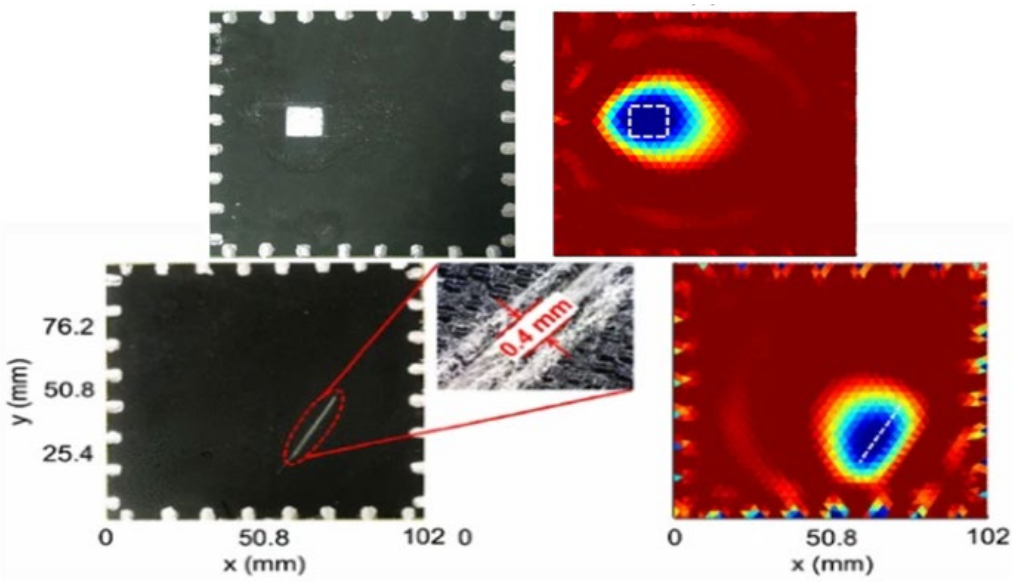

Figure 2-23 EIT-based tactile sensor for crack detection*[208]*. (Copyright 2016 Springer Science Business Media New York. Reused with permission).

Chossat et al.[137] clarified that using rubber-based piezoresistive sensing material for EIT-based electronic skins is unreliable. Unlike bulk conductive materials, piezoresistive composite does not have isotropic conductivity. Within these composites, electric current does not necessarily flow through a straight line as the shortest path between two electrodes; instead, it flows through a link formed by conductive particles[137]. The link may be an arbitrary path within the rubber. In this case, the mechanical stimulus applied to a spot that has a considerable distance from the shortest path between two electrodes may alter the impedance of the material more than the stimulus applied to a spot on a straight line. This instability issue produces severe

limitations that hinder the reliability of the sensor. Thus, Chossat took an alternative approach to fabricate a pressure distribution sensor. Instead of rubber-based material, an ionic liquid was used to constitute the sensing element of the sensor. Ionic liquids possess isotropic electrical conductivity, and therefore the current flow through the shorted conduction path between two spots can be ensured by using ionic liquid. Chossat also identified another advantage of using ionic liquids as the stability in sensitivity over time. The overall resistivity of a piezoresistive rubber-like material increases noticeably due to the ageing of the silicone matrix, whereas the resistivity of ionic liquids is stable over time[137]. In his work, an ionic liquid (1-ethyl-3-methylimidazolium ethyl sulfate) was injected into a grid-patterned fluid channel. The boundary nodes of the fluid channel were attached with soft electrodes fabricated by blending Nickle strands and Nickle-coated carbon fibres into Ecoflex using a planetary mixer. The deformed silicone rubber, which possesses a linear channel geometry, can quickly restore its original shape when the applied pressure is removed. Therefore, the sensor responds to pressure in a more predictable manner. The reconstructed results showed a reasonable estimation of the conductivity variation distribution caused by pressure applied to a single or two evenly positioned points. However, the reconstruction for more complex pressure distributions were not performed.

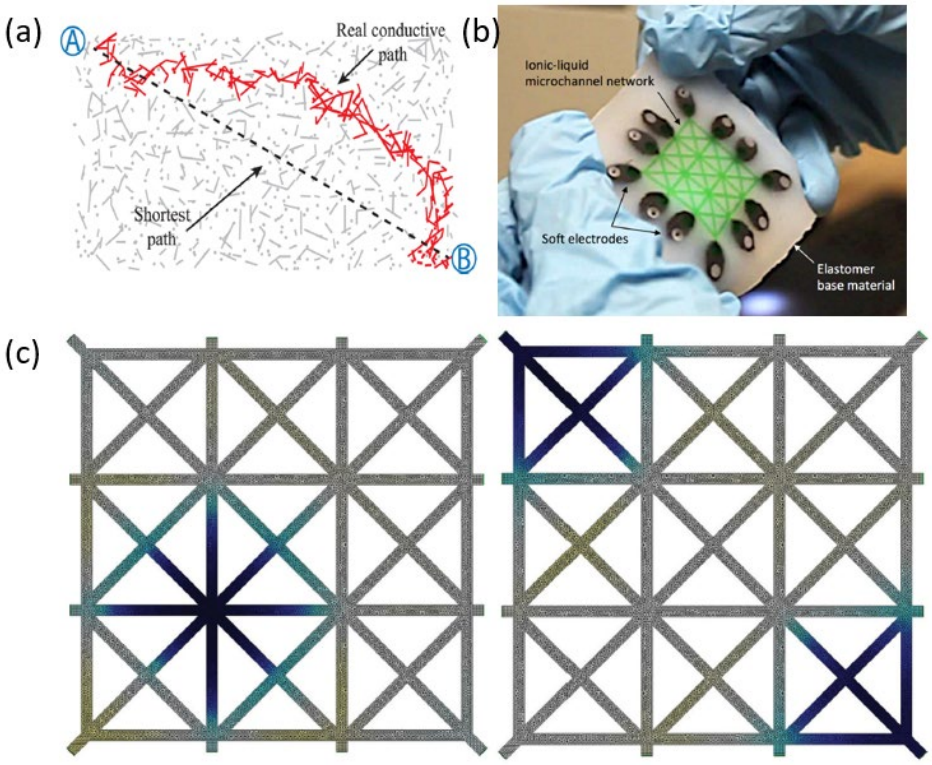

Figure 2-24 EIT-based tactile sensor using ionic liquid*[137]*. (a) Anisotropic conductivity possessed by conductive rubber results in instability issues. (b) The electronic skin whose fluid channels are filled with ionic liquid. (c) Reconstructed results pressure applied to a single point and double points. (Copyright 2015 American Society of Mechanical Engineers. Reused with permission)

Conductive fabrics have also been considered feasible candidates for realizing EIT-based tactile sensors. Yao et al.[209] implemented EIT on a conductive fabric made by coating silver onto Dolarstan nylon. Copper stripes were attached as electrodes along the boundary of the fabric. The sensor was tested for detecting pressure induced by manually pressing the fabric. The reconstructed results showed that a rough estimation of touchpoints was achieved; however, the area that was estimated of possessing notable conductivity variation occupies a significantly larger area than the spot that was actually pressed, implying that accurately locating the touchpoints is challenging.

Figure 2-25 EIT is applied to a piece of conductive fabrics to enable pressure detection*[209]*. (Copyright 2012 Emerald Publishing Limited. Reused with permission).

Flexible sensors integrated with EIT can also measure conductivity change caused by multiple types of stimuli. Hallaji et al.[210] developed an EIT-based double-layer electronic skin for simultaneous crack detection and chloride gas monitoring. The skin was made by coating two layers of fabrics with different conductive paint. The first sensing layer was coated with copper paint. Copper reacts rapidly with chlorides, and the resistivity of copper paint increases significantly due to the formation of copper chloride and copper oxide[210]. Thus, the conductivity of the copper paint changes in the presence of chlorides. On the other hand, silver particles react negligibly with chlorides, and their electrical conductivity is not affected by the presence of chlorides. The combined dual layers could hence respond to both chemical stimuli in the presence of chlorides and mechanical stimuli in the presence of physical cracks. The reconstructed results showed successful detection of the induced cracks with and without the presence of chlorides; however, the reconstructions were also contaminated by significant errors, and the exact shapes of the cracks could not be estimated.

Furthermore, Yao et al.[211] applied EIT on an EeonTex conductive fabric for estimating pressure distribution. The fabric was connected by 16 electrodes along its perimeter. The conductivity distributions in the presence of different types of applied pressure were reconstructed. It can be seen from Figure 2-26 that when a single load was placed onto the sensor, the reconstruction was able to roughly estimate the induced conductivity change near the contact area. However, in the second case where another

load was added, a notably mismatched conductivity distribution over the contact area of the same load was observed. This problem became more severe in the third case, where another load was added. Under the presence of the third load, the reconstructed image only showed a dominating conductivity variation caused by the pressure asserted by the third load. The estimated conductivity variation for the area beneath the second load was diminished, and the estimated conductivity variation caused by the pressure of the first load was nearly invisible.

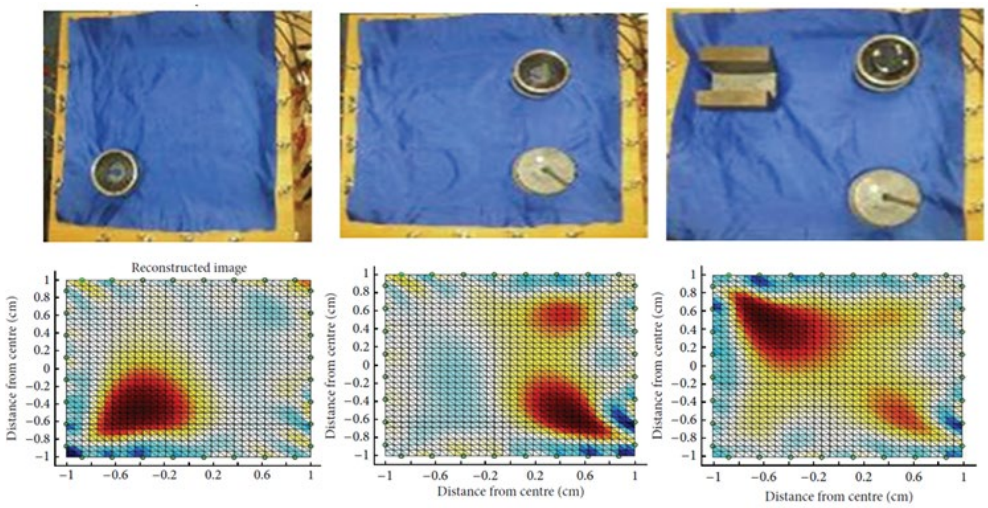

Figure 2-26 EIT-based fabric sensor for pressure distribution estimation*[211]*. (Copyright 2013 A. Yao et al. Reused with permission).

2.5 Summary and Research Gaps

This literature review chapter gathered knowledge from previous studies on EIT, strain sensing materials, and EIT-based electronic skins.

Section 2.2 introduced the EIT technology. First, the basic operation of EIT and its working principle were explained. In brief, the reconstruction algorithm solves a forward problem, which predicts the electric potential distribution over the domain of interest, and solves an ill-posed inverse problem, which estimates the conductivity

distribution. Next, different drive patterns for inducing an electric potential distribution by injecting a constant current to the domain were described.

Section 2.3 introduced various flexible strain-sensing materials, including piezoresistive and piezocapacitive nanocomposites, liquid metals, ionic liquids, and hydrogels. Their fabrication methods were described. To evaluate the reliability of these sensors, parameters associated with strain-sensing performance were explained, including gauge factors, linearity, hysteresis, overshoot, dynamic stability, and durability. The defects of each type of sensor were also discussed

In section 2.4, previous studies that integrated EIT with flexible sensors for enabling spatial tactile sensing were reviewed. EIT has been previously implemented on various sensing elements, including nanocomposites, ionic liquids, and textiles, and accomplished different applications, including pressure sensing, strain sensing, gas monitoring, and damage detection. It was observed that extensive errors hindered the results estimated by these sensors.

In a nutshell, although the existing approach of integrating EIT with flexible sensing materials possesses a vast potential in realizing low-cost electronic skins, it suffers from a severe lack of accuracy. This approach cannot achieve reliable estimations of strain distribution; instead, only a vague and erroneous approximation can be obtained. The lack of accuracy can be attributed to two factors:

- Reconstruction algorithms

The reconstruction algorithms of EIT are intrinsically based on a severely ill-posed system where non-unique solutions exist. A final solution can only be determined by error minimization according to specific criteria. It is challenging to obtain a solution with a guaranteed agreement or a reasonable similarity with the true solution.

- Material systems

Most flexible sensing materials that can compose electronic skins suffer from various defects, such as hysteresis, overshoot, dynamic instability, and insignificant signal

readings. These defects lead to incoherence during the signal interpretation from reconstructed electrical conductivity distribution into strain distribution.

The challenges raised by both factors should be overcome in order to improve the reliability of EIT-based electronic skins. Overcoming the challenges requires a new method that effectively enhances the reconstruction accuracy and a suitable material that can consistently transduce strains into electrical conductivity.

2.6 Research Methodology

This research aims to develop an EIT-based electronic-skin sensor that provides more genuine estimations of the strain distribution in a two-dimensional plane. The methodology of this study is as follows:

1. Simulate EIT using conventional reconstruction algorithms.

   This simulation provides a baseline for comparing the solutions reconstructed by EIT and identifying the limiting factors that may hinder the performance of EIT-based electronic skins.

2. Find a method to accommodate the identified limitations and validate the method via simulation.

   This requires finding a method that enhance the robustness of EIT reconstruction algorithms and allows an EIT-based electronic skin to sense strain distribution more efficiently than sensors reported by previous studies. This step involves algorithm adaptation.

3. Characterize strain-sensing materials.

   This experimental characterization verifies the strain-sensing performance of selected materials. It allows the determination of a suitable material that

constitutes a new electronic skin and has less material limitations (hysteresis, overshoot, dynamic instability) than the materials reported by previous works.

4. Implement a strain-sensing electronic skin and perform testing.

The new reconstruction method proposed in step 2 is implemented on a sensor made of the material determined in step 3 in order to actualize an electronic skin. The strain-sensing performance of the electronic skin is validated experimentally.

The pursuit of these tasks is described in each subsequent chapter, respectively.

Chapter 3 Simulation Study

3.1 Introduction

In previous studies, EIT-based E-skin sensors highlighted their spatial tactile sensing capability established by integrating EIT with piezoresistive materials; however, they suffered significant errors in their estimated solutions. The causes of their error lack sufficient analysis.

This chapter utilizes a simulation study to identify the limiting factors possessed by EIT-based E-skins, such that the limitations can be accommodated correspondingly in the subsequent chapters. Apart from the downsides of EIT imaging technology itself, other factors that may affect strain sensing performance, including the anisotropic conductivity of sensing material, measurement noise, electrode movement, and temporal resolution, are also addressed in the simulation study.

This chapter first introduces the governing equation for EIT algorithms, which constitute the foundation of image reconstruction. Then the forward problem, comprising the finite element method and the complete electrode model, is explicitly derived. After that, the inverse problem consisting of a Jacobian matrix and commonly used regularization methods is formulated. Finally, a simulation study that reconstructs the conductivity distribution resulting from various input scenarios is performed to analyze the obstacles encountered by E-skins during their spatial strain sensing.

An overall flow diagram that contains the above terminologies and summarizes the working mechanism of an EIT-based E-skin is illustrated in Figure 3-1. When a strain is induced in an E-skin, the electrical conductivity at the affected region in the E-skin is perturbed. The perturbation in the conductivity results in change of voltages at the boundary electrodes due to the excitation current. Using the finite element method, a mathematical model for predicting the boundary voltage variation is derived from the

governing equation and the complete electrode model. An inverse solver is further derived from the forward model using the concept of the Jacobian matrix and regularization methods. The inverse solver utilizes the voltage data measured from the E-skin's boundary electrodes to reconstruct the conductivity distribution change caused by the applied strain. Finally, the reconstructed conductivity variation is interpreted to obtain an estimation of the strain distribution.

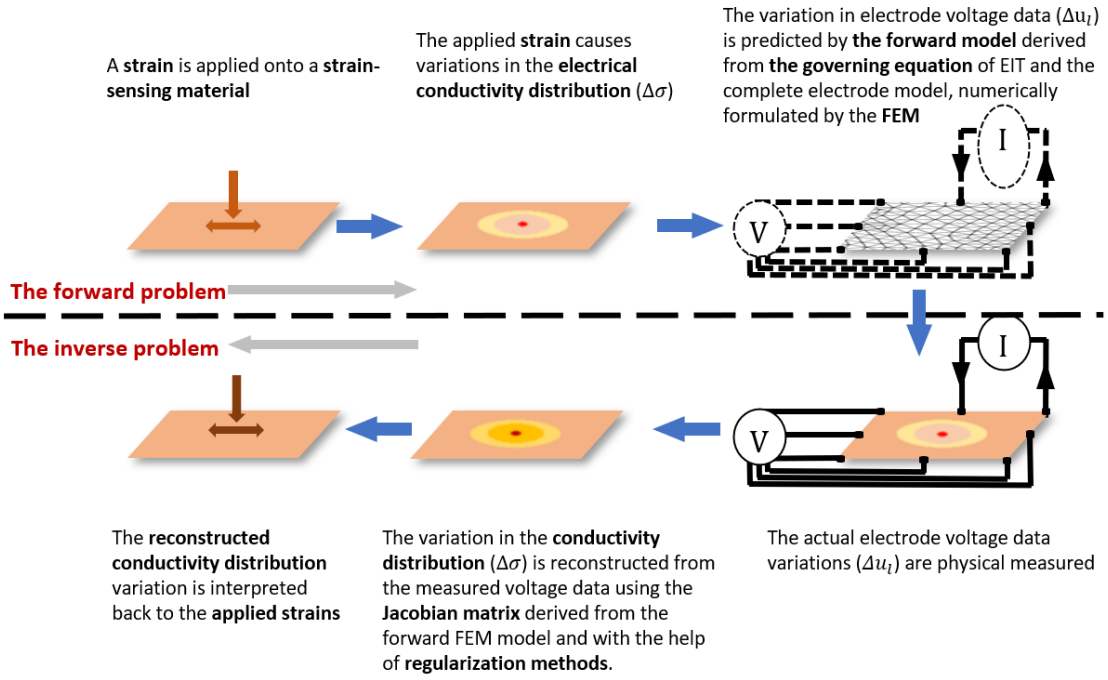

Figure 3-1 The working mechanism of EIT-based electronic skins and the terminologies related to the reconstruction algorithms of EIT.

3.2 The Governing Equation of EIT

The starting point of the EIT reconstruction algorithms is to determine a governing equation that describes the mathematical relation between the electric potential distribution (U) and the injected current (I). This section details the step-by-step

derivation of the mathematical model used for EIT. The derivation in this chapter is summarized from various previous studies[21], [55], [212]–[215].

The derivation of the governing equation originates from the Maxwell equations, which describe electromagnetism in space. The differential form of the Ampere-Maxwell law states that

$$\nabla \times B = \mu_0 \left(J + \varepsilon_0 \frac{\partial E}{\partial t} \right) \tag{3-1}$$

Equation 3-1 is for electromagnetism in free space, the ∇ symbol denotes the divergence operator, J is the conduction current density, $\varepsilon_0 \frac{\partial E}{\partial t}$ is the displacement current density, and B is the magnetic field describing magnetic flux density. For a physical material instead of free space, a tensor of relative permittivity ε_r is added, such that the equation becomes

$$\nabla \times B = \mu_0 \left(J + \varepsilon_0 \varepsilon_r \frac{\partial E}{\partial t} \right) \tag{3-2}$$

The permittivity of a material is frequency-dependent. If only direct or low-frequency current is assumed, then the effect of displacement current is relatively small and can be neglected, leaving only conduction current. In this case, the parameter $\varepsilon_0 \varepsilon_r \frac{\partial E}{\partial t}$ is negligible in comparison to J. Hence equation 3-2 can be simplified to

$$\nabla \times B = \mu_0 J \tag{3-3}$$

There are two types of magnetic fields considered in electromagnetism: B, the magnetic flux density, and H, the magnetizing field. The relationship between B and H is described by[216]

$$B = \mu_0 H \tag{3-4}$$

Substituting equation 3-4 into 3-3 results in

$$\nabla \times H = J \tag{3-5}$$

Next, a divergence operator ($\nabla \cdot$) is applied to both sides of equation 3-5 to obtain:

$$\nabla \cdot J = \nabla \cdot (\nabla \times H) \tag{3-6}$$

The divergence of the curl ($\nabla \times$) is always equal to 0, hence

$$\nabla \cdot J = 0 \tag{3-7}$$

Ohm's law states that

$$J = \sigma E \tag{3-8}$$

where E is the electric field, and σ is the electrical conductivity of the material. Equation 3-8 is substituted into equation 3-7 to obtain

$$\nabla \cdot (\sigma E) = 0 \tag{3-9}$$

The Maxwell-Faraday equation states that

$$\nabla \times E = \frac{\partial B}{\partial t} \tag{3-10}$$

When a direct or low-frequency current is assumed, B can be assumed as a constant value in time[217]. Thus, equation 3-10 becomes

$$\nabla \times E = 0 \tag{3-11}$$

The assumption of the constant value of B implies that the electric field (E) is conservative; with the condition expressed by equation 3-11, the electric field can be given as the negative gradient of electric potential[217], expressed as

$$E = -\nabla U \tag{3-12}$$

Equation 3-12 is substituted into equation 3-9 to obtain the final governing equation in the form of an elliptic partial differential equation (PDE) expressed as

$$\nabla \cdot (\sigma \nabla U) = 0 \tag{3-13}$$

Within the scope of this thesis, only two-dimensional (2D) EIT is considered. The imaging area of interest is a 2D domain (Ω) enclosed by a one-dimensional (1D) boundary ($\delta\Omega$), as illustrated by Figure 3-2. When the PDE described by equation 3-13 is applied to a 2D plane, its physical meaning is that the divergence of the current

density at any given points $\hat{x}(x, y)$ inside Ω is 0. In other words, the amount of current that enters a point must be equal to the amount of current that flows out of that point.

Electric potential distribution is produced by the current injected from electrodes positioned along δΩ. The current entering or leaving the region Ω via the electrodes is represented by a component normal to the boundary δΩ. This condition is represented using the generalized Neumann boundary condition[218], described by

$$\hat{\boldsymbol{n}} \cdot (\sigma \nabla U) = g \qquad 3\text{-}14$$

The parameter g is the density of the injected current. $\hat{\boldsymbol{n}}$ is a unit normal vector pointing into Ω, and U is the electric potential of the points on δΩ. The physical meaning of equation 3-14 is that the density of the current injected to any point on δΩ is equal to the electric potential gradient at that point in the normal direction to the boundary multiplied by the conductivity.

Finally, the governing equation to the forward problem of EIT is summarized as a PDE along with its boundary conditions, as indicated in Figure 3-2. Based on this model, the electric potential distribution (U) at any given point within the domain (Ω) can be calculated using a known current source (g) applied to the boundary (δΩ). However, the direct implementation of this model is typically too complex to achieve using analytical approaches. Numerical formulations are required to discretize the problem into a finite number of small elements, such that pointwise electric potential distribution can be determined. The numerical formulation is achieved via the finite element method (FEM).

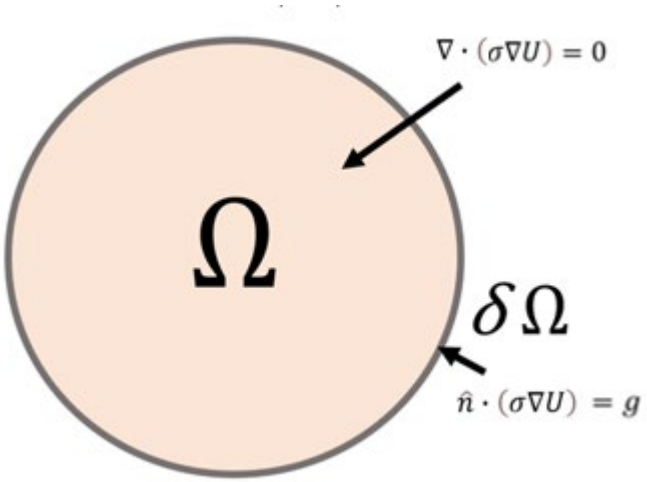

Figure 3-2 The governing equation of EIT, in the form of a PDE and its boundary conditions

3.3 Solving the Forward Problem Using FEM

3.3.1 Numerical Formulation

The finite element method (FEM) begins with the weighted residual (WR) method[55], [215], which is a common way of solving discretized problems. As shown in equation 3-15, both sides of the PDE are multiplied by a test function, V. The purpose of inserting test functions is for error minimization by weighting the solution such that the residual, which is the difference between two sides of the system of linear equations that are to be derived at the end of this section, is minimized and close to 0.

$$\mathrm{V}\big(\nabla \cdot (\sigma \nabla U)\big) = 0 \qquad 3\text{-}15$$

Green's first identity method is applied to separate the left side of the equation into the "bulk" and the "boundary" and eliminate the divergence operator in the meantime. The method starts with integrating both sides of equation 3-15 to obtain

$$\int_{\Omega} V\big(\nabla \cdot (\sigma \nabla U)\big)\, dA = 0 \qquad 3\text{-}16$$

According to the vector divergence identities, the divergence of a vector function ($\boldsymbol{f}$) multiplied by a scalar function (φ) can be reformulated as

$$\nabla \cdot (\varphi\, \boldsymbol{f}) = \varphi(\nabla \cdot \boldsymbol{f}) + \boldsymbol{f}\ \cdot \nabla\varphi \tag{3-17}$$

which can be rearranged as

$$\varphi(\nabla \cdot \boldsymbol{f})\ = \nabla \cdot (\varphi\, \boldsymbol{f}) - \boldsymbol{f}\ \cdot \nabla\varphi \tag{3-18}$$

Considering $\varphi = V$ and $\boldsymbol{f} = \ \sigma\nabla U$, this formula is applied to equation 3-16 to obtain

$$\int_{\Omega} \{\nabla \cdot (V\sigma\nabla U) - \sigma\nabla U \cdot \nabla V\}\, dA = 0 \tag{3-19}$$

The divergence theorem states that under the conservative condition, the change in density within a space of D dimensions must be equal to the density transported across the boundary of the space, i.e., a space of $\mathrm{D} - 1$ dimension. This relation is expressed as

$$\int_{R^N} \nabla \cdot F\, d\gamma^D = \int_{R^{N-1}} F \cdot \hat{\boldsymbol{n}}\ d\gamma^{D-1} \tag{3-20}$$

By applying the divergence theorem to the first term of the left-hand side of equation 3-19, the equation becomes

$$\int_{\delta\Omega} V(\sigma\nabla U) \cdot \hat{\boldsymbol{n}}\ dS + \int_{\Omega} \{-\sigma\nabla U \cdot \nabla V\}\, dA = 0 \tag{3-21}$$

which can be rearranged as

$$\int_{\Omega} \sigma\nabla U \cdot \nabla V\ dA = \int_{\delta\Omega} V\, \sigma \frac{\partial U}{\partial \hat{\boldsymbol{n}}}\ dS \tag{3-22}$$

Equation 3-22 successfully combines the PDE and its boundary conditions into a single equation that holds for all points within domain Ω and on boundary δΩ. The next step is to derive a system of algebraic equations that only holds for a finite number of nodes in the FEM, such that a best fitting solution to the forward problem can be approximated using this system of linear equations.

The FEM discretizes the domain Ω into a finite number of elements that can be studied individually. In the 2D case, as illustrated in Figure 3-3, the planar area is divided into

triangular elements indicated by k, and each element consists of three vertices (also called nodes) indicated by n.

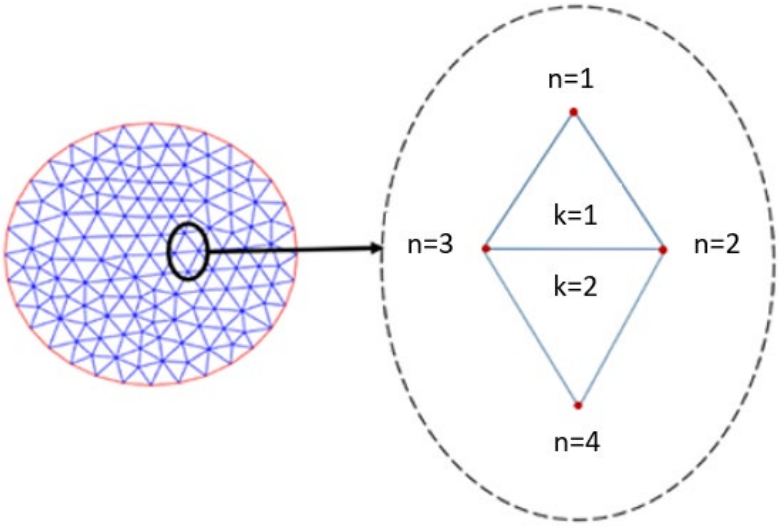

Figure 3-3 Finite elements in a meshed area.

Note that the test function, V, is involved in the formulation process from equation 3-15 to equation 3-22 to enable the implementation of the Galerkin method[219], [220]. The Galerkin method converts equation 3-22 into its weak form. In contrast to the 'strong' form, which forces continuity on solutions to the equation, the "weak" form means that the equation is no longer required to hold for all solutions but only for a finite number of points, for which the error of the linear system is tested and minimized using the test function. In the FEM, the electric potential (U) in its discretized form is represented in Hilbert space, using basis functions Φ. This relation is expressed as

$$U = \sum_{i=1}^{N} u_i \Phi_i \qquad 3\text{-}23$$

Note the $\sum$ symbol used in this thesis denotes the matrix or array element indices rather than the sum of values. For example, $\sum_{i=1}^{N} x_i$ denotes a N-by-one array of $x_1, x_2, \ldots, x_N$; $\sum_{i=1}^{N}\sum_{j=1}^{N} x_{i,j}$ denotes a N-by-N matrix where $x_{i,j}$ denotes the matrix element at the i_{th} row and the j_{th} column. The value of the basis function (ϕ_i) is either 1 on the vertex i or 0 on other nodes.

The test function, V, is also represented in the Hilbert space with the same form as

$$V = \sum_{j=1}^{N} v_j \Phi_j \qquad 3\text{-}24$$

Equations 3-23 and equation 3-24 are substituted into equation 3-22 to obtain

$$\sum_{i=1}^{N}\sum_{j=1}^{N}\left(\int_{\Omega}\sigma_e(\nabla u_i\Phi_i)\cdot\left(\nabla v_j\Phi_j\right)\,dA\right) = \sum_{i=1}^{N}\sum_{j=1}^{N}\left(\int_{\delta\Omega}\sigma_e\,\frac{\partial u_i\Phi_i}{\partial\hat{\boldsymbol{n}}}v_j\Phi_j\,dS\right) \qquad 3\text{-}25$$

The term v_j can be cancelled out from the equation, such that

$$\sum_{i=1}^{N}\sum_{j=1}^{N}\left(\int_{\Omega}\sigma_e(\nabla\Phi_i)\cdot\left(\nabla\Phi_j\right)\,dA\right)u_i = \sum_{i=1}^{N}\sum_{j=1}^{N}\left(\int_{\delta\Omega}\sigma_e\frac{\partial u_i}{\partial\hat{\boldsymbol{n}}}\Phi_i\Phi_j\,dS\right) \qquad 3\text{-}26$$

Equation 3-26 describes the relation among the FEM, the conductivity of individual finite elements (σ_e), and the boundary current density described by 3-14.

3.3.2 Complete Electrode Model

Equation 3-22 and its weak form described by equation 3-26 allow utilizing the current injection data and known conductivity distribution information to predict the electrical potential at each node in the FEM. This model has not yet considered the effect of contact impedance of electrodes. In the practice of EIT imaging for the human body, image reconstructions are severely contaminated by the effect of contact impedance of electrodes. Because the measured voltages on the boundary consist of the voltages on the boundary itself plus the voltages dropped across the electrode-boundary interface[55], neglecting the voltage drop will bring considerable inconsistency in the input to the reconstruction algorithm. A representation of the complete electrode model (CEM) is typically added to equation 3-22 to help accommodate this problem.

The CEM adds the following boundary conditions[221], [222] alongside equation 3-22:

$$U + z\sigma\frac{\partial U}{\partial \hat{\boldsymbol{n}}} = U_l, \qquad beneath\ each\ electrode \tag{3-27}$$

$$\int_{e_l} \sigma\frac{\partial U}{\partial \hat{\boldsymbol{n}}} dS = I_l, \qquad for\ each\ electrode \tag{3-28}$$

$$\sigma\frac{\partial U}{\partial \hat{\boldsymbol{n}}} = 0, \qquad between\ electrodes \tag{3-29}$$

In the above equations, z denotes the edge-wise electrode contact impedance, U denotes the point-wise potential predicted by equation 3-22, U_l denotes the potential on l_{th} electrode (e_l), I_l denotes the current that flows through e_l. Equation 3-27 indicates that the voltages measured on the l_{th} electrode are the sum of the boundary potential and the voltage drop across the contact layer. Equation 3-28 means that the total current flowing through the l_{th} electrode is the integral of the current density over that electrode. Equation 3-29 indicates that the current flowing through the other parts of the boundary that are not connected with electrodes is zero.

The boundary condition described by equation 3-27 can be reformulated as

$$\sigma\frac{\partial U}{\partial \hat{\boldsymbol{n}}} = \sigma\nabla U \cdot \hat{\boldsymbol{n}} = \frac{1}{z}(U_l - U) \tag{3-30}$$

Substituting equation 3-30 into previously derived equation 3-22 yields the following relation:

$$\int_{\Omega} \{\sigma\nabla U \cdot \nabla V\}\, dA = \int_{\delta\Omega} V\frac{1}{z}(U_l - U)\, dS \tag{3-31}$$

For numerical implementation using FEM, equation 3-31 is discretized by substituting it with equation 3-23 and equation 3-24 to obtain its weak form as

$$\sum_{i=1}^{N}\sum_{j=1}^{N} u_i v_j \int_{\Omega} \sigma_e\, \nabla\Phi_i \cdot \nabla\Phi_j\, dA = \sum_{j=1}^{N}\sum_{l=1}^{L} v_j u_l \int_{\delta\Omega} \frac{1}{z}\Phi_j dS - \sum_{i=1}^{N}\sum_{j=1}^{N} u_i v_j \int_{\delta\Omega} \frac{1}{z}\Phi_i\Phi_j\, dS \tag{3-32}$$

Equation 3-32 can be simplified by cancelling v_j from its both sides to obtain

$$\sum_{i=1}^{N}\sum_{j=1}^{N} u_i \int_{\Omega} \sigma_e \, \nabla\Phi_i \cdot \nabla\Phi_j \, dA \qquad 3\text{-}33$$

$$= \sum_{j=1}^{N}\sum_{l=1}^{L} u_l \int_{\delta\Omega} \frac{1}{z}\Phi_j dS - \sum_{i=1}^{N}\sum_{j=1}^{N} u_i \int_{\delta\Omega} \frac{1}{z}\Phi_i\Phi_j \, dS$$

which can be rearranged as

$$\sum_{i=1}^{N}\sum_{j=1}^{N} u_i \left(\int_{\Omega} \sigma_e \, \nabla\Phi_i \cdot \nabla\Phi_j \, dA + \int_{\delta\Omega} \frac{1}{z}\Phi_i\Phi_j \, dS \right) = \sum_{j=1}^{N}\sum_{l=1}^{L} u_l \int_{\delta\Omega} \frac{1}{z}\Phi_j dS \qquad 3\text{-}34$$

Equation 3-34 can be rearranged and represented in a simplified form as

$$\left(A_a + A_\beta\right)U - A_\gamma \, U_l = 0 \qquad 3\text{-}35$$

where $U = \sum_{i=1}^{N} u_i$, $U_l = \sum_{l=1}^{L} u_l$, and

$$A_a = \sum_{i=1}^{N}\sum_{j=1}^{N} \int_{\Omega} \sigma_e \, \nabla\Phi_i \cdot \nabla\Phi_j \, dA \qquad 3\text{-}36$$

$$A_\beta = \sum_{i=1}^{N}\sum_{j=1}^{N} \int_{\delta\Omega} \frac{1}{z}\Phi_i\Phi_j \, dS \qquad 3\text{-}37$$

$$A_\gamma = \sum_{j=1}^{N}\sum_{l=1}^{L} -\frac{1}{z}\int_{e_l} \Phi_j \, dS \qquad 3\text{-}38$$

Equation 3-35, which originates from the boundary condition described by equation 3-27, links the electric potentials at nodes within the domain and the contact impedance with the potentials at electrodes along the domain boundary. To further add the relation described in equation 3-28 and equation 3-29, which link the nodal potentials and contact impedance with the injected current, equation 3-30 is substituted into equation 3-28 to obtain

$$I_l = \int_{e_l} \frac{1}{z}(U_l - U) dS \qquad 3\text{-}39$$

which can be expanded and rearranged as

$$\int_{e_l} \frac{1}{z} U_l \, dS - \int_{e_l} \frac{1}{z} U \, dS = I_l \tag{3-40}$$

Equation 3-40 is discretized to construct the local matrices used in the FEM, expressed as

$$\sum_{l=1}^{L} \sum_{l=1}^{L} u_l \int_{e_l} \frac{1}{z} \Phi_l \, dS - \sum_{l=1}^{L} \sum_{i=1}^{N} u_i \frac{1}{z} \int_{e_l} \Phi_i \, dS = I_l \tag{3-41}$$

which is equivalent to

$$\sum_{l=1}^{L} \sum_{l=1}^{L} u_l \, |e_l| \frac{1}{z} - \sum_{l=1}^{L} \sum_{i=1}^{N} u_i \frac{1}{z} \int_{e_l} \Phi_i \, dS = I_l \tag{3-42}$$

In equation 3-42, $|e_l|$ is the length of the l_{th} electrode. Rearranging this equation provides the following expression:

$$\sum_{l=1}^{L} \sum_{i=1}^{N} u_i \left(-\frac{1}{z} \int_{e_l} \Phi_i \, dS \right) + \sum_{l=1}^{L} \sum_{l=1}^{L} u_l \left(|e_l| \frac{1}{z} \right) = I_l \tag{3-43}$$

Equation 3-43 can be represented in a simple form as

$$A_\gamma^T \, U + A_\delta \, U_l = I_l \tag{3-44}$$

where

$$A_\gamma^T = \sum_{l=1}^{L} \sum_{i=1}^{N} -\frac{1}{z} \int_{e_l} \Phi_i \, dS \tag{3-45}$$

$$A_\delta = \sum_{l=1}^{L} \sum_{l=1}^{L} |e_l| \frac{1}{z} \tag{3-46}$$

Equation 3-45 and equation 3-46 correspond to the boundary condition described by 3-28, which applies to nodes connected to electrodes. For the boundary condition described by equation 3-29, which applies to other boundary nodes that are not connected to electrodes, $\mathrm{A}_\delta = 0$.

Equation 3-35 and equation 3-44 can be combined to formulate a system of equations as

$$\begin{bmatrix} A_a + A_\beta & A_\gamma \\ A_\gamma^T & A_\delta \end{bmatrix} \begin{bmatrix} U \\ U_l \end{bmatrix} = \begin{bmatrix} 0 \\ I \end{bmatrix} \quad 3\text{-}47$$

which can be represented in a simplified form as

$$A\, U_{sum} = B \quad 3\text{-}48$$

The dimensions of the parameters in this model are associated with the settings of FEM. For an FEM with N nodes and L electrodes, A_a and A_β are both $N * N$ matrices (the " * " symbol denotes the dimension of a matrix, i.e., 3 * 2 indicates a 3-by-2 matrix), A_γ is a $N * L$ matrix, A_δ is an $L * L$ matrix, U has the size of $N * 1$, U_l has the size of $L * 1$, "0" represents an all-zero matrix with a size of $N * 1$, and I is the current injection matrix with a size of $L * 1$. Equation 3-48 then has the size of $[(N + L) * (N + L)] \times [(N + L) * 1] = [(N + L) * 1]$. The " * " symbol denotes the dimension of a matrix, i.e., 3 * 2 indicates a 3-by-2 matrix. The matrix implementation and the overall dimensions of equation 3-48 is visualized in Figure 3-4. The derivations above only describe the forward model for a single current injection pattern. When the number of current injection patterns is G, the size of the system becomes $[(N + L) * (N + L)] \times [(N + L) * G] = [(N + L) * G]$.

Using equation 3-48, the local stiffness matrices corresponding to each element in the FEM can be constructed individually, and a global stiffness matrix can be finally obtained by assembling all the local matrices. Equation 3-48 is the final form of the structural model for predicting the forward solutions. Based on this model, a reversed model that allows using electrode electric potentials (U_l) to reconstruct element-wise conductivity (σ) can be further derived to solve the inverse problem.

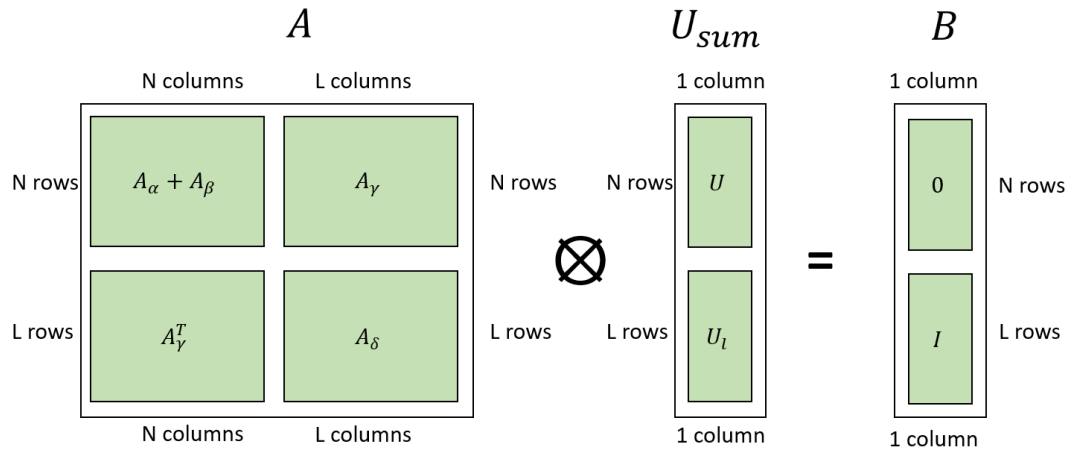

Figure 3-4 The structure and overall dimensions of equation 3-48. (“⊗” denotes matrix product)

3.4 Solving the Inverse Problem Using Regularization

3.4.1 Jacobian Matrix

EIT reconstruction is the process of finding a solution of conductivity distribution using electrode voltage data. This process requires reformatting equation 3-48 into a new equation. The previously derived equation 3-48 describes the relation among A (a matrix associated with the FEM, CEM, current injections, and the element-wise conductivity), σ (the solution that the inverse problem aims to obtain), B (the current injections sequence), U (the electric potential at each node) and U_l (the potential at each electrode). In the practice of EIT, U_l is the measured voltage data that serves as the input to the inverse problem for finding the solution, σ. Therefore, the objective of the new equation reformatted from equation 3-48 is to use U_l contained in U_{sum} to

calculate for σ that partially constitutes the A matrix. This is achieved using a Jacobian matrix, denoted as H.

The Jacobian matrix is a mapping function that maps the change in conductivity distribution *(*$\triangle \sigma$) to the change in electric potential measured at boundary electrodes, $\triangle U_l$, during a time interval, $\triangle T$. This relation is expressed as the following:

$$\triangle U_l = H \triangle \sigma = \sum_{i=1}^{K} H_i \triangle \sigma_i \qquad 3\text{-}49$$

H_i is a local Jacobian matrix, which maps the electrical conductivity variation of the $\mathrm{i_{th}}$ element, towards $\triangle U_l$, while ignoring the effect of other elements apart from the $\mathrm{i_{th}}$ element. Equation 3-49 is rearranged such that the Jacobian matrix is expressed in the form of the derivative of U_l with respect to σ. To relate the equation with the forward model, U_l is expressed as an extracted part from U_{sum}, using an extraction operator, *Ext*. This relation is expressed as

$$H = \frac{\triangle U_l}{\triangle \sigma} = \frac{Ext[\triangle U_{sum}]}{\triangle \sigma} \qquad 3\text{-}50$$

According to the model derived in the forward problem, the electric potentials U_{sum} can be represented as a function of the conductivity, σ. Thus, the denotation of U_{sum} becomes $U_{sum}[\sigma]$, and equation 3-50 can be reformulated as

$$H = \frac{Ext[\triangle U_{sum}]}{\triangle \sigma} = \frac{Ext\left[U_{sum}[\sigma + \triangle \sigma] - U_{sum}[\sigma]\right]}{\triangle \sigma} \qquad 3\text{-}51$$

Equation 3-51 is substituted into equation 3-49 to obtain

$$\triangle U_l = \frac{Ext\left[U_{sum}[\sigma + \triangle \sigma] - U_{sum}[\sigma]\right]}{\triangle \sigma} \triangle \sigma \qquad 3\text{-}52$$

When $\triangle \sigma$ is small, equation 3-52 is equivalent to

$$\triangle U_l = Ext\left[\frac{\partial U_{sum}}{\partial \sigma}\right] \triangle \sigma \qquad 3\text{-}53$$

Based on equation 3-49 and equation 3-53, the Jacobian matrix can be formulated as

$$H = Ext\left[\frac{\partial U_{sum}}{\partial \sigma}\right] \quad 3\text{-}54$$

From equation 3-48, U_{sum} is rearranged backwards as $U_{sum} = A^{-1}B$, and B is always a matrix of the same constant values during each time interval; therefore, equation 3-54 becomes

$$H = Ext\left[\frac{\partial (A^{-1}B)}{\partial \sigma}\right] = Ext\left[\frac{\partial (A^{-1})}{\partial \sigma}B\right] \quad 3\text{-}55$$

Then the chain rule is applied to the derivative in equation 3-55 to obtain

$$H = Ext\left[A^{-1}\frac{\partial A}{\partial \sigma}A^{-1}B\right] \quad 3\text{-}56$$

In terms of implementing equation 3-56, H is formed by summing together all the local Jacobian matrices

$$H = \sum_{i}^{K} H_i = \sum_{i}^{K} Ext\left[A^{-1}\frac{\partial A}{\partial \sigma_i}A^{-1}B\right] \quad 3\text{-}57$$

In equation 3-57, A is the overall stiffness matrix embedded with the complete electrode model. A has a dimension of $(N + L) * (N + L)$, N is the number of nodes, and L is the number of electrodes; σ is the conductivity at each element and expressed as a matrix with a size of $K * I$, where K is the number of elements; B is a matrix containing a matrix of zeros and current injection patterns, I. B has a size of $(N + L) * G$, where G is the number of current injections. The values of A^{-1} and B are readily obtained from the forward model. The only remaining parameter that needs to be further determined is $\frac{\partial A}{\partial \sigma_i}$. The derivative can be calculated directly.

The size of $\frac{\partial A}{\partial \sigma_i}$ is $(N + L) * (N + L)$. As derived in the forward problem, the A matrix consists of A_a, A_β, A_γ and A_δ. Among these parameters, A_β, A_γ and A_δ has no dependence on σ_I, and only A_a is a function of σ_I, as previously shown in equation 3-36. Thus, the value of $\frac{\partial A}{\partial \sigma_i}$ for each element is equal to $\int_\Omega \nabla \Phi_i \cdot \nabla \Phi_j \, dA$. An example of a calculated $\frac{\partial A}{\partial \sigma_i}$ is visualized as a sparse pattern in Figure 3-5. In this example, the

A matrix has a dimension of 533 * 533 (i.e., there are 533 nodes in this system). Each dot in the figure represents a non-zero value of $\frac{\partial A}{\partial \sigma_i}$ for the i_{th} element at its corresponding nodal coordinate. The values of $\frac{\partial A}{\partial \sigma_i}$ at other nodal coordinates are 0 since they are not relevant to the studied element.

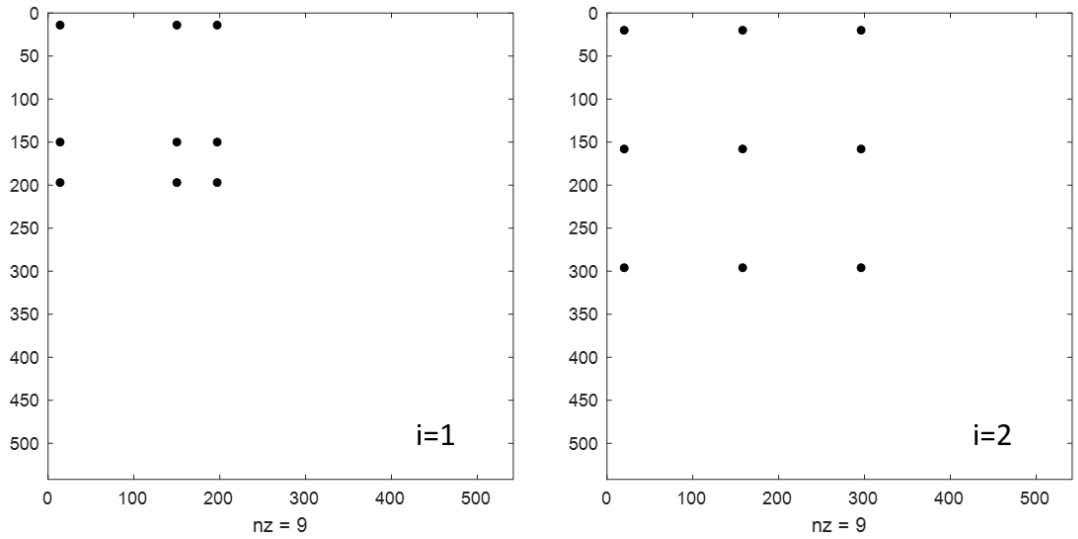

Figure 3-5 Visualization of a local derivative matrix. Left: element i=1. Right: i=2. "nz" denotes number of non-zeros

With the determined value of $\frac{\partial A}{\partial \sigma_i}$, the local Jacobian matrix, H_i, for each element is individually calculated following equation 3-57. In order to obtain a global Jacobian matrix, each H_i with an original dimension of $(N + L) * G$ is reshaped into a 1D array with a dimension of $(N + L) \times G * 1$ and assigned into an overall matrix in the form of

$$H = \sum_{i}^{K} H_i = [H_1, H_2; \dots, H_K] \qquad 3\text{-}58$$

If the extraction function in equation 3-57 is temporally ignored, the overall matrix, H, will have a dimension of $(N + L) \times G * K$, and the output of $H \triangle \sigma$ is the change in U, which is the electric potentials at all nodes and electrodes. In realistic imaging, only U_l which represents the electric potentials at electrodes is obtained from voltage

measurements; hence the extraction function must be applied to extract only U_l, which serves as the input to the inverse problem. In MATLAB (The MathWorks Inc., Natick, MA, USA), the extraction function is a matrix in the form of $[zeros\ (L, N);\ identity\ (L, L)]$. It is element-wisely multiplied with the Jacobian matrix to eliminate the nodal voltages, U, and to only keep the remaining U_l from the summation U_{sum}. After extraction, the Jacobian matrix becomes a matrix with the size of $(L \times G) * K$, and equation 3-49 has the size of $(L \times G * 1) = (L \times G * K) \times (K * 1)$.

3.4.2 Regularization and Reconstruction

Equation 3-49 describes a system of linear equations in which the multiplication between the Jacobian matrix (H) and the conductivity variation matrix ($\triangle \sigma$) results in a change in the electrode voltages ($\triangle U_l$). The reconstruction is to inversely find $\triangle \sigma$ using the same system in a reversed order

$$\triangle \sigma = H^{-1} \triangle U_l \tag{3-59}$$

The input parameter $\triangle U_l$ is only an extracted portion from the full nodal electric potential matrix, U_{sum}. The incompletion means that the system for inversely calculating $\triangle \sigma$ is underdetermined and has non-unique solutions. Thus, the objective of the inverse problem becomes finding a solution $\triangle U_l$ that minimizes the error, typically the least-square error (e_{LS}), described by the cost function described as:

$$e_{LS} = |H \triangle \sigma - \triangle U_l|^2 \tag{3-60}$$

The solution to such a problem is generally approached by linear regression through the method of ordinary least square (OLS), in the form of

$$\triangle \sigma = (H^T H)^{-1} H^T \triangle U_l \tag{3-61}$$

However, in equation 3-61, $\triangle \sigma$ cannot be determined because $H^T H$ has insufficient rank. This undetermined system needs to be regularized to provide a unique solution

according to a specific bias. To achieve regularization, an additional parameter in the form of " $\lambda R \triangle \sigma$ " is added to the system, such that the new objective function becomes

$$e_{LS} = |H \triangle \sigma - \triangle U_l|^2 + \lambda^2 |R \triangle \sigma|^2 \quad 3\text{-}62$$

In this equation, R is a regularization matrix. λ is a constant that controls the weight on the regularization. A valid value of λ must be greater than 0. Compared to equation 3-60, equation 3-62 is now well-posed; thus, a unique solution can be determined using[223]

$$\triangle \sigma = (H^T H + \lambda^2 R^T R)^{-1} H^T \triangle U_l \quad 3\text{-}63$$

In equation 3-63, a regularization parameter must be selected to produce a solution. As mentioned in section 2.2.3, there are various types of regularization parameters, resulting in different solutions.

The Tikhonov prior[223] is the original form of regularization parameter. It has a simple form of an identity matrix[25] with the same dimension of $\triangle \sigma$.

The Noser prior is relatively more complex than the Tikhonov prior. Adler and Guardo[224] proposed the Maximum a Posteriori method, also known as the MAP regularized inverse method. This method takes measurement noise from each channel into consideration and adds an inverse matrix of covariance of measurement, w, to equation 3-63 to obtain

$$\triangle \sigma = (H^T w H + \lambda^2 R^T R)^{-1} H^T w \triangle U_l \quad 3\text{-}64$$

For simplicity, the measurement from each channel is often assumed to have equal noise variance. The matrix w then becomes a multiple of the identity matrix[225], and the equation can be treated as the same as equation 3-63. The Noser prior is determined using $R = diag(H^T w H)^{\mu}$[226]. It is a diagonal matrix whose diagonal is the same as the diagonal of the response matrix, $H^T H$. This approach allows the Noser prior to adjusting the amount of regularization for each finite element by making a direct

relationship between each diagonal element of the response matrix and the corresponding finite element in the mesh[227].

The total variation (TV) prior is based on minimizing the total variation of the conductivity matrix along individual edges, each of which is shared by its two neighbouring elements in the mesh. TV regularization is expressed as

$$TV[\Delta\sigma] = \sum_i l_i \, |\sigma_m - \sigma_n| \qquad 3\text{-}65$$

The parameter l_I indicates the length of the $\mathrm{i_{th}}$ edge, m and n are the indices of the two neighbouring elements to that edge. In terms of matrices[40], the equation can be expressed as

$$TV[\Delta\sigma] = \sum_i |L_i \Delta\sigma| \qquad 3\text{-}66$$

where L is a sparse matrix whose every row, L_I, has two nonzero elements in the column. Hence,

$$L_i = [0, \dots, 0, l_i, 0, \dots, 0, -l_i, 0, \dots, 0] \qquad 3\text{-}67$$

The objective function for error minimization using the TV prior becomes a quadratic regularization in the form of

$$\triangle U_l = argmin\{|H \triangle \sigma - \triangle U_l|^2 + |\lambda \, TV[\Delta\sigma]|^2\} \qquad 3\text{-}68$$

which can be rearranged as

$$\triangle U_l = argmin\{|H \triangle \sigma - \triangle U_l|^2 + \lambda^2 \, |L\Delta\sigma|^2\} \qquad 3\text{-}69$$

Equation 3-69 can be expressed in the general form described by equation 3-62 as

$$\triangle U_l = argmin\{|H \triangle \sigma - \triangle U_l|^2 + \lambda^2 |R \triangle \sigma|^2 \}, \qquad R = L \qquad 3\text{-}70$$

Therefore, the solutions produced by 3-70 have the same form as equation 3-63.

3.5 Identifying Limitations

3.5.1 Uncertain Solutions

By implementing the algorithms derived in section 3.3 and section 3.4 via MATLAB (The MathWorks Inc., Natick, MA, USA), simulations were performed to examine the accuracy of EIT reconstruction and identify the limiting factors. For each simulation, one or more electrical conductivity contrasts, which possess different conductivity than the background, are created within a domain to represent the strains applied to a sensing material, as shown in Figure 3-6.

First of all, it was discovered that the solution obtained from EIT reconstruction suffers from uncertainty. Due to the underdetermined EIT system's intrinsically ill-posed nature, numerous non-unique solutions exist. Although these solutions are dissimilar, they are all mathematically correct because they fit the structural model; in other words, the result in the same electrode voltage data when used as the input to the forward problem.

In terms of the mathematical model of EIT itself, several input parameters lead to reconstructed solutions significantly different from each other. For example, the effect of the selection of regularization methods on the reconstructed solutions is exhibited in Figure 3-6. Three types of true conductivity distributions were reconstructed using the Moore-Penrose pseudoinverse, Tikhonov regularization, Noser regularization and TV regularization, respectively. The default regularization parameter was set to 1. The Noser parameter was set to 0.1. The bottom plot below each reconstructed image shows the conductivity value for each element in the FEM. The L_1 norms and the L_2 norms for the true and estimated conductivity were calculated and indicated at the bottom of each plot.

A percentage of contrast recovery (PCR) is determined for each obtained image to evaluate its reconstruction accuracy. The PCR[228] of a reconstructed image is defined

as the difference between the average of the reconstructed contrast conductivity (CC_{rec}) and the average of the reconstructed background conductivity (BC_{rec}) divided by the difference between their true values (CC_{true} and BC_{true}). The PCR is calculated by

$$\text{PCR} = \frac{CC_{rec} - BC_{rec}}{CC_{true} - BC_{true}} \times 100 \qquad 3\text{-}71$$

In the ideal case where the reconstructed conductivities perfectly matches the true conductivities, the PCR has an optimal value of 100. In the case of underestimation where the reconstructed conductivities are lower than the true conductivities, the resulted PCR is smaller than 100. In the case of overestimation where the estimated magnitudes exceed the true magnitudes, the resulted PCR is larger than 100.

It can be seen that the solutions reconstructed using different algorithms are mismatched. The pseudoinverse method provides solutions that can indicate the approximate locations of the conductivity contrasts. The Tikhonov method and the Noser method offered smoother solutions in which the conductivity contrasts were spun over a relatively large area. The TV algorithm showed the best PCR and offered a relatively clearer boundary of the conductivity contrasts than other algorithms.

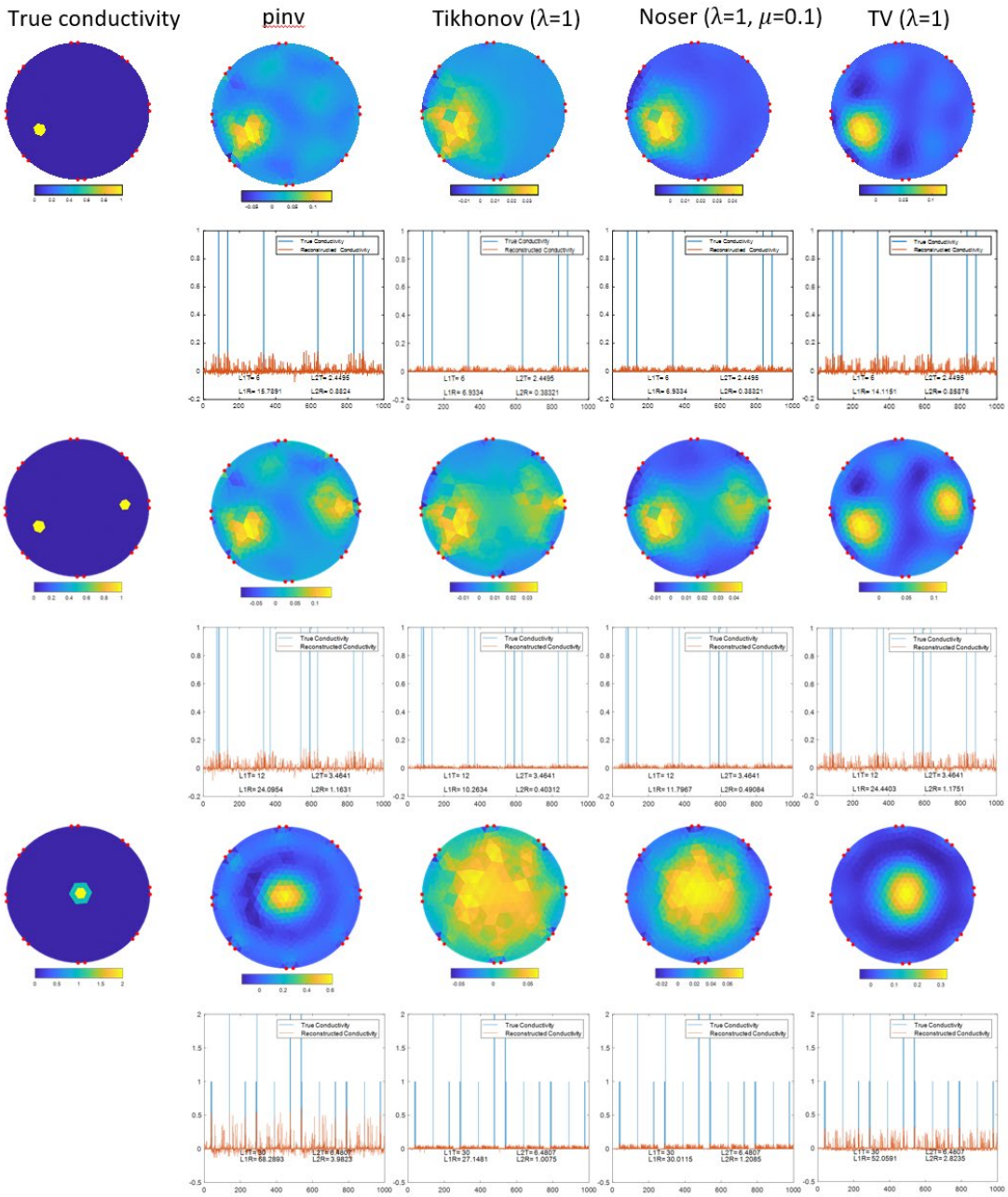

Figure 3-6 Reconstruction of three types of input using different algorithms and the adjacent current injection pattern. From left to right: true conductivity distribution, Moore-Penrose pseudoinverse, Tikhonov regularization, Noser regularization, TV regularization. The stem plots show the values of the conductivity of each element in the FEM with 1000 elements.

Apart from the choice of the reconstruction algorithms, the selection of the current injection patterns also affects the reconstructed solution. Figure 3-7 shows the reconstructed results using the opposite injection pattern. Compared to the previous

result obtained using the adjacent pattern, the results obtained using the opposite pattern possess different values.

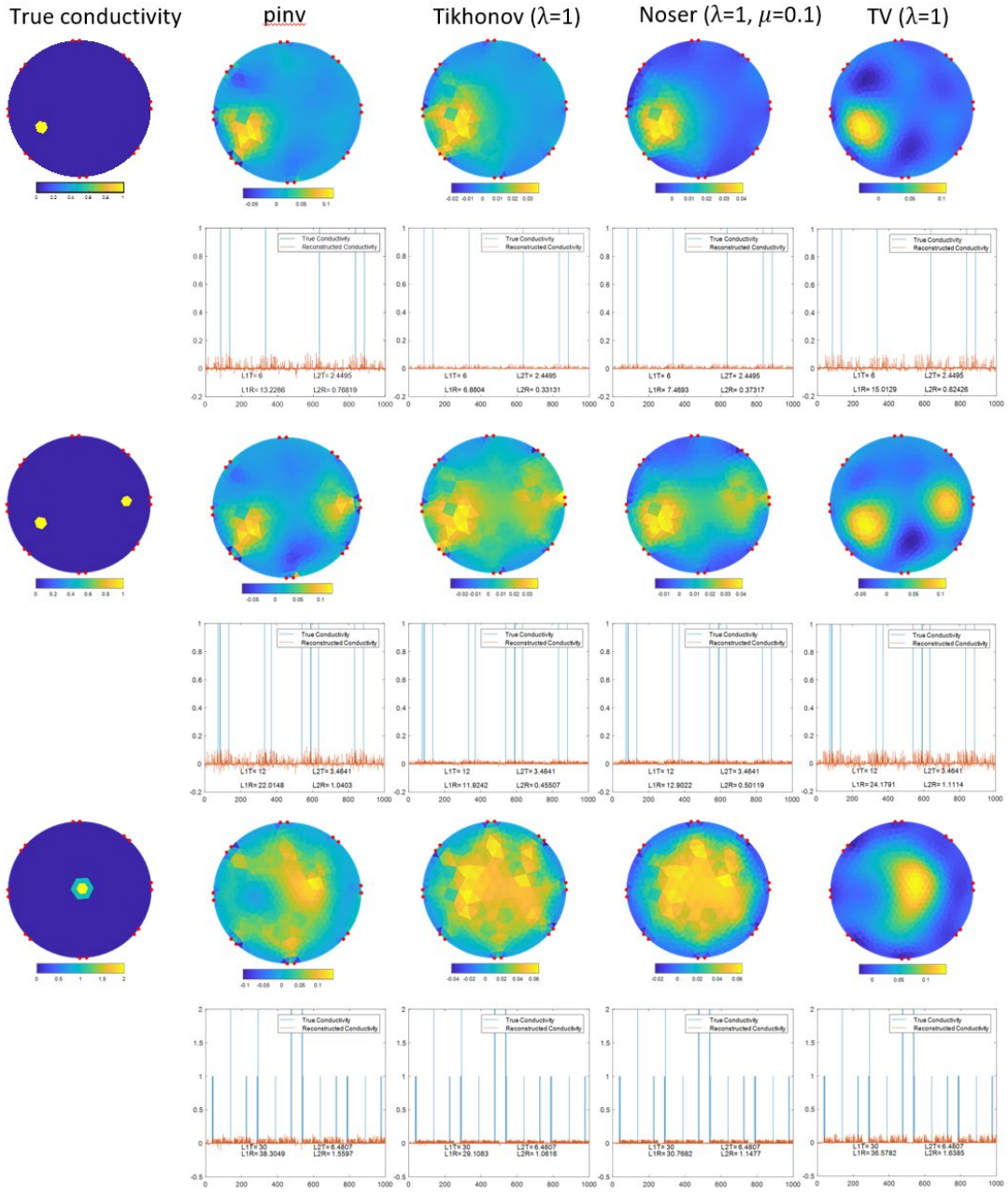

Figure 3-7 Reconstruction of three types of input using different algorithms and the opposite current injection pattern. From left to right: true conductivity distribution, Moore-Penrose pseudoinverse, Tikhonov regularization, Noser regularization, TV regularization. The stem graphs show the values of the conductivity of each element in the FEM with 1000 elements.

Another factor that affects the solution is the choice of the regularization hyperparameter, which plays a significant role in reconstructing the solution. Figure 3-8 illustrates the results reconstructed using different regularization methods, subject to the hyperparameter values ranging from 0 to 1. The hyperparameter controls the weight of the regularization; therefore, changing the hyperparameter leads to different solutions. This uncertainty means that the reconstructed solution is partially dependent on the value actively assigned to the hyperparameter. Numerous solutions can be obtained by actively changing the hyperparameter values, and all of the obtained solutions will fit the mathematical model.

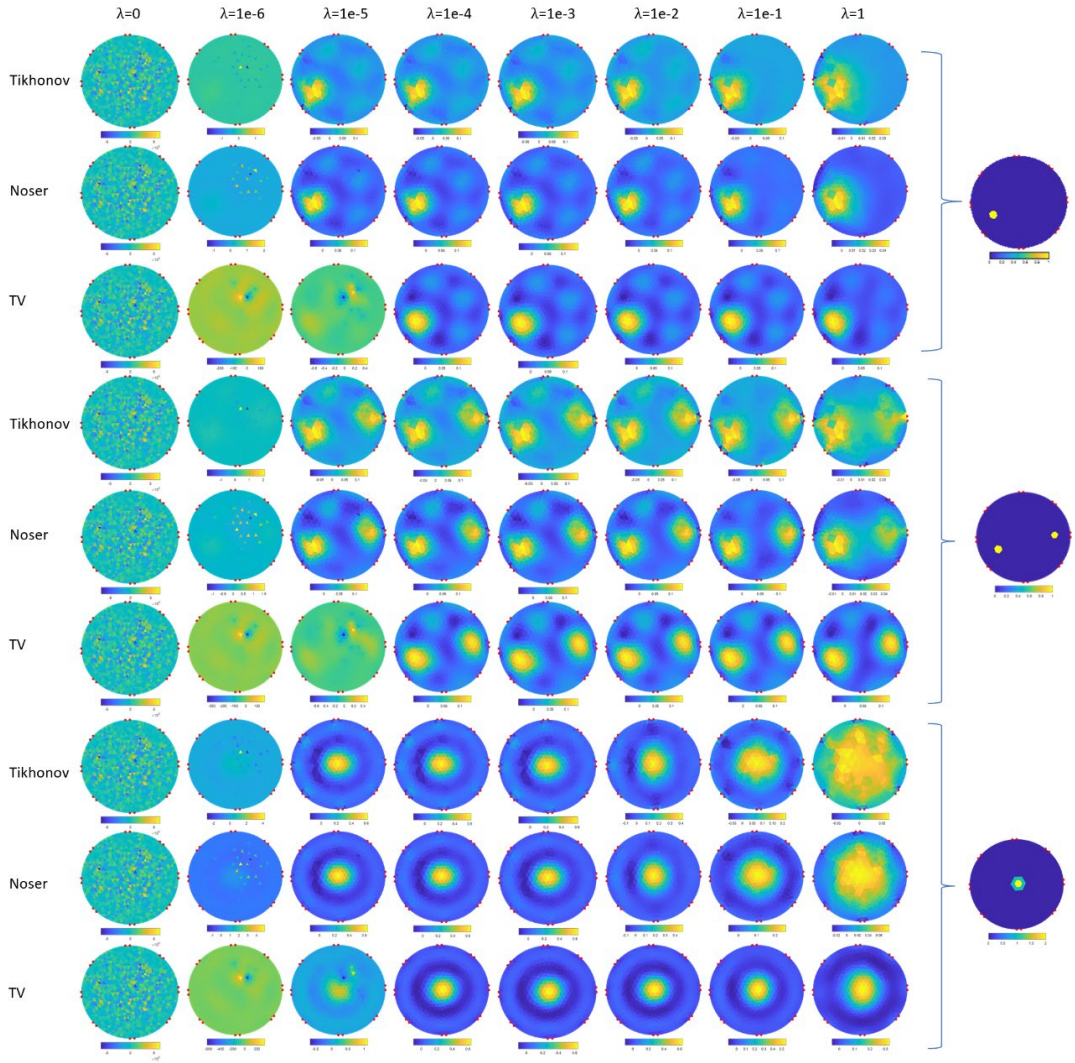

Figure 3-8 Reconstruction using different regularization methods with hyperparameter values ranging from 0 to 1.

Apart from the non-uniqueness of the reconstructed solutions, significant inaccuracy of each of the solutions was observed. It can be seen from the plotted data in Figure 3-6 and Figure 3-7 that the magnitudes of the estimated solutions are significantly different from that of the true solution and possessed poor PCRs, which are typically lower than 10. Due to the penalization of the reconstruction algorithms to the L_2 norms, the solutions tend to be smooth and disinclined to sharp discontinuities. Although the TV regularization does not penalize L_2 norms but L_1 norms and shows better PCRs and keeps more discontinuities, the solutions obtained from TV regularization are still considerably mismatched with the true solutions.

3.5.2 Poor Spatial Resolution

The poor spatial resolution of EIT is another defect observed in the simulation study. Figure 3-9 shows the simulation results, reconstructed using the TV regularization, for five cases of different conductivity inputs. The hyperparameter used in the simulation was set to 1, and the adjacent pattern was selected as the current injection pattern. The five cases were arranged in a specific order where the distance between the two conductivity contrasts in the true input is reduced step by step. In the last case, a large conductivity contrast was formed by assigning adjacent elements with different conductivity values. In the first case, the two conductivity contrasts could be clearly distinguished from the simulation when they were sufficiently distant from each other. However, when their distance was gradually reduced from the second to the fourth case, their distributions in the reconstructed solutions were merged, and their boundaries could not be visually identified. In the last case, although the true input was set to raise conductivity towards a specific direction, the reconstruction failed to show this trend; instead, it showed a result similar to a single and uniform conductivity contrast. Apart from failing to approximate the positions of the closely placed conductivity contrasts, the reconstructions for all the cases also fail to estimate their true magnitudes. The PCR

for each case is below 10. In brief, these simulation results suggest that EIT can only be used to vaguely indicate the positions of the conductivity contrasts.

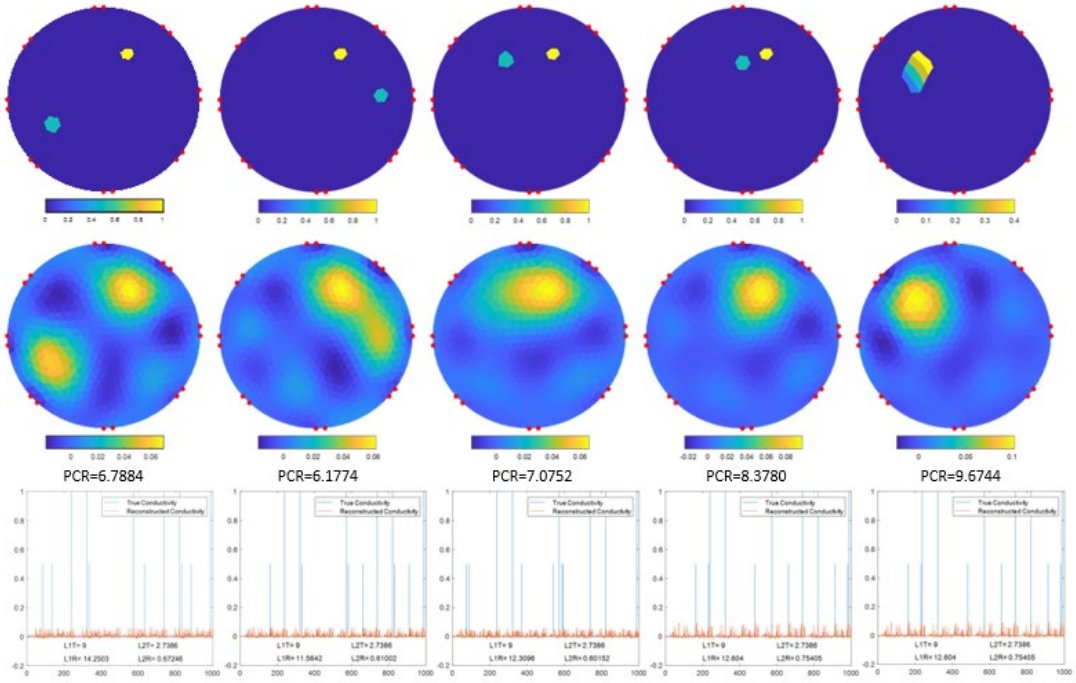

Figure 3-9 Reconstruction showing poor spatial resolution.

3.5.3 Non-Uniform Sensitivity Distribution

Previous studies[229], [230] addressed that EIT has non-uniform sensitivity distribution over the domain, and the sensitivity over the domain drops rapidly from the boundary to the interior. To examine the effect of non-uniform sensitivity on the accuracy of the reconstructed solution, a simulation was conducted by arranging the positions of several conductivity contrasts such that they have different distances to the boundary electrodes. As illustrated in Figure 3-10(a), three conductivity contrasts were initially positioned at a similar distance to the boundary electrodes. Then one of the contrasts was moved away from the electrode. The simulation also utilized the opposite current injection pattern as it has relatively better interior sensitivity than the adjacent

pattern[231]. The TV regularization was chosen to obtain the best image quality. It can be observed from the reconstructed solutions that the moving contrast was only clearly visible in the first instance and became obscured as it moved away from the nearest electrode. This result suggests that the sensitivity distribution is subject to the distance to the nearest electrode. The effect of non-uniform sensitivity distribution is more clearly exhibited in Figure 3-10(b), where two conductivity contrasts were both close to the centre in the first instance. Then one of them was moved towards the boundary electrode. Notably, although the two contrasts had the same true magnitudes of conductivity, the contrast moving towards the boundary electrode was estimated to have a higher reconstructed conductivity. The difference in the reconstructed conductivities between the two contrasts was enlarged as the moving contrast approached closer to the boundary electrode. These results imply that the non-uniform sensitivity issue will hinder the ability of an EIT-based sensor to detect strain and pressure applied to multiple points. For example, when two or more pressures or strains are applied simultaneously to an EIT-based sensor, the stimulus applied to a position

closer to the boundary electrodes will dominate over other stimuli applied closer to the centre; therefore, the estimated solutions provided by the sensor lack reliability.

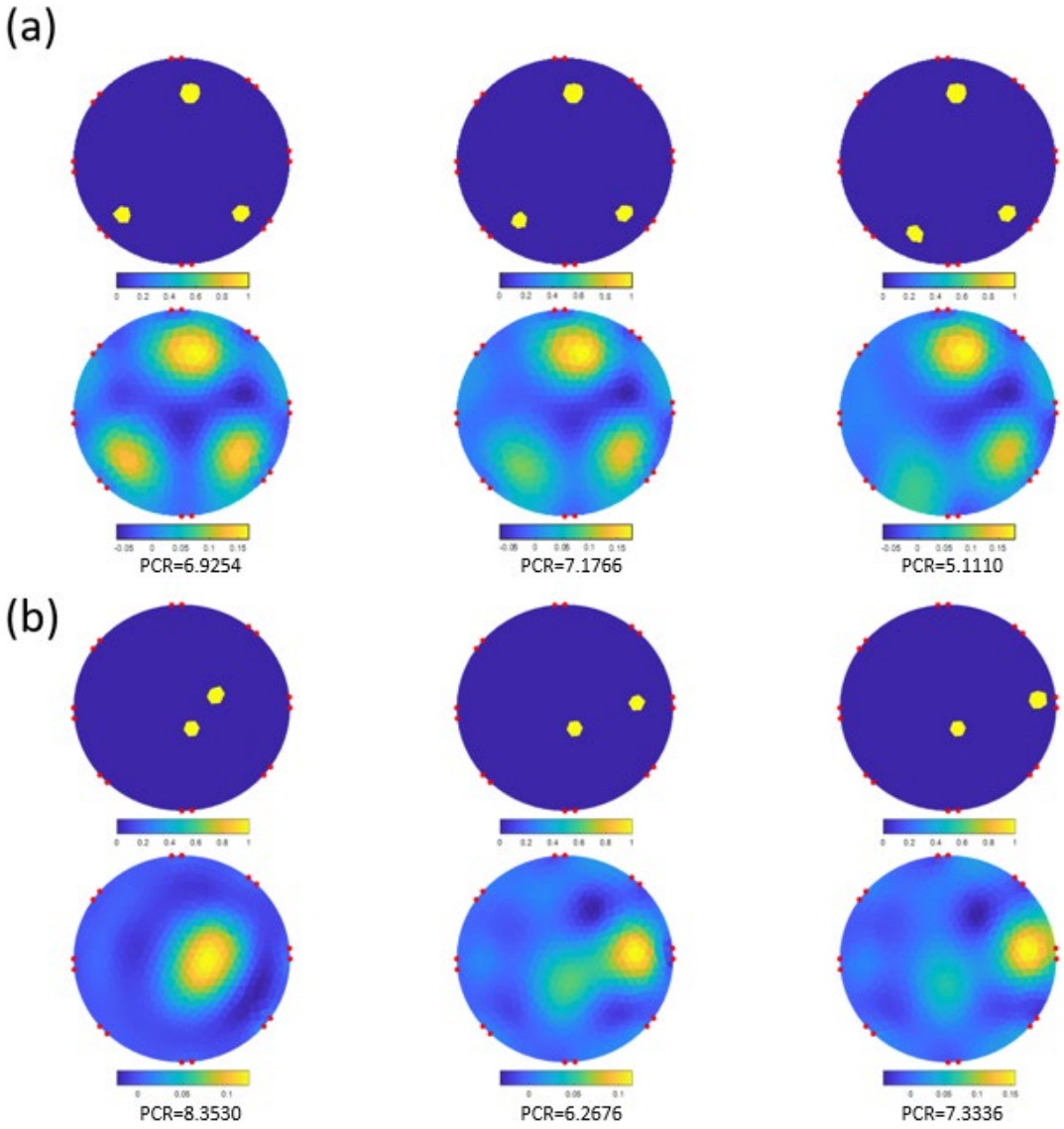

Figure 3-10 The effect of non-uniform sensitivity in EIT imaging. (a). Reconstructions showing one conductivity contrast is moving away from its nearest electrode. (b). Reconstructions showing one conductivity contrast is moving from the centre to the boundary.

3.5.4 Model Incompatibility

The mathematical model derived in the forward problem is accompanied by the assumption that the electrical conductivity of the material is isotropic. The conductivity, σ, used in the governing equation of EIT and the derived forward model is a set of scaler numbers that do not involve any directional information. Each element in the FEM is assumed to have a homogenous conductivity value in all directions. However, this isotropic assumption is often invalid with the electrical properties of sensing materials. As previously discussed in the literature review chapter, a large number of flexible strain-sensing materials are polymer-based. The electrical conductivity of polymer-based strain sensing material is realized by conductive paths formed by particles doped to the polymer matrix or coated on the surface. Upon stretching, their conducting layers tend to disconnect or crack in the transverse direction to the stretched axis[232]. Therefore, the change in the electrical conductivity along the stretched direction is different from that of the transverse direction, which means the material is anisotropic. This issue can be even more complex because the electrical conduction in polymer composites does not necessarily follow a straight line as the shortest path; instead, a curvature path may become the available path between two points, as pointed out by Chossat[137]. This anisotropic conductivity issue may be tolerable when the material is only used for pressure sensing. In that case, the pressure is applied in the normal direction to the material surface; the conducting paths along the planar direction receive similar deformation caused by the pressure. However, this issue can be significant for strain sensing applications that demand stretching in planar directions.

Previous works that utilized EIT on polymer materials to implement tactile sensors neglected the anisotropy issue. The mathematical model used for reconstruction still assumes isotropic conductivity, but it was used on materials with anisotropic conductivity instead; therefore, the obtained results are not reliable. On top of that, using the solution obtained from the isotropic model, one cannot interpret the direction of the estimated strain. Since strain is a ratio of relative displacement between two

reference points, it is a tensor quantity. The existing approach for implementing EIT on strain sensing can only indicate the presence of strain at approximate locations. A valid estimation of the magnitudes and the directions of the applied strain cannot be determined based on the isotropic solution unless a more complex EIT model that includes anisotropic conductivity as one of its input parameters is proposed and implemented for this type of application.

Apart from the incompatibility between the anisotropic conductivity of the material with the mathematical model of EIT, another incompatibility issue is that the model does not support boundary shape deformation when a sensing material is stretched. The forward algorithm and the subsequently derived inverse algorithm assume fixed nodal coordinates as a requirement of the FEM. Namely, the coordinate of each node is determined prior to the initialization of the forward algorithm, i.e., the coordinates remain fixed at all times. The EIT algorithm is applied based on those nodal coordinates, and the solution is affected by various FEM parameters, including the size of each element, the angle between each pair of adjacent edges, and the distance between each pair of adjacent nodes. When EIT is applied to a material whose boundary is not fixed and is free to deform, the assumption of fixed nodal coordinates is no longer valid, and the element sizes, edge angles and node distances are altered. Therefore, the forward problem solver based on the original FEM is incapable of reflecting the updated relation between the conductivity distribution and the electrode voltage data. Consequently, errors are induced in the model, and the solution to the inverse problem is reconstructed towards the undeformed circumstance rather than that of a deformed boundary shape.

3.5.5 Effect of Measurement Noise

The conductivity distribution reconstructed using EIT is based on the measured electrode voltage data. In reality, the measured voltages are inevitably contaminated by measurement noise to some extent. In order to examine the effect of the measurement

noise, a simulation was conducted by performing the reconstruction using voltage data with added Gaussian white noise as the input to the inverse problem. The noise is added to the voltage data using a MATLAB function, “awgn”, which allows convenient setting of the signal to noise ratio (SNR) of the obtained noisy voltage data. The reconstruction utilized the adjacent current injection pattern and the TV regularization for the best outcome. Three levels of SNR: 30 dB, 20 dB and 10 dB, were specified for

each of the five true inputs. These SNRs are equivalent to 0.1%, 1% and 10% on the linear scale, respectively. The simulation results are shown in Figure 3-11.

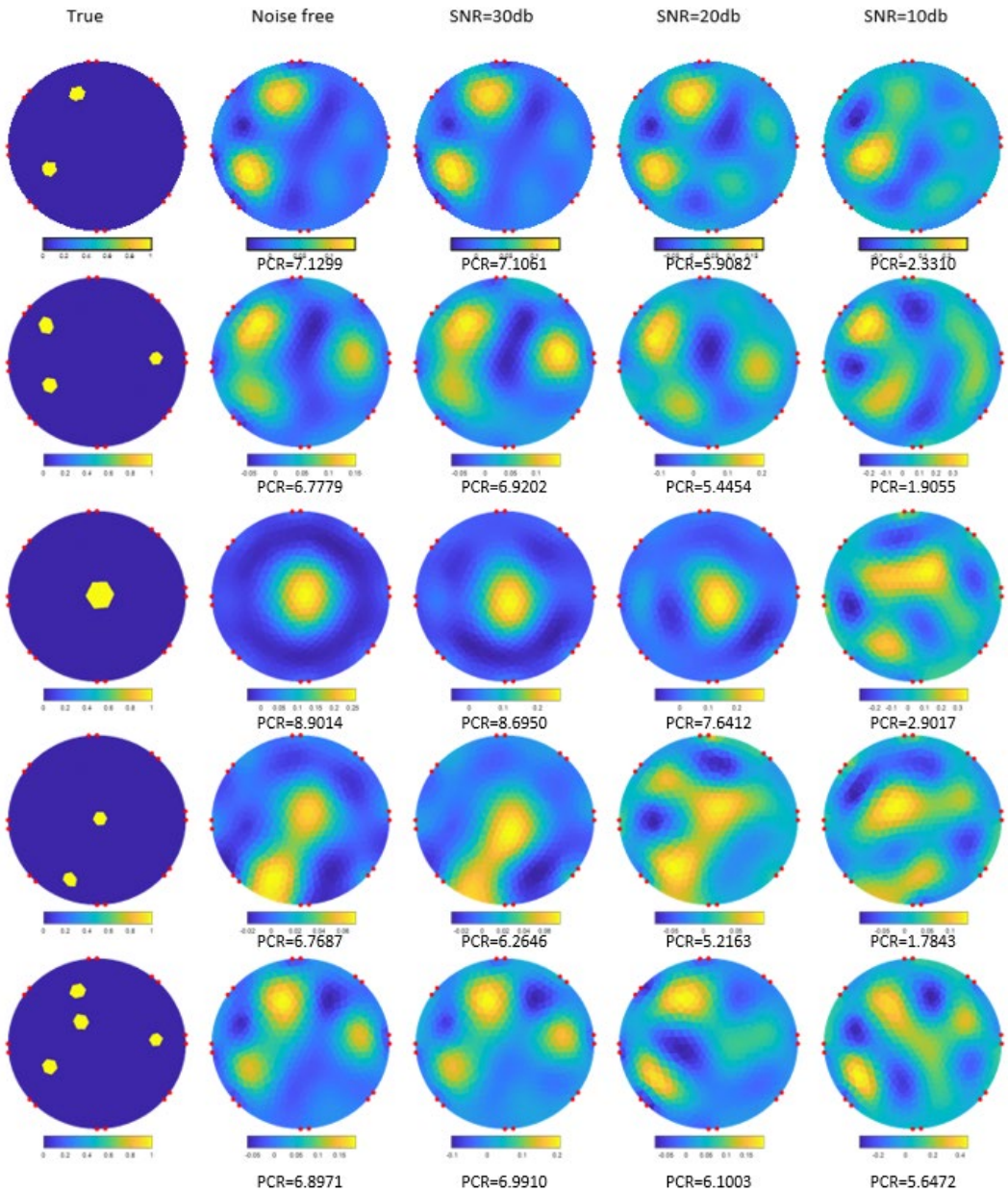

Figure 3-11 The effect of measurement noise in the voltage data.

It can be seen from the results that the effect of the added noise on the obtained image was insignificant at 30 dB. The reconstruction accuracy was slightly altered due to the added noise, but the images remain visually similar to the noise-free solution and could still indicate the approximate positions of each conductivity contrast. At 20 dB,

however, the reconstructed solutions became considerably mismatched with the true solution. At 10 dB, the reconstruction accuracy was severely reduced, and the obtained results failed to indicate the contrast positions. This simulation indicates that the solution of EIT is sensitive to the measurement noise, and therefore, the measurement instrument used for voltage data collection should be precise to avoid the potentially destructive impact caused by the measurement noise.

Because the solution of EIT is obtained by essentially mapping the electrode voltage data to the conductivity distribution using the derived Jacobian matrix, the noise added to the voltage data is also inevitably mapped towards the solution. The consequence is that the contribution of the noisy portion in the voltage data on the solution obtained from the Jacobian mapping is uncertain. For example, Figure 3-12 shows the results of the reconstructions performed for estimating the same true conductivity distribution using noisy voltage data of the same SNR, which was set to 20 dB, during five individual instances. The accuracy of each reconstruction is indicated at the bottom of each image. The simulation results show that the random noise present in voltage measurement will cause unpredictable variations in the reconstructed solutions.

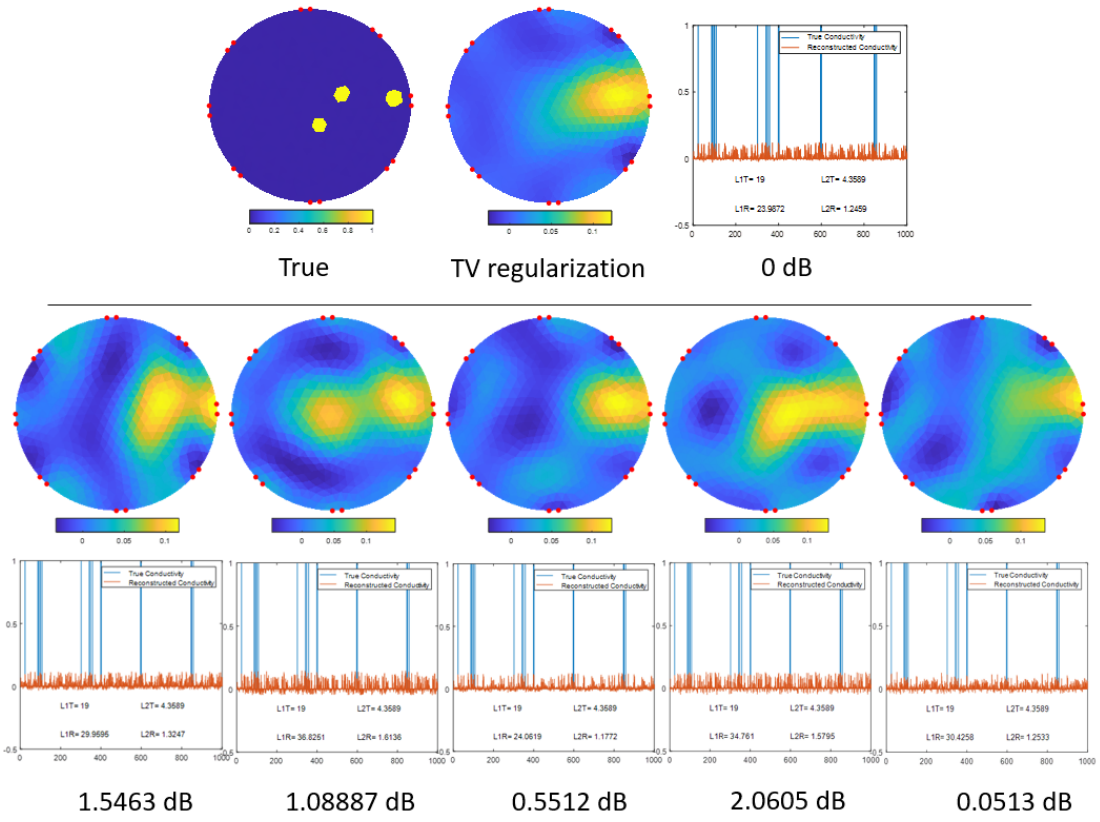

Figure 3-12 Reconstruction for the same true input conductivity distribution using voltage data contaminated with the same level of Gaussian noise at 20 dB.

3.5.6 Time Consumption

Temporal resolution, typically expressed as the number of frames per second (fps), is another factor to consider for strain sensing applications. A higher temporal resolution of a sensor signifies a more comprehensive collection of data, while a lower temporal resolution may be insufficient to capture necessary information for a rapidly changing motion.

A simulation was performed to compare the effect of several model-related parameters on the time consumption for the inverse solver. This time consumption only included the time spent for executing the inverse solver command; it did not include the additional time required for switching the current injection and collecting voltage data

which will further lower the temporal resolution during the actual implementation of real-time imaging. Although the EIT algorithm consists of both the forward problem solver and the inverse problem solver, only a tiny portion of the entire algorithm determines the reconstruction speed. The forward solver must only be executed once before the inverse solver can realize the real-time imaging. The inverse solver then takes the repetitively measured electrode voltage data as the input to continuously update the conductivity distribution solution. Thus, only the time consumed by the inverse solver is directly related to the temporal resolution in real-time imaging.

The model-related input parameters tested in this simulation included the mesh density of FEM, the number of current injections, and the type of the regularization methods. The mesh density was controlled by the "PdeModeler". The number of elements applied to the same circular-shape domain was set to 1000, 4000, or 16000, as illustrated in Figure 3-13. The number of current injections was controlled by assigning the corresponding nodes to 8, 16 and 64 electrodes such that the same number of injections can be applied using the adjacent pattern. The MATLAB functions "tic" and "toc" were used to record the time consumed by each setting. The simulation was conducted using a computer with an Intel Core i7-8565U CPU with a 1.80 Ghz processor and an 8GB RAM.

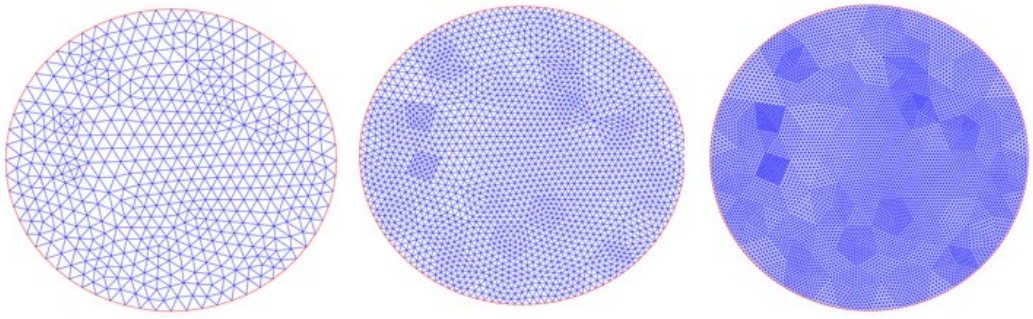

Figure 3-13 A round-shaped domain meshed with 1000, 4000 and 16000 elements, respectively

The result of the simulation is listed in Table 7. It can be seen firstly that the mesh density had a significant impact on the time consumed on all stages of the solvers. In particular, the time required for executing the one-off calculation of the Jacobian matrix

was increased from less than one minute for 1000 elements to several hours for 4000 elements. The time required by the inverse solver for calculating a solution during one frame was also raised from less than one second to several seconds. In the last two cases, the Jacobian calculation was terminated as the program requires over 24 hours to finish its executions. The impact of the number of current injections appeared to be less critical for the case of 1000 elements. The time required for calculating the inverse solution during each frame at this density was less than half a second. However, in the case of 4000 elements, the time consumption was significantly increased from several seconds for eight injections to over 10 seconds for 32 injections. Additionally, the effect of the regularization methods was relatively small compared to the mesh density and the number of injections.

Disregarding the time consumed by the hardware, the frame rate of reconstruction was determined mainly by the time consumed by the inverse solver. The most significant factor that affects the frame rate was found to be the mesh density. A trade-off between the spatial resolution and the temporal resolution should be considered depending on the purpose of the application, as a lower mesh density can offer a higher frame rate at the cost of reduced spatial resolution of the mesh and vice versa.

Number of elements	Number of current injections	Time consumed by the forward solver	Time consumed for calculating the Jacobian matrix	Time consumed by the inverse solve			
				Pinv	Tikhonov	Noser	TV
1000	8	0.1653 s	41.4153 s	0.2327 s	0.3607 s	0.3038 s	0.3130 s
1000	16	0.1740 s	84.1887 s	0.2697 s	0.3013 s	0.2842 s	0.3589 s
1000	32	0.1762 s	189.8754 s	0.4040 s	0.3113 s	0.3187 s	0.3613 s
1000	64	0.1962 s	464.3987 s	0.7016 s	0.4272 s	0.4246 s	0.4600 s
4000	8	3.5618 s	1 h 47 m	3.1902 s	3.5712 s	3.7717 s	5.2137 s
4000	16	3.9264 s	2 h 57 m	5.3444 s	7.2191 s	6.8817 s	7.0011 s
4000	32	4.1124 s	9 h 41 m	11.2993 s	14.1553 s	12.1191 s	16.8989 s
4000	64	4.3291 s	24 h+	-	-	-	-
16000	8	204.2812 s	24 h+	-	-	-	-

Table 7 Time consumption under different model settings. The same mesh was used by the forward solver and inverse solver.

3.6 Preliminary Attempts for Improving Accuracy

3.6.1 Imposing Constraints to the Inverse Solver

It can be seen from section 3.5 that the solutions obtained from EIT are severely mismatched with the true solution (i.e., they have poor PCRs). Due to the ill-posed nature of EIT, the objective of the inverse solver is to obtain a best-fitting solution from an underdetermined system of equations. The system is underdetermined, and therefore errors are inevitable. However, it is possible to use additional information beyond the EIT algorithm to refine its solutions such that the estimated solutions match better with the true solution.

For conventional EIT applications such as lung imaging and heart imaging, the body tissues being imaged have a broad range of electrical conductivity values. The solver approaches the solution with no additional constraints on the possible outcome.

Conversely, the sensing materials under different strains can have a known conductivity range for strain sensing applications. This range can be determined from experiments and used as a constraint to the inverse solver, such that the solver only provides solutions within this range. By adding the constraints, the solution to the underdetermined system becomes much more refined, and it is more likely to produce more reasonable solutions that match closely with the true conductivity of the material. This method for improving the solutions by imposing constraints on the range of conductivity values has not been reported by previous works in this field.

A simulation was conducted to examine the effectiveness of the method. Constraints were added to the inverse solver in several ways. First, solutions imposed with the non-negativity constraint are obtained using the non-negative least square (NNLS) solver, an iterative solver function provided by MATLAB. Secondly, solutions are obtained by combining the total variation regularization with the NNLS solver such that the solutions are biased towards both minimized element-wise total variation and non-negativity. Moreover, solutions within a specified range of values are acquired using the bounded-value least square (BVLS) solver, an iterative MATLAB function. The reconstruction was performed for six types of true conductivity distribution with different complexity. The BVLS solver was set to cover the range of the true conductivity contrasts and three different ranges in an expanding order. The result of the simulation is shown in Figure 3-14.

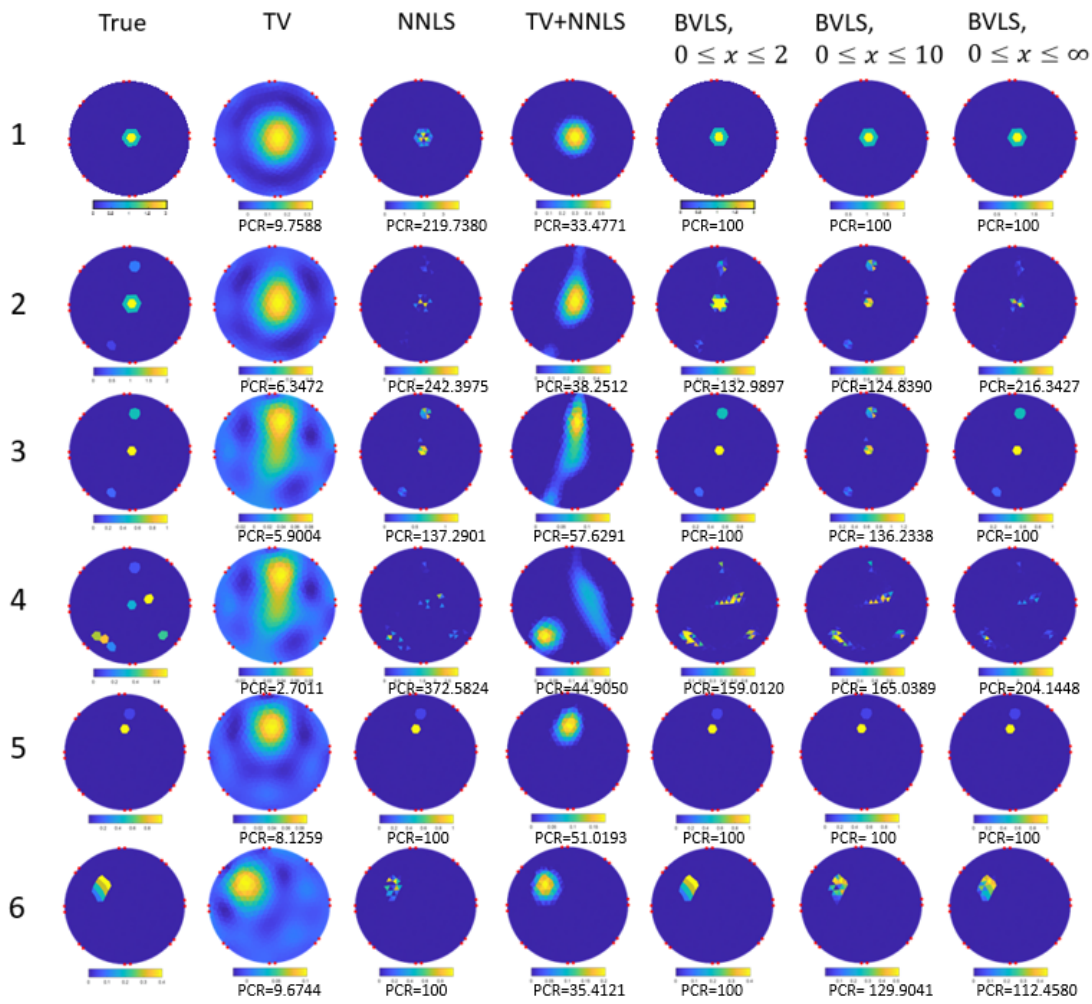

Figure 3-14 Solutions obtained from inverse solvers with constraints

It can be seen from the reconstructed solutions that, compared to the results obtained using the conventional TV algorithm without any constraints, the results obtained using solvers with constraints provide greatly improved solutions that match significantly more closely with the true solution. There is a chance that the reconstruction provides the same results (i.e., PCR=100) as the true solution. For example, in the fifth case, the solution reconstructed using NNLS and the solution reconstructed using BVLS matched precisely with the true solution. Obtaining such exact solutions is not feasible for conventional EIT solvers utilized by previous research on EIT-based strain sensors. For the first, second, third and sixth case, the BVLS solver perfectly reconstructs the true solution under a specific range of constraints. However, the solver fails to achieve

this for other constraint values, in which cases the results fragment into shards. This phenomenon makes sense because the ill-posed nature of the EIT still exists when constrained solvers are used; imposing the constraints only increases the odds of obtaining the true solution but obtaining the true solution cannot be guaranteed.

Notably, in the results obtained from TV regularization without constraints, all elements were estimated to have changing conductivities, even though the true conductivity for most of the elements was not changed. Comparably, the improved solutions obtained from the constrained inverse solvers show that most elements successfully kept their true conductivities. Only elements close to the assigned conductivity contrasts were estimated to have changing conductivities.

It was also observed that mismatched results were generally obtained in the form of discontinued shards. For example, in the fourth case, which had a relatively more complicated conductivity distribution than others, both NNLS and BVLS solvers only produced solutions in the form of shards that were disconnected from each other. The combination of TV regularization and the NNLS solver could avoid this type of result, but it did not noticeably improve the accuracy. Nonetheless, the results obtained from solvers with constraints were significantly more accurate than that of the conventional TV algorithm without constraints. The improvement implies that imposing constraints on the inverse solver is effective for enhancing the solution accuracy.

3.6.2 Image Dilation and Two-Step Reconstruction

As shown previously, inverse solvers with added constraints can effectively improve the solution accuracy; however, it is often observed that the solution is obtained in the form of scattered and discontinued shards, which do not reflect the realistic strain distribution. To accommodate this issue and further optimize the solutions, a method

based on the image dilation technique and two-step reconstruction is proposed and examined using a simulation.

The method of adding constraints to the solver is to better approach the true solution by reducing the solution space. From another perspective, the mathematical model itself may also be constrained to approach a better solution. As mentioned earlier, unlike conventional EIT, where all elements are affected and estimated to have conductivity variation, the constrained solvers provide solutions where only a part of elements are estimated to have varying conductivity; the majority of elements do not possess changing conductivity in the estimation. Thus, better solutions may be obtained by refining the Jacobian matrix. As the core of the EIT model, the Jacobian matrix is effectively a mapping function that maps the conductivity of each element to electrode voltage. It is possible to further extract only a portion of the Jacobian matrix corresponding to the elements with varied conductivity and use the extracted version of the Jacobian matrix to modify the system of equations. In such a way, the electrode voltage variation data results from the conductivity variation of only those extracted elements. This method is referred to in this thesis as the two-step reconstruction method.

As derived earlier in section 3.4.1, the Jacobian matrix has the size of L * E, where E is the number of elements. The first step is to get an initial inverse solution and extract the portion of the Jacobian matrix only relevant to the elements with varied conductivity in the initial solution. The MATLAB function, “logical”, converted the initial solution into logical values, namely, 0 or 1. Elements with conductivity variation in the initial solution were assigned with one as its logical value, and other elements whose conductivity remained the same or below a selected threshold were assigned with a value of zero. Then the extracted version of the Jacobian matrix could be obtained by extracting elements from the full Jacobian matrix that correspond to non-zero indices in the logical array.

Before the refined Jacobian matrix was used to obtain the second step solution, the image dilation technique was performed to mitigate the problem of discontinuous shards in the first-step solutions, such that more necessary elements could be included

in the second-step reconstruction. The purpose of dilation in image processing is to add pixels to the boundaries of objects in an image. Dilation was performed by the MATLAB function, “imdilate(Img,SE)”, where “Img” is an image object, and “SE” is a structuring element that determines the pixels to be dilated. For example, Figure 3-15 shows the dilation performed on a grey-scaled picture. The structuring element has a square form, which means the centre pixel is forced to have the highest value of the pixels within all the elements enclosed by the square. This procedure is repeated individually for all available pixels.

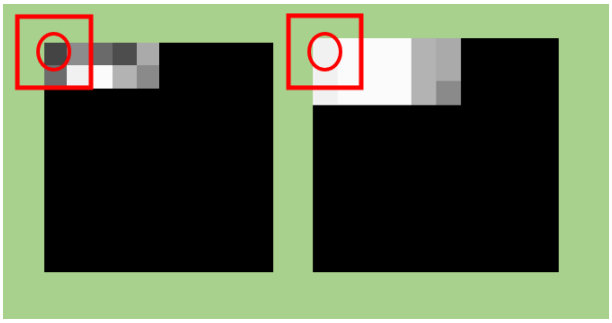

Figure 3-15 Image dilation using a square structuring element

The EIT model is not pixel-based; instead, it is element-based. Therefore, to dilate the element-wise conductivity distribution, the structuring element was formed by extracting the adjacent elements to each element. Then, dilation was performed by forcing the element being dilated to have the highest value of estimated conductivity among all adjacent elements and this element itself, as illustrated in Figure 3-16. This procedure was repeated for all elements.

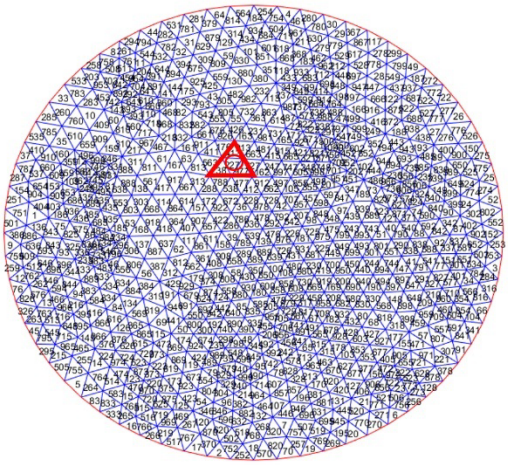

Figure 3-16 The structuring element for FEM

The result of the dilation is shown in Figure 3-17. It can be seen that the elements that were adjacent to each discontinuous shard in the first-step solution, obtained using the BVLS solver, were successfully dilated. Thus, the elements in the dilated solutions could be further extracted to refine the Jacobian matrix to obtain a new system of equations for predicting the electrode voltage data concerning only the dilated elements.

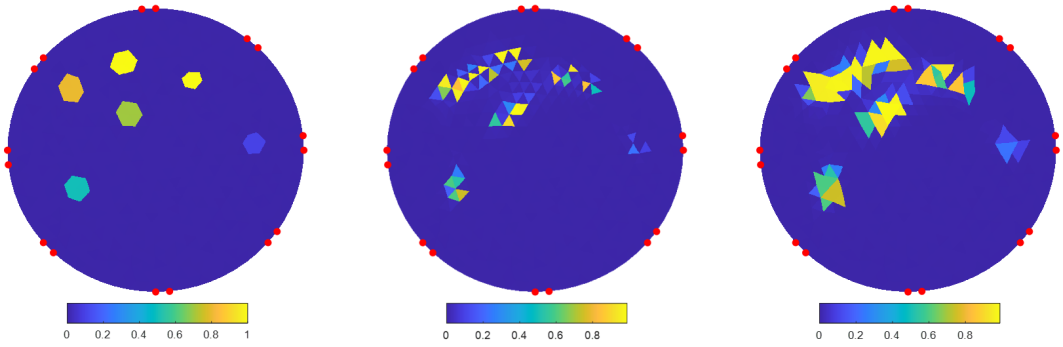

Figure 3-17 Dilation performed on a discontinuous solution. Left: true solution. Middle: solutions obtained using BVLS. Right: the dilated result.

Via the modified model, the second-step solutions were obtained using TV regularization, which leads to better solutions than other regularization methods and also avoids discontinuous shards in the results. As demonstrated in Figure 3-18, the results of the second-step solution obtained under different threshold values for the extracted elements successfully eliminated the issue of discontinuous shards. For the

threshold value above 0.1, the solution showed remarkable similarity with the true solution (PCR=82.182). However, when the threshold was lowered (i.e., more elements were extracted for the second step), the estimated solutions lost similarity with the true solution. For example, in the case where the threshold is set to x>0.001, nearly all elements in the mesh fit the new criterion and hence participate in the second-step reconstruction. This observation indicates that this method is highly dependent on the value of the manually selected threshold, and hence the method may lack stability in practice. In addition, other limitations identified from the previous sections, such as the anisotropy issue and the restriction on boundary shape deformation, could not be resolved by this method. Nevertheless, this method provided improved results compared to conventional EIT reconstruction used in previous works related to EIT-based tactile sensors.

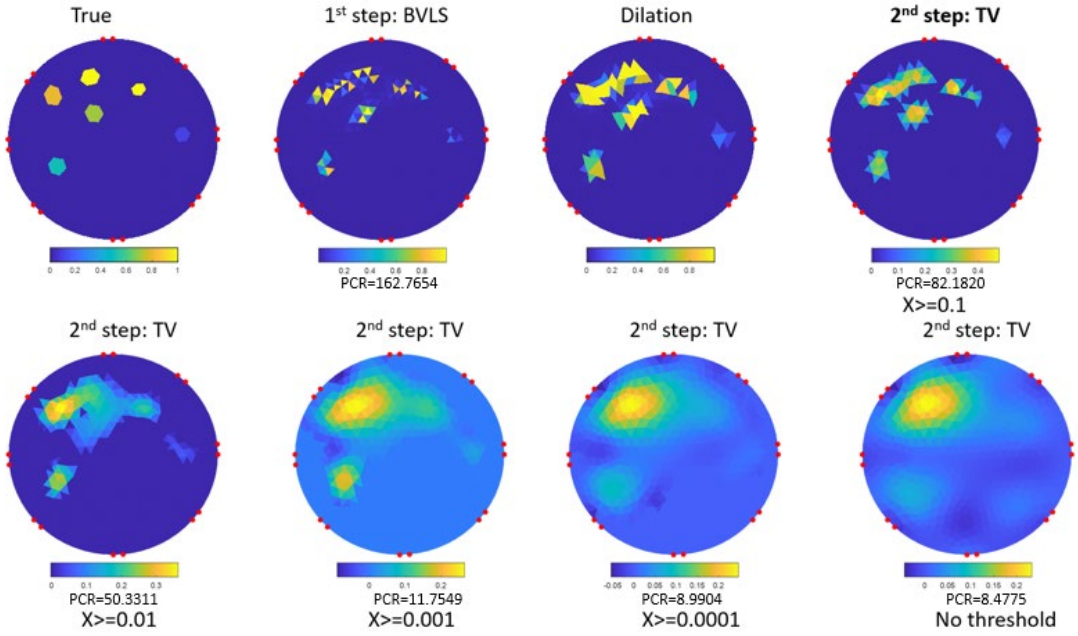

Figure 3-18 Results of the proposed two-step reconstruction method

3.7 Conclusion

Although EIT has already been applied to soft sensors in previous works to realize the concept of strain and pressure distribution sensing, the results obtained from the simulation study suggest that the existing approaches lack accuracy (indicated by PCRs). An enormous mismatch between the true electrical conductivity distribution and the estimated solutions is present. This simulation study identified several factors that are associated with the poor accuracy.

First of all, due to the intrinsically ill-posed nature of EIT, numerous solutions that fit the mathematical model exist. Hence a unique solution needs to be obtained from regularization. The choice of input parameters, including the regularization matrix and the hyperparameter value, significantly impacts the reconstruction and results in different solutions. Obtaining an estimated solution that resembles the true solution cannot be guaranteed.

The second issue identified was the lack of spatial resolution in the reconstructed image. In particular, when two or more strains represented in form of conductivity contrasts of different magnitudes, are applied to adjacent locations within the domain, these conductivity contrasts are merged together in the reconstructed image.

Another limiting factor is the nonuniform sensitivity distribution over the domain. The sensitivity distribution decreases rapidly from the boundary electrodes towards the interior. If two or more strains are applied to different positions in the domain, the strain applied to the position closer to the boundary electrodes will dominate over other strains further away from the boundary electrodes.

Furthermore, an incompatibility issue is present due to the imparity between the EIT model and the sensing material. The FEM used in the EIT model is assumed to have fixed nodal coordinates, and the conductivity of each finite element is assumed to be isotropic. However, both conditions cannot be met by the sensing material. When a strain is applied to a material and causes it to deform its shape, the deformed material

demands a new FEM with updated nodal coordinates and elements, and the electrical conductivity of composite-based sensing materials gain anisotropic conductivity, which no longer satisfies the isotropic assumption.

In addition to the limiting factors associated with the mathematical model of EIT, other factors that can affect the performance of EIT-based electronic-skin sensors were also tested. It was found that the random noise in the measured voltage data could notably affect the reconstructed solution. It was also found that the mesh density of the FEM had a notable impact on the time required by the inverse solver to calculate a solution. Using a denser mesh offers better spatial resolution, which benefits real-time imaging applications, but it leads to a lower frame rate.

In a nutshell, several limiting factors suffered by the existing approach of realizing EIT-based strain-sensing electronic skin sensors have been identified in this chapter. A modification to the reconstruction method is needed to accommodate the limitations. The modified method must be compatible with any anisotropic conductivity of the sensing material, and it should bypass the restriction of fixed nodal coordinates. The solution reconstructed using the modified method should be more consistent, disregarding the selection of regularization methods and hyperparameters. The estimated solution should be closer to the true solution and less affected by the issue of low resolution and non-uniform sensitivity distribution. Moreover, it is desired that the inverse solver derived for the modified model can execute faster to provide a higher frame rate for the strain sensing application. Furthermore, adding constraints to the inverse solver was found particularly effective for improving the solution accuracy during the preliminary attempt. It is possible to use the method to achieve a precise reconstruction (with a PCR close to 100). This method will be inherited by the new solver proposed in the following chapter.

Chapter 4 Algorithm Adaptation

4.1 Introduction

As discussed in Chapter 3, the previous approach of implementing EIT on flexible strain sensors suffers from various limitations. The causes of the limitations can be summarized in two aspects. First, the heavily ill-posed reconstruction algorithms of EIT result in significantly mismatched solutions. Second, the FEM model on which the EIT reconstruction is built is incompatible with the anisotropy and the boundary deformation of strain-sensing materials. Thus, overcoming the identified limitations should be approached by reducing the effect of the ill-posedness of the inverse problem and finding alternative models that accept anisotropic conductivity and allow nodal movement.

This chapter aims to derive a new model that can replace the FEM-based model used in the forward problem of EIT and construct a Jacobian matrix with respect to the new model. The overall structure of the EIT remains the same: the inverse solver still reconstructs solutions via a Jacobian matrix. The new model and the inverse solver should satisfy a range of expectations. For instance, the model should allow the electrical conductivity of each element to be defined in specific directions such that it is consistent with the anisotropic conductivity of the sensing materials. Also, the changes in nodal coordinates and electrode positions should not be fixed during the formation of the Jacobian matrix to allow boundary shape deformation. Moreover, the model should be compatible with the inverse solver imposed with non-negativity constraints to allow the elimination of unrealistic solutions.

This chapter first introduces the concept of a nodal admittance matrix (NAM), which is commonly used in power engineering, as a new model for solving the forward problem of EIT. Then the inverse solver is updated to fit the requirements of the nodal

admittance matrix and to produce estimations of the true solutions according to the voltage data predicted by the forward model. Afterwards, the effect of adding constraints to the solver is examined by imposing different bounded values. The physical significance of adding constraints under the new model is also explained. Finally, a simulation study is performed to verify the reliability of the new EIT model integrated with the constrained inverse solver. The performance of the proposed method is compared with the results obtained in section 3.5 to examine its effectiveness in mitigating the limitations possessed by the previous method.

4.2 Forward Model Based on the Nodal Admittance Matrix

In a power system, a nodal admittance matrix describes the nodal admittances of different buses. A bus in the system is a node where one or more lines are connected. A bus may be connected to external components such as loads, generators, and ground points. Each bus is linked to other different buses through transmission lines. The admittance diagram for an example of a three-bus system is illustrated in Figure 4-1. In this system, each bus, indicated by a shaded round shape, is interconnected by a transmission line indicated by a resistor symbol. The admittance matrix for this system can be constructed for analysing the distribution information of electrical voltages on each bus, subject to a given current injection pattern and a known admittance value for each transmission line.

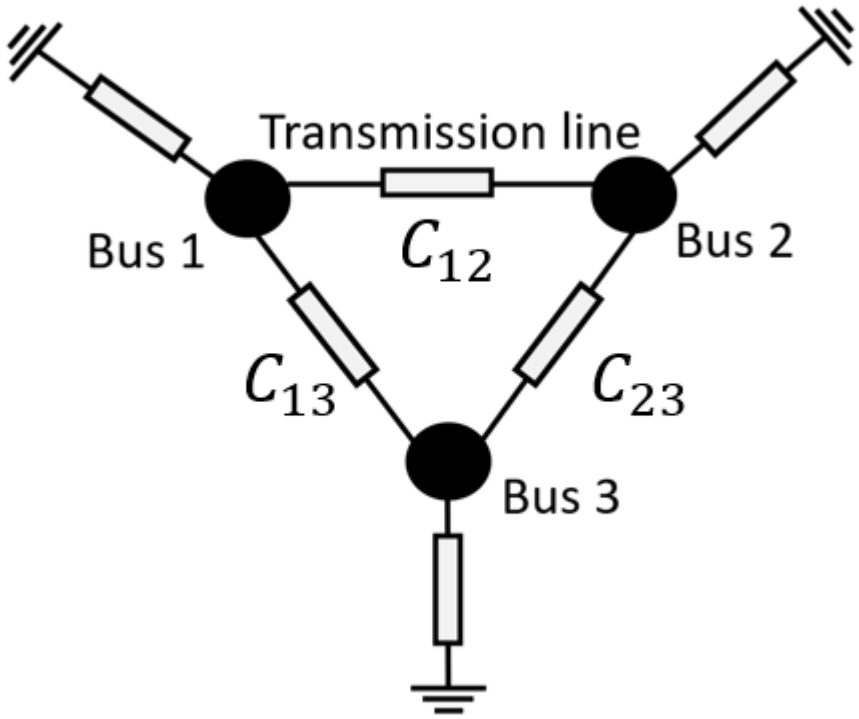

Figure 4-1 The admittance diagram for a three-bus system

The nodal admittance matrix, denoted by Y, has the form[233] of

$$Y = \sum_{i,j}^{N} Y_{ij} = \begin{bmatrix} Y_{11} & Y_{12} & \cdots & Y_{1N} \\ Y_{21} & Y_{22} & \cdots & \vdots \\ \vdots & \vdots & \ddots & \vdots \\ Y_{N1} & Y_{N2} & \cdots & Y_{NN} \end{bmatrix} \quad 4\text{-}1$$

where N is the total number of buses in the system, i and j are the indices for each bus. The matrix element, Y_{ij}, describes the relationship between the bus i, the bus j, and the admittance of the transmission line between the two buses. For the example system described in Figure 4-1, there are three buses and therefore N=3. The admittance matrix has the size of 3 * 3. The off-diagonal elements of Y where $i \neq j$ are referred to as the mutual admittances. They are given the value of the additive negative of the admittance of the transmission line between the bus i and the bus j. The diagonal elements are referred to as self-admittances and are the sum of admittances of all transmission lines connected to that bus. Thus, for the three-bus system in the above example, the value of Y is obtained as

$$Y = \sum_{i,j=1}^{3} Y_{ij} = \begin{bmatrix} Y_{11} & Y_{12} & Y_{13} \\ Y_{21} & Y_{22} & Y_{23} \\ Y_{31} & Y_{32} & Y_{33} \end{bmatrix} = \begin{bmatrix} C_{12}+C_{13} & -C_{12} & -C_{13} \\ -C_{21} & C_{21}+C_{23} & -C_{23} \\ -C_{31} & -C_{32} & C_{31}+C_{32} \end{bmatrix} \quad 4\text{-}2$$

where C denotes the admittance value for each transmission line. In this simple three-bus system, all the three buses are interconnected to each other; thus, all the matrix elements have non-zero values. In a larger sized system with many buses, a considerable portion of buses is not directly connected to each other via transmission lines. In this case, the admittance values for those elements are zero because transmission lines corresponding to those elements are missing. Therefore, the admittance matrix for a large system is typically a sparse matrix containing many zero-valued elements. An example that illustrates such a relatively larger system is shown in Figure 4-2. There are nine buses and twelve transmission lines in this system.

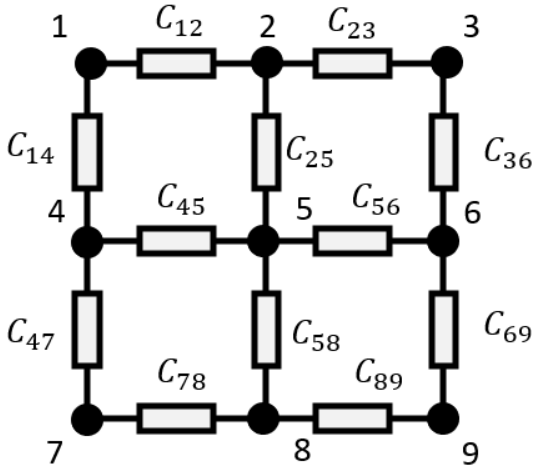

Figure 4-2 The admittance diagram for a nine-bus system in the form of a grid network

The admittance matrix for this system can then be determined using

$$Y = \sum_{i,j=1}^{9} Y_{ij} = \begin{bmatrix} Y_{11} & Y_{12} & Y_{13} & Y_{14} & Y_{15} & Y_{16} & Y_{17} & Y_{18} & Y_{19} \\ Y_{21} & Y_{22} & Y_{23} & Y_{24} & Y_{25} & Y_{26} & Y_{27} & Y_{28} & Y_{29} \\ Y_{31} & Y_{32} & Y_{33} & Y_{34} & Y_{35} & Y_{36} & Y_{37} & Y_{38} & Y_{39} \\ Y_{41} & Y_{42} & Y_{43} & Y_{44} & Y_{45} & Y_{46} & Y_{47} & Y_{48} & Y_{49} \\ Y_{51} & Y_{52} & Y_{53} & Y_{54} & Y_{55} & Y_{56} & Y_{57} & Y_{58} & Y_{59} \\ Y_{61} & Y_{62} & Y_{63} & Y_{64} & Y_{65} & Y_{66} & Y_{67} & Y_{68} & Y_{69} \\ Y_{71} & Y_{72} & Y_{73} & Y_{74} & Y_{75} & Y_{76} & Y_{77} & Y_{78} & Y_{79} \\ Y_{81} & Y_{82} & Y_{83} & Y_{84} & Y_{85} & Y_{86} & Y_{87} & Y_{88} & Y_{89} \\ Y_{91} & Y_{92} & Y_{93} & Y_{94} & Y_{95} & Y_{96} & Y_{97} & Y_{98} & Y_{99} \end{bmatrix} \quad 4\text{-}3$$

By assigning the admittance values into the elements of the admittance matrix based on the topology of the buses in the grid network, the final admittance matrix is obtained as

$$Y = \begin{bmatrix} C_{12}+C_{14} & -C_{12} & 0 & -C_{14} & 0 & 0 & 0 & 0 & 0 \\ -C_{12} & C_{12}+C_{23}+C_{25} & -C_{23} & 0 & -C_{25} & 0 & 0 & 0 & 0 \\ 0 & -C_{23} & C_{23}+C_{36} & 0 & 0 & -C_{36} & 0 & 0 & 0 \\ -C_{14} & 0 & 0 & C_{14}+C_{45}+C_{47} & -C_{45} & 0 & -C_{47} & 0 & 0 \\ 0 & -C_{25} & 0 & -C_{45} & C_{25}+C_{45}+C_{56}+C_{58} & -C_{56} & 0 & -C_{58} & 0 \\ 0 & 0 & -C_{36} & 0 & -C_{56} & C_{36}+C_{56}+C_{69} & 0 & 0 & -C_{69} \\ 0 & 0 & 0 & -C_{47} & 0 & 0 & C_{47}+C_{78} & -C_{78} & 0 \\ 0 & 0 & 0 & 0 & -C_{58} & 0 & -C_{78} & C_{58}+C_{78}+C_{89} & -C_{89} \\ 0 & 0 & 0 & 0 & 0 & -C_{69} & 0 & -C_{89} & C_{69}+C_{89} \end{bmatrix} \quad 4\text{-}4$$

It can be observed that the admittance matrix is a sparse matrix whose upper diagonal is in symmetry with the lower diagonal. This characteristic allows the matrix to be calculated using less time by only determining the values of a triangular portion of the matrix and then using its transpose as the values for the other triangular portion. Additionally, the sparse feature implies that the computer can store the matrix using less space and process calculations faster.

Next, in order to derive the model for the forward problem of EIT, nodal voltage analysis can be conducted based on the fundamentals of Kirchhoff's law and Ohm's law, as expressed by equation 4-4, which in this case describes the relation among admittance of transmission lines, voltages of buses, and current flow into or out of buses.

$$Y\,U = I \quad 4\text{-}5$$

where Y is the admittance matrix with a size of $N * N$; U contains the voltage of each bus with reference to a ground point and has a size of $N * 1$; I is the net current that flows into and out of each bus and also has a size of $N * 1$.

The forward problem of EIT is to predict the nodal voltage distribution using a known current injection pattern and known electrical conductivity distribution. Correspondingly, the nodal admittance matrix contains the admittance values for all transmission lines; each transmission line serves as a single element. The current injection I remains the same as its original form. The voltages in the U matrix are the sought solutions to the forward problem. The U matrix as the solution to the matrix equation in 4-5 can be expressed as

$$U = Y^{-1}I \tag{4-6}$$

Equation 4-6 represents the model used in the forward problem of the adapted EIT algorithms. It shows that the forward solution U is obtained by multiplying the inverse of the nodal admittance matrix Y with the current injection matrix I. For instance, when a current with a density of a unity magnitude is supplied into the grid network illustrated in Figure 4-2 via the first node and sunk through the third node, the voltage for each node can be calculated using equation 4-6 by assigning the net current of each node into the I matrix which is then multiplied with Y^{-1}. This relation is expressed as

$$\begin{bmatrix} u_1 \\ u_2 \\ u_3 \\ u_4 \\ u_5 \\ u_6 \\ u_7 \\ u_8 \\ u_9 \end{bmatrix} = Y^{-1} \begin{bmatrix} 1 \\ 0 \\ -1 \\ 0 \\ 0 \\ 0 \\ 0 \\ 0 \end{bmatrix} \tag{4-7}$$

It is worth noting that this model derived from NAM is distinct from the model based on the finite difference method (FDM)[234], which was aforementioned in section 2.2.2. Unlike the FDM, which mathematically discretizes a two-dimensional domain into a number of identical squares using intercepting lines, the NAM-based model

proposed in this work relies on patterning a conductive material into the structure of a grid system. In the grid system, a linear sensing element is constructed between each pair of adjacent nodes. Therefore, the current flow between two adjacent nodes is constrained within a path, such that the anisotropic electrical properties of the material are compatible with strain sensing, and the variation in electrical properties of each sensing element is related to only the longitudinal strain between two nodes rather than any other directions. Moreover, FDM does not allow free boundary deformation as this method is only compatible with simple and regular geometries[32], [33] that can be discretized into uniform squares; conversely, all the nodes in NAM-based model, including the nodes located on the boundary rows and columns, are free to move without constraints, and there is no fixed shape to be maintained.

In order to verify the accuracy of the new forward model described by equation 4-6, the model is implemented using MATLAB (The MathWorks Inc., Natick, MA, USA), and verified by comparing its results with the solutions obtained from simulations using NI Multisim (National Instruments Corporation, Austin, TX, USA). This model is more straightforward than the FEM-based model implemented previously in Chapter 3. The simplicity is because the new model does not need to calculate element sizes, edge lengths, gradients of basis functions, and the additional complete electrode model for enhancing accuracy, which is required for the FEM approach.

The admittance system used in this initial simulation was a square grid network system formed by buses in five columns and five rows. The default admittance values for all elements were set to 0.001 S, which corresponds to impedance values of 1 kΩ. The input current injection was set to 1 for the first node and -1 for the fifth node, meaning a current of unity magnitude (i.e., 1 ampere in this case) was injected into the system via the first node and sunk through the fifth node. The solutions output by the MATLAB program and NI Multisim are shown in Figure 4-3.

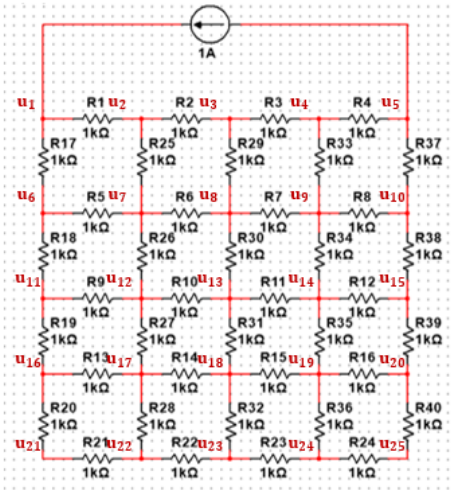

(Unit: Volt)

U_MATLAB=	U_Multism=
950.7576	951
405.3030	405
-0.0000	-0.00000712
-405.3030	-405
-950.7576	-951
496.2121	496
265.1515	265
0	-0.00000712
-265.1515	-265
-496.2121	-496
272.7273	273
159.0909	159
-272.7273	-273
162.8788	163
98.4848	98.5
-0.0000	-0.00000712
-98.4848	-98.5
-162.8788	-163
117.4242	117
71.9797	72.0
-0.0000	-0.00000712
-71.9697	-72.0
-117.4242	-117

Figure 4-3 Verifying the accuracy of the solutions obtained by the simplified model by comparing them with the results obtained by NI Multisim simulation. U_MATLAB lists the solutions for nodal voltages from u_1 to u_{25}, obtained using the simplified model. U_Multism lists the solutions determined using the NI Multisim simulation.

It can be seen that the results obtained from the two methods are well-matched with each other, indicating the model is accurate and reliable. Additionally, it is worth noting that this NAM-based model does not need to hold the assumption that only direct current or low-frequency alternating current is accepted, which was required by equation 3-3 during the derivation of the governing equation used in the conventional FEM approach for avoiding the effect of displacement current. Therefore, the NAM-based model is more robust in terms of the applicable frequency range of the injected excitation current.

4.3 Derivation of the Jacobian Matrix

A Jacobian matrix must be derived beforehand to implement an inverse solver for the new model. In this case, with NAM, the Jacobian matrix is a mapping function that maps the change in the admittance of each transmission line into voltage variation at each bus. Each transmission line serves as an individual sensing element, and each bus

is equivalent to a node. The new Jacobian matrix for the NAM approach takes a similar form to the previous Jacobian matrix used in the conventional FEM approach. Namely, the new Jacobian matrix, also denoted by H, needs to satisfy

$$Z = H\,\Delta C \tag{4-8}$$

where Z represents the change in voltage data at nodes that are selected as electrodes for current injection and voltage measurement; $\triangle\, C$ is the variation in admittance of all elements. The Z matrix can be reformulated as

$$Z = \frac{\text{Ext}[U(C+\Delta C) - U(C)]}{\Delta C}\Delta C \tag{4-9}$$

The function "Ext" is an extraction operator that extracts electrode voltage data from the complete nodal voltage data. The function is in the form of a logical matrix in MATLAB. If a small time interval between two sets of voltage measurement is assumed, and the admittance variation during each small time interval is assumed to be small, then the division in equation 4-9 can be represented using its limit as ΔC approaches to zero. This relation is expressed as

$$\lim_{\Delta C \to 0} \frac{\text{Ext}[U(C+\Delta C) - U(C)]}{\Delta C} = \frac{Ext[\partial U]}{\partial C} \tag{4-10}$$

Equation 4-10 can be therefore written as

$$z = \frac{\text{Ext}[\partial U]}{\partial C}\Delta C \tag{4-11}$$

By substituting the equation 4-11 into equation 4-8, the Jacobian matrix, H, can be therefore calculated using

$$H = \text{Ext}\left[\frac{\partial U}{\partial C}\right] \tag{4-12}$$

According to equation 4-6 which specifies $U = Y^{-1}I$, equation 4-12 can then written as

$$H = \text{Ext}\left[\frac{\partial U}{\partial C}\right] = \text{Ext}\left[\frac{\partial Y^{-1}I}{\partial C}\right] = \text{Ext}\left[\frac{\partial Y^{-1}}{\partial C}I\right] \tag{4-13}$$

To determine the derivative of Y^{-1}, the chain rule is applied. The equation becomes

$$H = \text{Ext}\left[Y^{-1}\frac{\partial Y}{\partial C}Y^{-1}I\right] \quad 4\text{-}14$$

For equation 4-14, the I matrix is a constant matrix readily available, and the inverse of the Y matrix can be easily calculated by MATLAB. The only parameter that requires further processing is the partial derivative of the Y matrix with respect to C. The C matrix is a $K * 1$ matrix where K is the total number of the sensing elements in the system. The derivative $\frac{\partial Y}{\partial C}$ can be determined as the gradient of the Y matrix with regard to each element, C_k, expressed as

$$\frac{\partial Y}{\partial C} = \nabla_C Y = \sum_k^K \frac{\partial Y}{\partial C_k} = \left[\frac{\partial Y}{\partial C_1}, \frac{\partial Y}{\partial C_2}, \cdots, \frac{\partial Y}{\partial C_K}\right] \quad 4\text{-}15$$

where k is the index for each element in the C matrix. Each derivative ($\frac{\partial Y}{\partial C_k}$) has the size of $N * N$, where N is the number of nodes. Using the derivates determined from equation 4-15, the local Jacobian matrix, H_k, that predicts the nodal voltage variations caused by a change in the admittance of the k_{th} element can be calculated using the following expression:

$$H_k = Ext\left[Y^{-1}\frac{\partial Y}{\partial C_k}Y^{-1}I\right] \quad 4\text{-}16$$

The size of a local Jacobian matrix, described by equation 4-16 without the extraction operator (i.e., when $H_k = Y^{-1}\frac{\partial Y}{\partial C_k}Y^{-1}I$) and during a single current injection, can be shown to be

$$[N * N]\,[N * N]\,[N * N]\,[N * 1] = [N * 1] \quad 4\text{-}17$$

Formulating the global Jacobian matrix from local matrices is not as straightforward as the conventional FEM approach discussed previously. The global Jacobian matrix for the FEM approach is directly obtained by assigning the elements of local matrices into a global matrix and then utilized as a part of the inverse solver. The global Jacobian matrix in the NAM approach needs to be arranged in a particular way to comply with the current injection data, the voltage data, and the admittance data.

For a system that has N nodes and K elements and is supplied with G current injection patterns, the size of a local Jacobian matrix without the extraction operator is expanded to

$$[N * N]\,[N * N]\,[N * N]\,[N * G] = [N * G] \tag{4-18}$$

The linear system used by the inverse solver is previously described by $Z = H \triangle C$ in equation 4-8, in which the size of the C matrix is *M * 1*. To maintain the validity of the equation, the number of columns in the Z matrix must also be equal to that of the ending C matrix, i.e., the Z matrix should only have a single column. Thus, the voltage data recorded during each current injection pattern and stored in the Z matrix is reshaped into a single column as

$$Z = \sum_{j}^{G}\sum_{i}^{N} z_{i,j} = \left[z_{1,1}, z_{2,1}, \dots, z_{N,1}, z_{1,2}, z_{2,2}, \dots, z_{N,2}, \dots, z_{N,G}\right]^{T} \tag{4-19}$$

where $z_{i,j}$ denotes the voltage data for the $\mathrm{i_{th}}$ node during the $\mathrm{j_{th}}$ current injection pattern. The sizes of parameters in the linear system, $Z = H \triangle C$, become consistent

$$\left[[N \times G] * 1\right] = [size\ of\ Jacobian]\,[K * 1] \tag{4-20}$$

To maintain the consistency described by equation 4-20, the size of the global Jacobian matrix without the extraction operator therefore must satisfy the condition of having M columns and $N \times G$ rows. In order to meet this requirement, the global Jacobian matrix without the extraction operator should be expressed as

$$\mathrm{H} = \sum_{i}^{N}\sum_{j}^{G}\sum_{k}^{K} H_{N\times(j-1)+i,k} \qquad \text{4-21}$$

$$= \begin{bmatrix} H_{1,1} & H_{1,2} & \cdots & H_{1,K}, \\ H_{2,1} & H_{2,2} & \cdots & H_{2,K} \\ \cdots & \cdots & \cdots & \cdots \\ H_{N,1} & H_{N,2} & \cdots & H_{N,K} \\ H_{N\times1+1,1} & H_{N\times1+1,2} & \cdots & H_{N\times1+1,K} \\ H_{N\times1+2,1} & H_{N\times1+2,2} & \cdots & H_{N\times1+2,K} \\ \cdots & \cdots & \cdots & \cdots \\ H_{N\times1+N,1} & H_{N\times1+N,2} & \cdots & H_{N\times1+N,K} \\ H_{N\times2+1,1} & H_{N\times2+1,2} & \cdots & H_{N\times2+1,K} \\ \cdots & \cdots & \cdots & \cdots \\ H_{N\times2+N,1} & H_{N\times2+N,2} & \cdots & H_{N\times2+N,K} \\ H_{N\times3+1,1} & H_{N\times3+1,2} & \cdots & H_{N\times3+1,K} \\ \cdots & \cdots & \cdots & \cdots \\ \cdots & \cdots & \cdots & \cdots \\ H_{N\times(G-1)+N-1,1} & H_{N\times(G-1)+N-1,2} & \cdots & H_{N\times(G-1)+N-1,K} \\ H_{N\times G,1} & H_{N\times G,2} & \cdots & H_{N\times G,K} \end{bmatrix}$$

The final system of equations consists of the global Jacobian matrix, the admittance variation matrix, and the voltage data matrix. Its structure is visualized in Figure 4-4. It can be seen that the global Jacobian matrix is obtained by compiling the combinations of local matrices for all current injection patterns together; this corresponds to the voltage data matrix in which the variation in nodal voltages during each current injection patterns are also stacked together into a single column. Without the extraction operator, the obtained global Jacobian matrix maps the admittance variation, ΔC, into voltage variations at all nodes. On the other hand, with the extraction operator applied to the Jacobian matrix, $Ext[H]$, the admittance variations are mapped towards the voltage variations at specific electrode nodes used for current injections and voltage measurements.

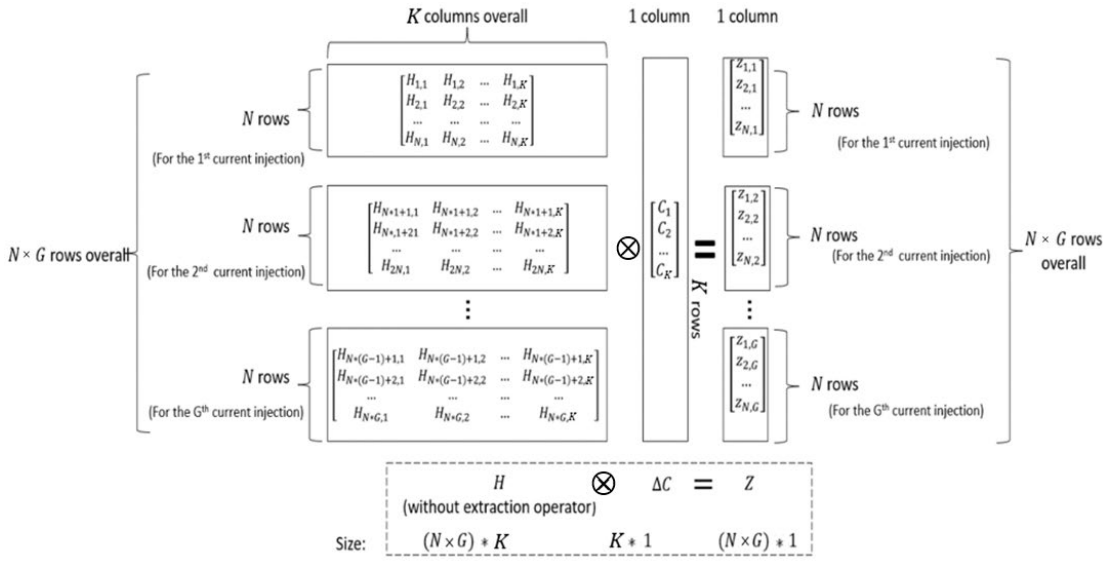

Figure 4-4 The structure and the sizes for parameters in the final system of linear equations. (“⊗” denotes matrix product)

The inverse problem uses known voltage data to calculate the admittance variation. When the extraction operator is added, the system becomes underdetermined. Hence, there are non-unique solutions. Similar to the conventional FEM approach, a unique solution can be determined by error minimization. The objective function for error minimization is defined as

$$x = argmin\,|Hx - Z|^2 \qquad 4\text{-}22$$

where x denotes the solution of ΔC at which the error is minimized. This problem can then be solved using the least square and regularization methods previously described in section 3.4.2.

4.4 Refining Solution Space

In section 3.6.1, it was found that adding additional constraints to the inverse solver is particularly effective in refining the reconstructed solutions into a narrower and more realistic space such that they are more closely matched with the true solution. In this

model based on a NAM system, the solutions to be determined are the admittance values of elements in the system. The admittance of each element can be determined from experiments to gain prior knowledge about its minimum and maximum, which can then be imposed as the constraint to the inverse solver, such that the solver produces solutions only within this valid range that has realistic meaning. For example, if the material that forms a grid-network system has an admittance variation value within a range from 0 to 1, then the constraints to the inverse solver can be imposed as 0 to 1. Therefore, the reconstructed solutions only consist of values within this range. Any values outside this range are considered unfeasible and are eliminated.

Simulations were performed to examine the effect of adding constraints to the solver. Figure 4-5 shows the solutions reconstructed using the pseudoinverse method without any constraints to the solutions. The background admittance of the network is set to unity. The obtained solutions are displayed in two styles. The first style is a "stem" plot that shows the numerical solution, including both true solutions and reconstructed solutions shown in the vertical axis, for each element whose index is represented in the horizontal axis. The second style is a visualization of the results in 3D. Half-sine waves are used to expand the plot in the vertical direction. Each peak of the sine waves represents the magnitude of the solution for each corresponding element.

In visual comparison to the reconstructed solutions based on the conventional FEM approach applied to unstructured regions shown in the previous chapter, the solutions reconstructed based on the NAM model are considerably more closely related to the true solution. However, uneven "background" was still observed in the solutions for elements with zero admittance variations. In (a), the true solution was set to have an admittance variation of 0.05 at the first element. Although the reconstructed result approximately preserved this change, the changes in the admittance values of other elements were not adequately estimated. "Hills" and "crests" were formed at other elements that are supposed to be unchanged according to the true solution. The same problem was also observed in other cases shown in (b), (c) and (d), in which more complicated true inputs were assigned and reconstructed. The presence of "hill" and

"crest" at each element is similar to the uneven colours observed in the results of the conventional EIT reconstruction in section 3.5. Because numerous non-unique solutions exist and they all led to the same electrode voltage variation data, all of them were correct solutions from the perspective of fitting the model. Without additional prior knowledge to refine the solution space, guaranteeing a solution that closely matches the true solution is unfeasible.

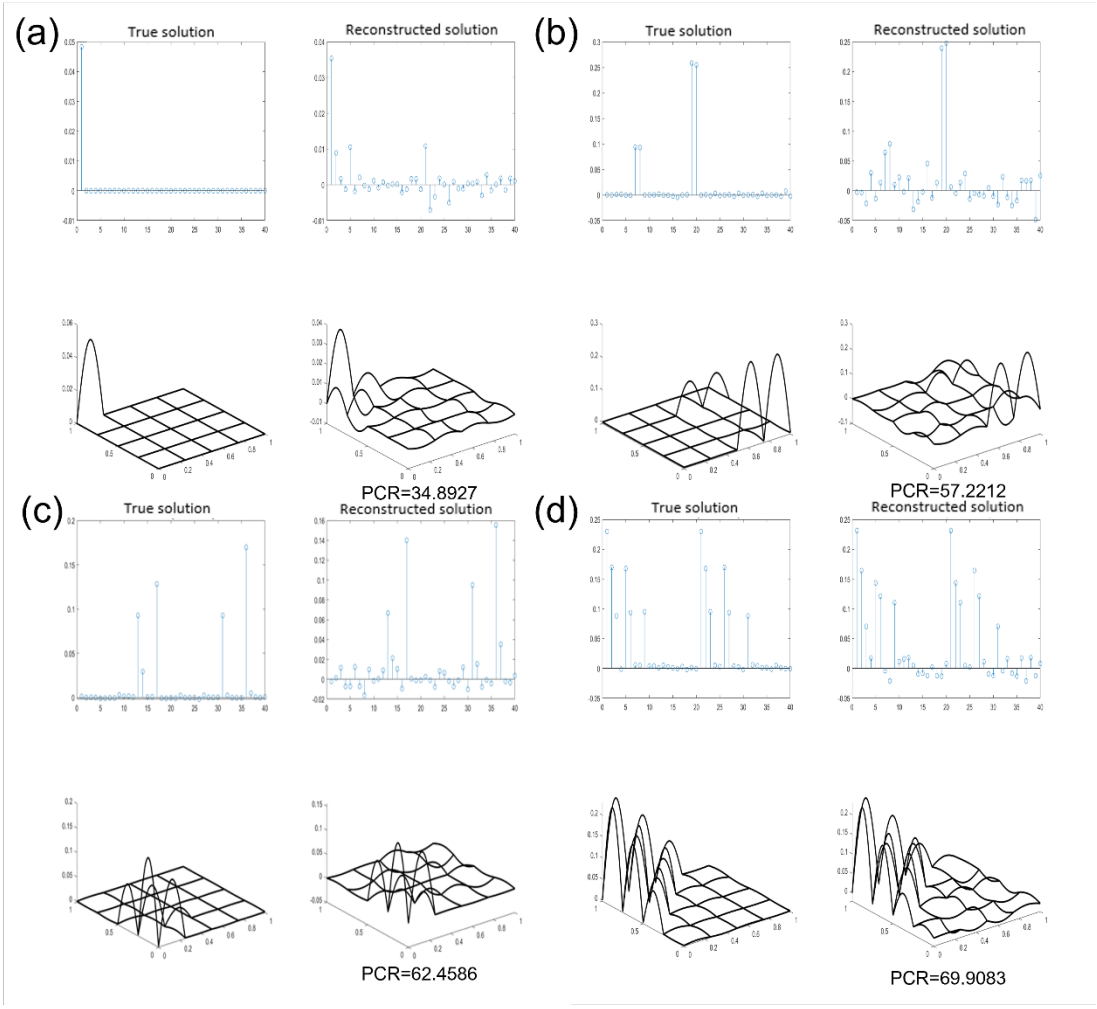

Figure 4-5 Reconstructed results for four types of inputs using the pseudoinverse method without constraints. For each pair of the plots, the left plot shows the true solution, and the right plot shows the reconstructed solution.

Reconstructions were then performed with the NNLS solver. The NNLS solver is implemented using the "lsqnonneg" function embedded in MATLAB. The function is

based on the active set method, which is an iterative algorithm proposed by Lawson and Hanson[235]. In this simulation, four types of inputs were assigned at arbitrarily selected elements. The assigned admittance variations were limited within the range from 0 to 1. As shown in Figure 4-6 (a), (b) and (c), the erroneous “hills” and “crests” were successfully eliminated in the reconstructed results. The reconstructed solutions were nearly identical to the true solutions, with only slight differences. Although small “hills” were occasionally observed, as illustrated in (d), at several elements indicated by the red-colour line segments, the reconstructed solutions successfully preserved approximate distribution information, which was unable to be achieved by the conventional reconstruction approach.

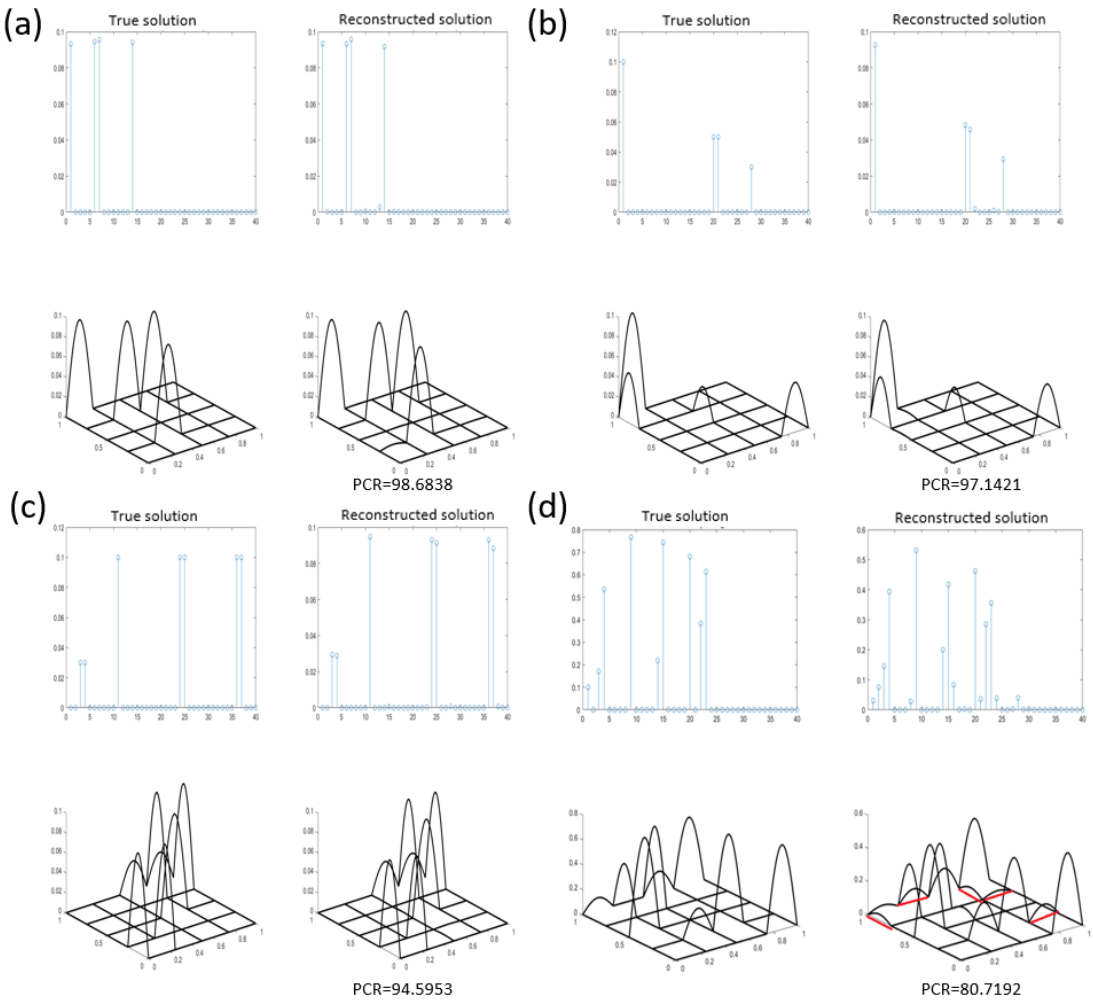

Figure 4-6 Reconstructed results for four types of inputs using the NNLS solver with nonnegativity constraint. For each pair of the plots in (a), (b), (c) and (d), the left plot shows the true solution, and the right plot shows the reconstructed solution.

In addition, simulations were further performed on systems with higher dimensions to test the effectiveness of the method for more extensive networks. Figure 4-7(a) and (b) exhibit the results of simulations performed on a 9 * 9 grid network system and a 21 * 21 grid network system, respectively. The obtained solutions were well matched with the true input with PCRs greater than 90, suggesting the reconstruction method is applicable to networks of various dimensions.

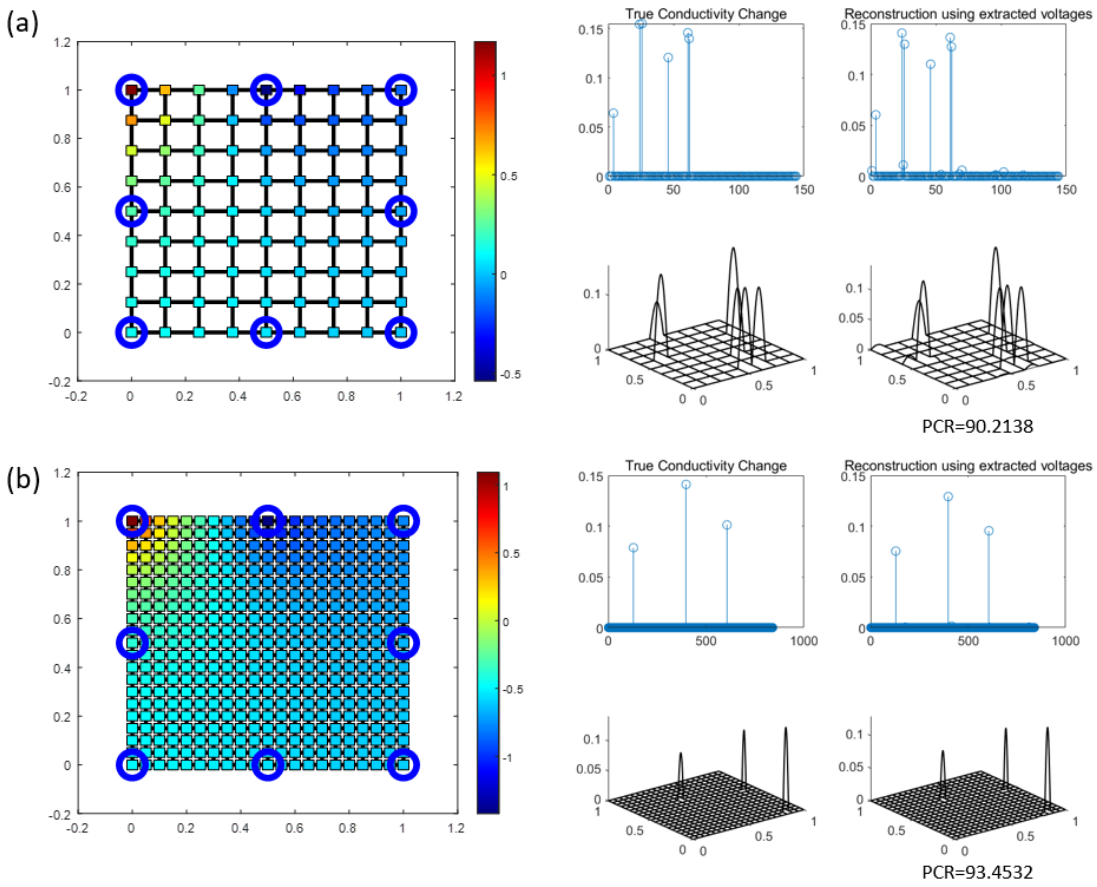

Figure 4-7 Reconstructed results for systems of higher dimensions. (a) a 9 * 9 grid-network system. (b) a 21 * 21 grid-network system. The left-side illustrations show the arrangement of each of the system. Blue circles indicate the nodes that are connected to electrodes. For each pair of the plots, the left plot shows the true solution, and the right plot shows the reconstructed solution.

4.5 Improvements

4.5.1 Improved Solution Consistency

As discussed previously in section 3.5.1, the solutions reconstructed using the conventional method are uncertain. The uncertainty is because the solutions are dependent on several input parameters to the inverse solver, including the type of

regularization matrix and the values of the hyperparameters that control the weight of regularization. In section 3.6.1, this uncertainty issue was relieved by adding additional constraints to the solver to refine the solutions. Although this method exhibits significantly improved consistency of solutions than that of the conventional approach without any constraints, the resulting solutions are still dependent on the types of solvers used, and noticeable differences are observed in solutions subject to different constraint values.

Simulations were performed to examine the improvement made by the NAM-based model accompanied with the NNLS solver. For a grid network system with randomly assigned admittance distribution at each element, the solutions were reconstructed using different types of solvers. The background baseline admittance of the network was set to unity. The simulation results are shown in Figure 4-8. In (a), the true admittance variation values of 0.1, 0.1, 0.15 and 0.25 were assigned to the 4^{th}, the 14^{th}, the 21^{st} and the 30^{th} element, respectively. The estimated result using the Tikhonov prior and non-negative constraints are shown in (b). Although a small error was observed at the 8^{th} element, the overall estimation was closely matched with the true solution. In (c), the same result, including the error, was obtained using the Noser prior with non-negative constraints. This consistency was not observed in simulations previously performed in section 3.5.1, in which changing the types of regularization matrix leads to considerably different solutions. Notably, the results exhibited in (b) and (c) were reconstructed using a hyperparameter value of 0.1; the same results were obtained when other different values were used, including 0.0001, 0.001, 0.01. To the extreme, when there is no regularization imposed, i.e., when the hyperparameter is set to 0, the NNLS solver stills provides the same result, as shown in (d). This consistency implies that the model incorporated by the non-negative constraints can provide good estimation without needing additional regularization. An exception was observed when a Tikhonov prior was used. The Tikhonov prior provided consistent results under hyperparameters below 0.01, but the results lost similarity to the true solution when the hyperparameter was increased to over 0.1. This agrees with the results previously

demonstrated in Figure 3-8, which shows that overregularization can hinder the solutions. It is difficult and problematic to avoid overregularization by choosing suitable values for the hyperparameters without prior knowledge. Considering that, in the case of the simulation, regularization is unnecessary for the NNLS solver because the results are the same with or without regularization, it is adequate to use the NNLS solver itself without any additional regularization to perform reconstructions and still obtain results closely matched to the true solution.

Apart from the NNLS solver, BVLS was also tested to examine the effect of choosing different upper bound constraint values on the solutions. The obtained results subject to different constraints are shown in (e) and (f), respectively. For this true admittance distribution, the reconstructed results subject to both constraints were the same, indicating the upper bound values may have an insignificant impact on the solutions. Notably, setting the upper bound value of BVLS to infinity, which is equivalent to the NNLS solver, results in the same solutions. This finding implies that the using NNLS solver is sufficient for solving for consistent solutions without a need to impose an upper limit.

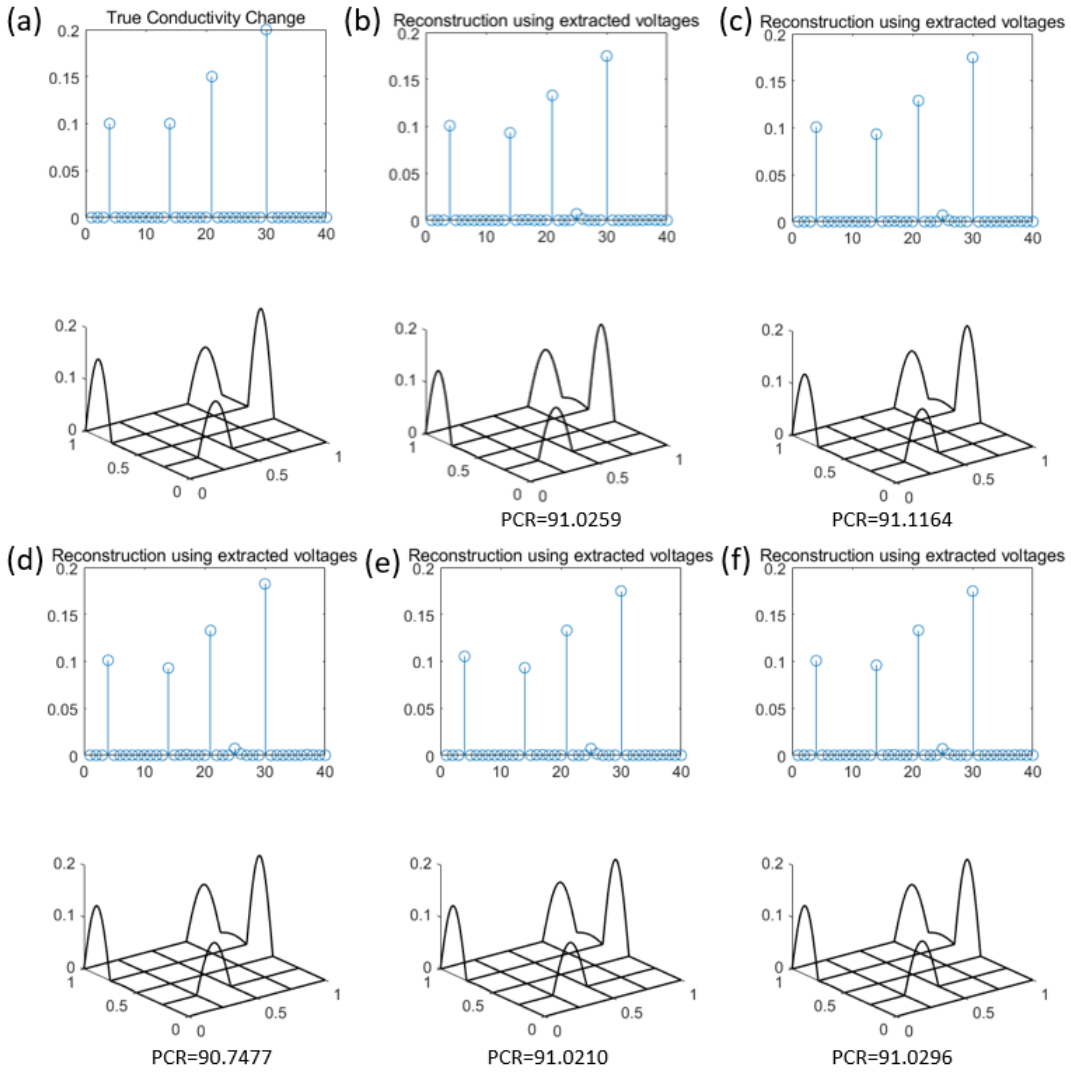

Figure 4-8 Reconstruction for a randomly assigned admittance distribution using the grid network model. (a) true solution. (b) Solution estimated using Tikhonov regularization and NNLS solver. (c) Solution estimated using Noser regularization and NNLS solver. (d) Solution estimated using NNLS solver without regularization. (e) Solution estimated using BVLS with the constraint that the solutions lay within the range between 0 and 1. (f) Solution estimated using BVLS with the constraint that the solutions lay within the range between 0 and 1000.

4.5.2 Improved Spatial Resolution

It was previously shown in section 3.5.2 that when two or more conductivity contrasts are applied to the domain at a close distance, they cannot be distinguished from the

reconstructed results; instead, they are generally estimated as a single merged contrast. In order to examine if the proposed NAM model incorporated with non-negativity constraints can better accommodate this limitation, simulations were performed by assigning various admittance values to elements in direct contact. They are then reconstructed using the NNLS solver.

The reconstructed results are exhibited in Figure 4-9. As shown in (a), the indicated elements were assigned the same admittance variation of 0.1. The three elements were at a close distance. The results showed that the reconstructed solutions were closely matched with the true solution. Minor errors were observed in their overall magnitudes. It is worth noting that the admittance value for the element surrounded by the three elements remained intact. This result suggests that the spatial resolution problem was significantly improved. In (b), another simulation was performed by further assigning additional admittances to the nearby elements. In this case, more errors were observed in the reconstructed solutions; however, the overall distribution was reasonably maintained, and zero value of admittance for the surrounded element was retained in the estimated results.

The simulations demonstrated in (a) and (b) were performed for a grid network with a dimension of 5 * 5. Further simulations were performed on a larger network. In (c), a simulation was performed on a network formed by nodes in 15 rows and 15 columns. Two centre elements, which were separated by a middle element, were both assigned with an admittance variation of 0.1. For this distribution, the solution obtained in the reconstruction successfully preserved similar magnitudes to the true solution. In (d), the admittance variations of the two selected elements were assigned with different values. One element was assigned with 0.1, and the other was assigned with 0.2. The reconstruction performed for this input also resulted in solutions closely matched to the true solution. In both (c) and (d), the admittance variation of the middle element was successfully reconstructed as zero, indicating that there was negligible interference from the nearby elements/ These results confirm that the proposed method offers

notable improvement to the low spatial resolution issue possessed by the conventional approach.

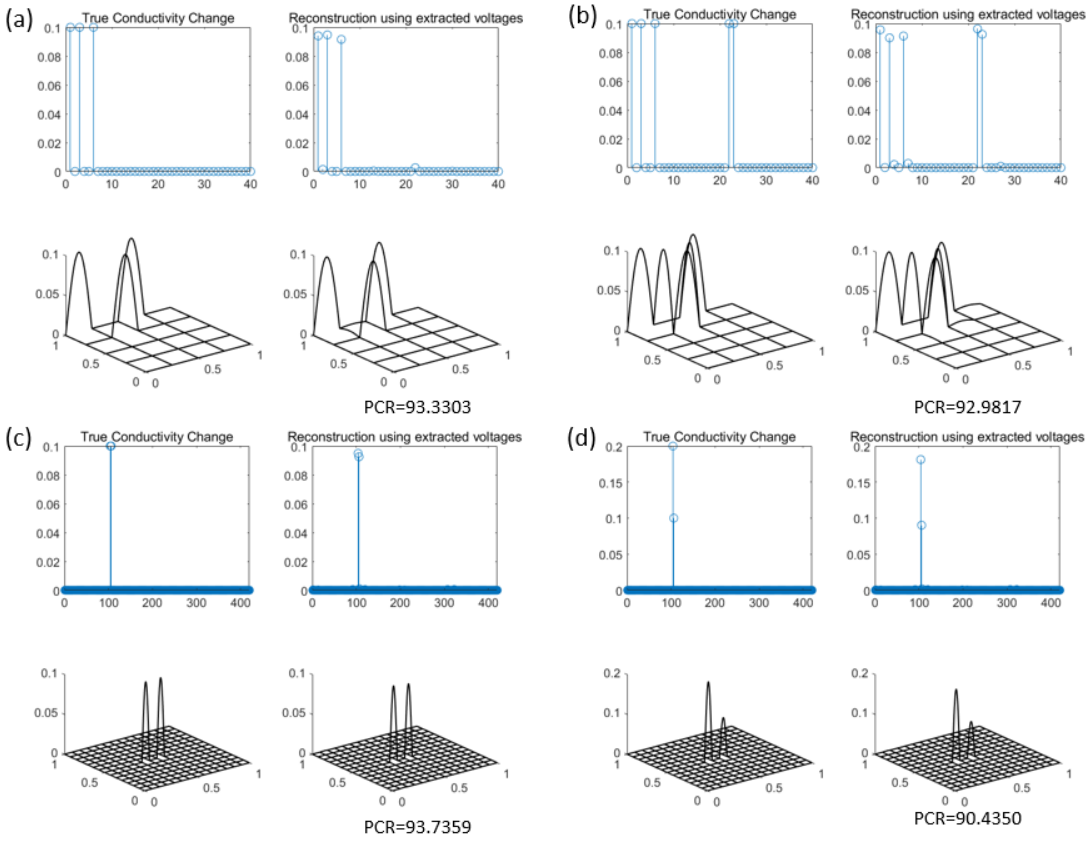

Figure 4-9 Reconstruction using NNLS solver on grid network models assigned with various admittance values to verify the improvement to the poor resolution issue. (a) Reconstructing three contrasts applied to a 5*5 network. (b) Reconstructing five contrasts applied to a 5*5 network. (c) Reconstructing two same contrasts applied to a 15*15 network. (d) Reconstructing two different contrasts applied to a 15*15 network.

4.5.3 Improved Interior Sensitivity

It can be seen from section 3.5.3 that the issue with non-uniform sensitivity distribution possessed by the EIT model based on FEM severely limited the solution reliability. Any mechanical stimulus applied closer to the boundary electrodes, where sensitivity is significantly higher than the interior, will dominate other stimuli applied closer to

the centre of the domain. Simulations were performed on grid network systems to verify the new model's improvement to accommodate this issue.

The solutions reconstructed using the NNLS solver for various types of true admittance distribution are shown in Figure 4-10. In (a), an element on the boundary was assigned an admittance variation value of 0.2. An internal element was assigned a value of 0.1. The reconstruction successfully estimated the results, in which the admittance variations for both the outer and the inner elements were clearly and accurately calculated. More unevenly distributed admittance variations were assigned to the system, as presented in (b), where two additional boundary elements were assigned with a value of 0.2. In this case, with higher values assigned to more boundary elements, the estimated admittance variation of the internal element was expected to be significantly reduced or eliminated if the conventional reconstruction approach was implemented. However, the proposed reconstruction method accurately estimated the true solution. The non-uniformity was further enhanced in (c), where the number of internal elements assigned an admittance variation was increased to four instead of the initial one. For this complex distribution, the reconstruction again offered excellent estimation. The complexity of the distribution was further extended in (d), where one of the four internal elements was assigned a value of 0.2, which was different from the remains elements that were assigned a value of 0.1. It is generally unfeasible to obtain reasonable estimations by performing reconstructions for this type of input using the conventional unconstrained FEM approach. Conventionally, the admittance values of internal elements would be severely underestimated, and they would also become merged due to the aforementioned spatial resolution issue. Remarkably, using the proposed method, the reconstruction successfully estimated the admittance variation values for internal elements under such an uneven distribution. These results indicated that the proposed method effectively mitigated the drawback of non-uniform sensitivity. Using this method for realizing an EIT-based strain-sensing electronic skin, a force, pressure, or a strain applied to the boundary no longer dominates over other stimuli applied closer to the centre. In other words, the estimated magnitudes of admittance for

each element are less likely to interfere with each other. Compared to the conventional FEM-based approach, where the stimuli must be applied at a similar distance to the boundary electrodes, this proposed method provides greater freedom in usage, allowing multiple mechanical stimuli to be applied to any location on the sensor.

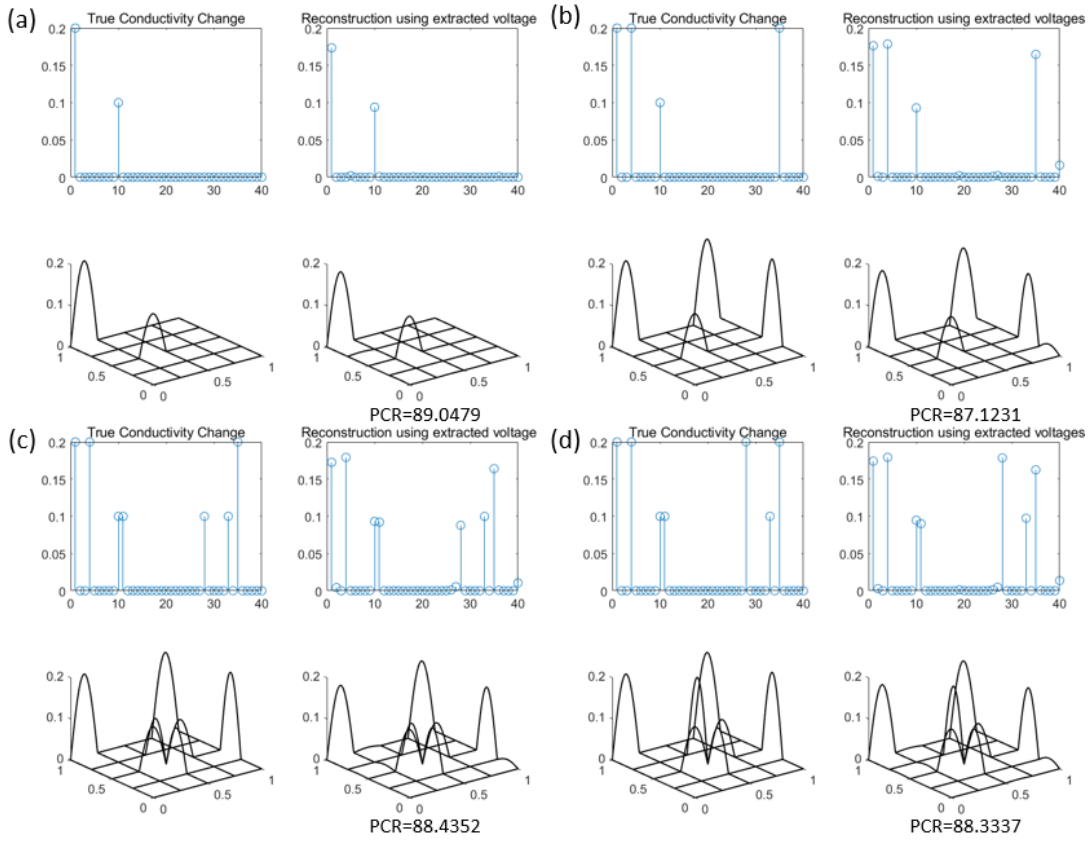

Figure 4-10 Reconstruction using NNLS solver on grid network models assigned with various admittance values to verify the improvement to the non-uniform sensitivity distribution issue. (a) Reconstructing one boundary contrast and one inner contrast. (b) Reconstructing three boundary contrasts and one inner contrast. (c) Reconstructing three boundary contrasts and four inner contrasts. (d) Reconstructing three boundary contrasts and four inner contrasts.

4.5.4 Model Compatibility

As previously discussed in section 3.5.4, one of the limitations of the FEM-based model is that the model only accepts isotropic conductivity, which causes conflicts with polymer-based sensing materials whose electrical conductivity is anisotropic and

depends on the direction of strains. Another limitation is that the model requires fixed nodal coordinates, resulting in fixed electrode positions and fixed boundary shapes. Thus, the sensor implemented using the conventional model is only suitable for sensing pressures but incapable of sensing applied strains that cause boundary shape deformation.

The proposed model derived from the nodal admittance matrix is free from these two limitations. In terms of electrical conductivity, the model based on the nodal admittance matrix itself does not impose any requirements on the directions of the conductivity. Instead of having fixed orientations imposed by the structural model, the directions of the conductivity are dependent on the actual deformation of the sensor. A schematic that explains the advantage is illustrated in Figure 4-11, where a node that connects to other adjacent nodes via two sensing elements is relocated due to an applied strain, the directions of the current flow via the two elements are also shifted to keep pointing towards the new position of the node. It does not matter whether the electrical conductivity of the sensing material is isotropic or anisotropic, because the new model only considers the conductance or the admittance of the element, which is a scalar rather than a vector quantity, to solve for the forward problem and the inverse problem. There is no directional information involved in the algorithm.

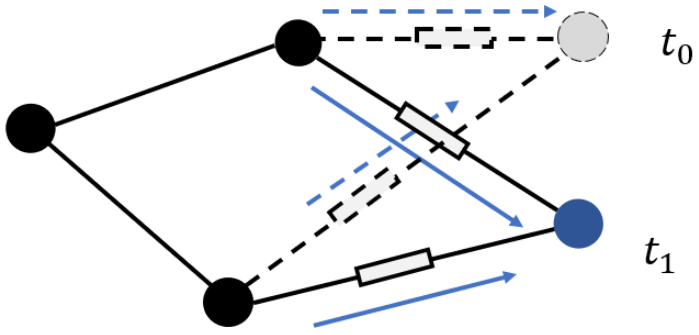

Figure 4-11 The Model based on the admittance matrix offers floating directions of conductivity and freedom of nodal positions.

The proposed model based on the nodal admittance matrix successfully avoids the limitation of requiring fixed nodal electrode positions and fixed boundary shape.

Unlike the FEM-based model, which must have clarified nodal coordinates prior to other parts of the reconstruction process, the model based on the nodal admittance matrix does not have any nodal coordinate information involved throughout the algorithm. The linkage between the nodes and the connecting elements is established during the formation of the nodal admittance matrix. The admittance of each element is assigned to a specific row and column that correspond to the nodes at both ends of that element. During material deformation, the nodes in the system are free to relocate without additional restrictions dictated by the FEM-based model. Therefore, for E-skins based on the new model, fixing the electrode positions and the boundary shapes of the sensing material is no longer needed. Strains can now be applied to any location on the sensor without hindering the model compatibility.

4.5.5 Effect of Measurement Noise

In order to examine the effect of measurement noise on the solutions estimated by the proposed reconstruction method, gaussian white noise was added to the input voltage data. Three levels of SNR, including 30 dB, 20 dB and 10 dB, equivalent to 0.1%, 1%, and 10% in linear scale, respectively, were assigned to the same voltage data calculated from the forward problem for the same randomly formed true admittance distribution. The results are shown in Figure 4-12. The true admittance distribution and the reconstructed solutions using noise-free voltage data are shown in (a) and (b), respectively; the solutions estimated using the 30 dB and 20 dB voltage data are shown in (c) and (d), respectively; and the solutions estimated using the 10 dB data at four different times are shown in (e)-(h). The Signal to Noise Ratio (SNR) for the solution was calculated by referencing the noisy solutions with respect to the noise-free solution. It can be seen that at 30 dB and 20 dB, the effect of noise on the solutions was

insignificant; however, at 10 dB, the added noise caused a significant impact on the reconstructed solutions.

Similar to the results previously obtained using the FEM-based reconstruction in section 3.5.5, the solutions obtained using the proposed method also showed uncertain perturbations at random locations due to the added noises. Although the elements assigned with peak admittance variations successfully retained their approximate magnitudes in the estimated solutions, measurement noise should be minimized to achieve the best estimations.

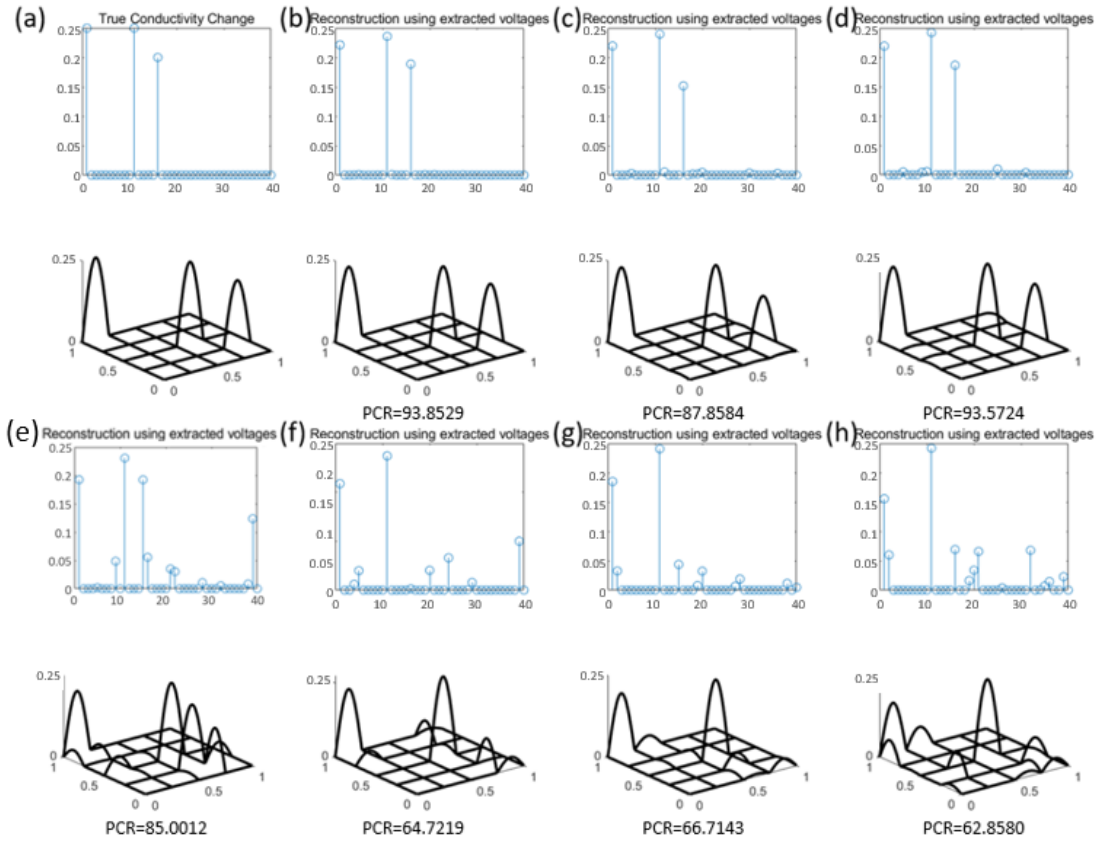

Figure 4-12 The effect of measurement noise on the reconstruction using the grid-network model. (a). the true solution. (b) The solution reconstructed using noise-free voltage data. (c) the solution reconstructed using the 30 dB voltage data. (d) the solution reconstructed using the 20 dB voltage data. (e)-(h) the solution reconstructed using the 10 dB voltage data.

4.5.6 Time Consumption

Further simulations were performed to examine the improvement of the proposed reconstruction method on the temporal resolution. The time consumptions for solving the forward problem, calculating the Jacobian matrix, and solving the inverse problem via different solvers were recorded individually. Grid network systems with dimensions ranging from 5 * 5 to 51 * 51 were tested.

The obtained results are shown in Table 8. It can be seen that the time spent on solving the forward problem was always less than 0.1 seconds for the systems of all sizes in the test. In addition, similar to the previous cases, the time required to calculate the Jacobian matrix increased exponentially as the dimension of the system increased. For the most straightforward 5 * 5 system, calculating the Jacobian matrix took less than 0.005 seconds. However, it took over 2 hours to determine the Jacobian matrix for the system with a size of 51 * 51. The time consumed by the inverse solvers, which plays a major role in determining the time resolution during real-time EIT reconstructions, was significantly shorter than the tested cases based on the FEM approach. In particular, the NNLS solver could obtain solutions within 0.02 seconds for networks of all the tested dimensions, suggesting this solver is more suitable for real-time imaging.

Dimensions of the grid network (rows * columns)	Time consumed by the forward solver	Time consumed for calculating the Jacobian matrix	Time consumed by the inverse solve				
			Pseudo inverse	Tikhonov	Noser	NNLS	BVLS ($0 \leq x \leq 1$)
5 * 5	0.00165 s	0.00485 s	0.00536 s	0.00319 s	0,00341 s	0.00482 s	0.0354 s
11 * 11	0.00194 s	1.776 s	0.0140 s	0.00896 s	0.00842 s	0.00925 s	0.174 s
21 * 21	0.0231 s	10.561 s	0.00925 s	0.0554 s	0.0367 s	0.00571 s	1.776 s
31 * 31	0.0469 s	166.352 s	0.0357 s	0.309 s	0.292 s	0.0130 s	13.372 s
41 * 41	0.0691 s	23 m 16 s	0.0281 s	1.319 s	1.204 s	0.0160 s	54.434 s
51 * 51	0.0929 s	2 h 23 m	0.0362 s	1.656 s	1.391 s	0.0182 s	65.217 s

Table 8 Time consumption for reconstructions performed using the grid network model

4.6 Limitations

Although the proposed reconstruction method effectively mitigated the critical defects possessed by conventional reconstruction methods, this method still suffers from several limitations.

The first limitation is that constraining the solution space does not entirely eliminate the ill-posedness of the system of equations that compose the inverse problem. Since the reconstruction process using the new method still seeks solutions from an underdetermined system, the method cannot always guarantee a reasonably accurate solution. There is a chance that the reconstruction performed for some scenarios results in solutions with a significant mismatch in an unpredictable manner. This problem is more frequently encountered when more admittance contrasts are introduced into the network, as shown in Figure 4-13, which demonstrates several examples of reconstructions that fail to generate reliable solutions. Therefore, the proposed reconstruction method is best-suited for realizing an E-skin that measures a small number of local strains rather than a sensor used for estimating its overall morphological deformation.

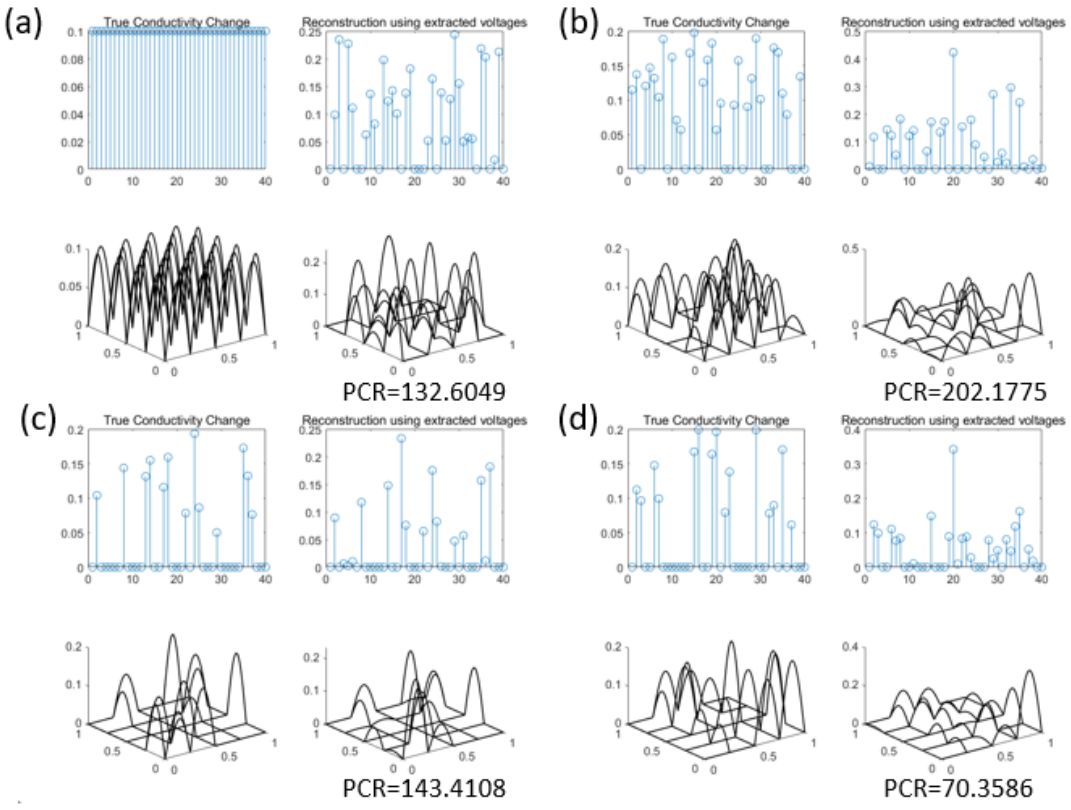

Figure 4-13 Examples of inaccurate reconstructions performed for various scenarios that involve a large number of admittance contrasts. (a) Admittance contrasts of a uniform magnitude are applied to all elements. (b) Admittance contrasts of random magnitudes are applied to all elements. (c) Admittance contrasts of random magnitudes are applied to some elements. (d) Admittance contrasts of random magnitudes are applied to some elements.

The second limitation is that the active-set algorithm adopted as a part of the inverse problem solver is only effective for reconstructing admittance variations whose magnitudes take a reasonably small portion of the background (i.e., baseline) admittance. The simulations performed previously in this chapter showed that, although the proposed method offered significantly better reconstruction accuracy (with a PCR generally greater than 80) than conventional reconstruction methods, a mismatch between the true solution and the reconstructed solution was still present. It is worth noting that, in these simulations, only admittance variations of less than 0.25 were assigned to elements in a network with a unity background admittance. For admittance variations that take a greater proportion of the background admittance, the mismatch of the reconstructed solution can be more significant. In Figure 4-14, this issue shows the results of simulations performed for reconstructing admittance

variations with a variety of magnitudes, including 0.01, 0.2, 0.5, and 0.8, for a network with a unity background admittance. The results indicate that the reconstructions that involve larger admittance variations lead to solutions with more errors and lower PCRs. The mismatch was also found related to the positioning and the number of admittance contrasts, making this issue challenging to overcome.

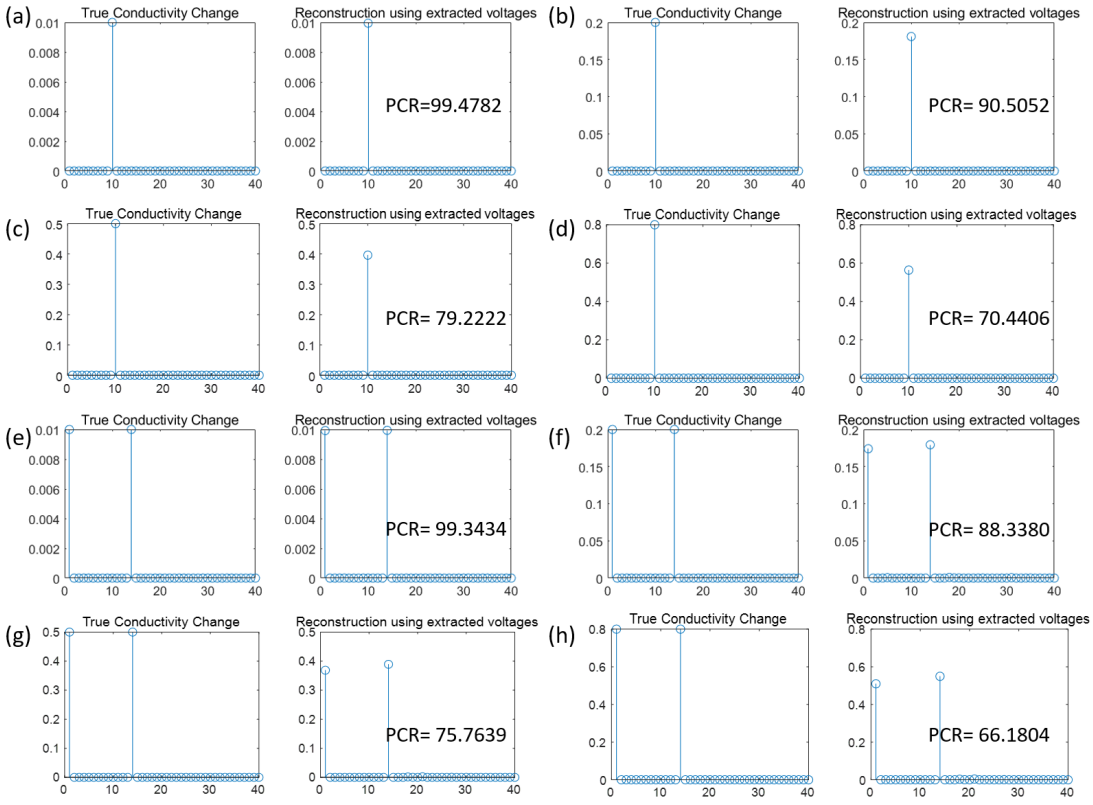

Figure 4-14 Examples of reconstructions performed for various scenarios that involve a variety of admittance variations. The baseline admittance of all elements is 1. (a) A single admittance variation of 0.01 at the 10th element. (b) A single admittance variation of 0.2 at the 10th element. (c) A single admittance variation of 0.5 at the 10th element. (d) A single admittance variation of 0.8 at the 10th element. (e) Two admittance variations of 0.01 at the 1st and the 14th element. (f) Two admittance variations of 0.2 at the 1st and the 14th element. (g) Two admittance variations of 0.5 at the 1st and the 14th element. (h) Two admittance variations of 0.8 at the 1st and the 14th element.

4.7 Conclusion

In this chapter, a new method was proposed to accommodate the critical limitations possessed by the conventional approach of implementing EIT on flexible sensors. The

proposed method combines a forward structural model derived from the nodal admittance matrix and a non-negativity constrained inverse solver. The new method was implemented using MATLAB, and a series of simulations were performed to examine its performance and reliability.

It was shown that the proposed method could effectively alleviate the limitations identified in the previous chapter. Compared to the conventional approach based on FEM and regularization, the grid-network model incorporated with the non-negative constraints offered consistent results independent of the types of regularizations used. The new method also greatly improved the low-resolution problem and allowed closely located individual strains to be successfully distinguished without evident interference. Additionally, the critical issue with the nonuniform sensitivity in the conventional approach became no longer noticeable in reconstructions performed using the new method. Multiple strains simultaneously applied to the boundary and the interior of the sensing material could be successfully estimated with a PCR close to 100.

Furthermore, the proposed model accepts the anisotropic conductivity of sensing materials and also supports electrode movement and boundary shape deformation. Therefore, the new model successfully resolved the material-model incompatibility issue possessed by the FEM-based approach. Apart from improving the accuracy in the reconstruction, the proposed method was able to produce reliable reconstructions under the presence of measurement noise when the signal to noise ratio was above 20dB. In addition, the proposed method was able to execute the inverse problem rapidly; hence it is promising for performing real-time reconstructions.

Compared to the conventional FEM-based approach used in previous studies, the proposed reconstruction method is a very promising alternative for realizing electronic skins that allow detecting and transducing spatially distributed strains.

Chapter 5 Material Characterization

5.1 Introduction

It was previously identified in Chapter 2 that, in addition to the error caused by the ill-posedness of EIT, the inconsistency in strain sensing materials constitutes another major source of errors in EIT-based electronic skins. To optimize the sensor accuracy, a material that provides consistent signal transduction is preferred to comprise the physical framework of an admittance network.

This chapter provides a comparative study between a sensor based on an ionic liquid and another sensor based on a hydrogel. First, the advantages and the weaknesses of various types of flexible strain sensors are briefly reviewed. Simple methods for fabricating the two types of sensors are introduced. Afterwards, a comprehensive set of experiments for examining their strain-sensing performance is introduced. The parameters tested for evaluating sensor performance include sensitivity, hysteresis, overshoot, dynamic stability, and long-term durability. The results obtained from experiments are compared and discussed. In the end, a material for realizing a strain-sensing electronic skin is determined based on the experimental results.

5.2 Material Selection

Previous studies discussed in the literature review showed that there is a wide range of methods for producing flexible strain sensors, which exhibit diverse characteristics. Piezoresistive sensors based on cracking of coated conductive particles possess considerably high sensitivity at the cost of suffering from significant hysteresis and overshoot. Piezoresistive sensors based on the disconnection of nanoparticle-

dispersion networks suffer from less severe defects than crack-based sensors. Both types of sensors possess poor signal consistency when used for sensing dynamic strain. For most application scenarios, strain is induced unpredictably; thus, these sensors lack reliability in practice.

Capacitive sensors have negligible hysteresis and overshoot and exhibit promising capability for sensing dynamic strains, but their capacitance values are too small to be precisely measured using portable instruments; thus, their suitability in practice is limited. It is also worth noting that integrating capacitive sensors with EIT is infeasible because their sensing mechanisms are not compatible with EIT.

Sensors based on room temperature liquid metals possess low hysteresis and overshoot, and their signals are consistent for sensing dynamic strains. However, due to their very high electrical conductivity, they must be embedded into long microfluid channels to enlarge their signal readings. Sensors based on ionic liquids behave similarly to sensors based on liquid metals. Because of their significantly lower electrical conductivity, they only require simple microfluid channels that can easily be fabricated. Sensors based on ionic hydrogels are remarkably more stretchable than other approaches and do not need fluid channels to maintain their physical morphology. Their strain sensing performance is similar to liquid-based sensors. Their main issue is that toxic chemicals are often involved during their fabrication.

A preferred material for constituting an EIT-based tactile sensor is selected from the above candidates by considering their compatibility with EIT and comparing their accuracy in transducing strain. The material should meet several criteria: it should possess the ability to transduce dynamic strains consistently; it should be able to transduce strain into its electrical resistance or impedance; it should be able to be patterned into a network layout that matches the proposed network model. Among the available candidates, only ionic liquids and hydrogels meet these criteria. Although liquid metals are also a promising choice, the considerably long and fine-featured microfluid channels required for enhancing their tiny signal readings raise challenges in fabrication and preventing leakage. In addition, only a few liquid-metal materials

are available for selection, such as EGaIn, Galinstan and mercury. Conversely, a wide range of materials can be used for ionic liquids and hydrogels, and many of them can be prepared using simple and low-cost methods. For example, an ionic liquid can be prepared by dissolving sodium chloride into water to form an electrically conductive solution. Therefore, a material for constituting a strain-sensing electronic skin is to be selected between ionic liquids and hydrogels. Experiments were conducted to examine and compare their strain-sensing performance.

5.3 Preparation of Strain Sensors

Sensors were fabricated by embedding the two types of sensing elements into linear fluid channels. For ionic liquid, a solution was prepared by dissolving sodium chloride (NaCl) into propylene glycol (PG). For hydrogel, gelatin was doped into a solution made of PG, deionized water and NaCl. These ingredients are non-toxic and can be used in food or as food additives. PG is a colourless and odourless liquid, and NaCl is an easily obtainable electrolyte commonly known as salt. Gelatin is a food-grade biopolymer extracted from the hydrolysis of animal collagen.

The fabrication procedures for the two sensors are illustrated in Figure 5-1. First, a polymer fluid channel for embedding the sensing medium was fabricated by a conventional moulding method. A plastic mould with a cuboid cavity was produced using 3D printing. A copper rod with a diameter of 1 mm was placed along its centreline. Ecoflex prepolymer was prepared by mixing part A and part B of the polymer (Ecoflex 00-20, Smooth-on) at a weight ratio of 1:1, followed by vigorously stirring. The prepolymer was cast into the mould and cured for four hours at room temperature at 15 °C. After the curing process was completed, the polymer was released from the mould, and the copper rod was removed, leaving an empty channel inside.

The ionic liquid was prepared by dissolving NaCl (ACS reagent, 99.0%, Sigma-Aldrich) in PG (USP grade, Pure Nature ltd, NZ) at a concentration of 5 grams of NaCl per litre of PG. The dissociation of NaCl into ions was accelerated using an ultrasonicator (VC-505, John-Morris Scientific, Australia). The output of the ultrasonicator was set to 20 kHz frequency and 40% of the maximum sonication amplitude that the device provides. The obtained solution was degassed using a vacuum chamber to remove the air bubbles formed during the preparation process. Two copper rods with a length of 4mm were then attached to both ends of the fluid channel to serve as the electrodes. The prepared ionic liquid was injected through the edge between the channel and electrode at one end using a needle syringe. The air inside the channel was pushed out through another syringe needle connected to the other end of the channel. The edges along the perimeters of the electrodes and the fluid channel were sealed using cyanoacrylate glue to prevent leakage.

The presolution for forming a hydrogel was prepared by dissolving NaCl (ACS reagent, 99.0%, Sigma-Aldrich), at a ratio of 5 grams per litre, into a binary liquid formed by PG (USP grade, Pure Nature ltd, NZ) and deionized water at a weight ratio of 1:1. The presolution was thoroughly mixed using a magnetic hotplate stirrer at a speed of 600 RPM and under a temperature of 90 °C for 5 minutes. Then gelatin (Nutra Organics, NSW, AU) was gradually added into the presolution till a weight percentage of 40% in the overall solution was reached. After continuous heating and stirring for 20 minutes, the solution was ready for cooling down to allow gelation. In order to prevent the hydrogel from scratching and contamination caused by the surroundings, the obtained prehydrogel solution was injected into the fluid channel using a syringe. After the hydrogel was settled for one hour to complete the gelation process, copper wires were pushed into the two ends of the channel to connect with the embedded hydrogel. The ends of the channel were then sealed with cyanoacrylate glue.

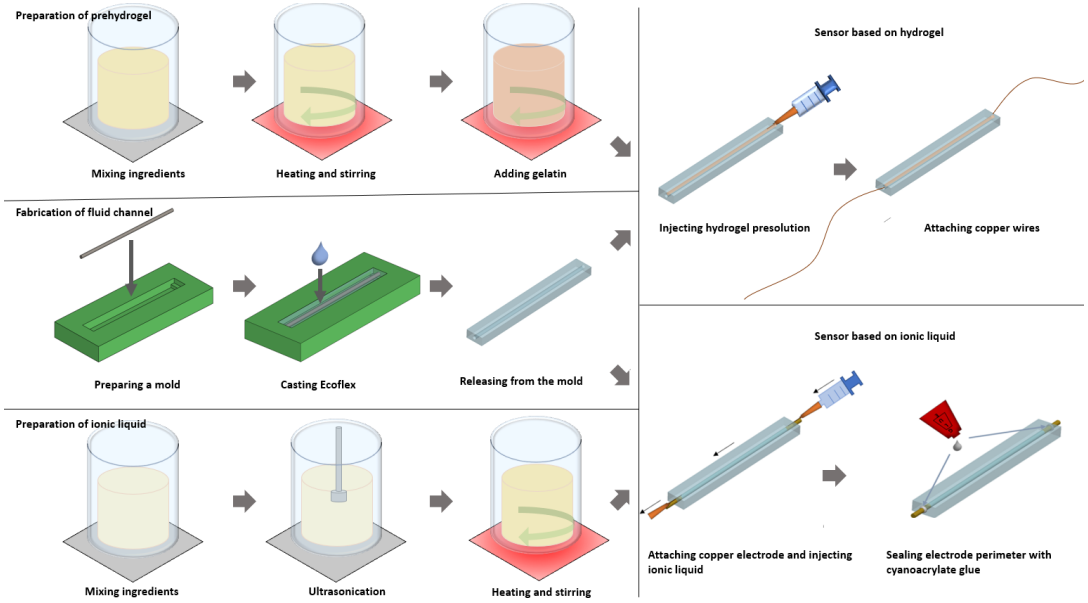

Figure 5-1 The fabrication procedure of the ionic liquid-based strain sensor and the hydrogel-based strain sensor.

5.4 Experiments

In order to evaluate the performance of the prepared sensors, the response of their electrical resistance to applied strains must be quantified. Two types of instruments were used to determine the response. One active instrument was required to precisely control the strain applied to the prepared sensors, and one passive instrument was required to record the variations in the electrical resistance of the sensors.

The experiment setup is shown in Figure 5-2. A TA.XT-plus Texture Analyser (Stable Micro Systems Ltd, UK) was utilized to induce strain with desired magnitudes. The device offers a high motion control resolution of 0.001 mm and a wide range of speed control between 0.01 and 40 mm/s. The two ends of the sensor under testing were mounted to the probes of the TA.XT-plus using two metal clips, which held the sensor in place stably during the operation. The magnitude of the strain imposed on the sensor was controlled through the Exponent software interface that accompanies the instrument.

An MFIA Impedance Analyzer (Zurich Instruments AG, Switzerland) was employed to record the electrical resistance of the sensor as the sensor was experiencing stretching and releasing. Through the LabOne software interface, the excitation signal voltage of MFIA was set to 300 mV, and the signal frequency was initially set to 1 kHz. The sensor under testing was connected to the MFIA through copper wires attached at both ends of the sensor. When a strain was applied to the sensor by the TA.XT-plus during each step, the real part of the sensor's impedance was recorded by the MFIA. The acquired data was exported to MATLAB for further processing.

The experiment was arranged in a few steps. First, the effect of excitation frequency was studied by recording the strain-resistance response of the sensors under several selected frequencies. Afterwards, cyclic loading tests were performed by applying strains to the sensors in a stretch-release manner to verify the repeatability of the signal in each measurement. From the acquired data, the hysteresis behaviour of the prepared sensors during each strain cycle was examined. Subsequently, repetitive stretch-and-hold tests were performed to examine the overshooting behaviour of the sensors. In the stretch-and-hold test, the prepared sensors were repetitively stretched to 100% strain at a strain rate of 100% per second and held at the maximum strain for 5 seconds before releasing them to zero strain at the same strain rate. In order to verify the dynamic stability of the prepared sensors, dynamic loading tests were conducted to examine the signal consistency by loading the sensor with strains of arbitrarily selected magnitudes. Finally, fatigue tests were performed to check the sensors' long-term signal stability and mechanical durability by letting them experience 10,000 cycles of strain with a 100% magnitude, applied at a strain rate of 100% /s. Apart from the stretching-and-hold test and the fatigue test, the strain rates used in other tests were set to 20% /s.

Figure 5-2 Experiment setup: a sensor was mounted to TA.XT-plus for receiving strain and was characterized by MFIA for its electrical response.

5.5 Results

5.5.1 Strain-Resistance Response Under Different Frequencies

Resistive strain sensors transduce applied strains into an electric signal, which typically has the form of a relative change in electrical resistance. The magnitude of the theoretical electrical resistance of a conductive material is determined by the material's resistivity, cross-sectional area, and length. When the excitation current is alternating current, the resistance also varies under different excitation frequencies. Therefore, it

is necessary to examine the performance of the prepared strain sensors under various frequencies.

The prepared sensors were stretched by the texture analyzer to a 100% strain, while their electrical resistance was measured by MFIA. Resistance measurements were repetitively performed under selected frequencies, including 0, 1, 5, 10, 15, 20, 100, 200, 300, 400 and 500 kHz. The obtained relations between electrical resistance and applied strains under these frequencies are shown in Figure 5-3.

The excitation frequency exhibited a notable effect on the two sensors' electrical response to the applied strains. For both sensors, increasing the frequency reduced their electrical resistance and led to decreased sensitivity. From calculations, it was found that the gauge factor of the hydrogel sensor was at the highest ($\mathrm{GF} = 1.61$) when the resistance of the sensor was measured using an excitation frequency of 1 kHz. Increasing the frequency to up to 100 kHz or changing it to DC resulted in a slight reduction in GF. When the frequency was further raised beyond 200 kHz, the reduction in GF became increasingly significant. For the signal acquired using a frequency of 500 kHz, a gauge factor of $\mathrm{GF} = 0.73$ was obtained.

On the other hand, the gauge factor of the ionic liquid-based sensor was found to be larger than that of the hydrogel sensor. A maximum gauge factor of $\mathrm{GF} = 6.19$ was obtained when the excitation frequency was DC. However, it was also found that the sensitivity of this sensor was more frequency-dependent than the hydrogel-based sensor. When the excitation frequency was successively reduced from DC to 20 kHz, a significant reduction in the gauge factor was observed. The gauge factor was reduced from 3.40 at 1 kHz to 0.997 at 20 kHz and was diminished beyond 20 kHz. In comparison, the hydrogel-based sensor exhibited a relatively more stable sensitivity for frequencies between 1 kHz and 100 kHz. Its reduction in sensitivity only became evident when the frequency further increased beyond 200 kHz.

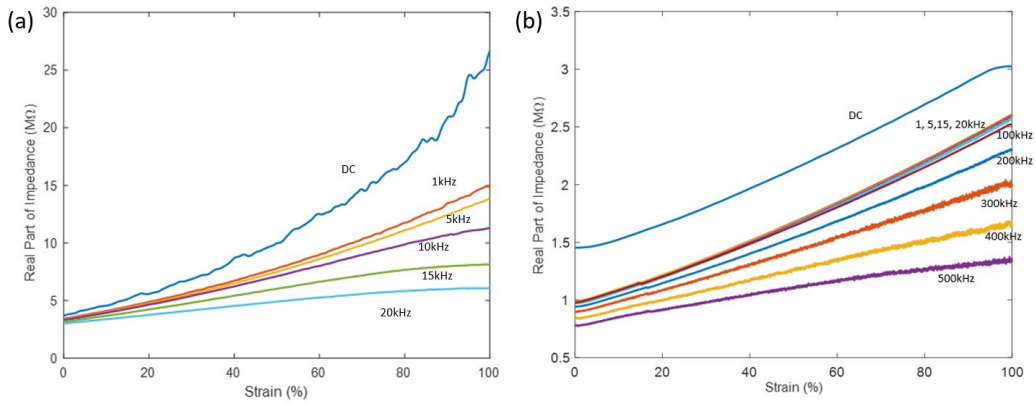

Figure 5-3 The relation between relative resistance variations and applied strain between 0 and 100%, under selected frequencies. (a) The sensor based on ionic liquids. (b) The sensor based on hydrogels.

5.5.2 Signal Repeatability and Hysteresis

A reliable strain sensor should produce consistent signals without significant mismatch when multiple strains are repetitively applied. The consistency of the prepared sensors was examined via cyclic loading tests. Using the texture analyzer, multiple strains with progressively increased magnitudes were applied to the sensors. Ten stretch-release cycles were implemented for each level of strain. Relative changes in the resistance of the prepared sensors were recorded under a default excitation current with a frequency of 1 kHz.

The obtained results for the ionic liquid sensor and the hydrogel sensor are shown in Figure 5-4(a) and (b), respectively. It can be seen that well-matched signals were acquired during all the ten stretch-release cycles at each strain level between 10% and 100%. These results indicated that both sensors possessed excellent signal repeatability for sensing cyclic strains.

Apart from signal repeatability, the hysteresis of the two sensors was also evaluated. Ideally, sensors with negligible hysteresis should output consistent signal readings when the same strains are applied in a different manner, i.e., stretching and releasing the sensor to the same strain should result in the same signal reading. The hysteresis of

the prepared sensor was examined by successively stretching and releasing the sensors at each strain level. The sensors were first gradually stretched to 10% before being released to the origin at the same speed. Then the same procedure was repeated for strains with magnitudes of 20%, 30%, etc., and up to a maximum of 100%. The relative changes in resistance of the sensor were recorded during the process.

The results obtained for the ionic liquid sensor and the hydrogel sensor are depicted in Figure 5-4(b), respectively. It can be observed that the signal produced by both sensors exhibited excellent consistency for each level of peak strains. The path of stretching and the path of releasing was well-matched with each other. In addition, during each stretch and release with progressively increased strains, the signals of both sensors did not show dependence on the strain history. This outcome indicates that both two sensors are promising for measuring cyclic strain with excellent consistency and negligible hysteresis.

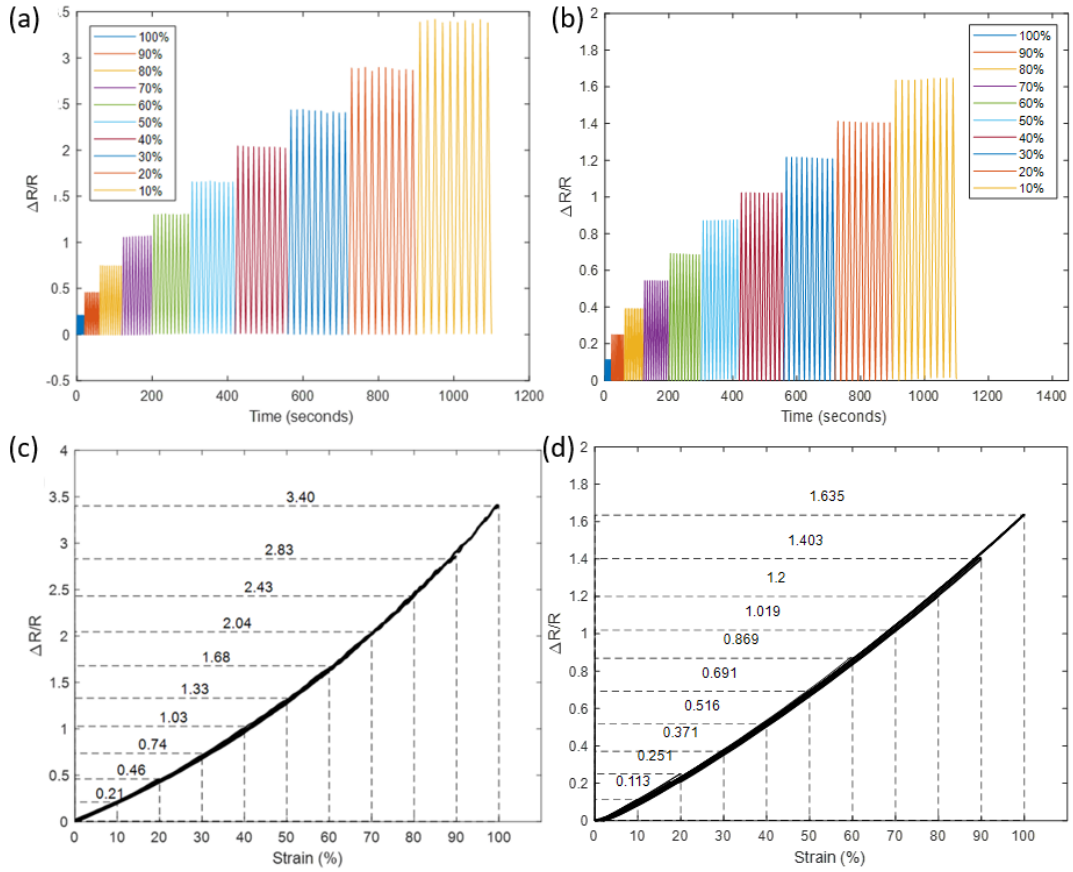

Figure 5-4 Relative change in resistance of the sensor. (a) The signal of the ionic liquid sensor during a cyclic loading test; (b) The signal of the hydrogel sensor during a cyclic loading test. (c) The signal of the ionic liquid sensor during a hysteresis test. (d) The signal of the hydrogel sensor during a hysteresis test.

5.5.3 Overshooting

Stretch-and-hold tests were performed to examine the overshooting behaviour of the prepared sensors. The prepared sensors were stretched to a strain of 100% and held in place statically for 5 seconds before they were released to zero strain. Because the strain rate, which describes the speed at which strains are applied, has a substantial impact on the severity of overshooting, a high strain rate of 100% /s was adopted for inducing the strains and deliberately causing more evident overshooting. A total of 10 stretch-and-

hold cycles were applied to the sensors while the electrical resistance of the sensors was recorded.

The obtained results for the ionic liquid-based sensor and the hydrogel-based sensor are shown in Figures 5-5 (a) and (b), respectively. It can be observed that, for both sensors, no visible overshooting occurred at each holding phase after the applied strain reached each local maximum. Both sensors produced precisely matched signals for all ten strain cycles, suggesting that they are overshooting-free and capable of accurately transducing strains applied at high speed.

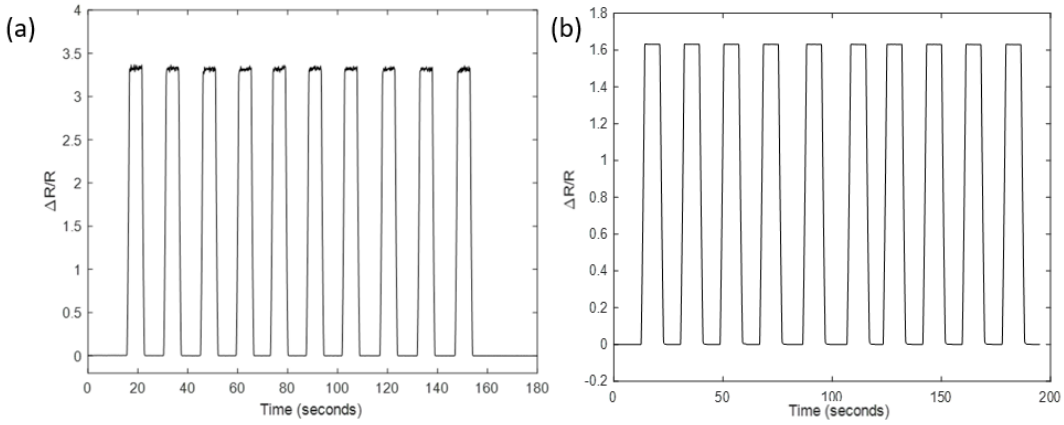

Figure 5-5 Signals corresponding to ten rapid stretch-and-hold cycles of 100% peak strain. (a) The ionic liquid-based sensor. (b) The hydrogel-based sensor.

5.5.4 Dynamic Stability

Although previously reported flexible strain sensors generally possess good signal repeatability during cyclic loading tests, they often exhibit considerable inconsistency in their signals when strains are not applied cyclically. As discussed in section 2.2.6, a significant signal mismatch is often observed when dynamic strains with changing magnitudes are measured. It is vital to examine the dynamic stability of the prepared sensors to ensure their reliable performance.

In this experiment, the performance of the prepared sensors was tested under a dynamic loading environment by applying a set of strains with arbitrarily selected magnitudes. Using the texture analyzer, arbitrary strains between 0 and 100% were applied to the sensors successively. The relative changes in the resistance of the sensors were recorded by MFIA.

The obtained results for the ionic liquid-based sensor and the hydrogel-based sensor are presented in Figure 5-6 (a) and (b), respectively. It can be seen that the signals produced by both sensors exhibited precisely matched magnitudes for the strains that had the same magnitudes, i.e., their signals were consistent when the applied strains reached 10%, 20%, 50% and 90%. In agreement with the earlier experiment, no overshooting was observed when each targeted strain was reached. The magnitudes of the signal obtained in this test were also closely matched with those previously obtained in the cyclic loading test. These results suggest that both sensors possess excellent dynamic stability.

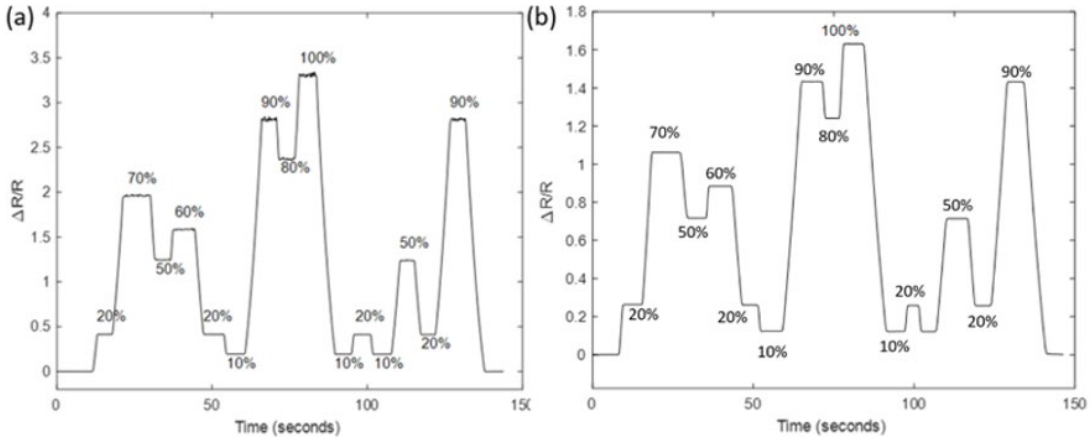

Figure 5-6 Signals in response to dynamically applied strain. (a) The ionic liquid-based sensor. (b) The prepared hydrogel-based sensor

5.5.5 Durability

The durability of a strain sensor indicates its ability to resist physical degradation and maintain its signal stability during continuous operation. Strain sensors require good durability to ensure that they can survive long-term and repetitive loading and unloading.

In this experiment, 10,000 cycles of continuous stretching and releasing were applied to the prepared sensors, with a peak strain of 100%. The strain rate of the texture analyzer was set to 100% /s for both the stretching phase and the releasing phase. The relative changes in the electrical resistance of the two sensors over 10,000 stretch-release cycles were continuously recorded by MFIA.

It was observed that, in terms of mechanical persistency, both sensors were able to recover their initial state after repetitive deformation throughout the process. No visible crack or tearing was observed in the hydrogel content. No leakage occurred in the sensor based on ionic liquid. In terms of the signal consistency, it can be seen from the result demonstrated in Figure 5-7 that the output signal produced by the ionic liquid-based sensor experienced a gradual reduction over the 10,000 cycles. The sensitivity of the sensor was also reduced from an initial value of 3.41 to 2.83 at the end. Notably, this shift in the signal was not permanent. After disconnecting the sensor from MFIA and allowing it to settle for a short period of 10 minutes, the sensor's signal was restored when the experiment was repeated. This phenomenon was possibly caused by the imbalanced electric charges accumulating at the interface between the ionic liquid and the copper electrodes, and the accumulation was gradually built up during the continuous excitation of MFIA. On the other hand, the signal recorded for the hydrogel sensor maintained good stability in both the base and the peak. After the 10,000 cycles, the sensor’s gauge factor was only slightly reduced from an initial value of 1.63 to a final value of 1.61,

These results indicate that both sensors possess excellent mechanical durability. The hydrogel-based sensor exhibited better signal consistency than the ionic liquid-based sensor. It was capable of consistently transducing cyclic strains applied in a large, rapid, and continuous manner. The ionic liquid-based sensor also exhibited an excellent signal response over the 10,000 cycles. Although a mismatch gradually developed in its signal, the mismatch was recoverable and could be possibly fixed by implementing other types of electrodes.

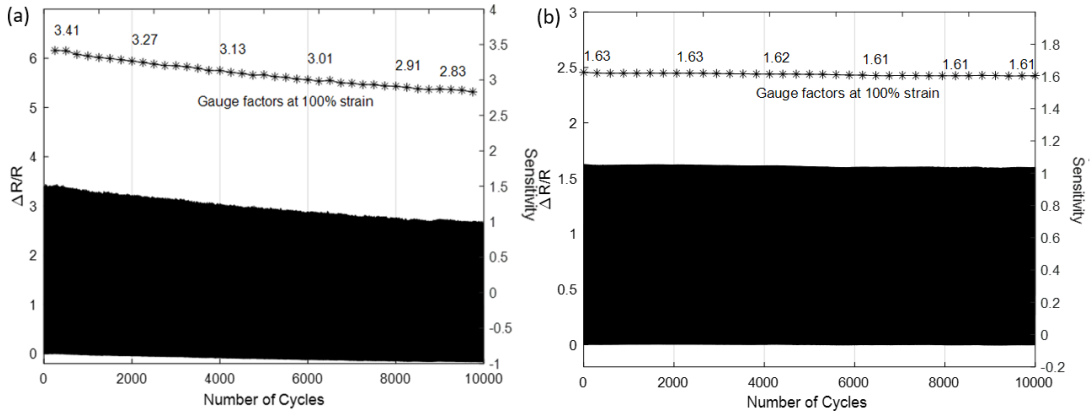

Figure 5-7 Relative change in resistance and corresponding gauge factors over 10,000 stretch-release cycles. (a) The prepared sensor based on ionic liquid. (b) The prepared sensor based on hydrogel.

5.6 Discussion and Conclusion

In summary, two types of flexible sensors were fabricated. A hydrogel-based strain sensor was prepared using a combination of gelatin, propylene glycol, deionized water and sodium chloride. An ionic liquid-based sensor was prepared by filling a fluid channel with a PG-NaCl solution. A variety of experiments were performed to examine the critical characteristics of the sensors that affect their reliability in performance, including measurement range, frequency response, hysteresis, overshoot, dynamic stability, and durability.

By comparison, it was found that the ionic liquid sensor possessed higher sensitivity than the hydrogel-based sensor. Both sensors exhibited excellent signal repeatability and consistency for transducing cyclic and dynamic strains, with negligible hysteresis. When strains were induced at 100% /s, no visible overshoot in the signal was present for both sensors. The hydrogel-based sensor maintained excellent mechanical durability and signal stability as it survived 10,000 cyclic loadings with a peak strain of 100%. The signal of the ionic liquid-based sensor was found to be less stable over an increased number of strain cycles, but the original signal was recoverable.

Both sensors are feasible candidates for strain-sensing electronic skin. In fact, they possess various characteristics in common. The performance of ionic liquids closely resembles that of ionic hydrogels. Essentially, their strain transduction mechanisms are the same, as they both rely on transporting charge-carrying ions within a conductive medium with varying electrical resistance depending on its geometrical deformation during stretching. The major difference between the two sensors is that ionic liquids must be embedded into a fluid channel to maintain their geometry, while hydrogels can function without additional mechanical support. The liquid component of a hydrogel, which offers electrical conductivity, is held by the hydrophilic polymer chains that maintain the gel structure. Therefore, using hydrogel for sensing strain can avoid the leakage issue commonly experienced by sensors based on ionic liquids. Another advantage of hydrogels is that they can be used to conveniently produce a crosstalk-free grid network for implementing the proposed EIT reconstruction method, formed by independent sensing elements, without a need for a sophisticated packaging process. In the case where a network is formed by liquid sensing elements, each node in the network must be accompanied by a soft electrode which prevents the liquid in each element from flowing into other elements. For a hydrogel network, each sensing element is confined in place due to the support offered by polymer chains; thus, the cross-talking issue is conveniently prevented.

On the basis of advantages that hydrogel-based sensors possess, including reliable transduction of dynamic strain, avoiding element-to-element cross-talking, ease of

leakage-free packaging, and good compatibility with the structure model of EIT, the hydrogel-based sensing approach was selected for realizing a strain-sensing electronic skin. The experimental results showed that the proposed method for preparing a cost-effective hydrogel material is reliable. In the next chapter, the same preparation method will be preserved as a part of the process for fabricating a strain sensor network.

Chapter 6 Realizing Electronic Skins

6.1 Introduction

In previous chapters, the EIT-based sensors' defects associated with both reconstruction algorithms and strain-sensing materials were effectively resolved. A new reconstruction method was proposed and verified by a simulation study, and a hydrogel-based strain sensing element was fabricated and confirmed by experiments. In this chapter, the proposed reconstruction method and hydrogel-based sensing material are integrated to constitute an EIT-based strain-sensing electronic skin.

This chapter first presents a hardware system that allows capturing the input data to the reconstruction algorithm. Then a preliminary test for confirming the effectiveness of employing the hardware to implement the proposed reconstruction method is demonstrated. Afterwards, a novel method for patterning hydrogel into a grid-network layout is introduced. EIT reconstructions are enabled by connecting the patterned hydrogel sensor with the data acquisition hardware. Finally, the performance of the electronic skin for sensing strain distribution is validated and discussed.

6.2 Design of EIT Circuitry and Hardware

A hardware system was developed to collect the input voltage data required for performing EIT reconstruction. The system consisted of three essential functional elements, including a current injector, a pair of multiplexers and an analog-to-digital converter (ADC). The current injector was responsible for producing and maintaining a constant excitation current, such that an electric potential distribution was generated in the strain-sensing material. The multiplexers were used to control the switching on

and off for each channel, through which the current was injected into the sensing material or sunk into the ground. The ADC was used to measure the differential voltages between each channel and a selected reference point during each instance of the current injection. The recorded voltage data was transmitted to a computer for further processing and performing reconstructions.

6.2.1 Current Source

A Howland current circuit was utilized for maintaining a constant current. A Howland circuit is a voltage-controlled current source, i.e., its current output depends on its voltage input. The circuit is widely used in the measurement field and can produce a constant current for a wide range of load values[236]. A schematic of the Howland circuit is depicted in Figure 6-1. The circuit is formed by four resistors and an operational amplifier. The input voltage is denoted as V_{in}, and the output voltage of the amplifier is denoted as V_{out}. A load that receives the constant current is connected to the non-inverting terminal of the amplifier, between R_3 and R_4. It is worth noting the polarity between V_{in} and the ground connected to R_1 is reversible, and therefore, the direction of the produced constant current in R_{load} is also reversible

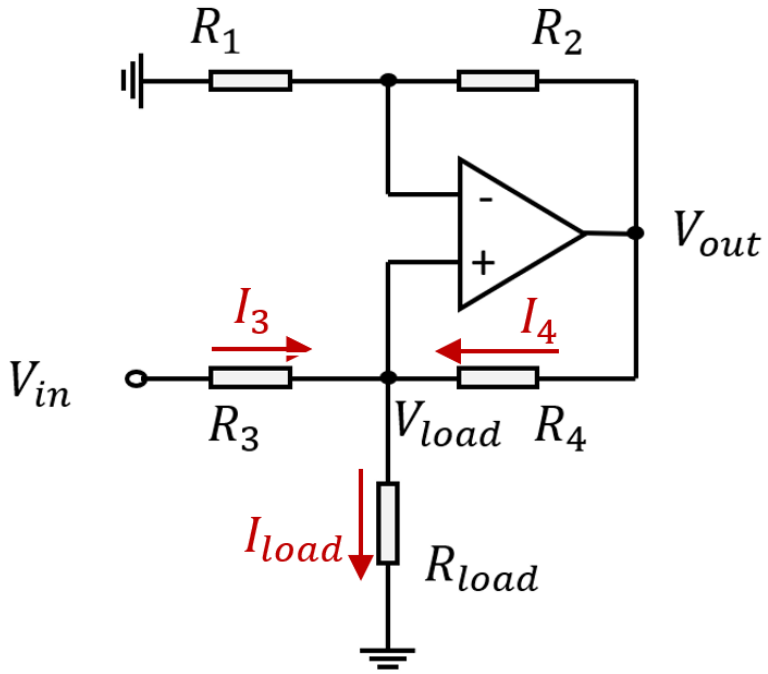

Figure 6-1 Howland current source circuit

The relation between the expected magnitude of the output current through the load, denoted by I_{load}, and the input voltage, V_{in}, can be determined using a set of derivations. According to Kirchhoff's current law, the total current flowing into and out of a node must be zero. Therefore, the following relation exists for the node between R_3 and R_4:

$$I_{load} = I_3 + I_4 \tag{6-1}$$

According to Ohm's law, equation 6-1 can be reformed as

$$I_{load} = \frac{V_{in} - V_{load}}{R_3} + \frac{V_{out} - V_{load}}{R_4} \tag{6-2}$$

Because R_1 and R_2 form a non-inverting amplifier, the following relation exists:

$$V_{out} = V_{load}\left(1 + \frac{R_2}{R_1}\right) \tag{6-3}$$

Equation 6-3 is substituted into equation 6-2 to obtain

$$I_{load} = \frac{V_{in} - V_{load}}{R_3} + \frac{V_{load}\left(1 + \frac{R_2}{R_1}\right) - V_{load}}{R_4} \quad 6\text{-}4$$

Then the equation is reformulated to separate V_{in} and V_{load}. i.e.,

$$I_{load} = \frac{V_{in} - V_{load}}{R_3} + \frac{R_2}{R_1 R_4} V_{load} \quad 6\text{-}5$$

$$I_{load} = \frac{V_{in}}{R_3} - \frac{V_{load}}{R_3} + \frac{R_2}{R_1 R_4} V_{load} \quad 6\text{-}6$$

$$I_{load} = \frac{V_{in}}{R_3} - \left(\frac{1}{R_3} + \frac{R_2}{R_1 R_4}\right) V_{load} \quad 6\text{-}7$$

$$I_{load} = \frac{V_{in}}{R_3} - \left(\frac{R_1 R_4 - R_2 R_3}{R_1 R_3 R_4}\right) V_{load} \quad 6\text{-}8$$

To ensure that I_{load} is independent on V_{load}, equation 6-8 is further reformulated as

$$I_{load} = \frac{V_{in}}{R_3} - \left(\frac{\frac{R_4}{R_3} - \frac{R_2}{R_1}}{R_4}\right) V_{load} \quad 6\text{-}9$$

Therefore, the independence of I_{load} on V_{load} can be guaranteed when the following condition is satisfied:

$$\frac{R_4}{R_3} = \frac{R_2}{R_1} \quad 6\text{-}10$$

When equation 6-10 is satisfied, the magnitude of the resulting constant current is equal to

$$I_{load} = \frac{V_{in}}{R_3} \quad 6\text{-}11$$

One important factor to consider is the maximum output voltage swing that a real operational amplifier can provide. A voltage swing is the voltage range that an amplifier can actually deliver at its output junction. Unlike an ideal amplifier which is always able to fulfil the output voltage described by equation 6-3, a real amplifier inevitably has an upper bound on V_{out}, which is limited by its power supply. For example, as a commonly used op-amp, LM358 can only provide an output of up to

3.5 V under a 5 V power supply. With the presence of the limitation in V_{out}, the maximum magnitude of V_{load} can be calculated by the reversed form of equation 6-3, expressed as

$$V_{load} = \frac{R_1}{R_1 + R_2} V_{out} \tag{6-12}$$

In the case where $R_1 = R_2$, the voltage across the load is 1.75 V, which is half of the maximum output voltage swing of the op-amp. If the objective is to maintain a constant current of 1 mA through the load, the maximum load resistance should not exceed 1.75 kΩ. If the resistance of the load increases beyond this value, the current that flows through it will lose its consistency and decrease accordingly to satisfy Ohm's law.

In addition to the characteristics of operation amplifiers, another consideration is the tolerance of resistors. A constant current can only be ensured if the relation described by equation 6-10 is precisely satisfied. However, real resistors always have some tolerance. For instance, if the four resistors are expected to possess the same resistance value, but R_2 and R_3 have 95% of the nominal resistance, and R_1 and R_4 have 105%, the current produced by the circuit can be calculated as

$$|I_{load}| = \frac{V_{in}}{0.95R_3} - \left(\frac{\frac{1.05R_4}{0.95R_3} - \frac{0.95R_2}{1.05R_1}}{1.05R_4} \right) V_{load} \tag{6-13}$$

$$= 1.0526 \frac{V_{in}}{R_3} - \frac{1.0526 \frac{R_4}{R_3} - 0.861 \frac{R_2}{R_1}}{R_4} V_{load}$$

This result shows that the current flowing through the load is partially dependent on V_{out}. It cannot maintain a precisely constant value under a changing load. Therefore, the precision of the resistors must be considered to ensure the precision of the output current.

6.2.2 Multiplexers

The current produced by the Howland circuit was injected into the sensing material and sunk to ground through a pair of multiplexers. A multiplexer is a multi-channel switch that allows one input signal to be selected from several input signals and transmits the selected input into a single medium. A bi-directional multiplexer allows current flow in both directions, i.e., current can flow from one of several input channels to a single output channel; it can also flow from the output channel to a selected input channel. EIT uses multichannel multiplexers to enable the switching of current injection patterns. The switching on and off for each channel in a multiplexer is controlled by its address pins. Address pins are digital pins that can be set to either a high or low voltage level. By controlling the logic level of digital pins according to the truth table of the multiplexer, the connection between one of the input channels and the single output channel is shifted.

MAX336 was selected for controlling the switching of current injection patterns. MAX336 is a 16-channel, bidirectional and low-leakage multiplexer. This device offers several features that suit the need for precision data acquisition for EIT. For example, it works on a wide range of power supplies between 4.5 V and 30 V, offers electrostatic charge protection for over 2000 V, and possesses a low off leakage current of less than 20 pA. Its bi-directional current signal handling offers flexibility in realizing current injection patterns. In addition, it offers a short transition time of fewer than 500 ns, which makes it suitable for rapidly switching current injection patterns.

Two MAX336 were utilized in this EIT data accusation system. The output pin (i.e., the common pin) of the first device was connected to the output channel of the Howland circuit to receive the constant current and redirect the current to a selected input pin. The output of the second device was connected to the negative (ground) terminal of the Howland circuit, such that the current received from a selected input pin was sunk to ground through the output pin.

6.2.3 Analog to Digital Converters

When the constant current produced by the Howland circuit is injected into the sensing material following a current injection pattern controlled by MAX336, an electric potential distribution is generated over the material. The differential voltages between different electrodes attached to the material and a reference point are required as the input data for performing EIT reconstructions. A multichannel ADC that allows differential voltage measurement is compulsory to obtain the required data. An ADC with a high data resolution and a fast sampling rate is preferred to ensure accuracy and speed of measurement.

ADS1115 was selected for performing voltage measurement. ADS1115 is a precision ADC that offers two differential input channels. Multiple ADS1115 can be concatenated together to increase the number of differential input channels to up to 8. The device requires a low power supply between 2 V and 5.5 V. It provides a sampling rate of up to 860 samples per second (SPS). The 16-bit resolution and the embedded programmable gain controller allows accurate voltage measurement with a customizable resolution between 187.5 μV and 7.8 μV. The measured voltage data can be transmitted to a computer using the I2C protocol.

6.2.4 Overall System

An EIT system was developed by integrating the Howland circuit, multiplexers, ADS1115 and miscellaneous components. The block diagram of the developed system is illustrated in Figure 6-2. The complete circuit diagram of the system can be found in appendix A. This system was implemented on a two-layer printed circuit board (PCB).

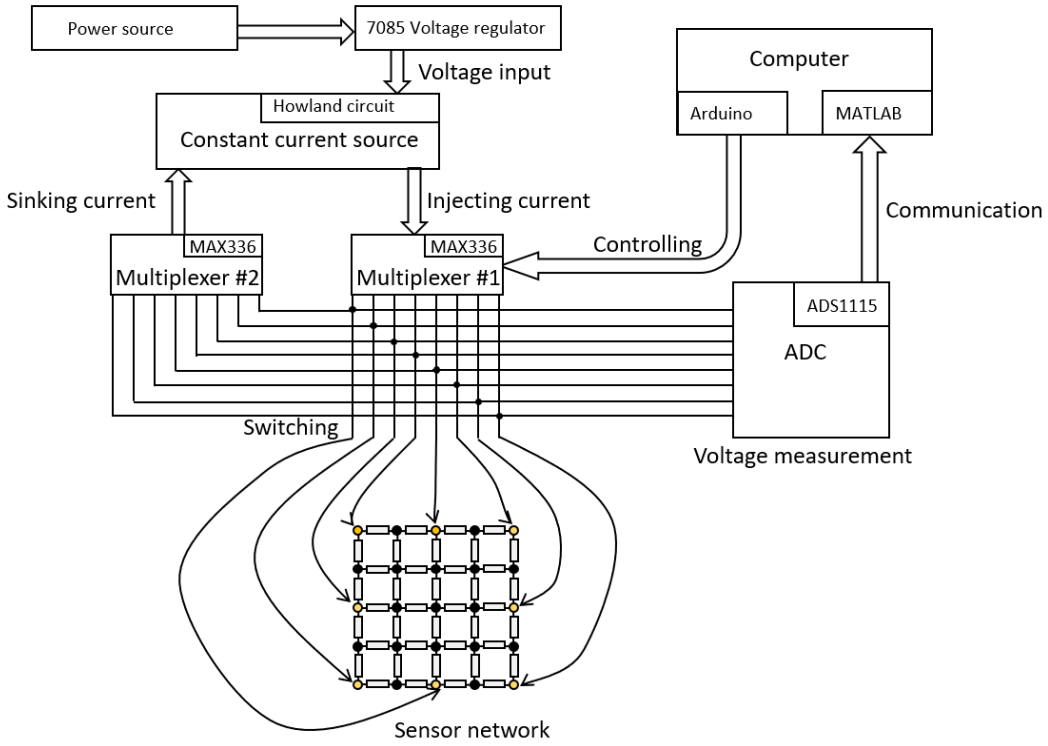

Figure 6-2 The block diagram of the developed EIT system

In this system, a voltage regulator (LM7805) was used to produce a stable 5 V electrical potential. The 5 V was varied using a voltage divider circuit that connected one fixed-valued resistor and one potentiometer in series. The voltage received by the Howland circuit could be controlled by shifting the resistance value of the potentiometer. Four ADS1115 were concatenated to enable differential voltage measurement through 8 separate channels. The reference channel of all ADS1115 was connected to a selected node in the anticipated sensor network, in accordance with the settings in the forward solver. The pins of MAX336 and ADS1115 were connected to each vertex and midpoint along the boundary of the anticipated sensor network. A microcontroller (Arduino Mega) was used for controlling the digital address pins for MAX336. The microcontroller was also responsible for receiving the voltage data transferred from ADS1115 via the I2C communication protocol. The received data was transferred to a computer via a USB connection. Finally, MATLAB was used to process the data, solve the inverse problem, and display the reconstructed results.

Although an alternating current is required for exciting hydrogel-based sensors that possess ionic conductivity, it is feasible to continuously apply DC excitation for hydrogels during the implementation of EIT without causing considerable electrode charge separation. EIT involves repetitive polarity shifting during the rapid switching of the current injection patterns. Suppose a direct current is injected, and each current injection only lasts a short period before the polarity is reversed; the direct current then behaves in the same way as a square-wave AC[159], provided that the polarity is switched swiftly and evenly. The polarity switching is readily achieved using the multiplexers that control the current injection patterns.

6.3 Preliminary Testing

6.3.1 Resistor Network

Prior to implementing a hydrogel sensor network, a preliminary test was performed to verify the confirm the reliability of the hardware system and the effectiveness of the proposed algorithm. In the preliminary testing, a resistor network was constructed by connecting a number of resistors together into a grid pattern. The schematic and the physical structure of the resistor network are illustrated in Figure 6-3. Each pair of adjacent resistors were soldered together using a soldering iron. An initial resistance value of 1 MΩ was selected for all the resistors. The nodes at vertices and midpoints along the boundary were connected with the analog pins of ADS1115 for voltage measurement.

Reconstructions were then performed via the adjacent current injection pattern. First, an initial set of voltages were measured and recorded as the reference voltage data. To mimic the scenario where a sensing element is stretched, a resistance change at one of the resistors was induced by swapping the resistor with another resistor that possessed a larger resistance value. After swapping the resistors, a new set of voltages were

measured, and the voltage variation data was calculated with respect to the initially acquired reference voltage data. The inverse solver reconstructed resistance variations by taking the voltage variation data as the input. The results were calibrated and compared with the actual variations.

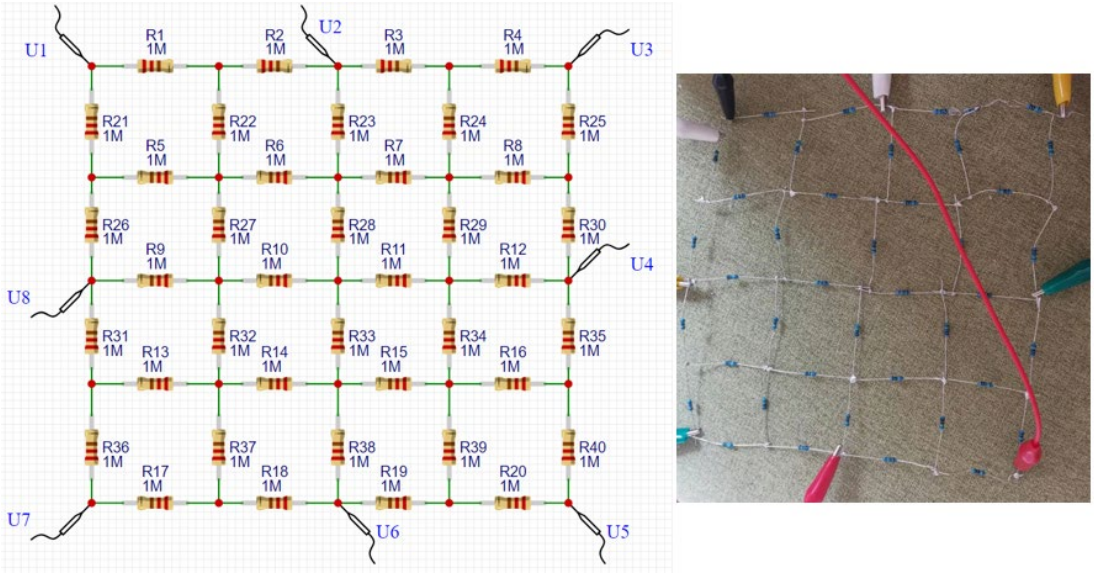

Figure 6-3 A schematic of the resistor network used in preliminary testing, along with its physical structure.

6.3.2 Model Calibration

When the admittance value of the physically implemented network is not matched with that of the model, a calibration for the inverse solver is required to ensure accuracy in terms of the scaling of reconstructed solutions. By default, the forward model utilizes a unity magnitude of admittances to predict the forward solutions. Because the inverse solver is derived from the forward model, in the mapping function (i.e., the Jacobian matrix) of the inverse solver, the weightings at which the electrode voltages are mapped towards element-wise admittance variations are determined based on this unity magnitude. Therefore, the reference admittance values taken for constructing the forward model have an impact on the scaling of the reconstructed solutions. Simulation results that demonstrate this calibration issue are shown in Figure 6-4. It was found that

the reconstructed solution is the squared ratio of mismatch times larger than the true solutions. For instance, as demonstrated in Figure 6-4(e), when a sensor network with an admittance distribution of 100 was reconstructed using a model derived from a unity reference admittance distribution, the reconstructed solution is 10000 times the true solution. For physical sensor networks that possess an initial admittance distribution that is unmatched by that of the forward model, the obtained solutions should be calibrated using

$$x = x_0 \left(\frac{C_{real}}{C_{model}} \right)^2 \tag{6-14}$$

where x_0 is the reconstructed solution before calibration, C_{real} denotes the admittance data of the implemented physical sensor network, and C_{model} represents the reference admittance data used by the forward model.

In addition to the reference admittance distribution, the magnitude of the current injection is another user-defined input parameter that should also be calibrated. By default, the magnitude of the current injection utilized in the forward solver is unity. For instance, when a current with a magnitude of ten times unity is implemented in a forward solver derived based on unity current injection, the resulted voltage variation is ten times larger, and the reconstructed solutions are also ten times larger. Therefore, when the physically injected current possesses a magnitude different from the current utilized in the forward model, the obtained solution should be calibrated by

$$x = x_0 \frac{I_{model}}{I_{real}} \tag{6-15}$$

where I_{real} denotes the magnitude of the physically injected current, and I_{model} represents the magnitude of the injected current adopted by the forward model. When calibrations for both reference admittance distribution and the magnitude of current injection are required, equation 6-14 and equation 6-15 are concatenated, such that calibrated solutions are obtained by

$$x = x_0 \frac{I_{model}}{I_{real}} \left(\frac{C_{real}}{C_{model}} \right)^2 \qquad 6\text{-}16$$

The ratios of calibration described by equation 6-17 can be explained by equation 4-14, which was previously discussed in section 4.3. It can be seen from that equation that the Jacobian matrix is derived by a set of multiplications that involve the admittance matrix, Y, and the current injection pattern, I. The admittance matrix is a summation of element-wise admittances. Among the four multiplication terms, two terms are the inverse of Y, one term is I itself, and the other is the derivative of Y with respect to C, which is essentially a summation of unities. When a mismatch in C between the model input and the reality is present, the ratio of the mismatch is inversed and multiplied twice when it is introduced into H. When a mismatch in I between the model input and the reality is present, the ratio of the mismatch introduced into H remains the same as in I.

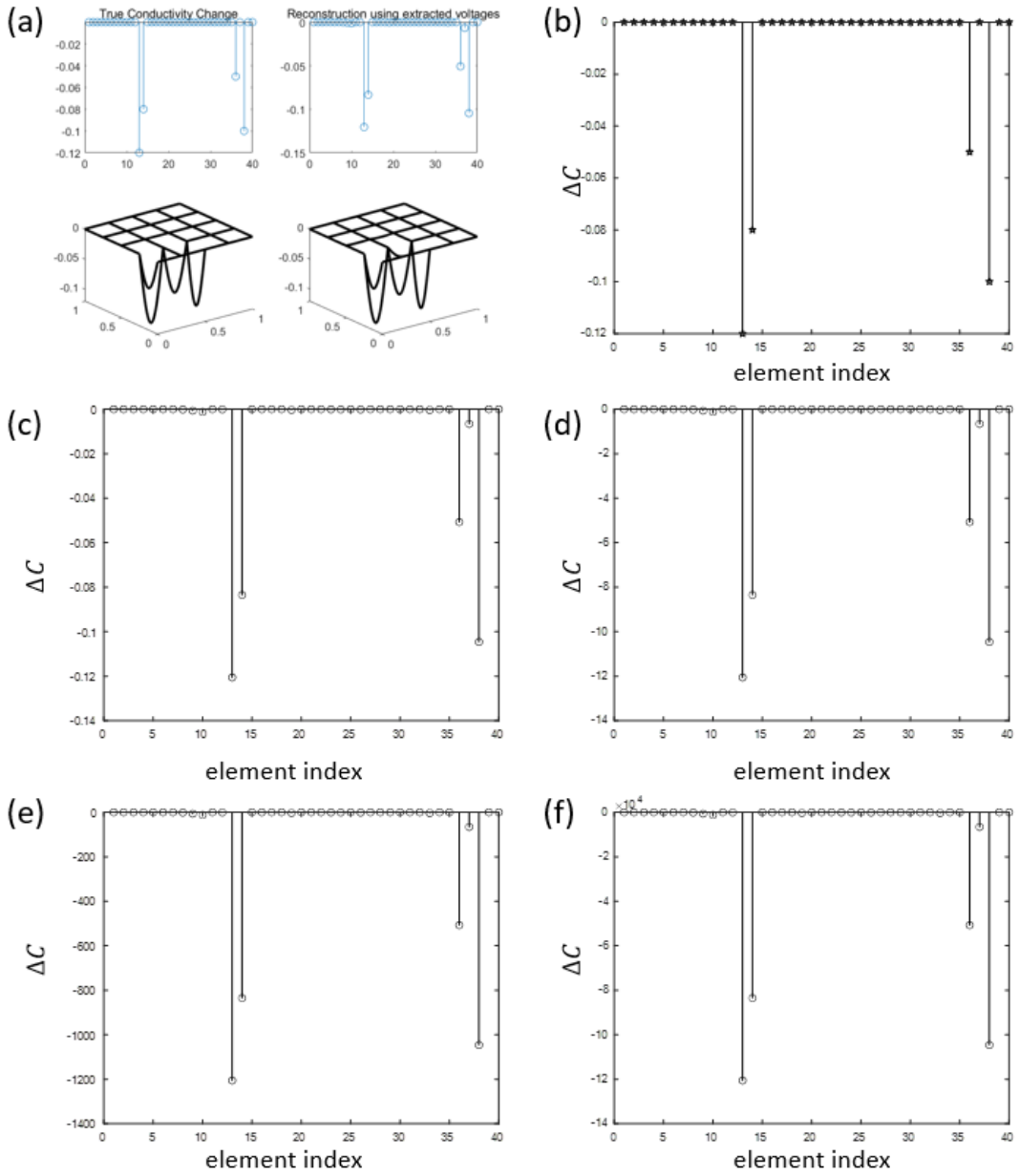

Figure 6-4 Calibration for the inverse solver. (a) Reconstruction for a random admittance variation distribution. (b) The true admittance variation of each element. (c) Reconstructed solutions were matched when the inverse solver was derived from a forward model with a unity admittance distribution. (d) Reconstructed solutions were 100 times the true solutions when the inverse solver was derived from a forward model, which had an admittance distribution with a magnitude of 10. (e) Reconstructed solutions were 10000 times the true solutions when the inverse solver was derived from a forward model with an admittance distribution with a magnitude of 100. (f) Reconstructed solutions were 1000000 times the true solutions when the inverse solver was derived from a forward model with an admittance distribution with a magnitude of 1000.

6.3.3 Test Results

The ability of the system to reconstruct the admittance variation of a single element was tested. An electrode voltage data variation was recorded by replacing the 1 MΩ resistor at the 4th element (denoted as R4 in Figure 6-3) with a 1.1 MΩ resistor. The inverse solver then utilized the voltage data for reconstructing the change in the conductance of the 4th element. In this case, a resistance variation from 1 MΩ to 1.1 MΩ was equivalent to a conductance variation from 1×10^{-6} S to 9.09×10^{-7} S; i.e., the magnitude of conductance variation of the 4th element was $\Delta C_4 = 9.1 \times 10^{-8}$ S. Therefore, a solution of $\Delta C_4 = 9.1 \times 10^{-8}$ S was expected from the reconstructed results. The obtained results are shown in Figure 6-5(a). In order to clearly distinguish the experimental results from the simulation results, a different style of display for presenting the solutions was utilized. It can be seen that a conductance variation of around 9.1×10^{-8} S was successfully reconstructed for the 4th element.

A similar test was also performed to reconstruct other resistance variation values at different elements. In (b), the 1 MΩ resistor at the 7th element (R7) was replaced with a 1.15 MΩ resistor. In this case, the conductance of R7 varied from 1×10^{-6} S to 8.70×10^{-7} S; thus, a conductance variation of $\Delta C_7 = 1.30 \times 10^{-7}$ S was expected in the reconstructed solutions. The obtained results showed that this value was also successfully estimated with a slight deviation. Another example is shown in (c), where the 1 MΩ resistor at the 33rd element (R33) was replaced with a 1.05 MΩ resistor. The conductance of R33 varied from 1×10^{-6} S to 9.52×10^{-7} S for a net change of $\Delta C_{33} = 4.76 \times 10^{-8}$ S. The estimation for this conductance change was successfully achieved.

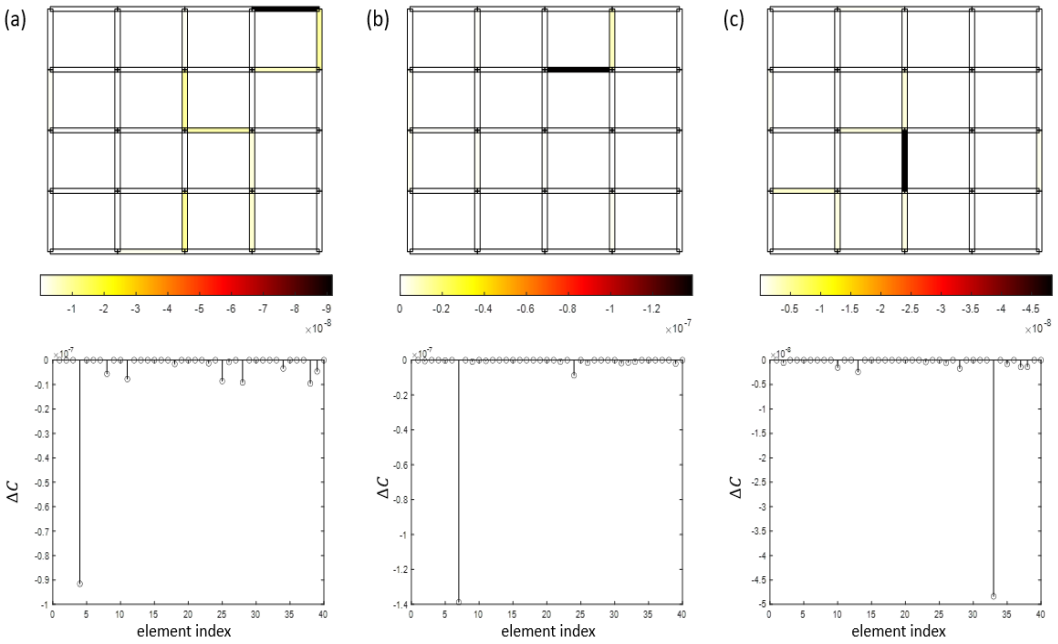

Figure 6-5 Reconstruction for a resistor network. (a) Reconstructing an admittance contrast of 9.1×10^{-8} S applied to R4. (b) Reconstructing an admittance contrast of 1.30×10^{-7}S applied to R7. (c) Reconstructing an admittance contrast of 4.76×10^{-8} S applied to R33.

Next, multiple resistance variations were simultaneously induced at different elements to verify the system's ability to mitigate the defect of boundary sensitivity dominance. In Figure 6-6(a), the 1 MΩ resistors at both the 4th element (R4) and the 11th element (R11) were replaced with 1.1 MΩ resistors. Conductance variations of $\Delta C_4 = \Delta C_{11} = 9.1 \times 10^{-8}$ S were expected from the reconstruction. Notably, the 4th element was close to the boundary where the sensitivity was higher than the interior, and the 11th element was at the centre where the sensitivity was poor. The reconstructed solutions showed that conductance variations for both elements were successfully estimated with only a minor deviation. No visible attenuation in magnitude was observed on the 11th element, indicating the problem of boundary sensitivity dominance was effectively mitigated. This mitigation was further tested by introducing more resistance perturbations into the resistor network. As shown in Figure 6-6(b) and (c), by replacing more 1 MΩ resistors with 1.1 MΩ resistors, additional resistance variations were applied to the 40th element in (b) and both the 40th element and the 26th element in (c). In both cases, the induced conductance variations were successfully reconstructed with

only minor errors. The conductance variation at the inner 11th element was well preserved without noticeable attenuation caused by the presence of boundary perturbations.

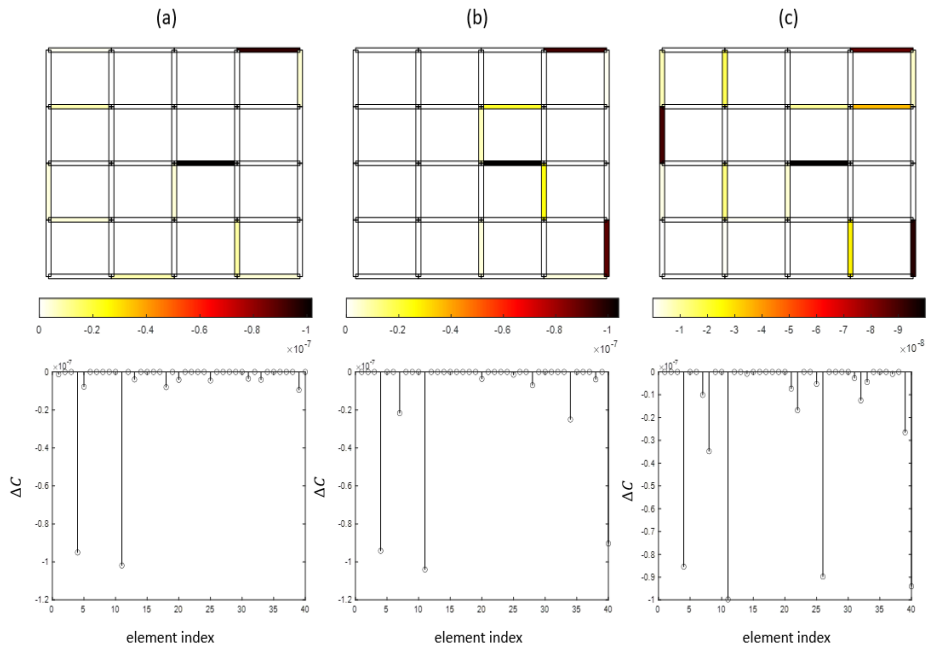

Figure 6-6 Reconstruction for a resistor network for checking the mitigation to the problem of boundary sensitivity dominance. (a) Reconstructing two contrasts in a resistor network. (b) Reconstructing three contrasts in a resistor network. (c) Reconstructing four contrasts in a resistor network.

Finally, in order to verify the capability of the system to accommodate the limitation of poor spatial resolution, multiple resistance variations were induced at adjacent elements. In Figure 6-7(a), the 1 MΩ resistors at both the 4th element (R4) and the 30th element (R30) were replaced with 1.1 MΩ resistors. Conductance variations of $\Delta C_4 = \Delta C_{30} = 9.1 \times 10^{-8}$ S were expected from the reconstructed results, and no significant interference should be introduced to the 25th element (R25) and 8th element (R8), which were between R4 and R30. The reconstructed solutions demonstrated that the expected outcome was successfully realized. The magnitudes of the obtained solutions for R4 and R30 were closely matched to reality. Both R25 and R8 were estimated as having negligible conductance variation. The experiment was also repeated for several other settings. In (b), both resistors at the 28th element (R28) and the 29th element (R29) were

replaced with 1.1 MΩ resistors. In this case, both resistors were located near the centre where the sensitivity was relatively poorer than the boundary elements. The reconstruction successfully achieved the expected outcome. In (c), the 1.1 MΩ resistors at the 10^{th} element (R10) and the 11^{th} element (R11) were replaced with resistors of different resistance values. A 1.05 MΩ resistor was imposed for R10, and a 1.15 MΩ resistor was imposed for R11. Therefore, a solution of $\Delta C_{10} = 4.76 \times 10^{-8}$ S was expected for R10 and $\Delta C_{11} = 1.30 \times 10^{-8}$ S was expected for R11. The reconstructed solutions showed that the two expected conductance variations were successfully obtained with a minor mismatch, and no interference was observed at other neighbouring elements. These results confirmed that the limitation associated with the poor spatial resolution was effectively accommodated.

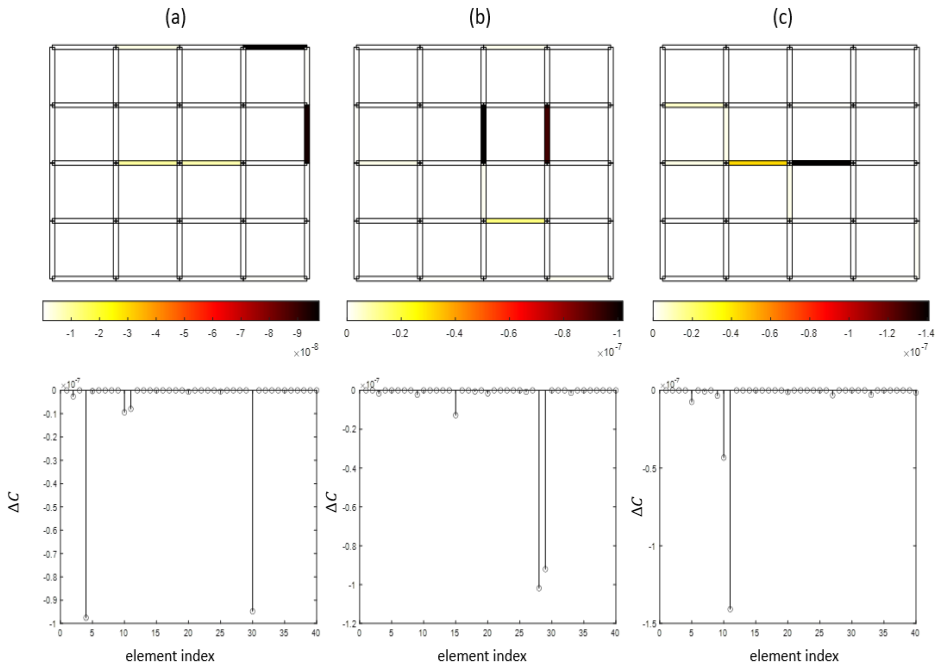

Figure 6-7 Reconstruction for a resistor network for checking the mitigation to the problem of poor spatial resolution. (a) Reconstructing admittance contrasts applied to R4 and R30. (b) Reconstructing admittance contrasts applied to R28 and R29. (c) Reconstructing admittance contrasts applied to R10 and R11.

The above results validated that the proposed reconstruction method can effectively mitigate the limitations possessed by the conventional reconstruction approach used in previous studies. With calibrations based on the prior information regarding the initial

conductance of the sensor network, which can be obtained from material testing, the proposed method was able to accurately obtain the exact magnitude of conductance variation without noticeable drawbacks in spatial resolution and sensitivity dominance. It was therefore promising to integrate the system with a hydrogel sensor network to realize a flexible electronic-skin sensor.

6.4 Fabrication of a Hydrogel Sensor Network

The self-healing feature of hydrogel materials is adopted to fabricate a hydrogel sensor network. The proposed fabrication method is illustrated in Figure 6-8(a). First, a binary pre-gel solution was prepared using the method formerly described in section 5.3. Propylene glycol (PG) (USP grade, Pure Nature Ltd, Auckland, NZ) and deionized water were mixed at a weight ratio of 1:1. Sodium chloride (NaCl) (ACS reagent, ⩾ 99.0%, Sigma-Aldrich, Auckland, NZ) was added to the mixture at a ratio of 5 grams per litre to enhance its electrical conductivity. The solution was heated at 90°C and thoroughly stirred at 600 RPM for 5 minutes on a magnetic hotplate stirrer. Then gelatin (Nutra Organics, NSW, AU) was gradually added into the solution till it reached a weight ratio of 40% in the overall solution. This process was then followed by continuous heating and stirring for 20 minutes.

The obtained solution was cast into a plastic mould and settled for two hours to complete the gelation process. The obtained hydrogel was cut into a number of stripes using a paper trimmer. The stripes were stacked together to form an interconnected grid pattern. A grid-network pattern of 5 rows by 5 columns was used for this experiment as an example. Networks with larger dimensions are also feasible. A heat gun was used to apply slight heat on the stacked stripes to allow their intercepting points to melt. After resettling, the two-layered stack transformed into a single-layered network. Afterwards, the network was dip-coated with Ecoflex (00-10, Smooth-on) such that it gains protection and electrical insulation from the surrounding environment. Finally,

the coated network was settled for four hours at room temperature (20 °C) to allow the curing of Ecoflex. The network was then ready to be connected with the data acquisition hardware proposed in section 6.2 to function as a spatial tactile sensor.

The obtained hydrogel network is shown in Figure 6-8(b). It can be seen that the prepared hydrogel network exhibited good stretchability and can endure deformation to a great extent without failure.

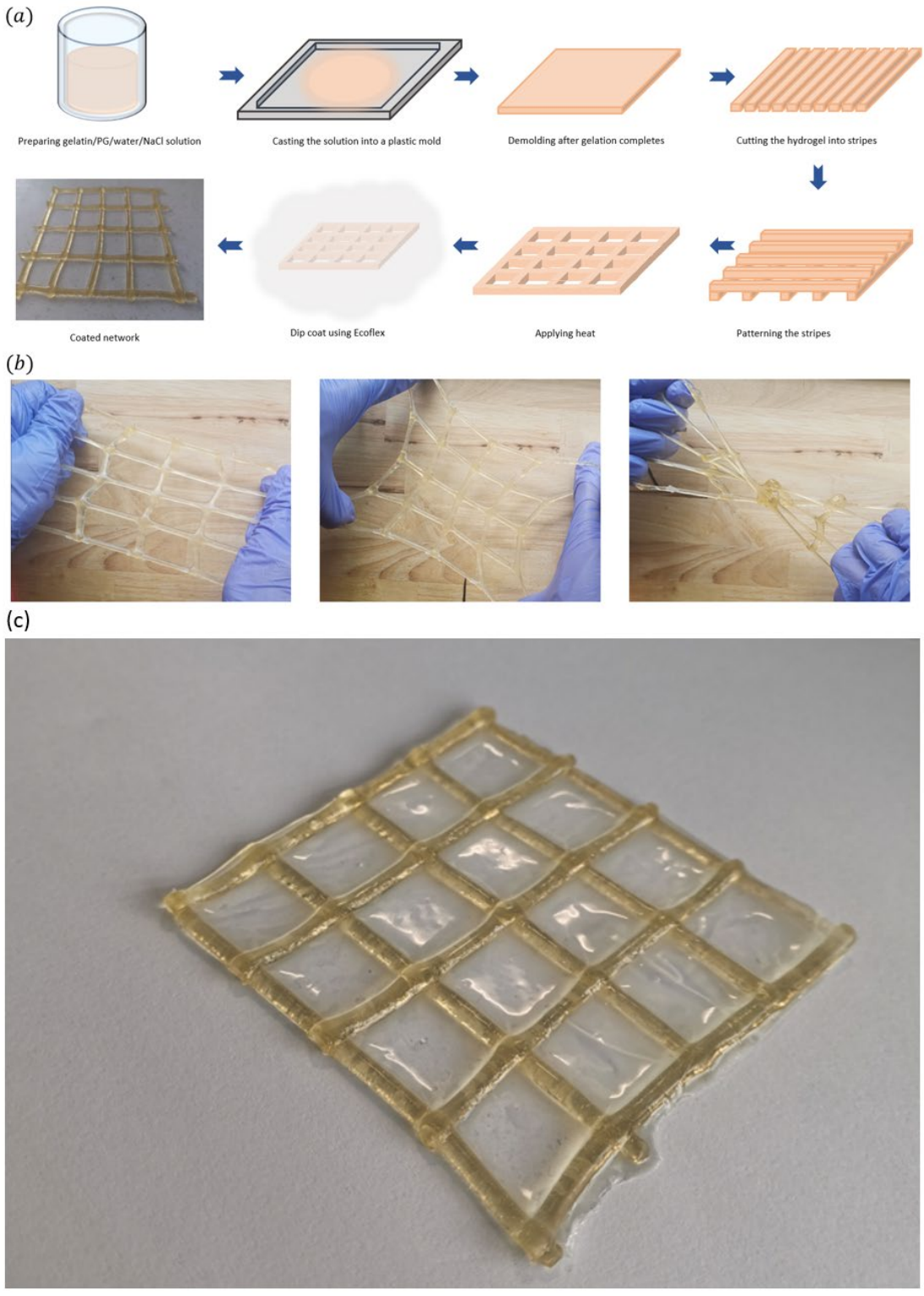

Figure 6-8 A hydrogel sensor network. (a) the fabrication procedure of the hydrogel network. (b) the network exhibiting good stretchability.

6.5 Data Acquisition From the Hydrogel Sensor Network

The obtained hydrogel sensor was connected to the EIT hardware system in accordance with the arrangement depicted previously in Figure 6-2. The electrical connection between the analog pins of ADS1115 and the vertex and midpoint nodes of the hydrogel sensor was established using enamelled copper wires. The first node of the network was selected as the reference node for differential voltage measurement; thus, this node was connected to the reference pins of ADS1115. By shifting the potentiometer, the magnitude of the injected current was adjusted to 1 μA. The adjacent drive pattern was selected as the principal current excitation strategy. The MAX336 multiplexers were set to have a 1 μs delay after switching the current injection to ensure the current transition was stabilized before voltages were measured.

Notably, unlike the resistor network used in the preliminary testing, whose electrical conduction is based on the movement of free electrons, the hydrogel network relies on ionic conductivity, i.e., the movement of charge-carrying ions. Therefore, the problem associated with charge separation in hydrogel must be accommodated during voltage measurement. In order to accommodate the charge separation problem, the polarity of the injected current was reversed at the end of each injection by swapping the source channel for current feeding and the sink channel for current sinking. When the polarity was swapped, the same process of voltage measurement was repeated. The time spent on each polarity of the current injection was equal. The voltage data measured when the polarity was reversed was discarded; only the voltage data obtained during current injections that followed the conventional adjacent strategy was saved to MATLAB for processing and performing reconstructions.

The time between two adjacent operations of polarity switching is the sum of the total conversion time of ADC and the settling time of multiplexers. The sampling rate of the utilized ADS1115 is 860 SPS. Equivalently, each differential voltage conversion takes

approximately 1.2 ms. In addition, a delay time of at least 1μs is required by MAX336 for settling the redirected current after each polarity switching. Therefore, the approximate frequency of the square-wave alternating current that was maintained in the hydrogel sensor can be calculated using the following relation:

$$f = \frac{1}{2 \times \left(1.2 \times 10^{-3} \times m + t_{delay}\right)} \quad \text{6-17}$$

where f is the frequency of the square-wave alternating current, m is the number of conversions per current injection, t_{delay} is the delay time after each polarity switching.

In order to verify the effect of the frequency of square-wave AC on the stability of the measured voltage data, a linear hydrogel sensing element was extracted from one of the prepared hydrogel networks and was connected to the proposed hardware system. The sensing element was injected with a 1 μA current, and the polarity of the current was swapped after different time intervals. The differential voltage across the two ends of the sensing element was recorded over five minutes. The results are presented in Figure 6-9. It can be seen that the measured voltage data was stable when a delay time of less than 1 ms was imposed (i.e., when the frequency of the square-wave AC was above 227 Hz). When the delay time was higher, the effect of the charge separation problem became more significant. Ions carrying opposite charges were gradually built up at each end of the sensing element, and thus a noticeable increase in the measured voltage was observed. A high frequency is desired to minimize the charge-separation effect and obtain stable voltage data.

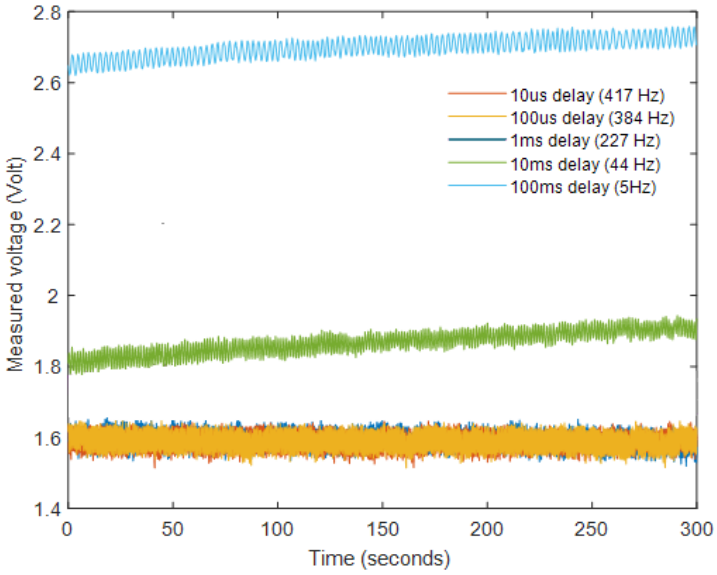

Figure 6-9 The impact of the frequency of the square-wave AC excitation on the signal stability of a hydrogel sensing element.

Because ADS1115 requires 1.2 ms for each voltage conversion, executing six conversions during each polarity requires 7.2 ms. This delay would result in a limited frequency below 70 Hz, producing unstable signals and hindering reconstructions. In order to overcome this issue, a modified strategy was utilized for current injection and voltage measurement. Instead of performing six voltage measurements per current injection, only a single voltage measurement was taken. After a single measurement was taken, the polarity of the injected current was reversed, and another voltage measurement was taken and discarded. The purpose of this second measurement was to pause for another 1.2 ms to balance the time consumption between the positive polarity and the negative polarity. Then the polarity was swapped back, and the voltage at the next electrode was measured. After repeating this process to obtain all the required voltages, the polarity of the injected current was switched according to the conventional adjacent drive pattern, and the same procedure was repeated until all the voltage data during each current injection pattern was acquired. The schematic of this strategy is depicted in Table 9. Via this strategy, the frequency of the square-wave excitation current was enhanced to over 400 Hz.

I_1		I_2		I_3		I_4		I_5		I_6		I_7		I_8	
m	u	m	u	m	u	m	u	m	u	m	u	m	u	m	u
1-2	3	2-3	1	3-4	1	4-5	1	5-6	1	6-7	1	7-8	1	8-1	2
2-1	3	3-2	1	4-3	1	5-4	1	6-5	1	7-6	1	8-7	1	1-8	2
1-2	4	2-3	4	3-4	2	4-5	2	5-6	2	6-7	2	7-8	2	8-1	3
2-1	4	3-2	4	4-3	2	5-4	2	6-5	2	7-6	2	8-7	2	1-8	3
1-2	5	2-3	5	3-4	5	4-5	3	5-6	3	6-7	3	7-8	3	8-1	4
2-1	5	3-2	5	4-3	5	5-4	3	6-5	3	7-6	3	8-7	3	1-8	4
1-2	6	2-3	6	3-4	6	4-5	6	5-6	4	6-7	4	7-8	4	8-1	5
2-1	6	3-2	6	4-3	6	5-4	6	6-5	4	7-6	4	8-7	4	1-8	5
1-2	7	2-3	7	3-4	7	4-5	7	5-6	7	6-7	5	7-8	5	8-1	6
2-1	7	3-2	7	4-3	7	5-4	7	6-5	7	7-6	5	8-7	5	1-8	6
1-2	8	2-3	8	3-4	8	4-5	8	5-6	8	6-7	8	7-8	6	8-1	7
2-1	8	3-2	8	4-3	8	5-4	8	6-5	8	7-6	8	8-7	6	1-8	7

Table 9. Strategy for performing current injections and voltage measurement. *I* denotes the index of each current injection pattern; m denotes the index of electrode couples that sourced and sunk the injected current, respectively; u denotes the index of electrodes at which voltage was measured. The shaded area indicates discarded data. The voltages at electrodes that directly receive excitation current were excluded from measurement. For instance, "1-2" indicates the case when a current was injected to the 1st electrode and sunk via the 2nd electrode; a separate "3" indicates that a voltage was measured between the 3rd electrode and the reference node. A total of 96 polarity switching and 96 voltage conversion were performed for one single frame of reconstruction.

It was observed that spikes often appeared in the reconstructed solutions in an unpredictable manner. A 1-dimensional median filter was applied to the reconstructed solution to remove the spikes, using a MATLAB function, "medfilt1". The order of the median filter was set to 5, such that the median value among the five nearest samples was assigned to the output.

In order to perform admittance reconstructions for strain sensing, the developed hydrogel sensor was initially left intact to allow an initial set of voltages to be measured and used as the reference voltage data. Strains were then applied by manually stretching some elements in the sensor network. A new set of voltages was recorded under the presence of the applied strain. The voltage variation data was determined by taking the difference between the reference voltage data and the perturbated voltage data. The voltage variation data was then reconstructed to estimate the admittance variation distribution. Finally, the estimated admittance variation data was interpreted into strain based on the experimentally determined strain-admittance response of the hydrogel sensing elements.

6.6 The Strain-Admittance Response of Hydrogel Sensing Elements

The strain-admittance response of an individual sensing element that constitutes the sensor network was tested to allow interpreting the admittance variation data into strain. As demonstrated in Figure 6-11(a), five samples of hydrogel sensing elements were extracted from a hydrogel sensor network. The samples were mounted to the texture analyzer for receiving strain stimuli. The hardware system developed in section 6.2.4 was used to measure the differential voltage across each sensing element. A square wave current of 1 μA was used for exciting the sensing elements at a frequency of 417 Hz. The admittance of each sensing element was determined by taking the inverse of the electrical impedance, which was calculated from the measured differential voltage data using Ohms law.

The calculated admittances of the five samples in response to applied strain between 0 and 100% are shown in Figure 6-10(b). It can be seen from the results that, although each sample exhibited good consistency in its signal, a mismatch among them was present. This mismatch may be caused by multiple factors. For example, one factor may be the unidentical cross-sectional areas or shapes caused by reheating the sensor network during the fabricating process. Another factor may be the nonuniformity in the gel content, caused by inconstant gelation speed during their sol-gel transition. Further possible factors include the non-uniform distribution of disassociated NaCl ions in the sensor network, temperature variation, and the presence of miniature air bubbles in hydrogel contents.

The mismatch in the admittances of the sensing elements implies that interpreting strain from reconstructed admittances of the hydrogel sensor network will suffer some errors. First, due to the mismatch, the initial reference admittance used for calibrating the inverse solver will not be uniform or precisely identical to that of the physical sensor network. Second, the unit variation of admittance per unit change of strain will not be

precisely the same among different sensing elements. In order to achieve the best outcome under these conditions, a first-degree polynomial was fitted to the signals obtained from the five samples, using the MATLAB function, "polyfit". The resulted polynomial is expressed as

$$y = (-0.0059x + 0.9047) \times 10^{-6} \qquad 6\text{-}18$$

where x denotes the applied strain in percentage, and y denotes the admittance in siemens. Based on this polynomial, a simplified mathematical relation between the admittance variation of each sensing element and the applied strain was approximated. For transducing strain using the prepared sensor network, each unity percentage increase in the strain of a single sensing element corresponded to a reduction of 0.0059 µS in its admittance and vice versa. During the calibration of the inverse solver, a uniform initial admittance of 0.9047 µS was assumed for all sensing elements in the network.

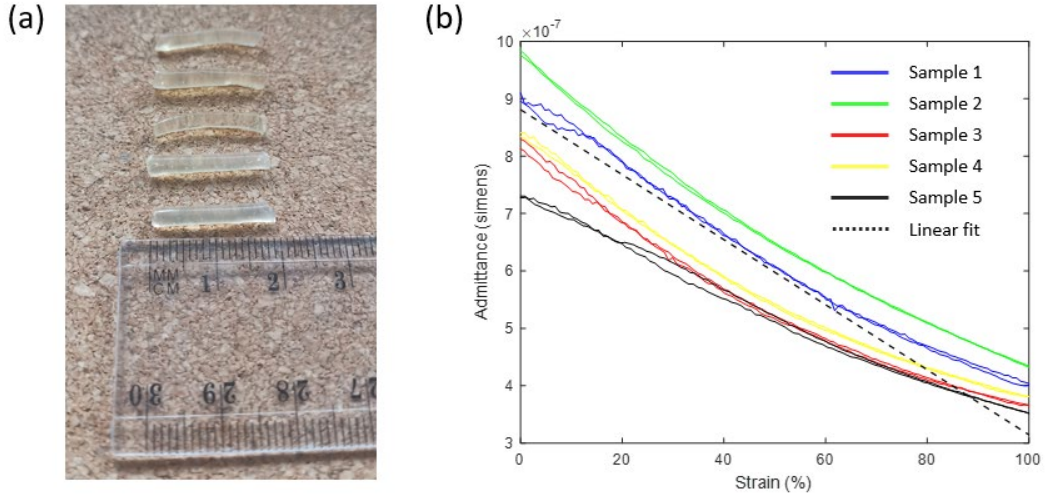

Figure 6-10 Strain-admittance response of hydrogel sensing elements. (a) Five samples of hydrogel sensing elements extracted from a prepared hydrogel sensor network. (b) The response of admittance of the five samples under applied strain between 0 and 100%.

6.7 Strain Distribution Sensing

At first, reconstructions were performed to estimate the distribution of admittance variation in the sensor network when a strain was applied to a single sensing element. As shown in Figure 6-11(a), (b) and (c), strains of 25%, 50% and 75% were successively applied to the first element (R1) in the fabricated hydrogel network by stretching the element with a digital calliper. The reconstructed solutions exhibited a close match between the true positions and the estimated positions of the applied strains, indicating the sensor was promising in localizing strains. For estimating strain magnitudes, the reconstructed admittance variations were converted into strains using the formerly approximated conversion ratio of 0.0059 μS per unit percentage of strain. For each of the three strain levels, the mean, the upper limit and the lower limit of the obtained results out of the five nearest reconstruction frames are recorded and plotted in the right-hand side of Figure 6-11. In this case, mean strains of 20.85%, 39.21%, 66.88% were estimated for the actual strains of 25%, 50% and 75%, respectively. The deviations between the upper limit and the lower limit of the estimated solutions were small, suggesting the sensor provided a reasonably stable output.

The concept of the percentage of strain recovery (PSR) can be used to quantify the overall accuracy of the sensor in terms of recovering the magnitudes of the applied strains. The PSR can be defined in a way similar to PCR, which was previously defined by equation 3-71 in section 3.5.1; i.e., the PSR can be defined as the difference between the average of the reconstructed contrast strains ($\mathrm{CS_{rec}}$) and the average of the reconstructed background strains ($\mathrm{BS_{rec}}$), divided by the difference between their true values ($\mathrm{CS_{true}}$ and $\mathrm{BS_{true}}$). This relation is expressed as

$$\mathrm{PSR} = \frac{\mathrm{CS_{rec}} - \mathrm{BS_{rec}}}{\mathrm{CS_{true}} - \mathrm{BS_{true}}} \times 100 \qquad 6\text{-}19$$

In an ideal case where the applied strains are perfectly reconstructed to their exact values, the PSR of such a reconstruction will be 100. The PSRs of the reconstructions

performed for the three cases shown in Figure 6-11(a), (b), and (c) are calculated as 83.14, 76.12, and 86.72 , respectively.

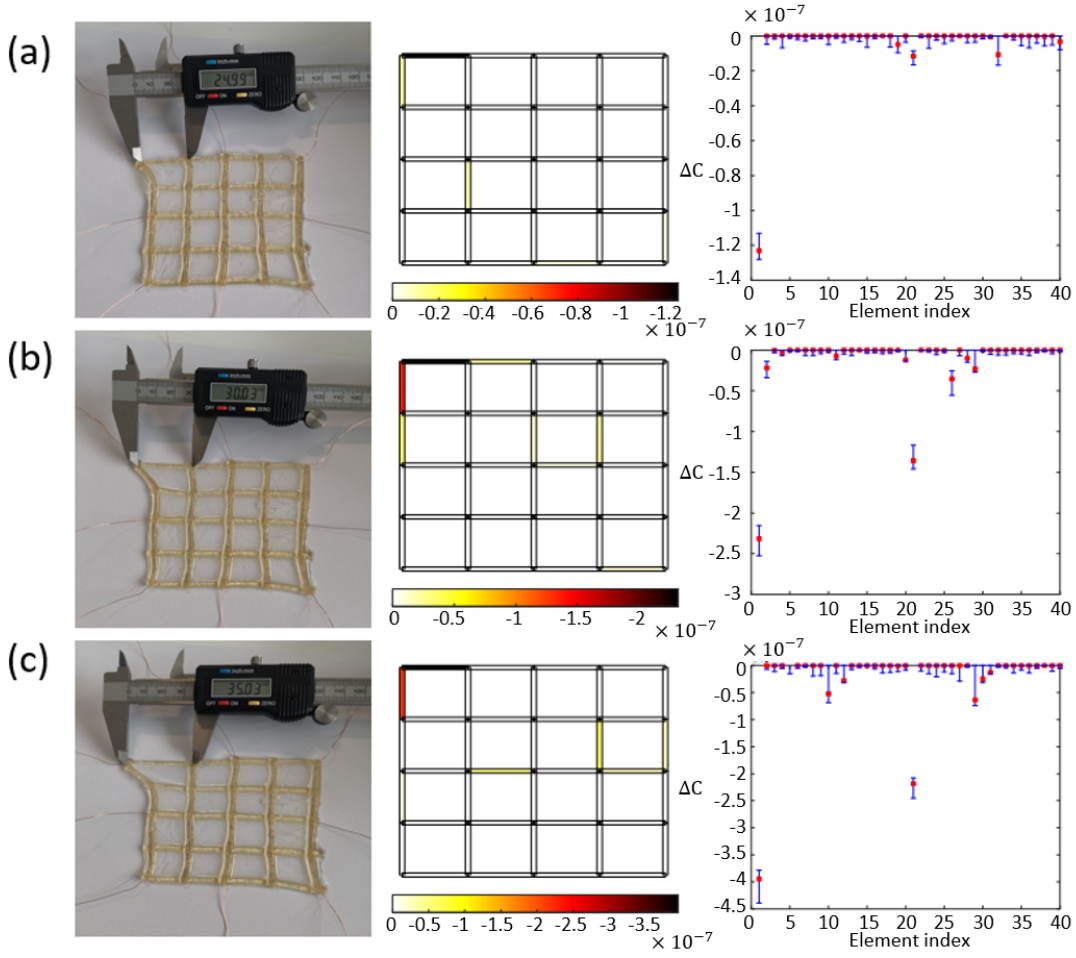

Figure 6-11 Reconstruction of admittance variation when a strain was applied to the first sensing element (R1) of the hydrogel sensor network. The left-hand side images show the sensor deformation when it is stretched. The middle images show the visualized mean solutions. The right-hand side images show the plotted solutions where the means of the solutions are indicated by red dots, the upper limit and the lower limit of the solutions are indicated by the top bars and the bottom bars connecting both ends of vertical line segments. ΔC denotes the change in the admittance value of each element in the network. (a) Reconstruction for 25% strain. (b) Reconstruction for 50% strain. (c) Reconstruction for 75% strain.

It was previously mentioned that conventional EIT-based sensors reported in previous studies generally lack sensitivity in their interior region. Therefore, to ensure the proposed sensor's capability to detect strains applied to its interior region, the same experiment was also performed on an internal sensing element (R10) located near the centre of the network. As shown in Figure 6-12, the reconstructed admittance variation

for each applied strain demonstrated good consistency with the mechanical input. The locations of the applied strains could be easily identified from the estimated solutions. By converting the reconstructed admittance variations into strains using the same ratio of 0.0059 μS per unit percentage of strain, 32.83%, 59.43% and 90.27% were estimated for true strains of 25%, 50% and 75%, respectively. And the PSRs for the three cases were calculated as 130.80, 116.59, and 118.16 respectively.

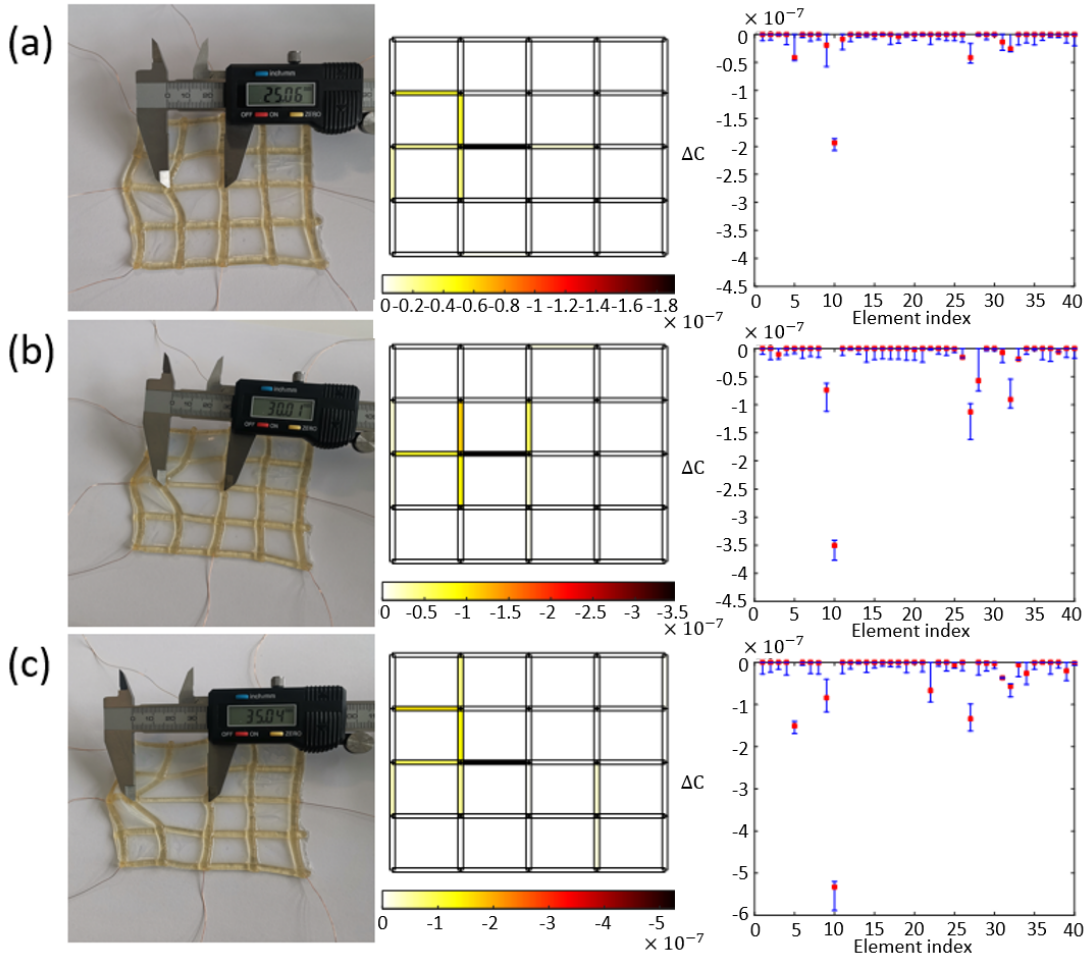

Figure 6-12 Reconstruction of admittance variation when a strain was applied to the 10th sensing element (R10) of the hydrogel sensor network. The left-hand side images show the sensor deformation when it is stretched. The middle images show the visualized mean solutions. The right-hand side images show the plotted solutions where the means of the solutions are indicated by red dots, the upper limit and the lower limit of the solutions are indicated by the top bars and the bottom bars connecting both ends of vertical line segments. ΔC denotes the change in the admittance value of each element in the network. (a) Reconstruction for 25% strain. (b) Reconstruction for 50% strain. (c) Reconstruction for 75% strain.

In addition to detecting a single strain, the ability of the sensor to simultaneously detect multiple strains was examined. As demonstrated in Figure 6-13(a), reconstructions were performed when two adjacent sensing elements (R1 and R2) were stretched to a strain of approximate 25%. The solutions showed notable admittance variation corresponding to the two stretched elements. Via admittance-strain conversions, R1 and R2 were estimated of having strains of 24.67% and 34.74%, respectively. The PSR of this reconstruction was calculated as 115.34. In (b), the number of applied strains was increased to four. Four sensing elements in the same row were simultaneously stretched to a strain of 25%. In this case, the locations of the applied strain could be identified from the reconstructed admittance variations clearly, and the magnitudes of the interpreted strains were estimated to be 16.45%, 35.09%, 38.47% and 33.77%, respectively. The PSR of this reconstruction was calculated as 119.27.

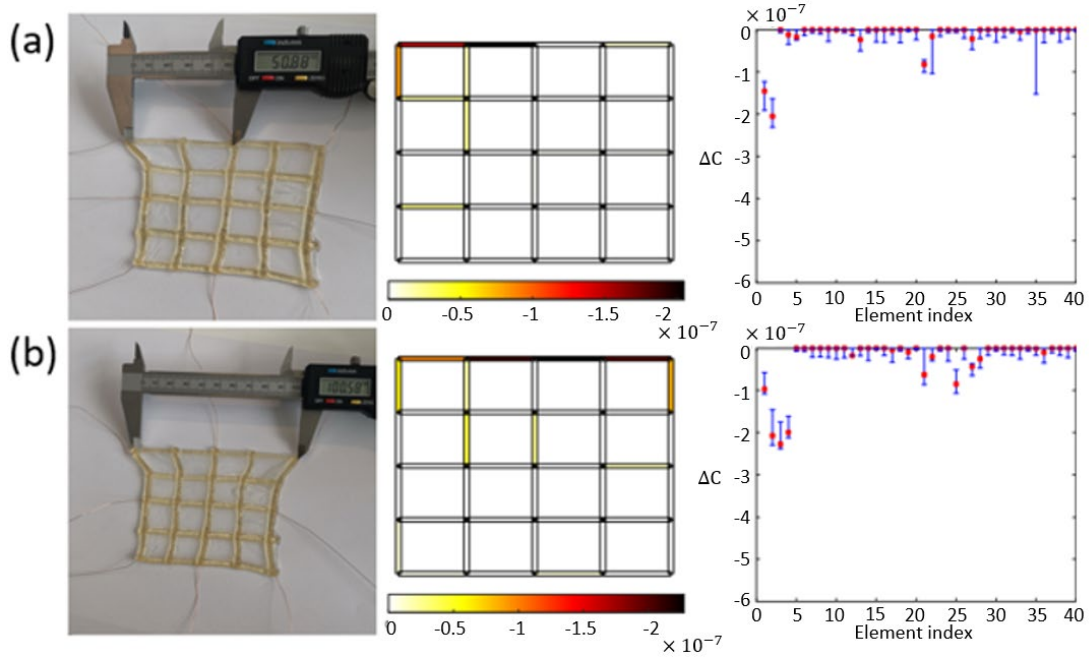

Figure 6-13 Reconstructions of admittance variation distribution when multiple strains were induced in the network. The left-hand side images show the sensor deformation when it is stretched. The middle images show the visualized mean solutions. The right-hand side images show the plotted solutions where the means of the solutions are indicated by red dots, the upper limit and the lower limit of the solutions are indicated by the top bars and the bottom bars connecting both ends of vertical line segments. ΔC denotes the change in the admittance value of each element in the network. (a) Strains are applied to R1 and R2. (b) Strains are applied to four elements in the top row.

Moreover, reconstructions were performed when two strains were simultaneously present on a boundary element (R3) and a centre element (R11) to test the mitigation to the boundary sensitivity dominance issue. Figure 6-14(a) demonstrated that R11 and R3 were both stretched to 25% strain. It can be seen from the reconstructed solutions that the admittance variation for the internal element was successfully preserved under the presence of the stretched boundary element. The admittance variations of both elements were estimated to have similar magnitudes, which were interpreted into strains of 30.64% and 37.11%, respectively. The PSR of this reconstruction was calculated as 130.39. In (b), the strain applied to the boundary element was further increased to approximately 75%; meanwhile, the strain maintained at the centre element remained the same at 25%. In this case, an increased admittance variation of the boundary element was observed. The admittance variation of the centre element was maintained; it did not diminish due to the presence of the larger admittance variation at R3. The admittance variations of the two elements were interpreted into strains of 83.83% and 34.62%, respectively. The PSR of this reconstruction was calculated as 114.91.

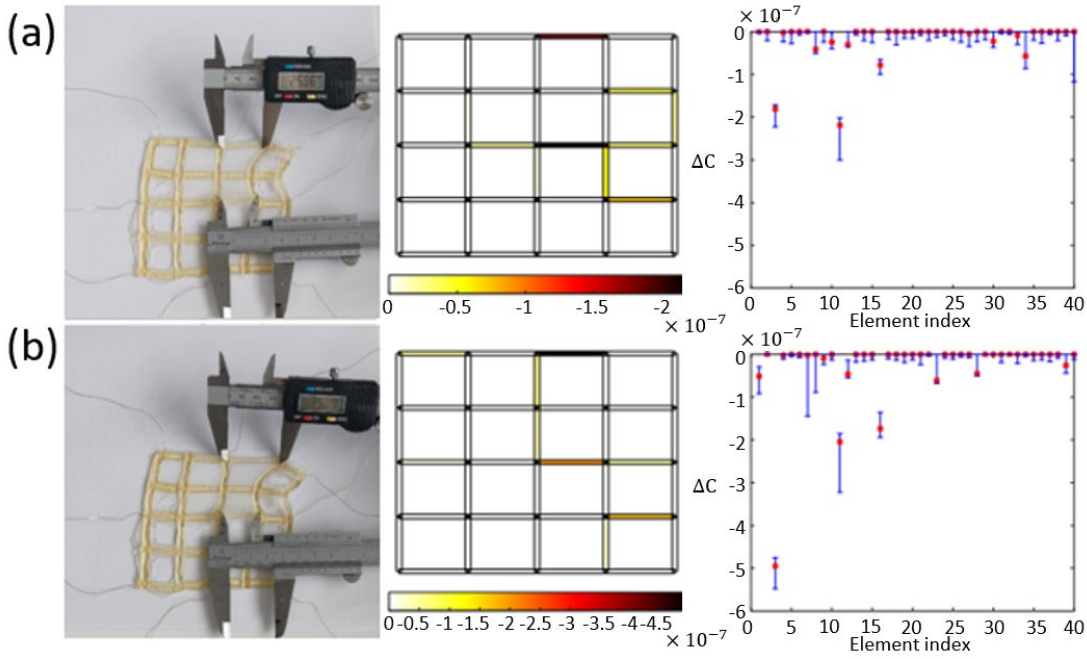

Figure 6-14 Reconstructions of admittance variation distribution when multiple strains were induced in the network. The left-hand side images show the sensor deformation when it is stretched. The middle images show the visualized mean solutions. The right-hand side images show the plotted solutions where the means of the solutions are indicated by red dots, the upper limit and the lower limit of the solutions are indicated by the top bars and the bottom bars connecting both ends of vertical line segments. ΔC denotes the change in the admittance value of each element in the network. (a) 25% strains are applied to R3 and R11. (b) A 75% strain is applied to R3 and a 25% strain is applied to R11.

Based on various reconstructions performed in this section, the PSR was found to lay within a range between 76.12 and 130.80, which are considerably better than the PCR values of typically less than 10 for the conventional reconstruction approach discussed in Chapter 3. An average PSR was calculated as 109.14, and the average of the absolute differences in the PSRs, calculated with respect to a baseline of 100, was found to be 19.95%. The obtained results confirmed that the proposed sensor successfully accommodated the sensitivity dominance problem and the spatial resolution problem encountered by EIT-based sensors reported in previous studies. The proposed sensor was capable of providing strain estimations that are reasonably matched with the applied strains.

Additionally, apart from sensing strain, the ability of the proposed sensor to detect distributed pressures was also tested. As demonstrated in Figure 6-15, pressures were

successively induced on one, two and four elements in the hydrogel sensor network by manually pressing the hydrogel sensing elements. It can be seen from the reconstructed results that notable reductions in the admittance of the compressed sensing elements were observed. This result indicated that the proposed sensor possesses the potential of sensing pressure distribution in addition to strains.

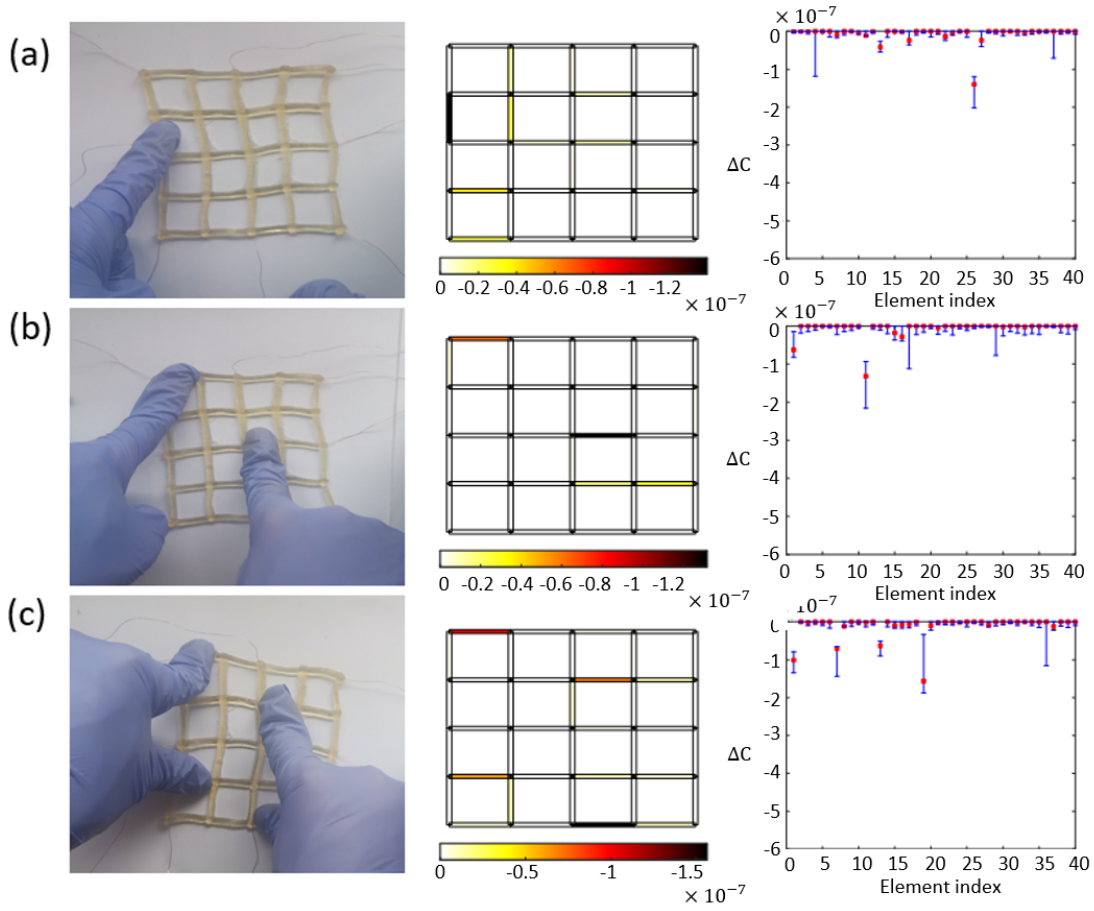

Figure 6-15 Reconstructions performed for pressure detection. The left-hand side images show the sensor deformation when it is pressed. The middle images show the visualized mean solutions. The right-hand side images show the plotted solutions where the means of the solutions are indicated by red dots, the upper limit and the lower limit of the solutions are indicated by the top bars and the bottom bars connecting both ends of vertical line segments. ΔC denotes the change in the admittance value of each element in the network. (a) Single pressure detection. (b) double pressure detection. (c) Triple pressure detection.

6.8 Discussion and Conclusion

In this chapter, the proposed reconstruction method for sensing strain distribution was experimentally validated on a hydrogel-based sensor network. A simple hardware system was developed for collecting the necessary input data to enable reconstructions. The system consisted of a Howland circuit for maintaining a constant and load-independent current, two multiplexers for switching the current injection patterns, and a multichannel analog-to-digital converter for measuring differential voltages.

A preliminary test was first conducted via the hardware system by implementing the reconstruction method on a network formed by concatenated resistors. Admittance variations were induced to the network by changing the values of the resistors. The reconstructed results showed that, by using known initial admittance information as the reference, the admittance variations induced in the network were accurately reconstructed. This outcome proved it was feasible to use the proposed reconstruction method to achieve both localization and estimation of applied strains.

After the preliminary testing, a hydrogel sensor was fabricated using a novel approach based on the self-healing characteristic of hydrogel materials. The proposed reconstruction method was then implemented using the hydrogel sensor to test its ability to sense strain. Based on the experimentally determined strain-admittance response of individual hydrogel sensing elements, the reconstructed admittance variations were interpreted into strains. The results showed that the strains applied to the hydrogel network were estimated with reasonable accuracy.

It was found that some errors were still present in the strain estimations due to several future challenges that are to be overcome. For instance, the hydrogel-based strain sensing material exhibited inconsistency among different samples of elements in an admittance network. The inconsistency was partially due to the manual handling involved in the sensor fabrication process, which resulted in mismatched dimensions of different sensing elements. The inconsistency brought difficulty in calibrating the

baseline admittance of the structural model and raised errors in the signal transduction between admittance and strain. The manual handling may add further inconsistency if the sensor was to be expanded to a larger sized network.

Apart from the sample inconsistency, the measurement noise is another notable factor to be considered. Reconstructions performed on the resistor network in the preliminary testing did not experience noticeable measurement noise and achieved stable admittance estimations; on the other hand, the reconstructions performed on the hydrogel sensor encountered noisy spikes that frequently appeared in the estimations. Therefore, the data acquisition hardware requires further improvement to achieve more stable results.

Nevertheless, the sensor proposed in this work offered reasonable accuracy for estimating strain distribution and effectively mitigated the problems associated with boundary sensitivity dominance and poor spatial resolutions. Compared to previous E-skins reviews in section 2.4, which were only able to provide vague and erroneous localizations to the applied strains, the proposed sensor allowed remarkably more promising estimations of locations, directions, and magnitudes of the applied strains.

Chapter 7 Conclusion and Future Work

7.1 Conclusions

Towards the ultimate objective of developing an electronic skin with enhanced performance for sensing spatially distributed strains, this thesis describes a variety of research aspects for both reconstruction algorithms and flexible sensing materials.

In chapter 3, the defects of EIT that hinder the accuracy of electronic-skin sensors were identified through a simulation study. This chapter summarized the mathematical principles behind the technology of EIT, including the governing equation derived from Maxwell's equations, numerical formation based on finite element method, the concept of the Jacobian matrix, and different types of regularization techniques for solving ill-posed problems. The algorithms were implemented on the MATLAB platform to allow computer simulations. Via a simulation study, it was found that EIT suffered from a variety of limitations, including solution uncertainty, poor spatial resolution, boundary sensitivity dominance, and model incompatibility in terms of anisotropic conductivity and boundary deformation of the material. Preliminary mitigations of these defects were attempted. It was found that using prior information to impose additional constraints on the inverse solver could effectively refine the obtained solutions and enhance the accuracy of reconstructions.

In chapter 4, in order to overcome the identified limitations and reduce the errors resulting from the reconstruction algorithms, a new structural model for solving the forward problem of EIT was proposed to replace the conventional FEM-based model. This chapter first introduced the concept of the nodal admittance matrix, based on which the forward problem was adapted to become compatible with strain sensing. Then the inverse solver was updated according to the change made in the forward solver. A non-negative least squares algorithm based on the active-set method was added to the program of the inverse solver. The physical significance of the non-

negative constraints imposed on the inverse solver was explained. A simulation study showed that combining the NAM-based model and the constrained inverse solver could effectively accommodate the defects identified in chapter 3. The new reconstruction method offered excellent model compatibility with strain sensing, remarkable solution consistency, significantly enhanced accuracy, and reduced time consumption.

In chapter 5, a suitable material for constituting individual sensing elements in a sensor network was selected to reduce the errors contributed by sensing materials. At the beginning of the chapter, the advantages and drawbacks of each type of flexible strain sensor reported in previous literature were compared and discussed. It was found that sensors based on ionic liquids and sensors based on hydrogels were more reliable than other types of sensors in terms of their consistency in sensing dynamic strains. An ionic liquid-based sensor was fabricated using propylene glycol and sodium chloride, and a hydrogel-based sensor was fabricated by further adding gelatin and water to the ingredients of the ionic liquid. The two sensors were tested for their strain-sensing ability. The experimental results showed that both types of sensors exhibited negligible hysteresis and overshoot, and both provided consistent signals when they were used to measure dynamic strains. However, the ionic liquid-based sensor suffered from leakage issues, and crosstalk among different sensing elements in an admittance network would hinder the accuracy of reconstructions; on the other hand, the hydrogel-based sensor was free from leakage and crosstalk. Therefore, the hydrogel-based approach was selected for producing a sensor network.

In chapter 6, a hydrogel-based sensor that possessed the structure of an admittance network was fabricated to allow the physical implementation of the proposed reconstruction method. A novel fabrication method that adopted the self-healing feature of hydrogel materials was proposed. A simple hardware system was developed to enable current injections and voltage measurement. In a preliminary experiment, the effectiveness of the hardware system and the proposed reconstruction method was first verified by carrying out reconstructions on a resistor network. Then reconstructions were performed on the prepared hydrogel sensor network. It was found that the applied

strains were successfully localized according to the reconstructed admittance variations. The strain-admittance relationship of hydrogel sensing elements was determined from experiments. In accordance with the obtained relationship, the reconstructed admittance variations were interpreted into strains. Although some errors were observed, the obtained results showed that the estimated strains were reasonably matched to the actual strains. Compared to EIT-based sensors reported in previous studies, which could only localize strains on a coarse scale, the proposed sensor offered considerably more reliable strain estimations.

7.2 Contributions

This research provides the following contributions to different fields involving EIT technology, flexible sensors, and EIT-based electronic skins:

1. A clarification of the limitations of utilizing EIT for sensing spatially distributed strains.

   Previous studies emphasised granting the spatial tactile sensing ability to various types of flexible piezoresistive materials. However, the sensors reported in these studies experienced a severe lack of accuracy. This thesis provides a comprehensive clarification of the limiting factors via a simulation study, detailing various critical issues, including uncertainty in solutions, poor spatial resolution, boundary sensitivity dominance, and model incompatibility in terms of anisotropic conductivity and boundary shape deformation.

2. A novel structural model that grants explicit mathematical compatibility between strain sensing and EIT.

   The conventional FEM-based structural model of EIT is incompatible with piezoresistive strain-sensing materials because the model assumes anisotropic electrical conductivity of the sensing material, requires fixed nodal coordinates

and assumes a low frequency of the excitation current. A novel structural model and its corresponding Jacobian matrix are derived based on the concept of the nodal admittance matrix to replace the FEM-based model. The new model accepts anisotropic electrical conductivity of materials and allows free boundary deformation.

3. A novel method for solving the inverse problem of EIT with enhanced accuracy.

   An active-set method is adopted to refine the solution space subject to an imposed non-negativity constraint. To our knowledge, this is the first time the active-set method has been utilized in the field of EIT. Compared to the methods reported in previous works, this method offers considerably improved accuracy in reconstructions.

4. Low-cost preparation methods and verified characteristics for strain-sensing materials based on ionic liquids and hydrogels.

   An ionic liquid (PG)-based strain sensor and a hydrogel (PG-gelatine)-based strain sensor were fabricated using simple and low-cost methods. Compared to previous sensors, both sensors possess excellent signal consistency in sensing dynamic strains and are free from hysteresis and overshoot.

5. A novel patterning method for producing a hydrogel-based sensor network

   Adopting the self-healing feature of hydrogel materials, an efficient method for patterning hydrogel materials into a grid-network layout is proposed. The method does not require sophisticated instruments or complicated procedures.

6. A strain-sensing electronic skin with enhanced accuracy.

   A strain-sensing electronic skin was realized by combining the proposed structural model based on nodal admittance matrix as the structural model, the constrained least-squares method as the inverse solver, the PG-gelatine hydrogel as the strain-sensing material, and the self-healing-based patterning method. Compared to EIT-based sensors reported in previous studies, the

sensor proposed in this work offers improved accuracy in localizing as well as estimating spatial strain distribution. The proposed methods in this work can significantly enhance the robustness of future EIT-based electronic skins and strengthen their practicality in various applications.

7.3 Recommendation for Future Work

The work presented in this thesis exhibited remarkable enhancement to the performance of strain-sensing electronic skins based on EIT technology. Future work may contribute towards mitigating several remaining unsolved problems and further testing sensors of other configurations. In particular, future work may be conducted to:

- Enhance the temporal resolution of the reconstruction

A more efficient data acquisition hardware for implementing EIT on the hydrogel sensor is preferred. Although the analog-to-digital converters (i.e., ADS1115) utilized in the proposed hardware system possess a high measurement resolution of 16 bit, their sampling rate at 860 SPS is considerably lower than what may be required in some applications. The multiplexers (MAX336) also possess a relatively long transition time, which further adds to the time consumed by executing a single reconstruction frame. Consequently, the frame rate at which the solutions were reconstructed was limited to 2 frames per second. This frame rate may be insufficient to capture comprehensive details of motions for applications that involve rapid sensor deformation. Faster voltage converters and multiplexers are recommended to enhance the sensor's temporal resolution.

- Reduce the noise in the data collection system

Apart from the temporal resolution limited by the data acquisition hardware, it was also found that considerable measurement noise was present during reconstructions implemented on the hydrogel sensor. The presence of measurement noise resulted in

unpredictable spikes in the reconstructed solutions, hindering the stability of the results. Therefore, improving the precision of the data acquisition hardware is recommended to reduce the measurement noise and properly demonstrate the sensor accuracy and stability. Examples of feasible approaches include utilizing a precise high-frequency alternating current source and voltage sensors, employing multiplexers with ultra-low leakage current, and developing flexible electrodes that smoothly conform to the hydrogel sensor.

- Enhance the precision of the fabrication method

As previously mentioned in section 6.8, the manual handling (including slicing, stacking, and rehealing the hydrogel) involved in the fabrication process of the hydrogel strain sensing material limited the precision of the dimension of individual sensing elements in the hydrogel network. The lack of precision resulted in inconsistent signal response to the strains applied to different sensing elements and hindered the accuracy of strain estimation. More precise fabrication methods and instruments are recommended to achieve a more reliable sensor. For example, optical lithography, programmed laser engraving, and the 3D printing technique may be more efficient for producing a patterned sensor network with a precise and uniform layout.

- Implement the reconstruction algorithm for other sensor configurations

The simulation results obtained in section 4.4 showed that the proposed reconstruction method supports sensor networks of various dimensions. Due to the constraints on equipment and time, only a relatively small hydrogel sensor was fabricated and tested in this work. In future work, sensor networks with larger dimensions and denser grids can be fabricated to provide strain estimations with better spatial resolution. For denser networks, the reconstruction accuracy may be further enhanced by various means such as increasing the number of boundary electrodes, introducing electrodes to the interior region of networks, and modifying the current injection strategy.

- Test other strain-sensing materials.

In section 4.6, it was observed that one limitation of the active-set method adopted by the inverse problem solver is that the reconstructions involving larger admittance variations lead to solutions with more errors. Hence strain sensing materials with lower gauge factors are more welcomed, such that the resulted sensor can be used to measure strains of large magnitudes more accurately. On that account, room-temperature liquid metals may be an excellent choice for realizing an electronic skin for sensing larger strains, provided that the challenge with patterning the fluid channel is overcome and the possible leakage issue is successfully prevented.

- Sense pressure and strain simultaneously

The sensor proposed in this work was tested with a particular emphasis on its strain sensing capability. Its competence in sensing pressure was checked preliminarily. For future work, it is possible to achieve simultaneous sensing strain and pressure sensing, which can offer the sensor better usage in a wider range of applications, such as a motion detection glove that detects both hand gestures and the contact force at each finger. Therefore, future work may include customizing the network layout and introducing pressure transducers at specific elements in the network to allow simultaneous transduction of pressure along with strain.

7.4 Summary

This thesis provides original knowledge towards integrating EIT with flexible conductive materials to realize strain-sensing E-skins. Specifically, the nodal admittance matrix was useful for solving the forward problem of EIT while being mathematically compatible with strain sensing. The non-negative least square method was effective for solving the inverse problem of EIT and providing more accurate solutions by limiting the solution space. The PG-gelatin hydrogel was consistent in transducing both cyclic and dynamic strains with negligible hysteresis and overshoot. An E-skin realized by combining the three things offered promising performance in

estimating two-dimensional strain distribution. Although future work is required to overcome or bypass some limitations, this research offered a new perspective for using EIT to achieve strain distribution estimation and using the prior information of material characteristics to enhance the reconstruction accuracy. This research may be beneficial for a range of potential applications in human-machine interfaces, soft robotics, and prosthetics.

Reference

[1] X. Wang, L. Dong, H. Zhang, R. Yu, C. Pan, and Z. L. Wang, “Recent Progress in Electronic Skin,” *Advanced Science*, vol. 2, no. 10, p. 1500169, 2015, doi: 10.1002/advs.201500169.

[2] J. C. Yang, J. Mun, S. Y. Kwon, S. Park, Z. Bao, and S. Park, “Electronic Skin: Recent Progress and Future Prospects for Skin-Attachable Devices for Health Monitoring, Robotics, and Prosthetics,” *Advanced Materials*, vol. 31, no. 48, p. 1904765, 2019, doi: 10.1002/adma.201904765.

[3] W. Feng *et al.*, “Sensitive Electronic-Skin Strain Sensor Array Based on the Patterned Two-Dimensional α-In $_2$ Se $_3$,” *Chem. Mater.*, vol. 28, no. 12, pp. 4278–4283, Jun. 2016, doi: 10.1021/acs.chemmater.6b01073.

[4] D. J. Lipomi *et al.*, “Skin-like pressure and strain sensors based on transparent elastic films of carbon nanotubes,” *Nature Nanotechnology*, vol. 6, no. 12, pp. 788–792, Oct. 2011, doi: 10.1038/nnano.2011.184.

[5] T. Takahashi, K. Takei, A. G. Gillies, R. S. Fearing, and A. Javey, “Carbon Nanotube Active-Matrix Backplanes for Conformal Electronics and Sensors,” *Nano Lett.*, vol. 11, no. 12, pp. 5408–5413, Dec. 2011, doi: 10.1021/nl203117h.

[6] Y. Cheng, R. Wang, H. Zhai, and J. Sun, “Stretchable electronic skin based on silver nanowire composite fiber electrodes for simultaneous sensing of pressure, proximity, and multidirectional strain,” *Nanoscale*, vol. 9, Mar. 2017, doi: 10.1039/C7NR00121E.

[7] R. P. Henderson and J. G. Webster, “An Impedance Camera for Spatially Specific Measurements of the Thorax,” *IEEE Transactions on Biomedical Engineering*, vol. BME-25, no. 3, pp. 250–254, May 1978, doi: 10.1109/TBME.1978.326329.

[8] Y. Zou and Z. Guo, “A review of electrical impedance techniques for breast cancer detection,” *Medical Engineering & Physics*, vol. 25, no. 2, pp. 79–90, Mar. 2003, doi: 10.1016/S1350-4533(02)00194-7.

[9] A. L. Raisis, M. Mosing, G. L. Hosgood, C. J. Secombe, A. Adler, and A. D. Waldmann, “The use of electrical impedance tomography (EIT) to evaluate pulse rate in anaesthetised horses,” *The Veterinary Journal*, vol. 273, p. 105694, Jul. 2021, doi: 10.1016/j.tvjl.2021.105694.

[10] I. Frerichs *et al.*, “Detection of local lung air content by electrical impedance tomography compared with electron beam CT.,” *Journal of applied physiology*, 2002, doi: 10.1152/JAPPLPHYSIOL.00081.2002.

[11] J.-J. Huang, Y.-H. Hung, J.-J. Wang, and B.-S. Lin, “Design of wearable and wireless electrical impedance tomography system,” *Measurement*, vol. 78, pp. 9–17, Jan. 2016, doi: 10.1016/j.measurement.2015.09.031.

[12] S. Russo, S. Nefti-Meziani, N. Carbonaro, and A. Tognetti, “Development of a High-Speed Current Injection and Voltage Measurement System for Electrical Impedance Tomography-Based Stretchable Sensors,” *Technologies*, vol. 5, no. 3, p. 48, Jul. 2017, doi: 10.3390/technologies5030048.

[13] “A High Frame Rate Wearable EIT System Using Active Electrode ASICs for Lung Respiration and Heart Rate Monitoring - IEEE Journals & Magazine.” https://ieeexplore.ieee.org/document/8438537 (accessed Jun. 12, 2020).

[14] A. Chortos, J. Liu, and Z. Bao, “Pursuing prosthetic electronic skin,” *Nature Materials*, vol. 15, Jul. 2016, doi: 10.1038/nmat4671.

[15] H. Lee, D. Kwon, H. Cho, I. Park, and J. Kim, “Soft Nanocomposite Based Multi-point, Multi-directional Strain Mapping Sensor Using Anisotropic Electrical Impedance Tomography,” *Scientific Reports*, vol. 7, p. 39837, Jan. 2017, doi: 10.1038/srep39837.

[16] J. Oh *et al.*, “Pressure Insensitive Strain Sensor with Facile Solution-Based Process for Tactile Sensing Applications,” *ACS Nano*, vol. 12, no. 8, pp. 7546–7553, Aug. 2018, doi: 10.1021/acsnano.8b03488.

[17] J. Wagner, S. Gschoßmann, and M. Schagerl, “On the Capability of Measuring Actual Strain Values With Electrical Impedance Tomography Using Planar Silkscreen Printed Elastoresistive Sensors,” *IEEE Sensors Journal*, vol. 21, no. 5, pp. 5798–5808, Mar. 2021, doi: 10.1109/JSEN.2020.3036736.

[18] Y. Hirose, J. Sagawa, Y. Sibamoto, and Y. Kukita, “Coping with electrode polarization for development of DC-Driven electrical impedance tomography,” *Flow Measurement and Instrumentation*, vol. 81, p. 102006, Oct. 2021, doi: 10.1016/j.flowmeasinst.2021.102006.

[19] C. Putensen, B. Hentze, S. Muenster, and T. Muders, “Electrical Impedance Tomography for Cardio-Pulmonary Monitoring,” *Journal of Clinical Medicine*, vol. 8, no. 8, Art. no. 8, Aug. 2019, doi: 10.3390/jcm8081176.

[20] S. Russo, S. Nefti-Meziani, N. Carbonaro, and A. Tognetti, “A Quantitative Evaluation of Drive Pattern Selection for Optimizing EIT-Based Stretchable Sensors,” *Sensors*, vol. 17, no. 9, p. 1999, Aug. 2017, doi: 10.3390/s17091999.

[21] W. R. B. Lionheart, “EIT Reconstruction Algorithms: Pitfalls, Challenges and Recent Developments,” *Physiological Measurement*, vol. 25, no. 1, pp. 125–142, Feb. 2004, doi: 10.1088/0967-3334/25/1/021.

[22] A. Adler *et al.*, “GREIT: a unified approach to 2D linear EIT reconstruction of lung images,” *Physiological Measurement*, vol. 30, no. 6, pp. S35–S55, Jun. 2009, doi: 10.1088/0967-3334/30/6/S03.

[23] B. H. Brown, “Electrical impedance tomography (EIT): a review,” *Journal of Medical Engineering & Technology*, vol. 27, no. 3, pp. 97–108, Jan. 2003, doi: 10.1080/0309190021000059687.

[24] E. L. Costa, R. G. Lima, and M. B. Amato, “Electrical impedance tomography,” *Current Opinion in Critical Care*, vol. 15, no. 1, pp. 18–24, Feb. 2009, doi: 10.1097/MCC.0b013e3283220e8c.

[25] M. Vauhkonen, D. Vadasz, P. A. Karjalainen, E. Somersalo, and J. P. Kaipio, “Tikhonov regularization and prior information in electrical impedance tomography,” *IEEE Transactions on Medical Imaging*, vol. 17, no. 2, pp. 285–293, Apr. 1998, doi: 10.1109/42.700740.

[26] J. C. de Munck, T. J. C. Faes, and R. M. Heethaar, “The boundary element method in the forward and inverse problem of electrical impedance tomography,” *IEEE Trans. Biomed. Eng.*, vol. 47, no. 6, pp. 792–800, Jun. 2000, doi: 10.1109/10.844230.

[27] R. P. Patterson and J. Zhang, “Evaluation of an EIT reconstruction algorithm using finite difference human thorax models as phantoms,” *Physiol. Meas.*, vol. 24, no. 2, pp. 467–475, May 2003, doi: 10.1088/0967-3334/24/2/357.

[28] E. J. Woo, P. Hua, J. G. Webster, and W. J. Tompkins, “Finite-element method in electrical impedance tomography,” *Med. Biol. Eng. Comput.*, vol. 32, no. 5, pp. 530–536, Sep. 1994, doi: 10.1007/BF02515311.

[29] M. Gehre, B. Jin, and X. Lu, “An Analysis of Finite Element Approximation in Electrical Impedance Tomography,” *Inverse Problems*, vol. 30, Dec. 2013, doi: 10.1088/0266-5611/30/4/045013.

[30] A. P. Bagshaw *et al.*, “Electrical impedance tomography of human brain function using reconstruction algorithms based on the finite element method,” *NeuroImage*, vol. 20, no. 2, pp. 752–764, Oct. 2003, doi: 10.1016/S1053-8119(03)00301-X.

[31] M. H. Sadd, “5 - Formulation and Solution Strategies,” in *Elasticity*, M. H. Sadd, Ed. Burlington: Academic Press, 2005, pp. 83–102. doi: 10.1016/B978-012605811-6/50006-3.

[32] J. Blazek, “Chapter 3 - Principles of Solution of the Governing Equations,” in *Computational Fluid Dynamics: Principles and Applications (Second Edition)*, J. Blazek, Ed. Oxford: Elsevier Science, 2005, pp. 29–75. doi: 10.1016/B978-008044506-9/50005-9.

[33] Y. Shi, Z. Yang, F. Xie, S. Ren, and S. Xu, “The Research Progress of Electrical Impedance Tomography for Lung Monitoring,” *Frontiers in Bioengineering and Biotechnology*, vol. 9, 2021, Accessed: Jan. 23, 2022. [Online]. Available: https://www.frontiersin.org/article/10.3389/fbioe.2021.726652

[34] N. K. Soni, K. D. Paulsen, H. Dehghani, and A. Hartov, “Finite element implementation of Maxwell’s equations for image reconstruction in electrical impedance tomography,” *IEEE Trans Med Imaging*, vol. 25, no. 1, pp. 55–61, Jan. 2006, doi: 10.1109/tmi.2005.861001.

[35] A. Adler and W. R. B. Lionheart, “Minimizing EIT image artefacts from mesh variability in finite element models,” *Physiol Meas*, vol. 32, no. 7, pp. 823–834, Jul. 2011, doi: 10.1088/0967-3334/32/7/S07.

[36] M. Cheney, D. Isaacson, J. C. Newell, S. Simske, and J. Goble, “NOSER: An algorithm for solving the inverse conductivity problem,” *International Journal of Imaging Systems and Technology*, vol. 2, no. 2, pp. 66–75, Jun. 1990, doi: 10.1002/ima.1850020203.

[37] N. V. Ranade and D. C. Gharpure, “Enhancing Sharp Features by Locally Relaxing Regularization for Reconstructed Images in Electrical Impedance Tomography,” *J Electr Bioimpedance*, vol. 10, no. 1, pp. 2–13, Jul. 2019, doi: 10.2478/joeb-2019-0002.

[38] B. Jin, T. Khan, and P. Maass, “A reconstruction algorithm for electrical impedance tomography based on sparsity regularization,” *International Journal for Numerical Methods in Engineering*, vol. 89, no. 3, pp. 337–353, Jan. 2012, doi: 10.1002/nme.3247.

[39] B. Gong, B. Schullcke, S. Krueger-Ziolek, U. Mueller-Lisse, and K. Moeller, “Sparse regularization for EIT reconstruction incorporating structural information derived from medical imaging,” *Physiol. Meas.*, vol. 37, no. 6, pp. 843–862, May 2016, doi: 10.1088/0967-3334/37/6/843.

[40] A. Borsic, B. M. Graham, A. Adler, and W. Lionheart, “In Vivo Impedance Imaging With Total Variation Regularization,” *IEEE Trans. Med. Imaging*, vol. 29, no. 1, pp. 44–54, Jan. 2010, doi: 10.1109/TMI.2009.2022540.

[41] T. Dai and A. Adler, “Electrical Impedance Tomography reconstruction using L1 norms for data and image terms,” in *2008 30th Annual International Conference of the IEEE Engineering in Medicine and Biology Society*, Vancouver, BC, Aug. 2008, pp. 2721–2724. doi: 10.1109/IEMBS.2008.4649764.

[42] J. Liu, L. Lin, W. Zhang, and G. Li, “A novel combined regularization algorithm of total variation and Tikhonov regularization for open electrical impedance tomography,” *Physiol. Meas.*, vol. 34, no. 7, pp. 823–838, Jul. 2013, doi: 10.1088/0967-3334/34/7/823.

[43] J. Nasehi Tehrani, A. McEwan, C. Jin, and A. van Schaik, “L1 regularization method in electrical impedance tomography by using the L1-curve (Pareto frontier curve),” *Applied Mathematical Modelling*, vol. 36, no. 3, pp. 1095–1105, Mar. 2012, doi: 10.1016/j.apm.2011.07.055.

[44] M. Farha and Endarko, “Combined algorithm of total variation and Gauss-newton for image reconstruction in two-dimensional Electrical Impedance Tomography (EIT),” in

2017 International Seminar on Sensors, Instrumentation, Measurement and Metrology (ISSIMM), Aug. 2017, pp. 37–41. doi: 10.1109/ISSIMM.2017.8124257.

[45] A. Borsic, B. M. Graham, A. Adler, and W. Lionheart, "Total Variation Regularization in Electrical Impedance Tomography," *undefined*, 2007, Accessed: Jan. 24, 2022. [Online]. Available: https://www.semanticscholar.org/paper/Total-Variation-Regularization-in-Electrical-Borsic-Graham/ee4de3e3dcba321a51b863858c78492a8d27c3d0

[46] L. Cao *et al.*, "A novel time-difference electrical impedance tomography algorithm using multi-frequency information," *BioMedical Engineering OnLine*, vol. 18, no. 1, p. 84, Jul. 2019, doi: 10.1186/s12938-019-0703-9.

[47] X. Bai, D. Liu, J. Wei, X. Bai, S. Sun, and W. Tian, "Simultaneous Imaging of Bio- and Non-Conductive Targets by Combining Frequency and Time Difference Imaging Methods in Electrical Impedance Tomography," *Biosensors (Basel)*, vol. 11, no. 6, p. 176, May 2021, doi: 10.3390/bios11060176.

[48] J. Kuen, E. J. Woo, and J. K. Seo, "Multi-frequency time-difference complex conductivity imaging of canine and human lungs using the KHU Mark1 EIT system," *Physiol Meas*, vol. 30, no. 6, pp. S149-164, Jun. 2009, doi: 10.1088/0967-3334/30/6/S10.

[49] S. Martin and C. T. M. Choi, "A novel post-processing scheme for two-dimensional electrical impedance tomography based on artificial neural networks," *PLOS ONE*, vol. 12, no. 12, p. e0188993, Dec. 2017, doi: 10.1371/journal.pone.0188993.

[50] X. Li *et al.*, "An image reconstruction framework based on deep neural network for electrical impedance tomography," in *2017 IEEE International Conference on Image Processing (ICIP)*, Beijing, Sep. 2017, pp. 3585–3589. doi: 10.1109/ICIP.2017.8296950.

[51] X. Fernández-Fuentes, D. Mera, A. Gómez, and I. Vidal-Franco, "Towards a Fast and Accurate EIT Inverse Problem Solver: A Machine Learning Approach," *Electronics*, vol. 7, no. 12, Art. no. 12, Dec. 2018, doi: 10.3390/electronics7120422.

[52] V. Antun, F. Renna, C. Poon, B. Adcock, and A. C. Hansen, "On instabilities of deep learning in image reconstruction and the potential costs of AI," *PNAS*, vol. 117, no. 48, pp. 30088–30095, Dec. 2020, doi: 10.1073/pnas.1907377117.

[53] T. K. Bera and N. Jampana, "A multifrequency constant current source suitable for Electrical Impedance Tomography (EIT)," in *2010 International Conference on Systems in Medicine and Biology*, Dec. 2010, pp. 278–283. doi: 10.1109/ICSMB.2010.5735387.

[54] C. Dimas and P. P. Sotiriadis, "Electrical impedance tomography image reconstruction for adjacent and opposite strategy using FEMM and EIDORS simulation models," in *2018 7th International Conference on Modern Circuits and Systems Technologies (MOCAST)*, Thessaloniki, May 2018, pp. 1–4. doi: 10.1109/MOCAST.2018.8376604.

[55] B. M. Graham, “Enhancements in electrical impedance tomography (EIT) image reconstruction for 3D lung imaging,” 2007.

[56] J. Malmivuo and R. Plonsey, “Bioelectromagnetism. 26. Impedance Tomography,” 1995, pp. 420–427.

[57] H. Rajaguru, P. Rathinam, and R. Singaravelu, “Electrical impedance tomography (EIT) and its medical applications: a review,” *Int J Soft Comp Eng*, vol. 3, pp. 193–8, Jan. 2013.

[58] S.-J. Park, J. Kim, M. Chu, and M. Khine, “Highly Flexible Wrinkled Carbon Nanotube Thin Film Strain Sensor to Monitor Human Movement,” *Adv. Mater. Technol.*, vol. 1, no. 5, p. 1600053, Aug. 2016, doi: 10.1002/admt.201600053.

[59] D. Vollath, F. D. Fischer, and D. Holec, “Surface energy of nanoparticles – influence of particle size and structure,” *Beilstein J. Nanotechnol.*, vol. 9, no. 1, pp. 2265–2276, Aug. 2018, doi: 10.3762/bjnano.9.211.

[60] Y. Zhou *et al.*, “Significant Stretchability Enhancement of a Crack-Based Strain Sensor Combined with High Sensitivity and Superior Durability for Motion Monitoring,” *ACS Appl. Mater. Interfaces*, vol. 11, no. 7, pp. 7405–7414, Feb. 2019, doi: 10.1021/acsami.8b20768.

[61] S. Zhang *et al.*, “Highly stretchable, sensitive, and flexible strain sensors based on silver nanoparticles/carbon nanotubes composites,” *Journal of Alloys and Compounds*, vol. 652, pp. 48–54, Dec. 2015, doi: 10.1016/j.jallcom.2015.08.187.

[62] C. Liu, S. Han, Z. Du, Y. Liu, and C. Liu, “Highly sensitive wearable strain sensors using copper nanowires and elastomers,” in *2018 International Conference on Electronics Packaging and iMAPS All Asia Conference (ICEP-IAAC)*, Apr. 2018, pp. 333–338. doi: 10.23919/ICEP.2018.8374317.

[63] Z. Yang *et al.*, “Simultaneously Detecting Subtle and Intensive Human Motions Based on a Silver Nanoparticles Bridged Graphene Strain Sensor,” *ACS Appl. Mater. Interfaces*, vol. 10, no. 4, pp. 3948–3954, Jan. 2018, doi: 10.1021/acsami.7b16284.

[64] K.-H. Kim, N.-S. Jang, S.-H. Ha, J. H. Cho, and J.-M. Kim, “Highly Sensitive and Stretchable Resistive Strain Sensors Based on Microstructured Metal Nanowire/Elastomer Composite Films,” *Small*, vol. 14, no. 14, p. 1704232, 2018, doi: 10.1002/smll.201704232.

[65] S.-H. Ha, S.-H. Ha, M.-B. Jeon, J. H. Cho, and J.-M. Kim, “Highly sensitive and selective multidimensional resistive strain sensors based on a stiffness-variant stretchable substrate,” *Nanoscale*, vol. 10, no. 11, pp. 5105–5113, 2018, doi: 10.1039/C7NR08118A.

[66] H. Hu and R. G. Larson, “Marangoni Effect Reverses Coffee-Ring Depositions,” *J. Phys. Chem. B*, vol. 110, no. 14, pp. 7090–7094, Apr. 2006, doi: 10.1021/jp0609232.

[67] C.-J. Lee *et al.*, “Crack-induced Ag nanowire networks for transparent, stretchable, and highly sensitive strain sensors,” *Scientific Reports*, vol. 7, no. 1, p. 7959, Aug. 2017, doi: 10.1038/s41598-017-08484-y.

[68] S. Ryu *et al.*, “Extremely Elastic Wearable Carbon Nanotube Fiber Strain Sensor for Monitoring of Human Motion,” *ACS Nano*, vol. 9, no. 6, pp. 5929–5936, Jun. 2015, doi: 10.1021/acsnano.5b00599.

[69] M. D. Tyona, “A theoritical study on spin coating technique,” *Advances in materials Research*, vol. 2, no. 4, pp. 195–208, Dec. 2013, doi: 10.12989/AMR.2013.2.4.195.

[70] B. D. Washo, “Rheology and Modeling of the Spin Coating Process,” *IBM J. Res. & Dev.*, vol. 21, no. 2, pp. 190–198, Mar. 1977, doi: 10.1147/rd.212.0190.

[71] M. Berber, V. Bulto, R. Kliß, and H. Hahn, “Transparent nanocrystalline ZnO films prepared by spin coating,” *Scripta Materialia*, vol. 53, no. 5, pp. 547–551, Sep. 2005, doi: 10.1016/j.scriptamat.2005.04.047.

[72] W. Zhang, R. Zhu, V. Nguyen, and R. Yang, “Highly sensitive and flexible strain sensors based on vertical zinc oxide nanowire arrays,” *Sensors and Actuators A: Physical*, vol. 205, pp. 164–169, Jan. 2014, doi: 10.1016/j.sna.2013.11.004.

[73] N. P. Pham, E. Boellard, P. M. Sarro, and J. N. Burghartz, “Spin, Spray coating and Electrodeposition of photoresist for MEMS structures – A comparison,” p. 7.

[74] A. R. Madaria, A. Kumar, F. N. Ishikawa, and C. Zhou, “Uniform, highly conductive, and patterned transparent films of a percolating silver nanowire network on rigid and flexible substrates using a dry transfer technique,” *Nano Research*, vol. 3, no. 8, pp. 564–573, Aug. 2010, doi: 10.1007/s12274-010-0017-5.

[75] J. Lee *et al.*, “Stretchable Strain Sensor based on Metal Nanoparticle Thin Film for Human Motion Detection,” p. 9.

[76] L. Lu *et al.*, “A flexible and self-formed sandwich structure strain sensor based on AgNW decorated electrospun fibrous mats with excellent sensing capability and good oxidation inhibition properties,” *J. Mater. Chem. C*, vol. 5, no. 28, pp. 7035–7042, 2017, doi: 10.1039/C7TC02429K.

[77] S. Wang *et al.*, “Controllable synthesis of nickel nanowires and its application in high sensitivity, stretchable strain sensor for body motion sensing,” *J. Mater. Chem. C*, vol. 6, no. 17, pp. 4737–4745, 2018, doi: 10.1039/C7TC05970A.

[78] A. N. Obraztsov, E. A. Obraztsova, A. V. Tyurnina, and A. A. Zolotukhin, “Chemical vapor deposition of thin graphite films of nanometer thickness,” *Carbon*, vol. 45, no. 10, pp. 2017–2021, Sep. 2007, doi: 10.1016/j.carbon.2007.05.028.

[79] G. Che, B. B. Lakshmi, C. R. Martin, E. R. Fisher, and R. S. Ruoff, “Chemical Vapor Deposition Based Synthesis of Carbon Nanotubes and Nanofibers Using a Template Method,” *Chem. Mater.*, vol. 10, no. 1, pp. 260–267, Jan. 1998, doi: 10.1021/cm970412f.

[80] P. Karfa, K. Chandra Majhi, and R. Madhuri, “Chapter 2 - Synthesis of two-dimensional nanomaterials,” in *Two-Dimensional Nanostructures for Biomedical Technology*, R. Khan and S. Barua, Eds. Elsevier, 2020, pp. 35–71. doi: 10.1016/B978-0-12-817650-4.00002-4.

[81] B. Chen *et al.*, “Low-Cost Flexible Strain Sensor Based on Thick CVD Graphene,” *NANO*, vol. 13, no. 11, p. 1850126, Nov. 2018, doi: 10.1142/S1793292018501266.

[82] Daewoong Jung, K. H. Lee, L. J. Overzet, and G. S. Lee, “A high sensitive strain sensor using a multi-walled carbon nanotube sheet,” in *2012 12th IEEE International Conference on Nanotechnology (IEEE-NANO)*, Birmingham, United Kingdom, Aug. 2012, pp. 1–4. doi: 10.1109/NANO.2012.6321949.

[83] M. Mohammed Ali *et al.*, “Printed strain sensor based on silver nanowire/silver flake composite on flexible and stretchable TPU substrate,” *Sensors and Actuators A: Physical*, vol. 274, pp. 109–115, May 2018, doi: 10.1016/j.sna.2018.03.003.

[84] S. Khan, L. Lorenzelli, and R. S. Dahiya, “Screen printed flexible pressure sensors skin,” in *25th Annual SEMI Advanced Semiconductor Manufacturing Conference (ASMC 2014)*, Saratoga Springs, NY, May 2014, pp. 219–224. doi: 10.1109/ASMC.2014.6847002.

[85] Z. Taleat, A. Khoshroo, and M. Mazloum-Ardakani, “Screen-printed electrodes for biosensing: a review (2008–2013),” *Microchim Acta*, vol. 181, no. 9–10, pp. 865–891, Jul. 2014, doi: 10.1007/s00604-014-1181-1.

[86] H. F. Castro, V. Correia, N. Pereira, P. Costab, J. Oliveiraa, and S. Lanceros-Méndez, “Printed Wheatstone bridge with embedded polymer based piezoresistive sensors for strain sensing applications,” *Additive Manufacturing*, vol. 20, pp. 119–125, Mar. 2018, doi: 10.1016/j.addma.2018.01.004.

[87] M. Gonzalez, F. Axisa, M. V. Bulcke, D. Brosteaux, B. Vandevelde, and J. Vanfleteren, “Design of metal interconnects for stretchable electronic circuits,” *Microelectronics Reliability*, vol. 48, no. 6, pp. 825–832, Jun. 2008, doi: 10.1016/j.microrel.2008.03.025.

[88] D. S. Gray, J. Tien, and C. S. Chen, “High-Conductivity Elastomeric Electronics,” *Advanced Materials*, vol. 16, no. 5, pp. 393–397, doi: 10.1002/adma.200306107.

[89] J. C. Yeo, H. K. Yap, W. Xi, Z. Wang, R. C.-H. Yeow, and C. T. Lim, “Flexible and Stretchable Strain Sensing Actuator for Wearable Soft Robotic Applications,” *Advanced Materials Technologies*, vol. 1, May 2016, doi: 10.1002/admt.201600018.

[90] U. Hashim *et al.*, “Comparison of drop casting vs. spray pyrolysis MWCNTs technique for surface modification based interdigitated electrode,” in *2015 2nd*

International Conference on Biomedical Engineering (ICoBE), Penang, Malaysia, Mar. 2015, pp. 1–3. doi: 10.1109/ICoBE.2015.7235903.

[91] A. Mishra, N. Bhatt, and A. K. Bajpai, "Nanostructured superhydrophobic coatings for solar panel applications," in *Nanomaterials-Based Coatings*, Elsevier, 2019, pp. 397–424. doi: 10.1016/B978-0-12-815884-5.00012-0.

[92] Q. Zhang, D. Sando, and V. Nagarajan, "Chemical route derived bismuth ferrite thin films and nanomaterials," *J. Mater. Chem. C*, vol. 4, no. 19, pp. 4092–4124, May 2016, doi: 10.1039/C6TC00243A.

[93] S. R. Larimi, H. Rezaei Nejad, M. Oyatsi, A. O'Brien, M. Hoorfar, and H. Najjaran, "Low-cost ultra-stretchable strain sensors for monitoring human motion and bio-signals," *Sensors and Actuators A: Physical*, vol. 271, pp. 182–191, Mar. 2018, doi: 10.1016/j.sna.2018.01.028.

[94] S. Chen, Y. Wei, X. Yuan, Y. Lin, and L. Liu, "A highly stretchable strain sensor based on a graphene/silver nanoparticle synergic conductive network and a sandwich structure," *J. Mater. Chem. C*, vol. 4, no. 19, pp. 4304–4311, 2016, doi: 10.1039/C6TC00300A.

[95] C. S. Boland *et al.*, "Sensitive, High-Strain, High-Rate Bodily Motion Sensors Based on Graphene–Rubber Composites," *ACS Nano*, vol. 8, no. 9, pp. 8819–8830, Sep. 2014, doi: 10.1021/nn503454h.

[96] J. Lee *et al.*, "Transparent, Flexible Strain Sensor Based on a Solution-Processed Carbon Nanotube Network," *ACS Appl. Mater. Interfaces*, vol. 9, no. 31, pp. 26279–26285, Aug. 2017, doi: 10.1021/acsami.7b03184.

[97] M. Eslamian, "Spray-on Thin Film PV Solar Cells: Advances, Potentials and Challenges," *Coatings*, vol. 4, no. 1, pp. 60–84, Jan. 2014, doi: 10.3390/coatings4010060.

[98] H.-J. Kim, A. Thukral, and C. Yu, "Highly Sensitive and Very Stretchable Strain Sensor Based on a Rubbery Semiconductor," *ACS Appl. Mater. Interfaces*, vol. 10, no. 5, pp. 5000–5006, Feb. 2018, doi: 10.1021/acsami.7b17709.

[99] X. Xiao *et al.*, "High-Strain Sensors Based on ZnO Nanowire/Polystyrene Hybridized Flexible Films," *Adv. Mater.*, vol. 23, no. 45, pp. 5440–5444, Dec. 2011, doi: 10.1002/adma.201103406.

[100] Y. Wang *et al.*, "Super-Elastic Graphene Ripples for Flexible Strain Sensors," *ACS Nano*, vol. 5, no. 5, pp. 3645–3650, May 2011, doi: 10.1021/nn103523t.

[101] M. Amjadi, Y. J. Yoon, and I. Park, "Ultra-stretchable and skin-mountable strain sensors using carbon nanotubes–Ecoflex nanocomposites," *Nanotechnology*, vol. 26, no. 37, p. 375501, Sep. 2015, doi: 10.1088/0957-4484/26/37/375501.

[102] K. K. Kim, I. H. Ha, and S. H. Ko, "Flexible and highly sensitive multi-dimensional strain sensor with intersecting metal nanowire arrays," in *2017 14th International*

Conference on Ubiquitous Robots and Ambient Intelligence (URAI), Jun. 2017, pp. 62–64. doi: 10.1109/URAI.2017.7992885.

[103] X. Wang, X. Xu, Z. Zhou, and J. Gou, "FLEXIBLE STRAIN SENSORS BASED ON PRINTED CARBON NANOTUBE LAYERS ON POLYDIMETHYLSILOXANE," p. 8, 2017.

[104] S. Ryu *et al.*, "Extremely Elastic Wearable Carbon Nanotube Fiber Strain Sensor for Monitoring of Human Motion," *ACS Nano*, vol. 9, no. 6, pp. 5929–5936, Jun. 2015, doi: 10.1021/acsnano.5b00599.

[105] Q. Zhang *et al.*, "Highly Sensitive and Stretchable Strain Sensor Based on Ag@CNTs," *Nanomaterials*, vol. 7, no. 12, p. 424, Dec. 2017, doi: 10.3390/nano7120424.

[106] J. Li and J.-K. Kim, "Percolation threshold of conducting polymer composites containing 3D randomly distributed graphite nanoplatelets," *Composites Science and Technology*, vol. 67, pp. 2114–2120, Aug. 2007, doi: 10.1016/j.compscitech.2006.11.010.

[107] J. Du *et al.*, "Comparison of electrical properties between multi-walled carbon nanotube and graphene nanosheet/high density polyethylene composites with a segregated network structure," *Carbon*, vol. 49, no. 4, pp. 1094–1100, Apr. 2011, doi: 10.1016/j.carbon.2010.11.013.

[108] A. V. Kyrylyuk, M. C. Hermant, T. Schilling, B. Klumperman, C. E. Koning, and P. van der Schoot, "Controlling electrical percolation in multicomponent carbon nanotube dispersions," *Nature Nanotech*, vol. 6, no. 6, pp. 364–369, Jun. 2011, doi: 10.1038/nnano.2011.40.

[109] S. Wu *et al.*, "Aligning Graphene Nanoplatelets with an External Electric Field to Improve Multifunctional Properties of Epoxy Nanocomposites," *Carbon*, vol. 94, pp. 607–618, Jul. 2015, doi: 10.1016/j.carbon.2015.07.026.

[110] M. Sureshkumar, H. Y. Na, K. H. Ahn, and S. J. Lee, "Conductive Nanocomposites Based on Polystyrene Microspheres and Silver Nanowires by Latex Blending," *ACS Appl. Mater. Interfaces*, vol. 7, no. 1, pp. 756–764, Jan. 2015, doi: 10.1021/am5071392.

[111] K. Chu, D. Kim, Y. Sohn, S. Lee, C. Moon, and S. Park, "Electrical and Thermal Properties of Carbon-Nanotube Composite for Flexible Electric Heating-Unit Applications," *IEEE Electron Device Lett.*, vol. 34, no. 5, pp. 668–670, May 2013, doi: 10.1109/LED.2013.2249493.

[112] Z. Tang *et al.*, "Highly-Stretchable Core-Sheath Fibers via Wet-Spinning for Wearable Strain Sensors," *ACS Applied Materials & Interfaces*, vol. 10, Jan. 2018, doi: 10.1021/acsami.7b18677.

[113] A. Nogales *et al.*, "Low Percolation Threshold in Nanocomposites Based on Oxidized Single Wall Carbon Nanotubes and Poly(butylene terephthalate)," *Macromolecules*, vol. 37, no. 20, pp. 7669–7672, Oct. 2004, doi: 10.1021/ma049440r.

[114] I. Moreno, N. Navascues, M. Arruebo, S. Irusta, and J. Santamaria, “Facile preparation of transparent and conductive polymer films based on silver nanowire/polycarbonate nanocomposites,” *Nanotechnology*, vol. 24, no. 27, p. 275603, Jun. 2013, doi: 10.1088/0957-4484/24/27/275603.

[115] N Yogeswaran, “Tuning electrical conductivity of CNT-PDMS nanocomposites for flexible electronic applications - IEEE Conference Publication,” 2015. https://ieeexplore.ieee.org/document/7388911 (accessed May 28, 2020).

[116] S. Burzhuev, A. Dana, and B. Orta?, “Laser synthesized gold nanoparticles for high sensitive strain gauges,” 2013, doi: 10.1016/j.sna.2013.08.034.

[117] E. Skotadis, D. Mousadakos, J. Tanner, D. Tsoukalas, and P. Broutas, “Flexible platinum nanoparticle strain sensors,” in *2013 Proceedings of the European Solid-State Device Research Conference (ESSDERC)*, Bucharest, Romania, Sep. 2013, pp. 354–357. doi: 10.1109/ESSDERC.2013.6818891.

[118] M. Zheng, W. Li, M. Xu, N. Xu, and B. Xie, “Strain sensors based on chromium nanoparticle arrays,” *Nanoscale*, vol. 6, no. 8, pp. 3930–3933, 2013, doi: 10.1039/C3NR04135B.

[119] A. Y. C. Yu, “Electron tunneling and contact resistance of metal-silicon contact barriers,” *Solid-State Electronics*, vol. 13, no. 2, pp. 239–247, 1970, doi: 10.1016/0038-1101(70)90056-0.

[120] J. G. Simmons, “Generalized Formula for the Electric Tunnel Effect between Similar Electrodes Separated by a Thin Insulating Film,” *Journal of Applied Physics*, 1963, doi: 10.1063/1.1702682.

[121] M. Amjadi, K.-U. Kyung, I. Park, and M. Sitti, “Stretchable, Skin-Mountable, and Wearable Strain Sensors and Their Potential Applications: A Review,” *Advanced Functional Materials*, vol. 26, no. 11, pp. 1678–1698, doi: 10.1002/adfm.201504755.

[122] R. Rahman and P. Servati, “Effects of inter-tube distance and alignment on tunnelling resistance and strain sensitivity of nanotube/polymer composite films,” *Nanotechnology*, vol. 23, no. 5, p. 055703, 2012, doi: 10.1088/0957-4484/23/5/055703.

[123] C. Li, E. T. Thostenson, and T.-W. Chou, “Dominant role of tunneling resistance in the electrical conductivity of carbon nanotube–based composites,” *Appl. Phys. Lett.*, vol. 91, no. 22, p. 223114, Nov. 2007, doi: 10.1063/1.2819690.

[124] F. Pawlek and D. Rogalla, “The electrical resistivity of silver, copper, aluminium, and zinc as a function of purity in the range 4–298° K,” *Cryogenics*, vol. 6, no. 1, pp. 14–20, Feb. 1966, doi: 10.1016/S0011-2275(96)90056-9.

[125] D. Simien, J. A. Fagan, W. Luo, J. F. Douglas, K. Migler, and J. Obrzut, “Influence of Nanotube Length on the Optical and Conductivity Properties of Thin Single-Wall Carbon

Nanotube Networks," *ACS Nano*, vol. 2, no. 9, pp. 1879–1884, Sep. 2008, doi: 10.1021/nn800376x.

[126] D. Langley, G. Giusti, C. Mayousse, C. Celle, D. Bellet, and J.-P. Simonato, "Flexible transparent conductive materials based on silver nanowire networks: a review," *Nanotechnology*, vol. 24, no. 45, p. 452001, Nov. 2013, doi: 10.1088/0957-4484/24/45/452001.

[127] S. Sepulveda and S. G. Cloutier, "Figures of Merit for High-Performance Transparent Electrodes Using Dip-Coated Silver Nanowire Networks," *Journal of Nanomaterials*, vol. 2012, Aug. 2012, doi: 10.1155/2012/286104.

[128] Y. Cao *et al.*, "A technique for controlling the alignment of silver nanowires with an electric field," *Nanotechnology*, vol. 17, no. 9, p. 2378, 2006, doi: 10.1088/0957-4484/17/9/050.

[129] Y. Ikada, "Surface modification of polymers for medical applications," *Biomaterials*, vol. 15, no. 10, pp. 725–736, Aug. 1994, doi: 10.1016/0142-9612(94)90025-6.

[130] K. R. B. Jr, A. G. Russell, P. A. Blake, and D. K. Roper, "Gold nanoparticles reducedin situand dispersed in polymer thin films: optical and thermal properties," *Nanotechnology*, vol. 23, no. 37, p. 375703, Aug. 2012, doi: 10.1088/0957-4484/23/37/375703.

[131] C.-X. Liu and J.-W. Choi, "Strain-Dependent Resistance of PDMS and Carbon Nanotubes Composite Microstructures," *IEEE Trans. Nanotechnology*, vol. 9, no. 5, pp. 590–595, Sep. 2010, doi: 10.1109/TNANO.2010.2060350.

[132] S. Yao, X. Nie, X. Yu, B. Song, and J. Blecke, "Highly Stretchable Miniature Strain Sensor for Large Dynamic Strain Measurement," *IEEE Sens. Lett.*, vol. 1, no. 3, pp. 1–4, Jun. 2017, doi: 10.1109/LSENS.2017.2709943.

[133] Chao-Xuan Liu and Jin-Woo Choi, "An embedded PDMS nanocomposite strain sensor toward biomedical applications," in *2009 Annual International Conference of the IEEE Engineering in Medicine and Biology Society*, Minneapolis, MN, Sep. 2009, pp. 6391–6394. doi: 10.1109/IEMBS.2009.5333873.

[134] X. Fu, M. Ramos, A. M. Al-Jumaily, A. Meshkinzar, and X. Huang, "Stretchable strain sensor facilely fabricated based on multi-wall carbon nanotube composites with excellent performance," *J Mater Sci*, vol. 54, no. 3, pp. 2170–2180, Feb. 2019, doi: 10.1007/s10853-018-2954-4.

[135] X. Song, S. Liu, Z. Gan, Q. Lv, H. Cao, and H. Yan, "Controllable fabrication of carbon nanotube-polymer hybrid thin film for strain sensing," *Microelectronic Engineering*, vol. 86, no. 11, pp. 2330–2333, Nov. 2009, doi: 10.1016/j.mee.2009.04.012.

[136] H. Lee, D. Kwon, H. Cho, I. Park, and J. Kim, “Soft Nanocomposite Based Multi-point, Multi-directional Strain Mapping Sensor Using Anisotropic Electrical Impedance Tomography,” *Scientific Reports*, vol. 7, p. 39837, Jan. 2017, doi: 10.1038/srep39837.

[137] J.-B. Chossat, H.-S. Shin, Y.-L. Park, and V. Duchaine, “Soft Tactile Skin Using an Embedded Ionic Liquid and Tomographic Imaging,” *Journal of Mechanisms and Robotics*, vol. 7, no. 2, p. 021008, May 2015, doi: 10.1115/1.4029474.

[138] P. Nie, D. Zhang, Y. Chen, S. Lu, and J. Han, “Carbon nanotubes thin film sensor and characterization of its strain sensing,” vol. 42, pp. 677–684, Apr. 2016, doi: 10.13700/j.bh.1001-5965.2015.0271.

[139] H.-C. Jung *et al.*, “CNT/PDMS composite flexible dry electrodesfor long-term ECG monitoring,” *IEEE Transactions on Biomedical Engineering - IEEE TRANS BIOMED ENG*, vol. 59, pp. 1472–1479, May 2012, doi: 10.1109/TBME.2012.2190288.

[140] X. Guo *et al.*, “Highly stretchable strain sensor based on SWCNTs/CB synergistic conductive network for wearable human-activity monitoring and recognition,” *Smart Mater. Struct.*, vol. 26, no. 9, p. 095017, Sep. 2017, doi: 10.1088/1361-665X/aa79c3.

[141] S. Sun *et al.*, “A wearable strain sensor based on the ZnO/graphene nanoplatelets nanocomposite with large linear working range,” *J Mater Sci*, vol. 54, no. 9, pp. 7048–7061, May 2019, doi: 10.1007/s10853-019-03354-6.

[142] S.-R. Kim, J.-H. Kim, and J.-W. Park, “Wearable and Transparent Capacitive Strain Sensor with High Sensitivity Based on Patterned Ag Nanowire Networks,” *ACS Applied Materials & Interfaces*, vol. 9, no. 31, pp. 26407–26416, Aug. 2017, doi: 10.1021/acsami.7b06474.

[143] R. Matsuzaki, T. Keating, A. Todoroki, and N. Hiraoka, “Rubber-based strain sensor fabricated using photolithography for intelligent tires,” *Sensors and Actuators A: Physical*, vol. 148, no. 1, pp. 1–9, Nov. 2008, doi: 10.1016/j.sna.2008.08.001.

[144] J. Li, J. P. Longtin, S. Tankiewicz, A. Gouldstone, and S. Sampath, “Interdigital capacitive strain gauges fabricated by direct-write thermal spray and ultrafast laser micromachining,” *Sensors and Actuators A: Physical*, vol. 133, no. 1, pp. 1–8, Jan. 2007, doi: 10.1016/j.sna.2006.04.008.

[145] K. T. Fujimoto *et al.*, “Aerosol jet printed capacitive strain gauge for soft structural materials,” *npj Flex Electron*, vol. 4, no. 1, pp. 1–9, Nov. 2020, doi: 10.1038/s41528-020-00095-4.

[146] L. Cai *et al.*, “Super-stretchable, Transparent Carbon Nanotube-Based Capacitive Strain Sensors for Human Motion Detection,” *Scientific Reports*, vol. 3, p. 3048, Oct. 2013, doi: 10.1038/srep03048.

[147] U.-H. Shin, D.-W. Jeong, S.-M. Park, S.-H. Kim, H. W. Lee, and J.-M. Kim, “Highly stretchable conductors and piezocapacitive strain gauges based on simple contact-transfer patterning of carbon nanotube forests,” *Carbon*, vol. 80, pp. 396–404, Dec. 2014, doi: 10.1016/j.carbon.2014.08.079.

[148] D. J. Cohen, D. Mitra, K. Peterson, and M. M. Maharbiz, “A Highly Elastic, Capacitive Strain Gauge Based on Percolating Nanotube Networks,” *Nano Letters*, vol. 12, no. 4, pp. 1821–1825, Apr. 2012, doi: 10.1021/nl204052z.

[149] S. Yao and Y. Zhu, “Wearable multifunctional sensors using printed stretchable conductors made of silver nanowires,” *Nanoscale*, vol. 6, no. 4, p. 2345, 2014, doi: 10.1039/c3nr05496a.

[150] H. Nakamoto, H. Ootaka, M. Tada, I. Hirata, F. Kobayashi, and F. Kojima, “Stretchable Strain Sensor With Anisotropy and Application for Joint Angle Measurement,” *IEEE Sensors J.*, vol. 16, no. 10, pp. 3572–3579, May 2016, doi: 10.1109/JSEN.2016.2535489.

[151] Y. Lu *et al.*, “Transformable liquid-metal nanomedicine,” *Nat Commun*, vol. 6, no. 1, p. 10066, Dec. 2015, doi: 10.1038/ncomms10066.

[152] J. Shao, L. Yu, A. L. Skov, and A. E. Daugaard, “Highly stretchable conductive MWCNT–PDMS composite with self-enhanced conductivity,” *J. Mater. Chem. C*, vol. 8, no. 38, pp. 13389–13395, Oct. 2020, doi: 10.1039/D0TC01735C.

[153] Z. Lei, B. Chen, Y.-M. Koo, and D. R. MacFarlane, “Introduction: Ionic Liquids,” *Chem. Rev.*, vol. 117, no. 10, pp. 6633–6635, May 2017, doi: 10.1021/acs.chemrev.7b00246.

[154] G. Keulemans, P. Pelgrims, M. Bakula, F. Ceyssens, and R. Puers, “An Ionic Liquid Based Strain Sensor for Large Displacements,” *Procedia Engineering*, vol. 87, pp. 1123–1126, Jan. 2014, doi: 10.1016/j.proeng.2014.11.362.

[155] S. Kim, J. Lee, and B. Choi, “Stretching and Twisting Sensing With Liquid-Metal Strain Gauges Printed on Silicone Elastomers,” *IEEE Sensors J.*, vol. 15, no. 11, pp. 6077–6078, Nov. 2015, doi: 10.1109/JSEN.2015.2462314.

[156] S.-H. Zhang, F.-X. Wang, J.-J. Li, H.-D. Peng, J.-H. Yan, and G.-B. Pan, “Wearable Wide-Range Strain Sensors Based on Ionic Liquids and Monitoring of Human Activities,” *Sensors*, vol. 17, no. 11, p. 2621, Nov. 2017, doi: 10.3390/s17112621.

[157] Yun Zhu, Chen Chao, Ching-Hsiang Cheng, and W. W.-F. Leung, “A Novel Ionic-Liquid Strain Sensor for Large-Strain Applications,” *IEEE Electron Device Lett.*, vol. 30, no. 4, pp. 337–339, Apr. 2009, doi: 10.1109/LED.2009.2013884.

[158] Y. Wang, S. Gong, S. Jia Wang, G. P. Simon, and W. Cheng, “Volume-invariant ionic liquid microbands as highly durable wearable biomedical sensors,” *Materials Horizons*, vol. 3, no. 3, pp. 208–213, 2016, doi: 10.1039/C5MH00284B.

[159] J.-B. Chossat, Y.-L. Park, R. J. Wood, and V. Duchaine, “A Soft Strain Sensor Based on Ionic and Metal Liquids,” *IEEE Sensors Journal*, vol. 13, no. 9, pp. 3405–3414, Sep. 2013, doi: 10.1109/JSEN.2013.2263797.

[160] Y.-N. Cheung, Y. Zhu, C.-H. Cheng, C. Chao, and W. W.-F. Leung, “A novel fluidic strain sensor for large strain measurement,” *Sensors and Actuators A: Physical*, vol. 147, no. 2, pp. 401–408, Oct. 2008, doi: 10.1016/j.sna.2008.05.013.

[161] S. He, S. Feng, A. Nag, N. Afsarimanesh, T. Han, and S. C. Mukhopadhyay, “Recent Progress in 3D Printed Mold-Based Sensors,” *Sensors (Basel)*, vol. 20, no. 3, p. 703, Jan. 2020, doi: 10.3390/s20030703.

[162] J. B. Chossat, Y. Tao, V. Duchaine, and Y. L. Park, “Wearable soft artificial skin for hand motion detection with embedded microfluidic strain sensing,” in *2015 IEEE International Conference on Robotics and Automation (ICRA)*, May 2015, pp. 2568–2573. doi: 10.1109/ICRA.2015.7139544.

[163] C. W. Park *et al.*, “Photolithography-Based Patterning of Liquid Metal Interconnects for Monolithically Integrated Stretchable Circuits,” *ACS Appl. Mater. Interfaces*, vol. 8, no. 24, pp. 15459–15465, Jun. 2016, doi: 10.1021/acsami.6b01896.

[164] S. Zhang, B. Wang, J. Jiang, K. Wu, C. F. Guo, and Z. Wu, “High-Fidelity Conformal Printing of 3D Liquid Alloy Circuits for Soft Electronics,” *ACS Appl. Mater. Interfaces*, vol. 11, no. 7, pp. 7148–7156, Feb. 2019, doi: 10.1021/acsami.8b20595.

[165] J. Yang *et al.*, “Defect-free, high resolution patterning of liquid metals using reversibly sealed, reusable polydimethylsiloxane microchannels for flexible electronic applications,” *J. Mater. Chem. C*, vol. 5, no. 27, pp. 6790–6797, Jul. 2017, doi: 10.1039/C7TC01918A.

[166] D. Y. Choi *et al.*, “Highly Stretchable, Hysteresis-Free Ionic Liquid-Based Strain Sensor for Precise Human Motion Monitoring,” *ACS Appl. Mater. Interfaces*, vol. 9, no. 2, pp. 1770–1780, Jan. 2017, doi: 10.1021/acsami.6b12415.

[167] S. Xu *et al.*, “Biocompatible Soft Fluidic Strain and Force Sensors for Wearable Devices,” *Advanced Functional Materials*, vol. 29, no. 7, p. 1807058, 2018, doi: https://doi.org/10.1002/adfm.201807058.

[168] J. Chen *et al.*, “Superelastic, Sensitive, and Low Hysteresis Flexible Strain Sensor Based on Wave-Patterned Liquid Metal for Human Activity Monitoring,” *ACS Appl. Mater. Interfaces*, vol. 12, no. 19, pp. 22200–22211, May 2020, doi: 10.1021/acsami.0c04709.

[169] C. Shi *et al.*, “Stretchable, Rehealable, Recyclable, and Reconfigurable Integrated Strain Sensor for Joint Motion and Respiration Monitoring,” *Research*, vol. 2021, Jul. 2021, doi: 10.34133/2021/9846036.

[170] X. Han, W. Lu, W. Yu, H. Xu, S. Bi, and H. Cai, “Conductive and adhesive gluten ionic skin for eco-friendly strain sensor,” *J Mater Sci*, vol. 56, no. 5, pp. 3970–3980, Feb. 2021, doi: 10.1007/s10853-020-05508-3.

[171] H. Qin, R. E. Owyeung, S. R. Sonkusale, and M. J. Panzer, “Highly stretchable and nonvolatile gelatin-supported deep eutectic solvent gel electrolyte-based ionic skins for strain and pressure sensing,” *J. Mater. Chem. C*, vol. 7, no. 3, pp. 601–608, 2019, doi: 10.1039/C8TC05918G.

[172] D. Hardman, J. Hughes, T. George Thuruthel, K. Gilday, and F. Iida, “3D Printable Sensorized Soft Gelatin Hydrogel for Multi-Material Soft Structures,” *IEEE Robot. Autom. Lett.*, pp. 1–1, 2021, doi: 10.1109/LRA.2021.3072600.

[173] X. Jing, X.-Y. Wang, H.-Y. Mi, and L.-S. Turng, “Stretchable gelatin/silver nanowires composite hydrogels for detecting human motion,” *Materials Letters*, vol. 237, pp. 53–56, Feb. 2019, doi: 10.1016/j.matlet.2018.11.078.

[174] J. P. Gong, “Why are double network hydrogels so tough?,” *Soft Matter*, vol. 6, no. 12, pp. 2583–2590, Jun. 2010, doi: 10.1039/B924290B.

[175] Q. Chen, L. Zhu, C. Zhao, Q. Wang, and J. Zheng, “A Robust, One-Pot Synthesis of Highly Mechanical and Recoverable Double Network Hydrogels Using Thermoreversible Sol-Gel Polysaccharide,” *Adv. Mater.*, vol. 25, no. 30, pp. 4171–4176, Aug. 2013, doi: 10.1002/adma.201300817.

[176] X. Yan *et al.*, “High strength and self-healable gelatin/polyacrylamide double network hydrogels,” *J. Mater. Chem. B*, vol. 5, no. 37, pp. 7683–7691, 2017, doi: 10.1039/C7TB01780D.

[177] W. Hou *et al.*, “Design of injectable agar/NaCl/polyacrylamide ionic hydrogels for high performance strain sensors,” *Carbohydrate Polymers*, vol. 211, pp. 322–328, May 2019, doi: 10.1016/j.carbpol.2019.01.094.

[178] S. Liu and L. Li, “Ultrastretchable and Self-Healing Double-Network Hydrogel for 3D Printing and Strain Sensor,” *ACS Appl. Mater. Interfaces*, vol. 9, no. 31, pp. 26429–26437, Aug. 2017, doi: 10.1021/acsami.7b07445.

[179] H. Sun *et al.*, “Ultra-Stretchable, durable and conductive hydrogel with hybrid double network as high performance strain sensor and stretchable triboelectric nanogenerator,” *Nano Energy*, vol. 76, p. 105035, Oct. 2020, doi: 10.1016/j.nanoen.2020.105035.

[180] M. Xia *et al.*, “Hybrid double-network hydrogel for highly stretchable, excellent sensitive, stabilized, and transparent strain sensors,” *Journal of Biomaterials Science, Polymer Edition*, vol. 32, no. 12, pp. 1548–1563, Aug. 2021, doi: 10.1080/09205063.2021.1922170.

[181] J. Yu *et al.*, “Highly stretchable, transparent and conductive double-network ionic hydrogels for strain and pressure sensors with ultrahigh sensitivity,” *J. Mater. Chem. C*, vol. 9, no. 10, pp. 3635–3641, 2021, doi: 10.1039/D0TC05242F.

[182] H. Li, H. Zheng, Y. J. Tan, S. B. Tor, and K. Zhou, “Development of an Ultrastretchable Double-Network Hydrogel for Flexible Strain Sensors,” *ACS Appl. Mater. Interfaces*, vol. 13, no. 11, pp. 12814–12823, Mar. 2021, doi: 10.1021/acsami.0c19104.

[183] N. J. D. Nagelkerke, “A Note on a General Definition of the Coefficient of Determination,” *Biometrika*, 1991, doi: 10.2307/2337038.

[184] “Sensors and Signal Conditioning, 2nd Edition | Wiley,” *Wiley.com*. https://www.wiley.com/en-sg/Sensors+and+Signal+Conditioning%2C+2nd+Edition-p-9780471332329 (accessed Apr. 29, 2020).

[185] C. Medeiros and M. Wanderley, “A Comprehensive Review of Sensors and Instrumentation Methods in Devices for Musical Expression,” *Sensors*, vol. 14, no. 8, pp. 13556–13591, Jul. 2014, doi: 10.3390/s140813556.

[186] D. Langley, “Silver nanowire networks: effects of percolation and thermal annealing on physical properties,” p. 153.

[187] “Highly Stretchable, Directionally Oriented Carbon Nanotube/PDMS Conductive Films with Enhanced Sensitivity as Wearable Strain Sensors_百度学术.” http://xueshu.baidu.com/usercenter/paper/show?paperid=100h0tu07j510ab0xf6f04g0t2539557&site=xueshu_se (accessed Apr. 30, 2020).

[188] Z. Yu *et al.*, “A Composite Elastic Conductor with High Dynamic Stability Based on 3D-Calabash Bunch Conductive Network Structure for Wearable Devices,” *Advanced Electronic Materials*, vol. 4, p. 1800137, Jun. 2018, doi: 10.1002/aelm.201800137.

[189] R. Tong, G. Chen, J. Tian, and M. He, “Highly Stretchable, Strain-Sensitive, and Ionic-Conductive Cellulose-Based Hydrogels for Wearable Sensors,” *Polymers*, vol. 11, no. 12, Art. no. 12, Dec. 2019, doi: 10.3390/polym11122067.

[190] A. P. Mouritz, Ed., “5 - Mechanical and durability testing of aerospace materials,” in *Introduction to Aerospace Materials*, Woodhead Publishing, 2012, pp. 91–127. doi: 10.1533/9780857095152.91.

[191] Y. Wu *et al.*, “Liquid metal fiber composed of a tubular channel as a high-performance strain sensor,” *J. Mater. Chem. C*, vol. 5, no. 47, pp. 12483–12491, 2017, doi: 10.1039/C7TC04311B.

[192] H. T. Banks, “A brief review of some approaches to hysteresis in viscoelastic polymers,” *Nonlinear Analysis: Theory, Methods & Applications*, vol. 69, no. 3, pp. 807–815, Aug. 2008, doi: 10.1016/j.na.2008.02.103.

[193] J. A. Gimbel, J. J. Sarver, and L. J. Soslowsky, “The Effect of Overshooting the Target Strain on Estimating Viscoelastic Properties From Stress Relaxation Experiments,” *J Biomech Eng*, vol. 126, no. 6, pp. 844–848, Dec. 2004, doi: 10.1115/1.1824132.

[194] A. Chhetry, Md. Sharifuzzaman, H. Yoon, S. Sharma, X. Xuan, and J. Y. Park, “MoS2-Decorated Laser-Induced Graphene for a Highly Sensitive, Hysteresis-free, and Reliable Piezoresistive Strain Sensor,” *ACS Appl. Mater. Interfaces*, vol. 11, no. 25, pp. 22531–22542, Jun. 2019, doi: 10.1021/acsami.9b04915.

[195] T. H. Park *et al.*, “Block copolymer structural color strain sensor,” *NPG Asia Mater*, vol. 10, no. 4, pp. 328–339, Apr. 2018, doi: 10.1038/s41427-018-0036-3.

[196] J. T. Muth *et al.*, “Embedded 3D Printing of Strain Sensors within Highly Stretchable Elastomers,” *Adv. Mater.*, vol. 26, no. 36, pp. 6307–6312, Sep. 2014, doi: 10.1002/adma.201400334.

[197] S. Chen *et al.*, “Acid-Interface Engineering of Carbon Nanotube/Elastomers with Enhanced Sensitivity for Stretchable Strain Sensors,” *ACS Appl. Mater. Interfaces*, vol. 10, no. 43, pp. 37760–37766, Oct. 2018, doi: 10.1021/acsami.8b16591.

[198] H. Lee, B. Seong, H. Moon, and D. Byun, “Directly printed stretchable strain sensor based on ring and diamond shaped silver nanowire electrodes,” *RSC Adv.*, vol. 5, no. 36, pp. 28379–28384, 2015, doi: 10.1039/C5RA01519G.

[199] L. Cai *et al.*, “Highly Transparent and Conductive Stretchable Conductors Based on Hierarchical Reticulate Single-Walled Carbon Nanotube Architecture,” *Adv. Funct. Mater.*, vol. 22, no. 24, pp. 5238–5244, Dec. 2012, doi: 10.1002/adfm.201201013.

[200] L. Jin *et al.*, “Microstructural origin of resistance-strain hysteresis in carbon nanotube thin film conductors,” *Proc Natl Acad Sci U S A*, vol. 115, no. 9, pp. 1986–1991, Feb. 2018, doi: 10.1073/pnas.1717217115.

[201] B.-Y. Lee, J. Kim, H. Kim, C. Kim, and S.-D. Lee, “Low-cost flexible pressure sensor based on dielectric elastomer film with micro-pores,” *Sensors and Actuators A: Physical*, vol. 240, pp. 103–109, Apr. 2016, doi: 10.1016/j.sna.2016.01.037.

[202] J. Shintake, E. Piskarev, S. H. Jeong, and D. Floreano, “Ultrastretchable Strain Sensors Using Carbon Black-Filled Elastomer Composites and Comparison of Capacitive Versus Resistive Sensors,” *Advanced Materials Technologies*, vol. 3, no. 3, p. 1700284, 2018, doi: https://doi.org/10.1002/admt.201700284.

[203] X.-P. Zhou, C. Liu, and K. Zhao, “A novel liquid metal sensor with three microchannels embedded in elastomer,” *Smart Materials and Structures*, vol. 29, Feb. 2020, doi: 10.1088/1361-665X/ab7433.

[204] S. O. Kim, C. J. Han, C.-R. Lee, and J.-W. Kim, “Highly transparent, stretchable, and conformable silicone-based strain/pressure-sensitive capacitor using adhesive

polydimethylsiloxane," *Journal of Alloys and Compounds*, vol. 841, p. 155773, Nov. 2020, doi: 10.1016/j.jallcom.2020.155773.

[205] H. Jin *et al.*, "Stretchable Dual-Capacitor Multi-Sensor for Touch-Curvature-Pressure-Strain Sensing," *Scientific Reports*, vol. 7, no. 1, Art. no. 1, Sep. 2017, doi: 10.1038/s41598-017-11217-w.

[206] V. Tsouti, V. Mitrakos, P. Broutas, and S. Chatzandroulis, "Modeling and Development of a Flexible Carbon Black-Based Capacitive Strain Sensor," *IEEE Sensors J.*, vol. 16, no. 9, pp. 3059–3067, May 2016, doi: 10.1109/JSEN.2016.2524508.

[207] M. K. Filippidou, E. Tegou, V. Tsouti, and S. Chatzandroulis, "A flexible strain sensor made of graphene nanoplatelets/polydimethylsiloxane nanocomposite," *Microelectronic Engineering*, vol. 142, pp. 7–11, Jul. 2015, doi: 10.1016/j.mee.2015.06.007.

[208] H. Dai, G. J. Gallo, T. Schumacher, and E. T. Thostenson, "A Novel Methodology for Spatial Damage Detection and Imaging Using a Distributed Carbon Nanotube-Based Composite Sensor Combined with Electrical Impedance Tomography," *J Nondestruct Eval*, vol. 35, no. 2, p. 26, Mar. 2016, doi: 10.1007/s10921-016-0341-0.

[209] A. Yao and M. Soleimani, "A pressure mapping imaging device based on electrical impedance tomography of conductive fabrics," *Sensor Review*, vol. 32, no. 4, pp. 310–317, Jan. 2012, doi: 10.1108/02602281211257542.

[210] M. Hallaji, "Monitoring Damage and Unsaturated Moisture Flow in Concrete with Electrical Resistance Tomography (ERT)," 2015. doi: 10.13140/RG.2.1.4892.3047.

[211] A. Yao, C. L. Yang, J. K. Seo, and M. Soleimani, "EIT-Based Fabric Pressure Sensing," *Computational and Mathematical Methods in Medicine*, 2013. https://www.hindawi.com/journals/cmmm/2013/405325/ (accessed Sep. 24, 2018).

[212] J. M. S. Caeiros and R. C. Martins, "Electromagnetic tomography: Real-time imaging using linear approaches," in *1st Portuguese Biomedical Engineering Meeting*, Lisbon, Portugal, Mar. 2011, pp. 1–7. doi: 10.1109/ENBENG.2011.6026096.

[213] N. Polydorides, "Image reconstruction algorithms for soft-field tomography," Ph.D., University of Manchester : UMIST, 2002. Accessed: Sep. 21, 2021. [Online]. Available: https://ethos.bl.uk/OrderDetails.do?uin=uk.bl.ethos.488242

[214] P. J. Vauhkonen, M. Vauhkonen, T. Savolainen, and J. P. Kaipio, "Three-dimensional electrical impedance tomography based on the complete electrode model," *IEEE Transactions on Biomedical Engineering*, vol. 46, no. 9, pp. 1150–1160, Sep. 1999, doi: 10.1109/10.784147.

[215] COMSOL, "Detailed Explanation of the Finite Element Method (FEM)," Mar. 15, 2016. https://www.comsol.com/multiphysics/finite-element-method#:~:text=The%20finite%20element%20method%20is%20a%20systematic%20way%2

0to%20convert,are%20tractable%20with%20numerical%20methods. (accessed Sep. 21, 2021).

[216] J. D. Jackson, *Classical Electrodynamics Third Edition*, 3rd edition. New York: Wiley, 1998.

[217] G. Elert, "Electric Potential," *The Physics Hypertextbook*, 2021. https://physics.info/electric-potential/ (accessed Sep. 21, 2021).

[218] M. Karnik, B. Dasgupta, and V. Eswaran, "A comparative study of Dirichlet and Neumann conditions for path planning through harmonic functions," *Future Generation Computer Systems*, vol. 20, no. 3, pp. 441–452, Apr. 2004, doi: 10.1016/j.future.2003.07.008.

[219] V.A. Trenogin, "Galerkin method," *Encyclopedia of Mathematics*. https://encyclopediaofmath.org/wiki/Galerkin_method (accessed Sep. 22, 2021).

[220] B. Rivière, *Discontinuous Galerkin Methods for Solving Elliptic and Parabolic Equations: Theory and Implementation*. Society for Industrial and Applied Mathematics, 2008. doi: 10.1137/1.9780898717440.

[221] D. Holder, *Electrical impedance tomography: methods, history, and applications*. Bristol; Philadelphia: Institute of Physics (Great Britain), 2005. Accessed: Apr. 22, 2022. [Online]. Available: https://doi.org/10.1201/9781420034462

[222] K. Paulson, W. Breckon, and M. Pidcock, "Electrode Modelling in Electrical Impedance Tomography," *SIAM Journal on Applied Mathematics*, vol. 52, no. 4, pp. 1012–1022, 1992.

[223] A. N. Tikhonov, A. Goncharsky, V. V. Stepanov, and A. G. Yagola, *Numerical Methods for the Solution of Ill-Posed Problems*. Springer Netherlands, 1995. doi: 10.1007/978-94-015-8480-7.

[224] A. Adler and R. Guardo, "Electrical impedance tomography: regularized imaging and contrast detection," *IEEE Trans Med Imaging*, vol. 15, no. 2, pp. 170–179, 1996, doi: 10.1109/42.491418.

[225] B. M. Graham, "Enhancements in Electrical Impedance Tomography (EIT) image reconstruction for three-dimensional lung imaging," Thesis, University of Ottawa (Canada), 2007. doi: 10.20381/ruor-12954.

[226] T. Huuhtanen, A. Lankinen, and A. Jung, "Target Tracking with Electrical Impedance Tomography," *arXiv:1911.04851 [eess]*, Nov. 2019, Accessed: Sep. 28, 2021. [Online]. Available: http://arxiv.org/abs/1911.04851

[227] A. Javaherian, A. Movafeghi, and R. Faghihi, "Reducing negative effects of quadratic norm regularization on image reconstruction in electrical impedance tomography," *Applied*

Mathematical Modelling, vol. 37, no. 8, pp. 5637–5652, Apr. 2013, doi: 10.1016/j.apm.2012.11.022.

[228] T. K. Bera, S. K. Biswas, K. Rajan, and J. Nagaraju, "Improving Image Quality in Electrical Impedance Tomography (EIT) Using Projection Error Propagation-Based Regularization (PEPR) Technique: A Simulation Study," *Journal of Electrical Bioimpedance*, vol. 2, no. 1, pp. 2–12, Jan. 2011, doi: 10.5617/jeb.158.

[229] M. Wang, Q. Wang, and B. Karki, "Arts of electrical impedance tomographic sensing," *Phil. Trans. R. Soc. A*, vol. 374, no. 2070, p. 20150329, Jun. 2016, doi: 10.1098/rsta.2015.0329.

[230] H. Kwon, A. L. McEwan, T. I. Oh, A. Farooq, E. J. Woo, and J. K. Seo, "A Local Region of Interest Imaging Method for Electrical Impedance Tomography with Internal Electrodes," *Computational and Mathematical Methods in Medicine*, vol. 2013, p. e964918, Jul. 2013, doi: 10.1155/2013/964918.

[231] P. Kauppinen, J. Hyttinen, and J. Malmivuo, "Sensitivity Distribution Visualizations of Impedance Tomography Measurement Strategies," vol. 8, no. 1, p. 11, 2006.

[232] Q. Li, K. Wang, Y. Gao, J. P. Tan, R. Y. Wu, and F. Z. Xuan, "Highly sensitive wearable strain sensor based on ultra-violet/ozone cracked carbon nanotube/elastomer," *Appl. Phys. Lett.*, vol. 112, no. 26, p. 263501, Jun. 2018, doi: 10.1063/1.5029391.

[233] "CHAPTER 2 - Electrical system analysis," in *Electrical Systems and Equipment (Third Edition)*, Oxford: Pergamon, 1992, pp. 84–192. doi: 10.1016/B978-0-08-040514-8.50010-0.

[234] S. Pisa, E. Pittella, and E. Piuzzi, "Comparisons among EIT data collection techniques and reconstruction algorithms," *Applied Computational Electromagnetics Society Journal*, vol. 32, pp. 473–483, Jun. 2017.

[235] C. L. Lawson, R. J. Hanson, and Society for Industrial and Applied Mathematics, *Solving least squares problems*. Philadelphia, Pa.: Society for Industrial and Applied Mathematics, 1995. Accessed: Dec. 29, 2021. [Online]. Available: http://epubs.siam.org/ebooks/siam/classics_in_applied_mathematics/cl15

[236] J. Anudev and I. J. Raglend, "Analytical study of howland current source model," in *2012 International Conference on Computing, Electronics and Electrical Technologies (ICCEET)*, Nagercoil, Tamil Nadu, India, Mar. 2012, pp. 314–318. doi: 10.1109/ICCEET.2012.6203843.

Appendix A: Hardware

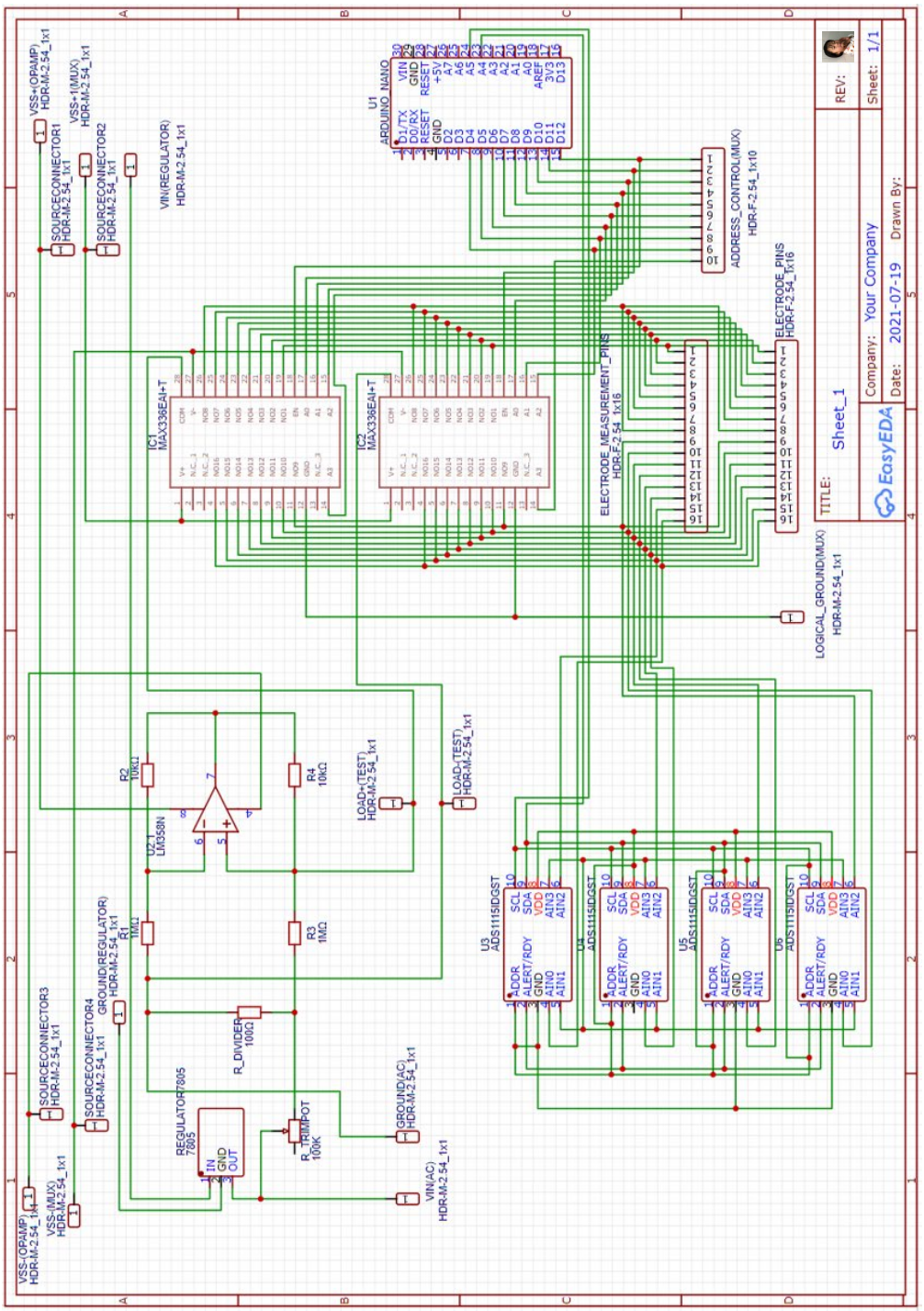

Appendix B: Software

1. **Mesh**: this function generates the finite element mesh using the PdeModeler.

   https://github.com/Rayonz/EIT_MATLAB/blob/main/Mesh

2. **Fwd_solve**: this function assigns some input parameters and solves the forward problem.

   https://github.com/Rayonz/EIT_MATLAB/blob/main/fwd_solve

3. **Calculate_Jacobian:** this function calculates the Jacobian matrix used in the inverse problem solver.

   https://github.com/Rayonz/EIT_MATLAB/blob/main/calculate_Jacobian

4. **voltage_each_injection:** this function calculates and visualizes the electrode voltage data during each current injection.

   https://github.com/Rayonz/EIT_MATLAB/blob/main/voltage_each_injection

5. **Inverse_solve:** this function sets up various regularization matrices and solvers to solve the inverse problem and visualize the solutions.

   https://github.com/Rayonz/EIT_MATLAB/blob/main/Inverse_solve